Studies on the Ion-Droplet Mixed Regime in Colloid Thrusters

by

Paulo C. Lozano
IFI'93, Physics Engineering, ITESM, México
M. en C.'96, Physics, CINVESTAV, México
SM'98, Aeronautics and Astronautics, MIT

Submitted to the Department of Aeronautics and Astronautics in partial fulfillment of the requirements for the degree of

Doctor of Philosophy in Aeronautics and Astronautics
in the field of
Space Propulsion

at the

MASSACHUSETTS INSTITUTE OF TECHNOLOGY

February 2003

Author ……...
Department of Aeronautics and Astronautics
December 12, 2002

Certified by ……
Manuel Martínez-Sánchez
Professor, Aeronautics and Astronautics
Thesis Supervisor

Read by ……..
Juan Fernández de la Mora
Professor, Yale University

Read by ……..
Markus Zahn
Professor, Electrical Engineering and Computer Science

Read by ……..
Jeffrey Lang
Professor, Electrical Engineering and Computer Science

Read by ……..
Daniel Hastings
Professor, Aeronautics and Astronautics

Accepted by ……..……..
Edward M. Greitzer
Chair, Committee on Graduate Students

STUDIES ON THE ION-DROPLET MIXED REGIME IN COLLOID THRUSTERS

by
Paulo C. Lozano

Submitted to the Department of Aeronautics and Astronautics on January, 2003 in partial fulfillment of the requirements for the degree of Doctor of Philosophy in Aeronautics and Astronautics

ABSTRACT

Colloid thrusters working with mixtures of ions and droplets are gradually becoming an alternative technology for space micro-propulsion needs in missions requiring high position controllability, compactness and low power consumption. The mechanics of the colloid thruster emission process are discussed through a theoretical review of its general properties and by means of experimental characterization.

Droplets are the most energetic particles in the beam, while ions are emitted with energies that overlap those of the droplets but extend down a few hundreds of volts in comparison. A small fraction of the ion current is emitted from the jet breakup region with considerably lower energies. This energy variety transforms the optical hardware elements into energy filters by taking advantage of the chromatic aberration property of electrostatic lenses. The relatively wide ion energy distribution is conceptually explained as a result of emission from different locations in the cone-jet structure where the normal electric field is most intense and where the convective current produces drastic changes in the local potential. The energy spread of purely ionic emission from EMI-BF_4 is measured and is found to be of the order of a few tens of volts.

A high-speed electron multiplier detector is used for the first time to analyze the ion component emitted directly from electrospray sources. Ion identification is performed and is found that the most probable degree of solvation is $n = 5.1$ for $(CH_3NO)_nNa^+$ ions in formamide doped with NaI for a conductivity of 2.15 siemens per meter. Two ions are observed for the ionic liquid EMI-BF_4: EMI^+ and $(EMI\text{-}BF_4)EMI^+$. It is found that these ions are emitted with a small energy differential.

The use of 5 micron ID capillary emitters, working with flow rates close to 20 pico-liters per second, is successfully achieved. Under such conditions, highly charged droplets with specific charges in excess of 10 coulombs per gram are obtained, representing the highest charge state obtained so far in experiments of this kind.

The applicability of colloid thrusters for space propulsion is discussed in terms of performance parameters in the ion-droplet mixed regime, along with other practical considerations, such as the problem of beam neutralization.

Thesis Supervisor: Manuel Martínez-Sánchez
Title: Professor of Aeronautics and Astronautics

Acknowledgements

How to convey so many significant things without writing a whole new book on appreciation, humbleness and awe? This is the case for me, right now. Trying to give thanks and credit to all the meaningful people with whom I have shared what I like to call the greatest adventure of all; at MIT and other places. It would be hard, if not impossible, to mention every name, every circumstance. Instead, I would just like to say thank you to all my friends and colleagues at MIT, to the members of my doctoral committee, teachers and mentors. It was with all your help that I was able to study, open a critical mind and explore what I was capable to achieve. In particular, I want to express my gratitude to Manuel, my advisor and good friend. He owns the most lucid mind I have ever known. It has been a privilege to work with him and testify his disposition and excitement when interacting with each and every one of his students.

I want to say thank you to my family: to my parents Alfredo and Vicky for teaching me what life is all about and putting me on the right track. To my brother Jorge and my sister Wendy, they represent both the struggle for success and the tenderness of love. To my brother Juan, his wife Anabella and my three nephews, Bellita, Juanito and Ian Paulo, without any doubt, the best reminder of the immense power that a strong family can have.

Finally, I want to dedicate this thesis along with the time working on it, in the lab and in front of computers, to Marce, my wife, and especially to my unborn child. I still do not know you, not even your name. What I know is that you exist and soon will be here in my arms. Be sure that your dad has been thinking about you all along, and believe also that you have provided him with the ultimate happiness, which he simply cannot describe with words.

Paulo Lozano

MIT, December 2002

Nomenclature

b	Impact parameter (m)
c	Exhaust gas velocity (m/s)
$\bar{c}_i$	Ion thermal velocity (m/s)
C	Capacitance (F ≡ C/V)
d_c	Needle tip ID (m)
D	Electrode separation (m) Tubing diameter (m)
E_L	Laplacian Electric field (V/m)
E_n	Electric field normal to *n* (V/m)
E_r	Radial Electric field (V/m)
f_i^m	Ion mass fraction
f_i	Ion current fraction
$f(\varepsilon)$	F. de la Mora's factor for electrosprays
F	Thrust (N ≡ kg·m/s^2)
G_0	Ion evaporation energy (eV)
i_c	Input current (A ≡ C/s)
I	Total current (A)
I_s	Surface convection current (A)
I_{sp}	Specific impulse (sec)
$\hat{I}_{sp}$	Specific impulse normalized to ions
j	Current density (A/m^2)
K	Conductivity (S/m ≡ C^2·s/kg/m^3)
L	Tubing length (m) Separation distance (m)
L_0	TOF drift distance (m)
m	Particle mass (kg)
$\dot{m}$	Mass flow rate (kg/s)
n	Particle number density (m^{-3})
n_s	Most probable degree of ion solvation
P	Perveance (A/V$^{3/2}$) Pressure (Pa ≡ N/m^2) Jet power (W ≡ J/s)
P_c	Vacuum chamber pressure (Pa)
P_{in}	Gas supply pressure (Pa)
P_m	Mechanical pump pressure (Pa)
P_r	Rocket momentum (N·s)
P_v	Vapor pressure (Pa)
P_o	Liquid container pressure (Pa)
$P_{1/2}$	Legendre polynomial of order 1/2
P^*	Modified perveance (A/V$^{3/2}$)
q	Particle electric charge (C)
q_D	Droplet charge (C)
q/m	Specific charge (C/kg)
Q	Volumetric flow rate (m^3/s)
Q_c	Elastic collision cross section (m^2)
Q_{iD}	Ion-droplet collision cross section (m^2)
$Q_{1/2}$	Legendre function of 2nd kind order 1/2
r	Radial coordinate (m)
r_m	Distance of closest approach (m)
r_o	Initial beam radius (m)
r^*	Electrical relaxation length (m)
R	Gas constant (J/kg)
R_c	Input resistance (Ω ≡ V/A)
R_D	Droplet radius (m)
R_J	Jet radius (m)
S_p	Pumping speed (l/s)
t_d	Signal time delay (s)
t_f	Time of flight (s)
t_r	Signal rise time (s)
t_{rel}	Charge relaxation time (s)
t_{res}	Liquid residence time (s)
t_w	Time of ripple wave propagation (s)
T	Temperature (K)
T_{nm}	Maxwell stress tensor (Pa)
u_s	Fluid surface velocity (m/s)
$\bar{v}_e$	Electron thermal velocity (m/s)
v_g	Gravitational speed loss (m/s)
v_{rel}	Relative velocity (m/s)
v_s	Particle source velocity (m/s)
v_z	Velocity in the *z* direction (m/s)
v_∞	Particle final velocity (m/s)
V_{out}	Output voltage (V ≡ kg·m^2/C/s^2)
W	Energy (J ≡ N·m)
x_m	Gate grid position (m)
x_T	Particle position at gate closing (m)
x_∞	Gate grounded electrode position (m)
x_0	Particle position at gate opening (m)
Z	Partition function

α Angular coordinate (rad)
α_T Taylor cone angle (49.92°)
χ Scattering angle (rad)
$\Delta\left(\frac{q}{m}\right)$ Specific charge spread (C/kg)
Δt Flight time spread (s)
Δv Mission velocity increment (m/s)
$\Delta\varepsilon$ Particle energy change through gate
$\Delta\phi_B$ Beam potential spread (V)
$\Delta\phi_s$ Stopping potential spread (V)
ε Relative dielectric constant
ϕ_a Applied (needle) potential (V)
ϕ_B Beam potential (V)
ϕ_{ex} Extraction voltage $\phi_a - \phi_x$ (V)
ϕ_f Focusing potential (V)
ϕ_m Maximum gate voltage (V)
ϕ_s Stopping (retarding) potential (V)
ϕ_x Extractor potential (V)
ϕ_o Axial potential (V)
γ Surface tension (N/m)
Γ Particle flux ($m^{-2}s^{-2}$)
η Nondimensional flow rate parameter:

$$\eta^2 = \rho KQ/\gamma\varepsilon\varepsilon_o$$

η_p Electric power efficiency
η_{poly} Polydispersity efficiency
η_0 Overall efficiency
λ_D Debye length (m)
λ_{iD} Ion-droplet mean free path (m)
μ Ion mobility (C·s/kg/m)
μ_g Gaseous viscosity (cP)
μ_i Ion chemical potential (J)
μ_l Liquid viscosity (cP)
μ_r Reduced mass (kg)
θ Beam angular deflection (rad)
θ_m Angle of closest approach (rad)
ρ Liquid mass density (kg/m^3)
ρ_c Charge density (C/m^3)
σ Free surface charge density (C/m^2)
ζ Droplet to ion specific charge ratio

amu Atomic mass unit (1.66×10^{-27} kg)
e Electronic charge (1.6×10^{-19} C)
g Earth surface gravitational constant (9.8 m/s^2)
h Planck's constant (6.626×10^{-34} J·s)
k Boltzmann's constant (1.38×10^{-23} J/kg)
m_e Electron mass (9.11×10^{-31} kg)
N_A Avogadro's constant (6.022×10^{23} mol^{-1})
ε_o Permittivity of vacuum (8.854×10^{-12} F/m ≡ $C^2\cdot s^2/kg/m^3$)

1. Introduction

Space Propulsion is the engineering discipline that deals with methods for moving man-made objects once they leave Earth's atmosphere. Since the beginning of the *space age* in the mid 20th Century, an essential part for the success of every mission has been related to the ability to produce in-space velocity changes in a predictable and controllable way.

The fundamental distinction between space propulsion and that used to boost the spacecraft from the planet's surface is the thrust level for each of them. In general, several tons of metal and fuel comprise the bulk of the rocket launcher, which is required to send a given payload into space. In order to be able to counteract the gravitational pull, the booster engine needs to provide a thrust larger than the overall weight for enough time to reach orbital velocities.

Once the vehicle is in orbit, it is usually the case that smaller on-board thrusters take over the spacecraft's control to maintain proper directional attitude or to make corrections to orbital elements. These maneuvers usually require relatively small changes in velocity. On the other hand, sometimes a booster rocket places the vehicle on an initial orbit and a secondary space propulsion engine is used to take the spacecraft to its final orbit or escape trajectory. This *main on-board propulsion* maneuver is more demanding in terms of velocity changes.

Since the amount of hardware mass that can be sent into an initial orbit is limited by the capabilities of the rocket booster, it is highly desirable to optimize the payload's propulsion subsystem: it needs to provide the required performance with minimum weight and power consumption. In particular, every rocket propulsion device consumes propellant as it is ejected at high speeds. The propellant takes, in most instances, a significant proportion of the overall payload mass. Quantitatively speaking, the amount of propellant mass m_p required to perform a given velocity change Δv can be found by applying Newton's second law to a mass varying system moving at a velocity $v = v(t)$ as shown in Figure 1.1.

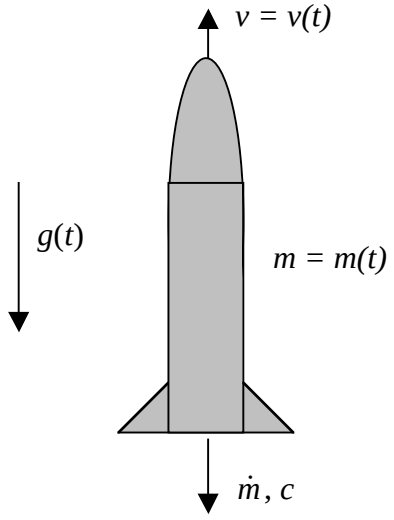

Figure 1.1. Mass varying rocket moving at a velocity *v* under a gravitational field

Assume that the rocket losses mass at a rate $\dot{m} = -dm/dt$ while the exhaust is ejected at a relative velocity *c*. The momentum of the system (rocket + exhaust) is,

$$P_r = m(t)v(t) + \int \dot{m}\big(v(t) - c\big)dt. \tag{1.1}$$

The equation of motion is then (the only external force is gravity),

$$\frac{dP_r}{dt} = -m(t)g(t). \tag{1.2}$$

Substitution of Equation (1.1) into Equation (1.2) yields,

$$m\frac{dv}{dt} = F - mg \qquad \text{with} \qquad F = \dot{m}c = \left(-\frac{dm}{dt}\right)c, \tag{1.3}$$

where F is the engine thrust. Equation (1.3) can be solved to obtain the *rocket equation* in terms of the propellant mass $m_p = m_0 - m_{final}$,

$$m_p = m_0\left(1 - e^{-\frac{\Delta v + v_g}{c}}\right) \qquad \text{with} \qquad v_g = \int_{t_0}^{t_f} g(t)dt. \tag{1.4}$$

Δv is the ideal velocity change, i.e., that with no account for gravity, specified by the mission objectives, m_0 and m_{final} are the initial and final masses of the vehicle and v_g represents a *gravitational speed loss* to account for the finite duration of the impulse in which gravity is accelerating the vehicle backwards. In gravity-free space, $v_g = 0$. The payload mass m_{pay} is simply given by $m_{pay} = m_{final} - m_s$, where m_s represents the structural mass of the propellant containers and other hardware elements, including the mass of the main engines and other subsystems not to be used by the payload. Equation (1.4) ignores the effect of other external forces acting on the vehicle, like atmospheric drag when launching from the Earth's surface.

Nevertheless, it is evident that, unless the exhaust gas velocity is large enough, $m_p \to m_0$ in the limit for large Δv's, thus decreasing the payload mass to very small values, even for the case when the structural mass and the gravitational speed loss are neglected.

The optimization of the propulsion subsystem strongly depends on the ratio $\Delta v/c$, with suitable constraints, such as mass and power. The details of such optimization vary considerably for different mission objectives, but in the most general case, higher exhaust speed translates into better performance.

The exhaust velocity *c* is linked to the amount of kinetic energy contained in the particles that leave the engine. This energy can be derived from a number of sources. Traditionally, chemical reactions have been widely used to provide the heat that eventually turns into the kinetic energy of the combustion products. Other ways of heating the propellant have been explored, for instance, by concentrating solar radiation into a small gas container or using nuclear reactors to transfer energy from the hot fuel elements to the propellant. By far, chemical reactions have been the dominant propulsion technology, especially for booster launcher applications. There is, however, another way to provide the exhaust particles with energy: it is possible to accelerate particles to high speeds using electricity. Engines working under this physical principle are usually known as *electric propulsion* thrusters.

Traditionally, the performance of rocket propulsion systems has been put in terms of a quantity known as *specific impulse* or I_{sp}. From its definition, specific impulse represents the amount of thrust (F) that can be obtained for a given mass flow rate ($\dot{m}$). As an engineering practice, the units of specific impulse are given in seconds, therefore,

$$I_{sp} = \frac{F}{g\dot{m}} \equiv \frac{c}{g}, \tag{1.5}$$

where $g = 9.8$ m/s^2 is the Earth's gravitational constant at ground level. The I_{sp} is closely related to the exhaust velocity *c*. For a fixed thrust level, the higher the I_{sp}, the smaller the required mass flow, consistent with (1.4). The *jet power* of the exhaust is given by $P = \frac{1}{2}\dot{m}c^2$. The thrust can then be written as,

$$F = \frac{2P}{c}. \tag{1.6}$$

In chemical propulsion, the kinetic energy imparted to the gas molecules in the exhaust is correlated to the stored energy in the electronic bonds of molecules and atoms. In fact, a way to produce good chemical fuels is to take molecules with very strong and stable bonds (H_2O, HF, N_2, etc.) and use some energy to break them into weaker, less energetic ones and, if possible, light (H_2, O_2, F_2, HNO_3, etc.). When these substances recombine they give up the bonding energy differential as heat, which then transforms into the kinetic energy of the combustion products. Since the molecular bonding energy per unit mass is a finite quantity, the exhaust gas velocity is restricted to < 5 km/s, or an $I_{sp} < 500$ s for the most energetic reactions. This figure includes the thermodynamic expansion of the combustion products through a nozzle. The chemical limit is reached when every molecule is broken up into free radicals (F, H, O, N, etc.), thus virtually increasing the specific impulse to about 1500 sec. Unfortunately, there is no technology available to store free radicals in a stable way [1].

On the other hand, electric propulsion engines are only limited by the amount of power available on the spacecraft. Optimization parameters are therefore shifted. Power is now the relevant quantity, while mass and the $\Delta v/c$ ratio, among others, become the mission-specific constraints. From Equation (1.6), thrust is proportional to the jet power delivered by the engine and inversely proportional to the gas exhaust velocity. Electric propulsion devices derive their energy from sources that have relatively high mass/power ratios (photovoltaic cells, batteries). As a consequence, the thrust levels are low in comparison to chemical rockets. This is one of the reasons why chemical engines will most certainly remain as the only alternative for booster applications for the foreseeable future.

Electric propulsion is ideal for power-limited, time-insensitive missions that require large overall changes in spacecraft velocities for either attitude control or main on-board propulsion. Higher specific impulses translate into considerable propellant mass savings when compared with chemical options for a given Δv, as given by (1.4). The resulting

lighter spacecraft allows the use of a less powerful, less expensive launch vehicle or, for the same payload weight, propellant mass can be exchanged for more instruments and components, thus increasing the overall value of the mission.

There are two sub-divisions in the electric propulsion family: electrothermal and electromagnetic thrusters. In the first one, electric energy is used to increase the gas temperature before expanding it in a nozzle, while in the second, electric and magnetic fields are used to accelerate the exhaust gas, which is comprised of charged particles. Examples of electrothermal thrusters are the resistojet and the arcjet, while members of the electromagnetic family includes the ion thruster, the Hall-effect thruster, the pulsed plasma thruster (PPT), the magnetoplasmadynamic thruster (MPD), the field emission electric propulsion thruster (FEEP) and the colloid thruster. A brief description of each technology follows.

Resistojets and Arcjets

There are many types of chemical propulsion thrusters, roughly divided in two categories: those using solid propellants and those that work with liquid fuels. Gas-pressurized, monopropellant liquid fuels are widely used in space propulsion. As mentioned before, the performance of chemical engines is determined by the energy released from the propellant reaction. A way to increase this energy is by adding heat from an electrical source.

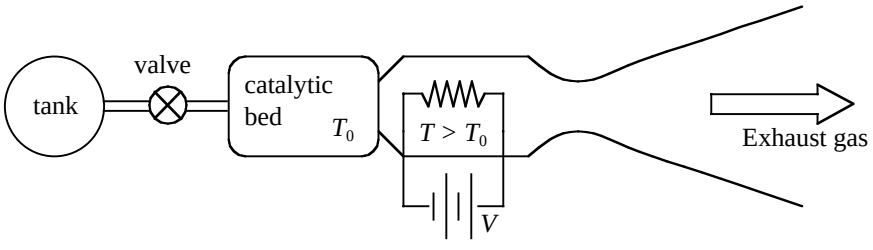

Figure 1.2. Monopropellant resistojet thruster

Figure 1.2 shows a schematic of a monopropellant resistojet thruster. Most of these devices work with liquid fuels such as hydrazine (N_2H_4), which undergoes a very exothermic reaction when exposed to a catalytic bed. The combustion products from this reaction are further heated by means of an electric source, schematically depicted by the battery-resistor pair in Figure 1.2. The superheated gas is allowed to expand through a convergent-divergent nozzle to maximize the exhaust gas velocity. Without the electric heater, the specific impulse of this sort of chemical monopropellant engine is restricted to about 230 sec. The electric heat added is limited by the material thermal properties, such that it maintains its structural integrity. Hydrazine resistojet thrusters can reach a specific impulse of 310 sec. Additional increases are possible if the propellant gas has smaller molecular weight. Heated H_2, for example, can be used to obtain specific impulses as high as 700 sec.

Arcjets work under similar principles. They also increase the energy content of a gasified propellant. The way they work, as seen in Figure 1.3, is by passing some current through a cathode-anode pair in such a way that an electric arc is generated, heating the gas to very high temperatures. The power conversion efficiency is slightly less than for electrojet thrusters, but the specific impulse is higher. For example, hydrazine based arcjets can reach $I_{sp} \approx 600$ s. This value can be increased to 1000 sec if hydrogen is used as propellant.

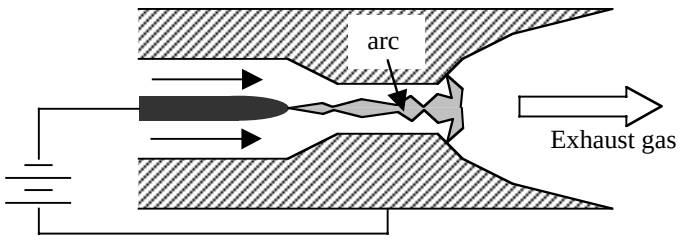

Figure 1.3. Arcjet thruster

Unfortunately, the high specific impulse for hydrogen-based arcjets and resistojets is not easy to implement. Handling of cryogenic propellants, like liquid hydrogen, is difficult, especially if long-term storage is required. The specific impulse gain is offset by the additional complexity. Because of this, electrothermal thrusters are, in general, just marginally superior to their chemical counterparts.

Ion Thrusters

A thruster of this type uses electrostatic fields to accelerate positively charged ions to very high speeds. Ions are created inside the engine cavity by a cathode discharge while neutral gas (Xenon, Argon) is injected. Figure 1.4 shows a schematic of the thruster.

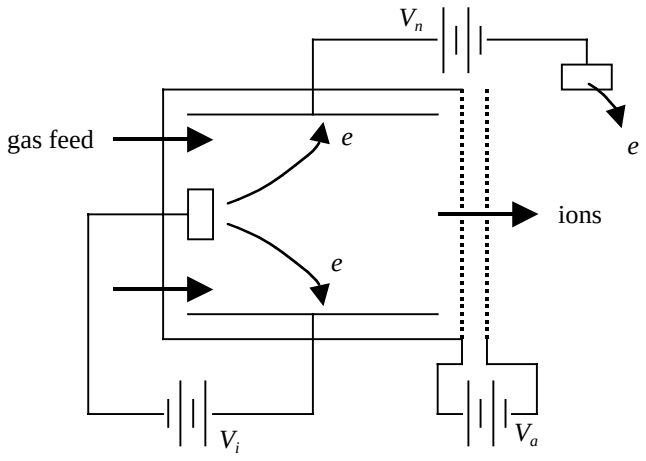

Figure 1.4. Ion thruster

There are three power supplies depicted in the figure. One (V_i) provides the necessary current for the electron current inside the engine body. These electrons collide with neutral particles while diffusing towards the body anode where they are collected. A number of these collisions rip electrons from the outer shell of the propellant gas, ionizing it. In some designs, external magnetic fields provide some electron trapping to lengthen their lifetime in the chamber thus increasing the ionization efficiency. The

electronic current collected by the anode is pumped towards an external cathode by the potential difference of another power supply (V_n). These electrons are emitted by the external cathode to provide neutralization of the ion beam, which is generated by the ionization process inside the thruster chamber and accelerated through a potential difference (V_a) applied to a set of two parallel grids. The potentials on these surfaces are selected in a way that the grids repel electrons, both inside the ionization chamber and outside the engine. As a result, a region of positive charge is created within the acceleration grids. This charge increases to a point where the field is modified and the amount of ion current, therefore thrust, that can be extracted approaches a maximum value. It is said that this device is *space-charge limited*.

The energy conversion efficiency of this thruster is relatively high, as are the specific impulses that can be obtained from them, which in practice vary from 2500 to 4000 sec. They are very good candidates for missions that require large velocity changes. Their power processing units (PPU), however, are complex and relatively heavy.

Hall Effect Thrusters

Developed in Russia, this type of engine makes use of an electrostatic field to accelerate ions to high speeds. The main difference between this device and Ion thrusters, is that the acceleration region is quasineutral, in other words, there are both electrons and ions present, thus eliminating the space-charge limitation. Figure 1.5 shows a cross-sectional schematic of a Hall thruster.

These thrusters possess an annular shape, thus having symmetry around the axial direction, as depicted in Figure 1.5. The structure of the thruster is built in such a way that a radial magnetic field B_r is generated, as shown, by either permanent magnets or external coils. The accelerating axial electric field E_x is introduced by a set of electrodes; an anode inside the body of the thruster and an external cathode, which is also the electron source for beam neutralization. Electrons are axially trapped as they perform Larmor gyrations around the magnetic lines and drift in the azimuthal $\vec{E} \times \vec{B}$ direction. They are also radially trapped by thin electrostatic non-neutral sheaths generated close to

the walls. The neutral gas is ionized by the trapped electrons when collisions occur. Each collision diffuses the electron into a new trajectory closer to the anode, until it is collected. Ions are not trapped since their Larmor radius is large compared to that of electrons; they are simply accelerated by the electrostatic field.

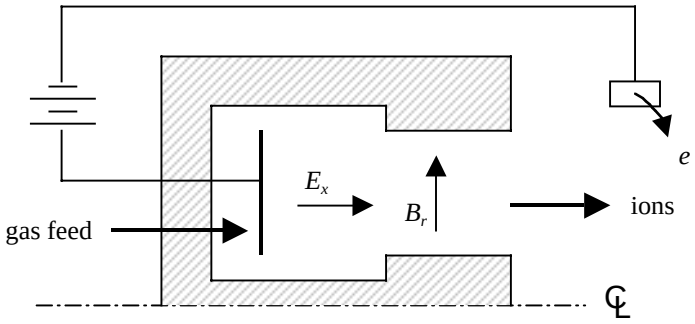

Figure 1.5. Hall-effect thruster

Since the space-charge limitation is removed, there is no theoretical restriction, other than on-board power, to the current and thrust that can be obtained with these devices. Typical specific impulses vary between 1500 and 1800 sec. Hall thrusters receive that name because the thrust mechanism is related to the Lorentz force $\vec{j}_e \times \vec{B}$, where $\vec{j}_e$ is the electronic Hall current of the circulating electrons.

Pulsed Plasma Thrusters (PPT)

Perhaps one of the simplest devices in the space propulsion family, PPT's conceptual design consists of a Teflon block pushed by a spring between two electrodes, as shown in Figure 1.6. A power supply/capacitor system is used to provide fast (μs) high current pulses that evaporate and ionize some of the Teflon. The electric current induces a magnetic field that couples with the ionized gas producing a Lorentz force $\vec{j} \times \vec{B}$ that accelerates the ionized material to high speeds. The efficiency of these devices is

extremely low, while the specific impulse lies between 1000 and 1200 sec. The pulsed nature of these engines makes them suitable for missions requiring fine control or small orbital adjustments.

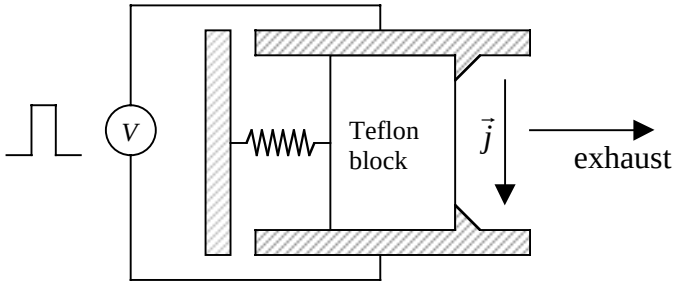

Figure 1.6. Plasma Pulsed Thruster

Magnetoplasmadynamic Thrusters (MPD)

The MPD thruster is a very interesting device in which intense currents are used to induce magnetic fields to produce plasma acceleration. The axially symmetric configuration is shown in Figure 1.7. As in other electric propulsion devices, the thrust mechanism is provided by the Lorentz force $\vec{j} \times \vec{B}$. The azimuthal magnetic field is sustained by a current discharge produced by the power supply between a cathode-anode pair. The same discharge ionizes the propellant gas, which is ejected at very high speeds. Depending on the gas used, the specific impulse can be anywhere from 2000 to 6000 sec. These thrusters, however, have very low efficiencies when the applied currents are small. Most spacecraft rely on photovoltaic cells to generate the power required by electric propulsion thrusters. This power is limited to a few tens of kW for the largest communication satellites. MPD's work best in the mega watt regime, producing relatively high thrust levels. Achieving these powers with conventional methods would be extremely difficult. On the other hand, nuclear reactors could be used to supply the required energy. This would be the ideal situation for MPD's to be considered as a viable

propulsion technology. There is, however, a continuous debate of whether the use of nuclear energy in space is safe. As long as this debate continues, MPD's will remain on the shelf, along with high-power versions of Ion and Hall thrusters.

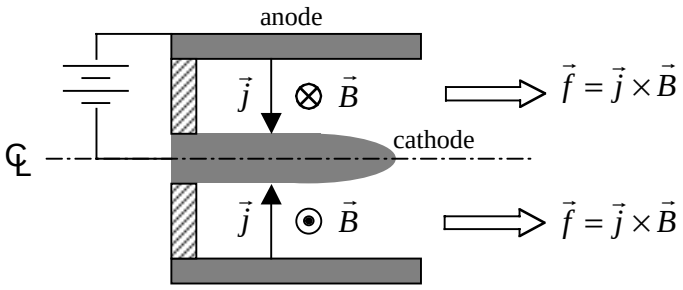

Figure 1.7. MPD thruster

Field Emission Electric Propulsion Thruster (FEEP)

The electromagnetic thrusters described so far rely on gas phase ionization to produce the charged species that are accelerated through suitable fields. An alternative way of producing charged particles is to use liquid phase ionization. In the case of FEEP, a power supply is used to generate an electrostatic field between a liquid metal surface and an electrode, as shown in Figure 1.8. The shape of the liquid meniscus is deformed into a conical shape, thus increasing the local strength of the field, which reaches values high enough to extract ions directly from the liquid surface. An external electron emission cathode (not shown) is required to neutralize the positive ion beam. Most metals need continuous heating to keep them in the liquid phase. The field required to evaporate ions is linked to the surface tension of the liquid metal. Except for Cesium (Cs), the surface tension is very high in most metals, so typical voltages for FEEP operation are > 5 kV. The specific impulse is therefore extremely high, in excess of 10,000 sec. The mass flow rate, however, is very low, so the thrust and current are, in general, small. Given this, these engines are good candidates for missions requiring very fine orbital control.

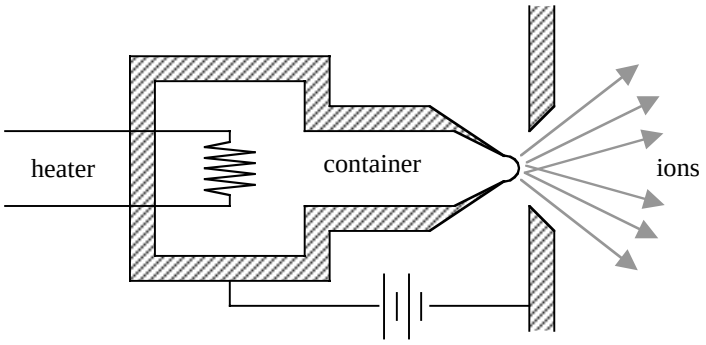

Figure 1.8. FEEP thruster

Colloid Thrusters

Similar to FEEP thrusters, these devices rely on the principle of electrostatic extraction and acceleration of charged particles from the surface of relatively highly conductive liquids (still, orders of magnitude lower than metallic conductivities). The emission mechanics can be viewed as an application of a more general problem in the field of electro-hydrodynamics, usually known as *electrosprays*, where droplets are emitted from a conical-shaped electrically-stressed liquid meniscus.

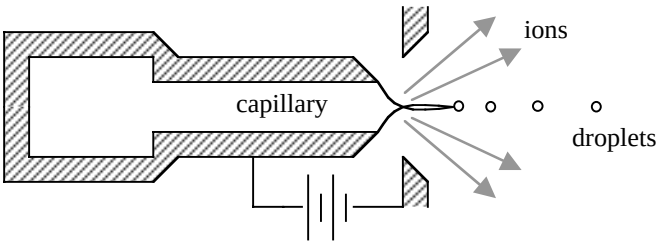

Figure 1.9. Single emitter colloid thruster

One of the main differences with FEEP thrusters is that, under the right conditions, colloid thrusters eject charged droplets, ions or a *mixture* of both. Furthermore, the surface tension of electrospray liquids allows the use of moderate voltages (~1.5 kV for emitter ID ~20 μm). Figure 1.9 shows a schematic of a single emitter colloid thruster. As it will be seen, it is the case that droplets have relatively low specific charge, thus limiting the specific impulse. On the other hand, higher specific impulses and higher currents can be obtained by extracting ions from the liquid surface. This additional flexibility of colloid thrusters makes them very attractive for missions requiring either high resolution in thrust determination (droplets only, low I_{sp}, low current) or high performance (high ion fractions, high I_{sp}, high current).

Brief Review of Colloid Thruster Technology

The idea of using electrospray emissions as the momentum exchange mechanism for space propulsion started in the early 1960's with the work of Krohn [2,3], in which liquid metals and very viscous organic liquids, like glycerol, were first considered. In particular, the ion-droplet mixed regime in colloid thrusters was experimentally observed for the first time in his work. Some understanding of the behavior of glycerol as propellant was gained by work like that of Hendricks and Pfeiffer [4] in which models were developed to explain the flow rate and applied field dependence on specific charge. The first notions related to a decrease in thruster performance due to mixtures of ions and droplets are attributed to Hunter [5].

Time-of-flight measurement techniques to characterize colloid emissions were first developed by Shelton [6] along with Cohen [7] using doped glycerol solutions. The emitters consisted of arrays of Platinum (Pt) tubing of 200 μm ID, and the extraction voltages were around 10 kV. Due to the low conductivity achievable with glycerol, the specific charge was limited to a few hundreds of coulombs per kilogram. In those days, the main interest in developing colloid thrusters was centered in applications requiring relatively large thrust densities to serve as main propulsion engines for spacecraft. To increase the

specific impulse of these engines, an external 120 kV accelerator was added. Such high voltages eventually lead to a number of complications, including x-ray emission. Glycerol was probably selected because of its low volatility (vapor pressure of 0.013 Pa), which minimized the amount of evaporated propellant when exposed to the vacuum of space.

Perel et al. [8] also performed experiments with highly conductive liquids, including Cs and sulfuric acid (H_2SO_4). Such propellants were adequate for obtaining beams containing only ions. On the other hand, sulfuric acid was difficult to handle due to its highly corrosive nature and Cs is also a very reactive element, which spontaneously ignites when exposed to a large number of elements, including water. Instead of those *exotic* propellants, Perel et al. switched back to glycerol and eventually developed a thruster with annular-shaped emitters [9,10]. The reason for this geometry was linked to an increase in thrust density, in agreement with the technological expectations. These thrusters reached specific impulses of about 1500 sec and thrusts of the order of 1 mN using an extraction voltage of 13 kV. In their work, several thruster parameters, like emitted current and thrust, were correlated with flow rate. It is interesting to note that such correlations were in initial agreement with the electrospray scaling laws developed later [11], even though at such high voltages a multitude of cones should form at the tip of the emission sites. The annular thruster geometry was also explored by Huberman and Rosen [12], who built an engine designed to yield about a hundred μN of thrust, using (probably) glycerol as propellant.

In parallel with Perel's work, Kidd and Shelton [6] developed a ~5 mN thruster prototype consisting of 12 arrays, each made out of 36 needles of 130 μm ID. One of such blocks was tested for 4350 hours, providing the first indication on lifetime for colloid thrusters. The operation voltage was 12 kV, with the extractor biased to –2 kV to repel plasma electrons and avoid emitter bombardment. As in all other designs, the liquid was glycerol, this time doped with NaI.

A relatively recent review by Shtyrlin [13] reports on the state-of-the-art in colloid propulsion in Russia, with designs contemporary to those in the US described above. The most relevant feature is the development of a 5 kg *monoblock* thruster capable of producing 1 mN of thrust and specific impulse of 1000 sec, operating at 15 kV.

Other than this early work, the field of colloid thruster development practically vanished for nearly three decades, in part due to the fact that main on-board propulsion was envisioned as its niche application, thus imposing the fundamental requirement of relatively high thrust density and the subsequent need for very high voltages, which made component packaging difficult and increased overall losses. Ion engines, on the other hand, provided the necessary thrust and specific impulse with less complexity, so their development grew up considerably just before colloid thrusters were abandoned.

Recently, there has been an increasing tendency to miniaturize space components, given the economic incentive in launching small and light payloads. This trend has given birth to a categorization of the satellite family by size. Of these categories, of particular interest are the micro and nano-satellites, which are payloads with sizes ranging from several centimeters to about one meter and masses around and below 100 kg. Of course, these values are not rigorously defined, but the important fact is that this family of small satellites also has limited power generation capabilities, so they require low-power, miniature propulsion systems to maintain their orbits and/or perform attitude control maneuvers. Another relatively new application involves the precise control of spacecraft, for example in formation flying between two or more vehicles that perform combined measurements (i.e., interferometry). Thrust levels in the μN range are required to cancel out orbit perturbations, such as the non-homogeneity of the gravitational field of celestial bodies, the solar pressure over spacecraft surfaces, or high altitude atmospheric drag.

It turns out that these types of applications are ideal for low power, low thrust space engines, such as FEEP and colloid thrusters, or miniaturized versions of gas phase electric thrusters. The advantages or disadvantages of each concept is mission dependent and are studied elsewhere [14,15].

Colloid thruster technology is gradually earning an important place given its promises of relative simplicity, performance and compactness. An important step, however, in the thruster development is to have a complete description of its characteristics, from the emission mechanisms to the interaction of these emissions with the spacecraft.

The description of the emission mechanisms has been a matter of continuous research motivated by advances in the field of spray ionization, which practically revolutionized the area of analytical mass spectrometry [16] by allowing the extraction of intact macro-molecules from the surface of liquid solutions. There is a vast amount of literature regarding these advances and it would be practically impossible to make a comprehensive review. Instead, it will only be mentioned that a good number of such works deal with the description and elucidation of the processes involved in the formation of droplets from the cone-jet structures formed on the emitter tips, and their gradual evaporation until individual ions remain, which are then mass-analyzed [17,18,19].

From an engineering perspective centered on space propulsion, one is mostly interested in analyzing the accelerated products of the electrospray, namely, droplets, ions or both. In particular, it is important to quantify their specific charge and energy distributions, since they provide enough information to compute the thrust and determine also the performance in terms of efficiency and specific impulse. The emission processes at the cone-jet level are not completely well understood, even though it is almost certain that they play an important role on the charged particle's distributions.

Thesis Content, Objectives and Contributions

The purpose of this thesis is to trace the lines of research followed in the understanding of colloid thruster emission mechanics in the ion-droplet mixed regime. The document is organized in six chapters, including this introduction. A brief description of colloid thrusters' performance parameters, such as specific impulse and efficiency, are presented in Chapter 2 as functions of the current ion fraction. Since the exhaust of the engine is

comprised of a mixture of particles with diverse inertia properties, a decrease in efficiency can be expected as these particles drift away with different velocities. It will become clear that, unless the ion fraction is relatively high (> 80 %), there is no increase in specific impulse from the lighter ions, and therefore no incentive in designing colloid thrusters working with small ion fractions.

The physics involved in the production of charged particles is discussed in Chapter 3, along with phenomena relevant to thruster operation in the laboratory and in space. In particular the interactions between ions and droplets (scattering and collisions) are analyzed. It is expected that such interactions will be weak, which is fortunate for two reasons: (1) no interaction provides a way to individually characterize the properties of these particles and, (2) there is no additional decrease in thruster performance since both species are independently accelerated.

As in any other charged particle source, the presence of space-charge near the acceleration region could interfere with the emission process. Several 1-D models suggest that these effects are small and can be neglected in most cases. The effect of beam spreading due to self-repulsion forces is analyzed and characterized in terms of operational parameters using a simple model in the absence of axial forces. It is found that beam spreading is strong in most cases of interest and therefore should be taken into account when designing experiments. Finally in this chapter, a brief discussion about electrical and chemical neutralization is presented.

In Chapter 4, the methods, procedures and limitations in performing experimental characterization of electrosprays are outlined. In particular, this is the first work of its kind where 5 μm ID tip emitters are used, thus reducing significantly the evaporation losses when studying volatile solutions in vacuum. Although commonly used in electron and ion beams, electrostatic optical elements are designed and tested for their use on colloid thrusters, therefore increasing the resolution on specific charge measurements and allowing a detailed analysis of the energy characteristics of beams in the ion-droplet mixed regime. The use of an electron-multiplier detector is also introduced to study

colloid beams in this regime, thus providing a way to significantly increase the resolution of ion time-of-flight measurements. A complete characterization of the electrostatic gates used to interrupt the flow of charged particles towards the detector in time-of-flight measurements is presented. It is found that such gates could effectively trap or accelerate some particles thus modifying the outcome of the experiments. On the other hand, this analysis is used to determine under what conditions measurements should be performed to avoid particle-gate interactions.

Experimental results are presented in Chapter 5. The goal of obtaining ion rich particle beams is obtained by using a highly conductive formamide (CH_3NO) solution heavily doped with 28%W (by weight) of NaI and working with small flow rates close to the minimum for stability (20 pl/s). As expected from previous works, the ion fraction and the droplet specific charge increase as the flow rate is decreased. Due in part to the small emitter ID diameters (5 μm) used in this work, a step forward is achieved by minimizing the evaporation losses and obtaining the highest droplet specific charges (> 10 C/gr) observed so far.

The individual energy distributions of ions and droplets is analyzed after recognizing that the chromatic aberration property of electrostatic lenses can be used to separate particles by energy and by using a combination of time-of-flight and retarding potential measurements. It is found that droplets have the highest energies in the beam, while ions posses a rich energy distribution that overlaps with that of the droplets and extends to lower values, showing a considerable energy spread. Even lower energy ions are observed in decreased numbers. Correlated measurements show that these low energy ions are most probably emitted from the liquid jet breakup region. The wide energy distribution of ions is qualitatively explained by the relatively strong change in electric potential along the liquid cone-jet transition region.

In addition, the relatively large energy spread in divergent beams is explained with a simple geometrical model and experimental results show how it can be reduced after beam collimation. The possibility of operating in the highly-stressed regime is discussed

with some experimental results, which suggest that a given thruster can yield very different performance by just increasing the applied potential.

Ions emitted from electrospray sources are identified using the electron multiplier detector for a formamide solution doped with NaI and the ionic liquid 1-Ethyl-3-Methyl-Imidazolium Tetrafluoroborate (EMI-BF_4). The energy spread from the EMI-BF_4 ionic liquid in the purely ionic regime is found to be small compared to the energy widths observed in formamide.

Finally, some concluding remarks and recommendations are written in Chapter 6, followed by some complementary information and references. Although not specifically written for this purpose, this thesis also tries to make the case for colloid thrusters as a viable technology for future spacecraft. The reasons are to be explicitly discussed in the chapters ahead. But perhaps the most appealing one is their simplicity. The underlying physics of electrosprays is very common and was first observed many years ago in the natural world, for example, in the small water sprays produced by convective weather at the tips of pine trees, thus generating the characteristic blue haze on dark nights observed over dense forests [20].

The technology of using electrosprays as space thrusters will advance as long as their simplicity is translated to the engineering area. The first step to achieve this is to better understand the way electrosprays work and determine the best conditions for their application to space thrusters.

2. Characteristics of Colloid Thrusters

2.1. Efficiency

As mentioned in the introduction, missions involving very small and precise velocity changes would benefit from electric propulsion. Current technologies are unable to meet efficient micro-propulsion requirements. Chemical rockets not only lack the desired high specific impulse, but also the precise control capability required by some of these missions [15]. However, electric propulsion also has its limitations when dealing with miniaturization. Plasma effect thrusters do not scale down in a clean way. To maintain the thruster parameters and performance at small sizes, the plasma charge density, for instance, must be larger. In turn, larger densities mean higher rates of material erosion and decreased thruster lifetimes [21].

The best solution to satisfy micro-propulsion requirements involves a combination of the ruggedness of chemical propulsion with the benefits gained from an electric propulsion technology that is intrinsically miniaturized. This is precisely why colloid thrusters represent a viable technology. They work on the principle of charged particle extraction from liquid materials, i.e., they are not based on gas phase ionization.

The performance of any electric thruster, including colloid, can be measured in terms of the energy conversion efficiency from the electric source in the spacecraft to the thrust

power delivered. It is a measure of how well the energy spent in the propulsion subsystem is used to produce the required velocity changes.

The electric energy is in most cases furnished by on-board photovoltaic cells, which, by the way, have relatively low efficiencies. Energy can be further lost by the action of many mechanisms. For example, the power processing units have an intrinsic energy throughput that depends on their particular design and operating conditions. These energy sinks will not be discussed here, since they do not depend directly on the thruster physics.

An efficiency factor η_p can be defined to take into account the different ways in which energy can be lost in the propulsion device. In the case of a colloid thruster, this factor is dominated by the energy spent in the formation of the liquid structure from which charged particles are emitted. Assuming that current is conserved along the transmission line from the power supply to the thruster itself, this energy loss is reflected on a decreased acceleration voltage, so that $\eta_p = \phi_B / \phi_a$, where ϕ_B is the beam acceleration voltage and ϕ_a is the thruster applied voltage.

Colloid thrusters have the interesting property of being able to accelerate both ions and charged droplets in a controlled way. This offers an additional degree of freedom that increases significantly the flexibility of this technology over fixed-composition thrusters. On the other hand, ions and droplets have very different inertia properties. Since both are accelerated with the same potential field, an effect on the thruster efficiency can be expected. This effect, along with that discussed above, can be quantified by the overall efficiency η_0, defined here as the ratio of the minimum power carried by a polydisperse beam to the actual power delivered by the electric subsystem. It is straightforward to see that both parts in this ratio are identical in the case of a monodisperse beam as long as $\eta_p = 1$, therefore,

$$\eta_0 = \frac{F^2 / 2\dot{m}}{\phi_a I}, \tag{2.1.1}$$

where $\dot{m} = \sum_k \dot{m}_k$ is the total mass flow rate, $I = \sum_k I_k$ is the total emitted current, $F = \sum_k \dot{m}_k v_k$ is the total thrust, and v_k is the k^{th} particle velocity, found by applying energy conservation,

$$\tfrac{1}{2} m_k v_k^2 = q_k \phi_B \quad \Rightarrow \quad v_k = \sqrt{2(q/m)_k \phi_B}\,. \tag{2.1.2}$$

For the simple case of *two* types of particles, ions and droplets, the overall efficiency can be written in a simple form as,

$$\eta_0 = \eta_p \eta_{poly} \qquad \text{with} \qquad \eta_{poly} = \frac{\left[1-\left(1-\sqrt{\zeta}\right) f_i\right]^2}{1-(1-\zeta) f_i}, \tag{2.1.3}$$

where η_{poly} is the *polydispersity* efficiency due to the presence of different particles in the beam, $f_i = \dfrac{I_i}{I_i + I_d}$ is the fraction of electric current taken by the ions and $\zeta = \dfrac{(q/m)_d}{(q/m)_i}$ is the droplet to ion specific charge ratio.

The specific impulse (1.5) follows from these definitions, and can be written for this two-particle system as a function of the current ion fraction, normalized by the specific impulse of the ions:

$$\hat{I}_{sp} = \frac{\sqrt{\zeta} - \left(\sqrt{\zeta} - \zeta\right) f_i}{1-(1-\zeta) f_i}. \tag{2.1.4}$$

Finally, in the mixed regime, the amount of ions by mass that leave the thruster are also of importance. To relate this quantity to previous definitions, the ion mass fraction f_i^m is written as,

$$f_i^m = \frac{f_i}{1+\left(\zeta^{-1}-1\right)\left(1-f_i\right)}. \tag{2.1.5}$$

Figure 2.1.1 shows a typical plot of Equations (2.1.3-5) for a mixture of droplets and ions with $\zeta = 0.09$ and considering that $\eta_p = 1$. In later chapters it will be seen that the value of the power efficiency is less than one. In fact, for the typical ion-droplet mixtures used in the experiments, it varies from 80% to 90%.

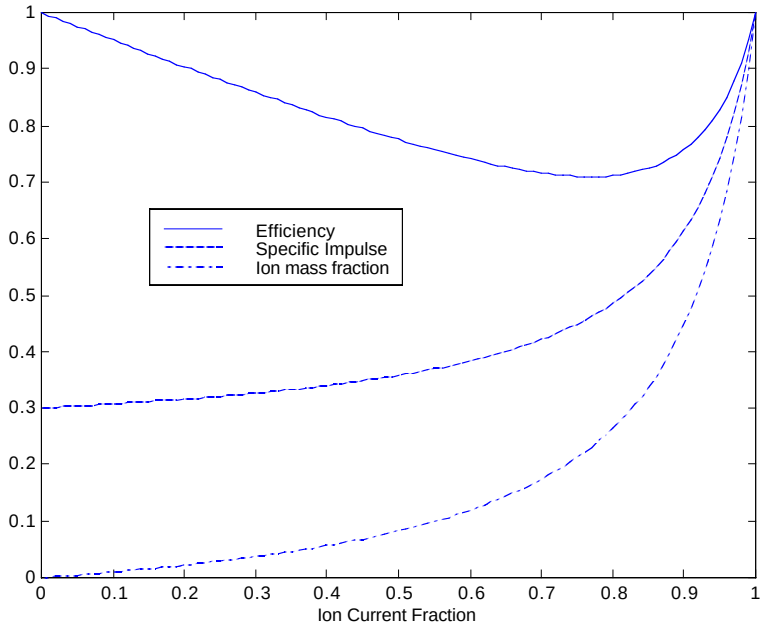

Figure 2.1.1. Efficiency, normalized specific impulse and mass ion fraction with ζ = 0.09 and η_p = 1

It can be seen that the highest efficiencies are only attainable for cases when the thruster operates with only ions or only droplets. The efficiency penalty of operating in the mixed regime, however, is not so large as to be a limiting factor in the performance of colloid thrusters. Nevertheless, it is clear that in the case of Figure 2.1.1 only ion fractions larger than 80% will eventually provide substantial increases in specific impulse.

Yet, colloid thrusters operating in the ion-droplet mixed regime can flexibly adapt to different mission requirements by varying their operational conditions. For example, from Figure 2.1.1, a colloid thruster can be run with zero ion fraction and relatively low specific impulse under certain conditions to cover some mission requirements with 100% polydispersity efficiency. To meet other mission objectives, conditions could be changed to operate with an ion fraction of 90%, thus doubling the specific impulse by having 50% by mass ejected in the form of droplets, allowing larger thrusts with an efficiency penalty of only 20%, or to pure ions, again with full efficiency and over 3 times the specific impulse.

Given the importance of the mixed regime on the eventual application of colloid thruster technology, an important part of the following chapters, in particular the experimental section, will study it in greater detail.

2.2. Implementation

As mentioned in the introduction, colloid thrusters have already been considered for space propulsion applications, but the idea was abandoned after finding several difficulties in providing the required thrust levels. It is almost certain that if the new set of applications that require high precision, low thrust control of spacecraft had been included in those days, colloid thrusters would have been considered as a very viable alternative. As it turns out, scientific and engineering advances in recent years provide a new avenue for considering colloid propulsion even for those applications requiring higher thrusts, placing this developing technology back on track to eventually compete with other systems, chemical or electrical. A few considerations about what can be obtained from these thrusters will help us to understand this perspective.

The most simply and widely used form of electrospray comes in the form of a capillary tubing. The liquid to be ejected moves inside the capillary from a reservoir at a given flow rate. Normally, the end of the capillary is made out of conductive material, such that

an electric contact can be made between the liquid and the power supply. The end itself is also tapered down, so that the outer diameter and inner diameter of the capillary almost coincide, thus helping to avoid wetting of the tubing surfaces that could modify the properties of the electrospray emission process.

The capillaries vary in size and large inner diameters require very high voltages. Higher diameters also mean larger surface areas of liquid exposed to vacuum. If the liquid is volatile, evaporation from the capillary tip could cause several problems, including propellant loss or even freezing. Because of this, small capillary sizes are strongly preferable; they behave better, they are easy to use and their operational requirements are not hard to meet. The size of colloid thrusters is not limited by the physics involved in the emission process. Its lower bound is otherwise limited by manufacturing issues at the smallest scales, along with several operational difficulties, such as clogging due to impurities contained in the liquid.

In practice, electrosprays are efficiently obtained from capillary inner diameters ranging from roughly 1 μm to 100 μm or more. When operating, each of them consumes propellant at a rate of less than 1 nl/s emitting charged particles for current levels in the nA level. Thrust per capillary is typically in the sub μN range. It is not surprising that great efforts were required to obtain mN thrusts for the main on-board applications targeted in the past. This was accomplished by changing the geometry of the emitters [9,10]. Instead of individual capillaries, annular arrangements were explored in which very large electric fields produced the necessary currents to reach those thrust levels.

Alternative geometries were the best choice to increase the amount of thrust that can be obtained from colloid thrusters. The reason for this is simple: given the microscopic thrust per capillary, a very large amount of them would be required. It was just impractical to manufacture an array of thousands or even millions of emitters in a reasonable space, with high reliability, low weight and cost.

When these thrusters were studied, the area of micro-fabrication was just starting to evolve from the strong technological developments generated by the electronic industry. By now, this micro, and nano-technology tool permeates practically all areas of engineering and keeps on growing in response to demanding requirements.

Micro-fabrication of emitter arrays can be performed to obtain practically every thrust level reached by any electric thruster, thus re-opening the door of on-board main propulsion applications and giving more flexibility to those requiring high precision control. There are currently some designs in development [22,23] aimed at converting the colloid emitter into the nucleus of space propulsion technology, in a way similar to what the transistor did for the electronic industry. Most of these designs are exploratory in nature, but would eventually lead to advances in other areas, like pharmaceutical or in the analytical industry [24].

Another alternative to the capillary system that could benefit from the micro-fabrication technology would be something similar to what is done with FEEPs, where liquid metals are used instead of organic solutions. Some liquid metal emitters use solid needles instead of capillary tubes. Flow towards the needle tip is external and self-controlled by the applied potential and the shape and texture of the needle surface. As will be discussed in Chapter 4, there are some liquids that can be used as colloid propellants that exhibit zero vapor pressure and are therefore excellent candidates for external wetting of solid needles.

3. Physics of Colloid Thrusters

3.1. Droplet Emission Mechanics: Taylor Cones

Whenever an electric field is applied in a region where a liquid/solid interface is located, there will be charge migration to the material interfaces where the conductivity is discontinuous. In a colloid thruster, a conductive liquid moves inside a capillary cavity while an electric field is applied by means of an extraction electrode positioned at some distance from the capillary tip as shown in Figure 3.1.1.

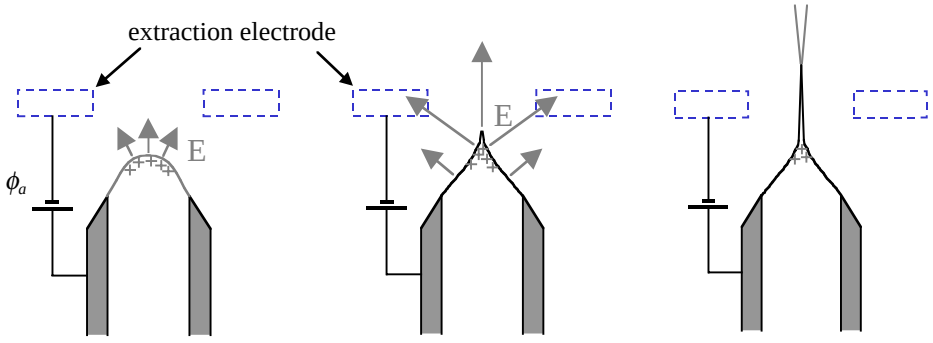

Figure 3.1.1. A single emitter colloid thruster – sequence with increasing ϕ_a

As the applied potential ϕ_a is increased, the normal electric field E_n (assuming that the liquid is a perfect conductor, tangential components are equal to zero) increases. The normal force is,

$$f_n = \oint T_{nm}\, n_m da, \tag{3.1.1}$$

where n_m is the m^{th} component of the unitary normal vector and T_{nm} is the Maxwell stress tensor,

$$T_{nm} = \varepsilon E_n E_m - \tfrac{1}{2}\varepsilon \delta_{nm} E_k E_k . \tag{3.1.2}$$

The normal component of the stress tensor (related to the local normal force per unit area, sometimes known as the electric pressure) is obtained after taking $m = n$ in (3.1.2),

$$T_{nn} = \tfrac{1}{2}\varepsilon\left(E_n^2 - E_{t1}^2 - E_{t2}^2\right). \tag{3.1.3}$$

For a perfect conductor, the tangential components of the electric field in Equation (3.1.3) vanish, therefore $E_{t1} = E_{t2} = 0$. At some specific ϕ_a, the surface deforms into a conical structure. G.I. Taylor, in his classic papers [25] studied the characteristics of this phenomenon in great detail. Taylor established that the internal angle of these cones is uniquely determined after constructing a model in which the forces at play are equilibrated. On one hand, there is the electrostatic pull, or traction, given by (3.1.3). This force is opposed by the local surface tension force, which strives to keep the liquid together and is given, per unit area, by,

$$f_{st} = \gamma \nabla \cdot \hat{n} \qquad \text{with} \qquad \nabla \cdot \hat{n} = \left(\frac{1}{R_1} + \frac{1}{R_2}\right), \tag{3.1.4}$$

where $\hat{n}$ is the unit vector normal to the surface, γ is the liquid interfacial surface tension and R_1 and R_2 are the principal radii of curvature at a particular point over the liquid

surface. In spherical coordinates (Figure 3.1.2) with the origin set at the apex of a cone with inner semi-angle α, $R_1 = \infty$ (straight line along the $\hat{r}$ direction on the cone surface) and $R_2 = r\tan\alpha$ (Meusnier theorem). Making Equation (3.1.3) equal to (3.1.4), an expression for the normal electric field is found,

$$E_n = \sqrt{\frac{2\gamma\cot\alpha}{\varepsilon_o r}}. \tag{3.1.5}$$

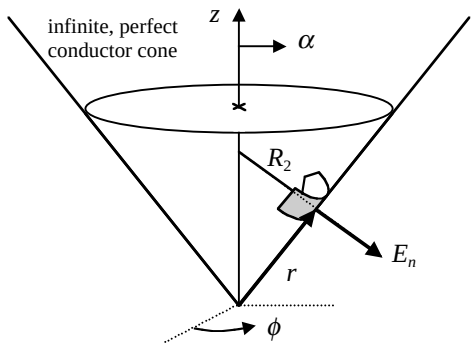

Figure 3.1.2. Geometry of a Taylor cone with inner angle α

The electric field increases with decreasing *r* and exhibits singular behavior as $r \to 0$. If it is assumed that the region outside the cone is charge-free, then Laplace's Equation can be solved in the axisymmetric case ($\partial/\partial\phi = 0$),

$$\nabla^2\Phi \equiv \frac{1}{r^2}\frac{\partial}{\partial r}\left(r^2\frac{\partial\Phi}{\partial r}\right) + \frac{1}{r^2\sin\alpha}\frac{\partial}{\partial\alpha}\left(\sin\alpha\frac{\partial\Phi}{\partial\alpha}\right) = 0. \tag{3.1.6}$$

The solution of (3.1.6) is a superposition of functions containing Legendre Polynomials,

$$\Phi_1 = \sum_v A_{1,v}P_v(\cos\alpha)r^v \quad \text{and} \quad \Phi_2 = \sum_v A_{2,v}Q_v(\cos\alpha)r^v. \tag{3.1.7}$$

The normal electric field ($E_n = E_\alpha$) can be calculated from the electric potential definition,

$$E_n = -(\nabla\Phi)_\alpha = -\frac{1}{r}\left(\frac{\partial\Phi_1}{\partial\alpha} + \frac{\partial\Phi_2}{\partial\alpha}\right). \tag{3.1.8}$$

Direct substitution of (3.1.7) into (3.1.8) yields,

$$E_n = \sum_\nu \left(A_{1,\nu}\frac{\partial P_\nu}{\partial\cos\alpha} + A_{2,\nu}\frac{\partial Q_\nu}{\partial\cos\alpha}\right)\frac{\sin\alpha}{r^{1-\nu}}, \tag{3.1.9}$$

which can be compared against Equation (3.1.5). The two expressions are equal only when $\nu = \frac{1}{2}$, therefore the potential outside the cone is,

$$\Phi = \left(A_1 P_{1/2}(\cos\alpha) + A_2 Q_{1/2}(\cos\alpha)\right) r^{1/2}. \tag{3.1.10}$$

In Figure 3.1.3, plots of Legendre polynomials with $\nu = \frac{1}{2}$ are shown as functions of α.

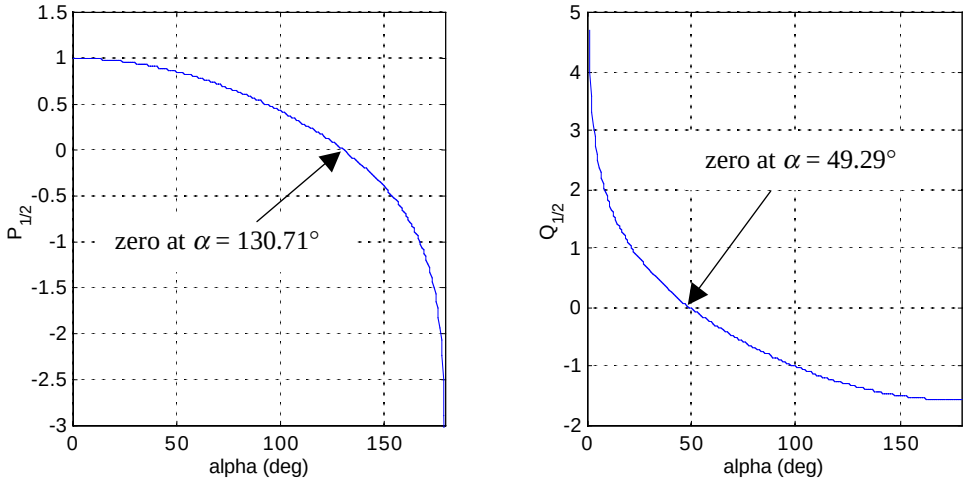

Figure 3.1.3. Legendre polynomials with ν = 1/2 as functions of α

The Legendre function $P_{1/2}$ is singular when $\alpha = \pi$, while $Q_{1/2}$ is singular at $\alpha = 0$. (More information on these functions can be found in Appendix A). The goal here is to compute the electric potential in regions outside of the cone, therefore, for the axis selection shown in Figure 3.1.2, it is required that $A_1 = 0$, for the potential to remain finite.

Furthermore, since the cone surface is an equipotential, a specific angle $\alpha = \alpha_T$ for which Φ is independent of *r* must exist. Defining the cone potential at the ground level, this condition is met if (3.1.10) vanishes for any *r*, in other words $Q_{1/2}(\cos\alpha_T) = 0$. Only one root for this equation exists, yielding what is known as the Taylor angle, with a value of $\alpha_T = 49.29°$. This angle determines the cone surface geometry and is independent of the liquid parameters or the fields involved. Taylor's result is supported by photographic studies of electrostatically stressed menisci, some of them showing a remarkable agreement with his predictions, especially for liquid metals. The constant A_2 in (3.1.10) can be evaluated at the cone's surface with the help of (3.1.5) to obtain the final form of Taylor's solution,

$$\Phi(r,\alpha) = \sqrt{\frac{2\gamma\cot\alpha_T}{\varepsilon_o}\left[\frac{Q_{1/2}(\cos\alpha)}{Q'_{1/2}(\cos\alpha_T)}\right]}\frac{r^{1/2}}{\sin\alpha_T}, \qquad \text{with} \quad Q'_{1/2}(\cos\alpha_T) = \left.\frac{\partial Q_{1/2}(\cos\alpha)}{\partial\cos\alpha}\right|_{\alpha=\alpha_T}. \tag{3.1.11}$$

It is evident from (3.1.5), that something has to yield before the singularity is reached as $r \to 0$. The issue is resolved as the electric stress overcomes the surface tension force, deforming the tip of the cone into a thin liquid jet that moves away from the conical structure at high speeds. The force balance close to the tip is broken as the liquid residence time becomes comparable to the electrical relaxation time. This means that not enough charge reaches the surface of the liquid and therefore it is not possible to maintain the conical shape.

Once the thin jet emerging from a Taylor Cone travels a certain distance, a mechanism similar to that found in uncharged liquid columns appears, and the jet breaks up into a spray of droplets. A linear analysis of this mechanism introduces the effect of the electric field [26] and produces droplets that are slightly smaller than the 1.89 droplet-to-jet radius predicted by the classic Rayleigh instability analysis for free liquid jets. The model also predicts a faster instability onset. The emitted droplets are charged approximately to the Rayleigh limit, depending on the liquid polarity. Although not rigorous, a simple static analysis in which the internal pressure of $2\gamma/R_D$ is balanced by the electric pressure of $\frac{1}{2}\varepsilon_o E^2$ at the droplet surface (R_D is the droplet radius) can be used to estimate the scale of the Rayleigh limit. Assuming that the droplet is spherical, the electric field at the surface is $E = q_D/\left(4\pi\varepsilon_o R_D^2\right)$ with q_D being the droplet charge. The equilibrium condition specifies the maximum charge that could be stably held in a spherical droplet,

$$q_D^{\max} = 8\pi\sqrt{\gamma\varepsilon_o R_D^3}\,. \tag{3.1.12}$$

This maximum, however, is usually not reached since the complete problem should be treated from a dynamic perspective [27]. In practice, the droplet becomes unstable when $0.5q_D^{\max} < q_D < q_D^{\max}$ in (3.1.12) due to fast instability growth when its shape departs appreciably from the spherical baseline. In a non-neutralized droplet beam made of a volatile liquid exposed to vacuum, evaporation would increase the charge level beyond this point, causing *coulombic explosions* [28] that would create secondary charged species, smaller in size.

Another important consideration has to do with ion emission. For now it is enough to say that even though a maximum of the electric field appears near the cone apex, the droplets emitted can be very small and therefore the self-electric field on their surface could reach the condition for ion emission. These ions would have energies considerably lower than those emitted from the cone tip, since they are born at a potential level that is closer to the extractor voltage.

The coulombic explosion phenomenon is widely used in mass spectroscopy to extract ions directly from charged droplets, which, after being electrostatically sprayed, are gradually evaporated by successive collisions with a heated gas on their way to the analytical chamber. This technique, primarily developed by Fenn et al. [16], has provided the means for extracting intact macromolecules from liquid solvents. Previous methods rely on gas phase ionization, which frequently destroys the molecules, precluding an accurate study of their masses.

Understanding the mechanics of the transition from the conical shape to the jet has been a matter of vigorous research in recent years. Several authors [29,30,31,32,33,34,35] have explored the possibility of building analytical and numerical models to predict the transition and to quantify the variables involved. However, the problem is not simple since the system of differential equations needed to be solved is very stiff, given the large disparities in scales. For example, a Taylor cone base of 0.1 mm in diameter could generate a 100 nm wide jet, three orders of magnitude difference in size. In addition, most changes occur in a very small region close to the cone tip. Numerical methods require cumbersome discretization procedures with adaptive grids, while most analytical approaches, with a few exceptions [36], can only show the asymptotic behavior at regions far away from the transition region.

Besides the liquid shape change, another distinctive variation that occurs in the cone-jet transition region is the charge transport mechanism. For a fixed flow rate, far upstream in the cone base the fluid velocity is small and only conduction is important, while downstream in the jet, the contribution from surface charge convection becomes increasingly relevant. F. de la Mora and Loscertales [11] have proposed an interesting and useful theoretical approach to estimate the electrospray current from operational conditions by exploiting this charge transport distinction.

The main assumption behind the model developed in Ref. [11], states that surface charge convection becomes dominant at regions close to the cone tip where the liquid residence time,

$$t_{res} \approx \frac{r^3}{Q}, \tag{3.1.13}$$

(where Q is the liquid flow rate and r the local cone-jet radius), becomes comparable to the electric relaxation time,

$$t_{rel} = \frac{\varepsilon\varepsilon_o}{K}, \tag{3.1.14}$$

where ε is the relative dielectric constant of the liquid and K its conductivity. The condition $t_{res} = t_{rel}$ defines a characteristic length r^*, called the *electrical relaxation length* in Ref. [11] and is given by,

$$r^* = \left(\frac{\varepsilon\varepsilon_o Q}{K}\right)^{1/3}. \tag{3.1.15}$$

If the fluid surface velocity is u_s, then that part of the current carried by convection is,

$$I_s = (2\pi r \sin\alpha_T)\sigma u_s. \tag{3.1.16}$$

u_s is obtained from the flow rate $Q = Au_s$, where,

$$A = 2\pi r^2(1-\cos\alpha_T), \tag{3.1.17}$$

is the cross-sectional area, which can be calculated directly for the hemispherical surface delimited by the base of the Taylor cone and σ is the free surface charge density. Neglecting the field inside the liquid, by assuming full relaxation, the surface charge,

$$\sigma = \varepsilon_o E_n, \tag{3.1.18}$$

follows from Gauss' law, where the normal field E_n is given by (3.1.5) at $\alpha = \alpha_T$. In this way, the surface current can be written as,

$$I_s = Q\sqrt{\frac{2\gamma\varepsilon_o \sin\alpha_T \cos\alpha_T}{r^3(1-\cos\alpha_T)^2}}. \tag{3.1.19}$$

It is assumed that the actual current I emitted from the cone-jet structure approaches the surface convection current I_s when $r \to r^*$, thus,

$$I = \sqrt{\frac{\sin 2\alpha_T}{(1-\cos\alpha_T)^2}\frac{\gamma K Q}{\varepsilon}}. \tag{3.1.20}$$

Extensive experimentation performed by F. de la Mora and Loscertales [11] shows an excellent correlation between measured current and an expression similar in form to Equation (3.1.20),

$$I = f(\varepsilon)\sqrt{\frac{\gamma K Q}{\varepsilon}}, \tag{3.1.21}$$

where $f(\varepsilon)$ is a liquid dependent factor of order 20 for liquids with relatively high dielectric constants ($\varepsilon > 40$ [11]). The model discussed to obtain (3.1.20) predicts a unique value for the function $f(\varepsilon)$ that depends exclusively on the Taylor cone angle. Evaluation of the function in (3.1.20) results in $f(\varepsilon) = 2.86$. The difference between this theoretical value and the experimental observations is possibly linked to the internal field in the liquid, which is neglected in (3.1.18), but would depend on the dielectric constant ε if it had been kept in the analysis. Nevertheless, the functional $\sqrt{Q}$ dependence on the emitted current is extremely important, and with the empirical corrections established in Ref. [11], it is expected that Equation (3.1.21) will predict accurately the properties of electrosprays working in the droplet regime.

The experimental conditions under which (3.1.21) is valid are determined with respect to the non-dimensional flow rate parameter given in Ref. [11], by

$$\eta = \sqrt{\frac{\rho K Q}{\gamma \varepsilon \varepsilon_o}}, \tag{3.1.22}$$

where ρ is the liquid mass density. The current calculated by (3.1.21) holds for high values of η (up to the experimental limitations), but as the flow rate decreases, there is a point for values of η of order unity where droplet emission becomes intermittent and eventually stops. The reason why the flow reaches this minimum is still a matter of debate, but it could be related to a couple of reasons:

a) The specific charge of the emitted droplets increases as the flow rate decreases. This can be seen by using (3.1.21),

$$\frac{q}{m} = \frac{I}{\rho Q} = \frac{f(\varepsilon)}{\rho}\sqrt{\frac{\gamma K}{\varepsilon Q}}. \tag{3.1.23}$$

The total charge per unit mass, however, cannot increase beyond the point where full charge depletion occurs, i.e., the droplets contain the original ion concentration, but no counter-ions, then,

$$\left.\frac{q}{m}\right|_{\max} = \frac{\rho_c}{\rho}, \tag{3.1.24}$$

where ρ_c is the charge density. The classical conductivity model assumes charges moving at speed *u* in a medium due to an external electric field E_c. This force field is closely (but not completely) balanced by drag, so the equation of motion is,

$$qE_c - m\nu u \approx 0, \tag{3.1.25}$$

where q and m are the particle's charge and mass and ν is the frictional drag coefficient (in s^{-1}). Defining the charge mobility as $\mu = q/(m\nu)$, the conduction current density is,

$$j_c = KE_c \quad \text{where} \quad K = \rho_c \mu. \tag{3.1.26}$$

Setting Equation (3.1.23) equal to (3.1.24) and using (3.1.26) and (3.1.22), an expression for the non-dimensional minimum flow rate in terms of the ion mobility μ is found,

$$\eta_{\min} = \sqrt{\frac{\rho}{\varepsilon_o}} \frac{f(\varepsilon)}{\varepsilon} \mu. \tag{3.1.27}$$

Experimental evidence with several solvents [11] has shown that the value of (3.1.27) is close to unity. The weakness of this explanation is, of course, the proportionality to the mobility, which can vary considerably for different liquids in a similar way to viscosity.

b) From linear analysis theory, the frequency of surface tension waves (similar to ripple waves generated under the wind action on a flat lake surface) is,

$$\omega = \left(\frac{\gamma}{\rho r^3} \right)^{1/2} \approx \frac{1}{t_w}, \tag{3.1.28}$$

where r is the characteristic size of the waves. The inverse of (3.1.28) is proportional to the time of wave propagation t_w. The residence time of the liquid in the cone-jet transition region scales as Equation (3.1.13). If the residence time is longer than the wave propagation time, then the perturbations created by such waves (assuming, as is likely, that they are unstable) will have enough time to grow and eventually disturb the conical structure. The instability condition $t_{res} > t_w$ can be put in terms of the non-dimensional flow rate (3.1.22) by taking

the characteristic size of the transition region to be equal to the electrical relaxation length (3.1.15).

After some simple algebraic manipulations, it is found that the instability criterion $t_{res} > t_w$ for this order-of-magnitude estimation is precisely $\eta < 1$. This argument still needs to be formally developed in a conical geometry with flow properties and electric stresses, but it at least provides an indication that the cone-jet disruption may be a result of mechanical instabilities.

3.2. Ion Emission

From (3.1.5), the normal electric field along the liquid surface increases towards the cone tip. Eventually, the normal field could reach values high enough to start extracting ions directly from the surface. This process is known as field evaporation, and as mentioned before, is the mechanism by which liquid metal ion sources work.

Ion emission is an activated process that used to be described using the rate theory of reactions of ideal substances [37]. Such descriptions, however, are frequently obscure and imprecise. Instead, statistical mechanical arguments can be directly applied to obtain a rigorous description of the emission process [38], results of which were first used by Iribarne and Thomson [39] to explain ion evaporation from charged droplets.

Assume a system of ions that are distributed in a material surface and in a gas adjacent to it. The equilibrium condition for the reaction,

$$(ion)_{surface} \leftrightarrow (ion)_{gas}, \tag{3.2.1}$$

which brings ions from the surface of the material to the gas and vice versa is,

$$(\mu_i)_{surface} = (\mu_i)_{gas}, \tag{3.2.2}$$

where μ_i is the ion chemical potential. For a Maxwell-Boltzmann dilute system this condition translates into,

$$-kT\ln\left(\frac{Z_{i,s}}{N_{i,s}}\right) = -kT\ln\left(\frac{Z_{i,g}}{n_{i,g}}\right), \tag{3.2.3}$$

where k is Boltzmann's constant and T is the temperature of the system, which is assumed constant. $N_{i,s}$ is the number of ions per unit area in the material surface, while $n_{i,g}$ is the number of ions per unit volume in the gas. The partition functions, Z ,must reflect that dimensionality in Equation (3.2.3).

For an ion in the surface, assuming that it is free to move in 2 dimensions only, the partition function is given by,

$$Z_{i,s} = Z^{\text{int}}\left(\frac{2\pi m_i kT}{h^2}\right), \tag{3.2.4}$$

where m_i is the ion mass and h is Planck's constant, and the ion's internal partition function Z^{int} due to rotational, vibrational and excitational degrees of freedom, has been separated from the 2-D translational partition function. In a similar way, and considering that the energy zero is established with respect to the surface ions, the partition function in the gas phase is,

$$Z_{i,g} = Z^{\text{int}}\left(\frac{2\pi m_i kT}{h^2}\right)^{3/2} e^{-\frac{G_0}{kT}}, \tag{3.2.5}$$

where 3-D translational degrees of freedom have been considered and G_0 is the evaporation energy, again, with respect to the zero energy set to the ions in the surface. Therefore, from (3.2.3),

$$\frac{n_{i,g}}{N_{i,s}} = \frac{Z_{i,g}}{Z_{i,s}} = \left(\frac{2\pi m_i kT}{h^2}\right)^{1/2} e^{-\frac{G_0}{kT}}, \tag{3.2.6}$$

where it has been assumed that the internal partition functions for ion in the surface and in the gas are comparable. Assuming further that the distribution function of ions in the gas phase is isotropic, the ion flux through any plane is given by,

$$\Gamma = \frac{n_{i,g}\bar{c}_i}{4}, \tag{3.2.7}$$

which is also the rate of arrival ions to the surface. For a maxwellian distribution function, the ion thermal velocity is,

$$\bar{c}_i = \sqrt{\frac{8kT}{\pi m_i}}. \tag{3.2.8}$$

The ion flux is then,

$$\Gamma = N_{i,s}\frac{kT}{h}e^{-\frac{G_0}{kT}}. \tag{3.2.9}$$

Multiplying times the charge and noting that $N_{i,s}$ is precisely the surface charge density σ, the current density coming from the gas side is,

$$j = \sigma\frac{kT}{h}e^{-\frac{G_0}{kT}}. \tag{3.2.10}$$

Now, in equilibrium, this same current must be leaving in the opposite direction (surface to gas). If one removes the gas ions, the emission rate in this non-equilibrium situation

should not be very different, because the liquid is only weakly affected by the presence or absence of the ion gas.

Equation (3.2.10) describes a thermally activated process in which the temperature of the material surface determines the amount of ion current that can be obtained. The thermal limitation can be reduced substantially by applying an external electric field normal to the surface in the direction of ion extraction.

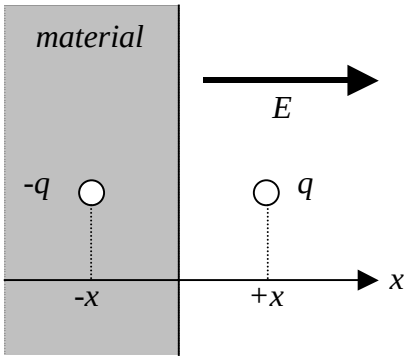

Figure 3.2.1. Image charge model for potential energy calculation with material of infinite dielectric constant

To quantify this situation, the work W (potential energy) of an extracted ion with charge q in the presence of an electric field E is computed assuming the only force that binds it to the surface is that of its image inside the material as depicted in Figure 3.2.1. It is assumed also that the dielectric constant of the material is large enough so that the image particle has the same charge in magnitude, but with opposite polarity, as the extracted ion. This is consistent with experimental and theoretical analysis [40] using dielectric liquids, even though the difference in conductivities with metals is extremely large.

The potential energy is formed by two parts: that of bringing the particle from infinity to a position x from the material surface under the image force, plus that of applying the electric field, which is assumed to vanish at infinity

$$W = \int_x^{\infty} F dx \qquad \text{with} \qquad F = \frac{-q^2}{4\pi\varepsilon_o (2x)^2} + qE \,. \tag{3.2.11}$$

Integration of (3.2.11) is straightforward, and the potential energy is

$$W = -\frac{q^2}{16\pi\varepsilon_o x} - qEx \,. \tag{3.2.12}$$

This potential energy has a maximum, which can be found by setting the derivative of (3.2.12) to zero and solving for *x*,

$$x_m = \left(\frac{q}{16\pi\varepsilon_o E} \right)^{1/2} . \tag{3.2.13}$$

The value of the potential energy at this point is given by,

$$W_{\max} = -\left(\frac{q^3 E}{4\pi\varepsilon_o} \right)^{1/2} . \tag{3.2.14}$$

This is the so-called Schottky depression, and its net effect is to decrease the potential barrier G_0 in (3.2.10) by (3.2.14). Finally, the emitted ion current density with an external field can be written as

$$j = \sigma \frac{kT}{h} e^{-\frac{1}{kT}\left(G_0 - \left(\frac{q^3 E}{4\pi\varepsilon_o} \right)^{1/2} \right)} . \tag{3.2.15}$$

For many solutes, the energy barrier G_0, also called the free energy of solvation is of the order of 1-2 eV [39,41], meaning that, for this case, the condition required for abundant ion emission is reached when,

$$E > \frac{4\pi\varepsilon_o G_0^2}{q^3} \approx 1-2\,\mathrm{V/nm}. \tag{3.2.16}$$

In colloid thrusters, it is expected that ions could be emitted from the surface of the stressed liquid in regions where the electric field satisfies (3.2.16). Gamero [41] has postulated that in a cone-jet structure, the electric field reaches a maximum value near the transition region discussed in Section 3.1. His argument follows from Equation (3.1.5), in which the electric field increases towards the tip from the base of the cone. The field generated by the thinning cylindrical jet also increases towards the transition region. As can be seen by applying Gauss' law to a jet of radius R_J carrying a current I and a flow rate Q, this field is given by $E = R_J I/(2Q\varepsilon_o)$. These results suggest that the electric field will be largest in this region. Following similar arguments as those shown in Section 3.1, Gamero estimates the value of the maximum field in the transition region as [41],

$$E_{\max} = \frac{\gamma^{1/2} K^{1/6}}{\varepsilon_o^{2/3} Q^{1/6}}. \tag{3.2.17}$$

The relevant feature of this equation is its dependence on conductivity and flow rate. If K is sufficiently large and Q is small, the field could meet the condition of (3.2.16) for ion emission. Intuitively, the conductivity is related to the amount of ions in the liquid, so the greater its value the higher the charge concentration on the surface will be, while the relaxation time will be smaller. The flow rate determines the mechanical behavior of the cone-jet structure, in particular the curvature, which can be very large in the transition region, providing a mechanism for electric field magnification.

Figure 3.2.2 shows a plot of Equation (3.2.17) as a function of the non-dimensional flow rate parameter η as defined by (3.1.22) for three different conductivities. Values used are liquid density of $\rho = 1130$ kg/m^3, dielectric constant of $\varepsilon = 111$, and surface tension of $\gamma = 0.058$ N/m, corresponding to a solvent called formamide (CH_3NO). It is observed that

for small conductivities, condition (3.2.16) cannot be fully reached, since very low flow rates, well below the minimum for stability, would be required.

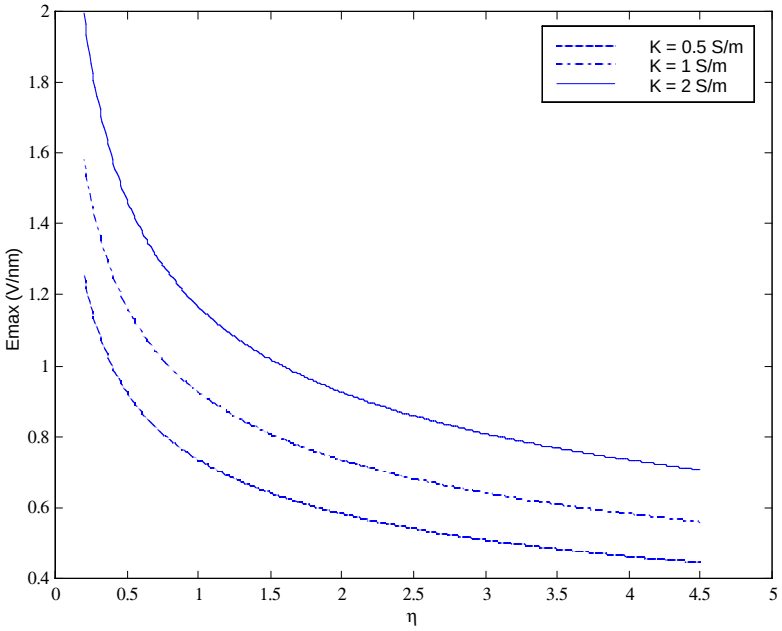

Figure 3.2.2 Maximum normal electric field vs. non-dimensional flow rate η for a formamide solution with ρ = 1130 kg/m^3, ε = 111 and γ= 0.058 N/m

The energy of the ions depends strongly on the location at which they are emitted. For example, for liquid metal ion sources, the emission surface is a small hemispherical area at the end of a thin jet-like protrusion near the cone apex. This surface is practically equipotential and therefore, the energy difference of ions emitted from different parts of this surface will be very small. In general, metallic sources have energy spreads of at most a few eV [42,43]. On the other hand, in a colloid cone-jet, the ion emission region is ill-defined, and as will be shown later, it can cover regions where the potential energy changes considerably. As a result, broad energy spreads for ion emission can be expected.

3.3. Space Charge Effects

Laplace's solution for the ideal Taylor cone eventually loses its validity if the charge emitted increases in such a way that it appreciably modifies the structure of the field. In this case, the more general solution of Poisson's Equation is required. In fact, some experimental observations have shown the formation of cones with angles different from those predicted by Taylor. A qualitative explanation would be to assume that the space charge contribution to the field depresses the shape of the liquid surface [44]. These observations and theoretical developments suggest that space charge effects are not negligible and should be studied to determine their influence on theoretical and experimental approaches and results.

It is expected that the particles emitted from colloid thrusters will follow axially directed trajectories, forming a conical beam. There exists a vast amount of work [45,46,47] focused on the explanation of the nature of charged particle beams and on the description of their trajectories. In general, the *perveance*, defined from scaling laws as $P = I\phi_B^{-3/2}$, where I is the beam current and ϕ_B its potential, is commonly used to quantify the effects of the space charge on beam trajectories. Typically, for electron beams, a value of the perveance lower than $1\times10^{-8}\,\mathrm{AV}^{-\frac{3}{2}}$ indicates that space charge effects can be neglected [48,49]. Ions and charged droplets move more slowly under a given potential than electrons, having more time for interactions. It can be expected that the effects of space charge on these particles will be greater. For instance, an electron beam and an ion or droplet beam will have the same perveance as long as their local charge densities are related by,

$$\frac{\rho_{c,k}}{\rho_{c,e}} = \sqrt{\frac{(q/m)_e}{(q/m)_k}} \qquad \text{or} \qquad \frac{\rho_{c,k}}{\rho_{c,e}} = 4.2\times10^5\left(\frac{q}{m}\right)_k^{-1/2}, \tag{3.3.1}$$

where *k* represents the group of either ions or droplets. The ratio $\rho_{c,k}/\rho_{c,e}$ is large, which means that the ion or droplet charge density is much larger than the corresponding electron charge density, thus the stronger interaction.

Using Equation (3.3.1), the perveance definition can be conveniently modified in order to generalize the $1\times10^{-8}\,\mathrm{AV}^{-\frac{3}{2}}$ limit for any charged species,

$$P^{*}=4.2\times10^{5}\left(\frac{q}{m}\right)^{-\frac{1}{2}}I\phi_{B}^{-3/2}. \tag{3.3.2}$$

For example, assuming a current of 400 nA and a potential of 900V, a 400 amu singly-charged ion beam (similar to those reported later in this thesis) would have a perveance of $P^{*}=1.3\times10^{-8}\,\mathrm{AV}^{-3/2}$, while $P^{*}=1.4\times10^{-7}\,\mathrm{AV}^{-3/2}$ for a droplet beam with a specific charge of $q/m=2000$ C/kg. These values, although small, suggest that space charge may not be negligible under some circumstances.

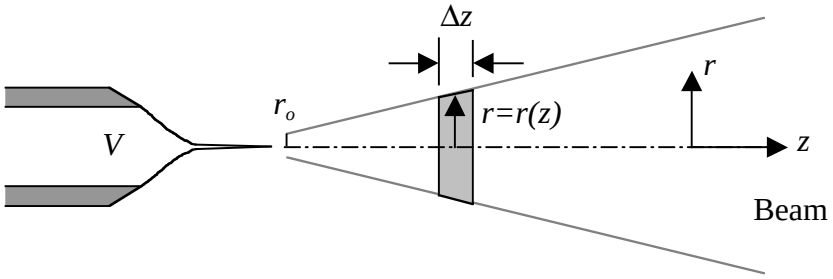

Figure 3.3.1. Beam spreading of a uniform beam

The effects of space charge on a particle beam could be numerous, but perhaps the most important are the radial spreading of the beam under self-repulsion forces and the possible space charge current limitation at emission surfaces. To estimate the spreading amount, a simple model of a beam composed of particles with identical specific charge is constructed, as seen in Figure 3.3.1.

The idea is to trace the trajectory of a charged particle under the influence of the electric field generated by the rest. It is assumed that there are no axial forces, therefore the beam

moves in the z direction at a constant speed v_z, which is determined, by energy conservation, from the emission potential ϕ_B,

$$v_z = \sqrt{2\frac{q}{m}\phi_B}\,. \tag{3.3.3}$$

Under this condition, the beam self-field lies in the radial direction only. The radial equation of motion for a particle in the outermost trajectory of the beam is then,

$$m\frac{d^2r}{dt^2} = qE_r \quad \text{or} \quad r'' = \frac{q}{mv_z^2}E_r \quad \text{where} \quad r'' = \frac{d^2r}{dz^2}. \tag{3.3.4}$$

If the trajectory does not change much in a small region Δz, then the radial field can be approximated by Gauss' law,

$$\int \vec{E}\cdot d\vec{S} = \frac{Nq}{\varepsilon_o}, \tag{3.3.5}$$

where N is the number of particles inside the small volume delimited by Δz. The axial components of the Gauss integral cancel each other approximately, while the radial part gives

$$E_r = \frac{q}{2\pi\varepsilon_o r}\frac{N}{\Delta z}. \tag{3.3.6}$$

The linear density of charged particles $N/\Delta z$ can be related to the total current in the beam by observing that,

$$I = \left(n\pi r^2\right)qv_z = \frac{N}{\Delta z}qv_z, \tag{3.3.7}$$

where n is the number density. Solving for the linear density in (3.3.7) and substituting into (3.3.6) an expression for the radial electric field is found,

$$E_r = \frac{I}{2\pi\varepsilon_o v_z r}. \tag{3.3.8}$$

Substituting (3.3.8) into the trajectory Equation (3.3.4),

$$r'' = \frac{A}{r} \qquad \text{where} \qquad A = \frac{I}{4\pi\varepsilon_o}\sqrt{\frac{m}{2q}}\phi_B^{-3/2}. \tag{3.3.9}$$

To solve (3.3.9), multiply both sides with r',

$$r''r' = A\frac{r'}{r} \qquad \text{which is equivalent to} \qquad \left(r'^2\right)' = 2A(\ln r)'. \tag{3.3.10}$$

As for boundary conditions, it is assumed that the beam has an initial radius r_o at $z = 0$ and zero slope, or $r' = 0$ (initially collimated beam) also at $z = 0$. Integrating (3.3.10) yields,

$$r' = \sqrt{2A}\sqrt{\ln\frac{r}{r_o}} \qquad \text{or} \qquad \left(\frac{r}{r_o}\right)' = \sqrt{\frac{2A}{r_o^2}}\sqrt{\ln\frac{r}{r_o}}. \tag{3.3.11}$$

By defining $u = \sqrt{\ln r/r_o}$, (3.3.11) can be written as,

$$e^{u^2}du = \sqrt{\frac{A}{2r_o^2}}dz, \tag{3.3.12}$$

which can be integrated to obtain a functional form for $r = r(z)$,

$$z = \sqrt{\frac{2r_o^2}{A}} \int_0^{\sqrt{\ln r/r_o}} e^{u^2} du. \tag{3.3.13}$$

A plot of Equation (3.3.13) is shown in Figure (3.3.2), where the normalization factor is defined as $z_o = \sqrt{2r_o^2/A}$. Note that the initial spreading of the beam is exponential close to $z = 0$, while its growth gradually slows down as it moves downstream until it becomes approximately linear.

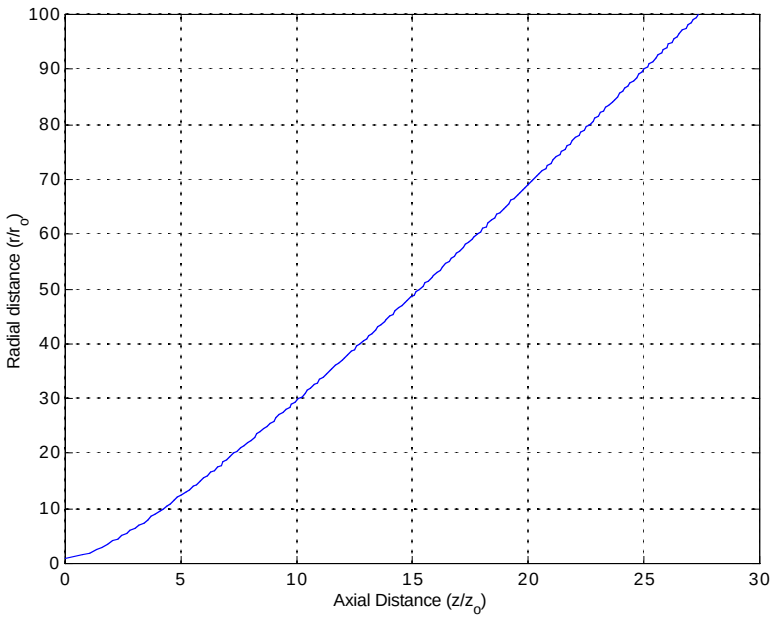

Figure 3.3.2. Beam spreading in field-free region

To explore the asymptotic behavior of Equation (3.3.13), make use of Dawson's integral, defined as,

$$F(\xi) = e^{-\xi^2} \int_0^{\xi} e^{u^2} du, \tag{3.3.14}$$

which is shown (solid line) in Figure 3.3.3 as a function of the parameter ξ. Integration by parts of (3.3.14) reveals that in the limit, for large values of ξ,

$$F(\xi) \to \frac{1}{2\xi} + O\left(1/\xi^3\right). \tag{3.3.15}$$

The cubic and higher terms in this expansion can be neglected, leaving the first part, which is shown as the dashed line in Figure 3.3.3. In terms of $F(\xi)$, Equation (3.3.13) is,

$$\frac{z}{z_o} = \frac{r}{r_o} F\left(\sqrt{\ln \frac{r}{r_o}}\right). \tag{3.3.16}$$

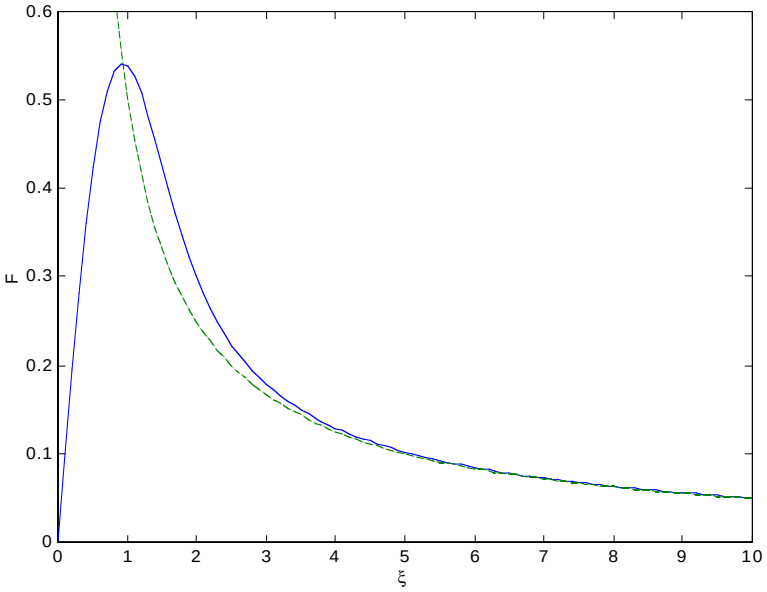

Figure 3.3.3. Dawson's integral and its asymptotic behavior

Substitution of (3.3.15) into (3.3.16) gives the behavior of the beam profile in the limit,

$$r(z) = \left(2A \ln \frac{r}{r_o} \right)^{1/2} z, \tag{3.3.17}$$

where A is given by (3.3.9). Even for large variations of r/r_o, the square root of the logarithm changes only slightly. This weak dependence on the beam radius makes (3.3.17) a good approximation to find the ultimate dispersion angle for a particle beam. Since the initial beam radius is about the size of one jet diameter, it is expected that r_o is nanometer sized. Typical experimental dimensions of the expanded beam lie in the cm scale, therefore $\sqrt{\ln r/r_o} \approx 4.5$. Given this, the dispersion semi-angle will be in the vicinity of,

$$\theta \approx \tan^{-1} \frac{9}{2} \left(\frac{I}{2\pi\varepsilon_o} \sqrt{\frac{m}{2q}} \phi_B^{-3/2} \right)^{1/2} \qquad \text{or} \qquad \theta \approx \tan^{-1} \left(783 \sqrt{P^*} \right). \tag{3.3.18}$$

Or, assuming a droplet beam charged to the Rayleigh limit (3.1.12), the spreading semi-angle can be written as a function of the non-dimensional flow rate η (3.1.22),

$$\theta \approx \tan^{-1} \frac{9}{\left(8\pi\sqrt{2} \right)^{1/2}} \left(\frac{f(\varepsilon)\varepsilon\gamma^2}{K\phi_B^3} \eta^3 \right)^{1/4} \left(\frac{1}{\varepsilon_o \rho} \right)^{1/8}. \tag{3.3.19}$$

The relevant parameters in this equation are the flow rate (represented by η) and the beam emission potential. Figure 3.3.4 shows the spreading semi-angles as a function of η for several emission potentials for $K = 2$ S/m $\rho = 1130$ kg/m^3, $\varepsilon = 111$, and $\gamma = 0.058$ N/m, corresponding to a concentrated formamide solution of NaI.

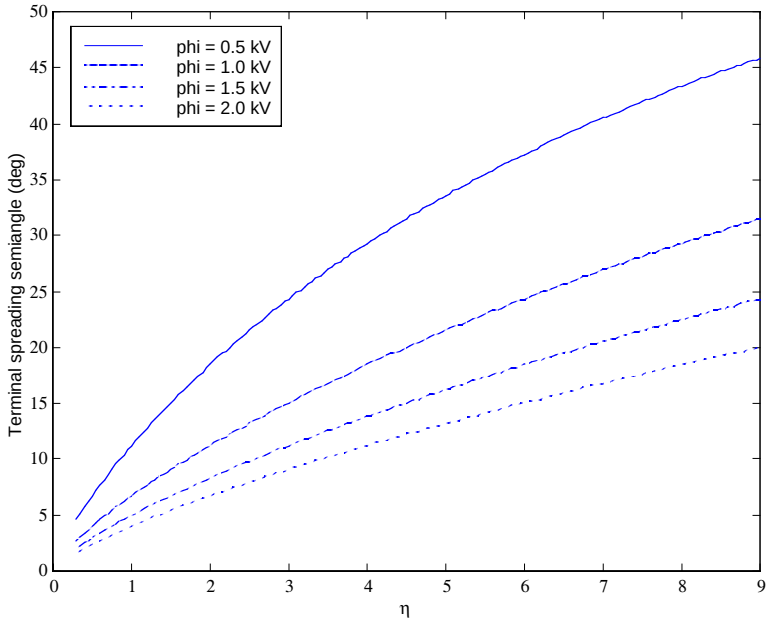

Figure 3.3.4. Spreading semi-angles (deg) for a charged droplet beam (phi = ϕ_B), for a formamide solution with K = 2 S/m ρ = 1130 kg/m^3, ε = 111 and γ = 0.058 N/m

Also important to consider is the effect that space charge could have on emission, especially when operating in an ion-droplet regime, since it is well-known that charge accumulation near emission sites could effectively reduce the local electric field, thus limiting the amount of current that can be extracted. An initial estimation for this limitation can be obtained by solving the 1-D Poisson problem,

$$\frac{d^2\phi}{dz^2} = -\frac{\rho}{\varepsilon_o} = \frac{-j}{\varepsilon_o\sqrt{2\frac{q}{m}(\phi_B - \phi)}} \tag{3.3.20}$$

where j is the beam current density. As for boundary conditions, the potential at the emission site is set to $\phi(z=0)=\phi_B$, while the electric field at that point is $\frac{d\phi}{dz}(z=0) = -E$, where E is the extraction electric field. The potential is assumed to drop

to zero a distance D from the emission site, thus $\phi(z=D)=0$. If space charge were to be neglected, then the electric field at the emitter site would be simply $E_L=\phi_B/D$.

To solve (3.3.20), multiply both sides by $2\frac{d\phi}{dz}$ and, noting that $2\frac{d\phi}{dz}\frac{d^2\phi}{dz^2}=\frac{d}{dz}\left(\frac{d\phi}{dz}\right)^2$, integrate once with the proper boundary condition to obtain,

$$\frac{d\phi}{dz}=E\sqrt{1+3\varsigma\sqrt{\frac{\phi_B-\phi}{\phi_B}}}\,, \tag{3.3.21}$$

where the parameter ς quantifies the amount of space charge,

$$\varsigma=\frac{4j}{3\varepsilon_o E^2}\sqrt{\frac{\phi_B}{2\frac{q}{m}}}\,. \tag{3.3.22}$$

Using (3.3.22), integrate (3.3.21) and arrange terms [43,50] to obtain,

$$\frac{E}{E_L}=\frac{8}{27\varsigma^2}\left[1+\sqrt{3\varsigma+1}\left(\tfrac{3}{2}\varsigma-1\right)\right]. \tag{3.3.23}$$

In the limit when the effects of space charge are known to be small, $\varsigma<<1$ and (3.3.23) reduces to $E\approx E_L(1-\varsigma)$, as well as when $\varsigma>>1$ (with $E^2\varsigma$ finite), Child-Langmuir's law for space charge limited flow is recovered,

$$j=\frac{4\varepsilon_o}{9D^2}\sqrt{2\frac{q}{m}}\phi_B^{3/2}. \tag{3.3.24}$$

Field reduction can be of concern for some liquid metal ion sources, since the extraction fields are of the order of $15\,\mathrm{V/nm}$ and the currents are in the micro Amp level [43]. The way nature corrects this problem is to form the jet-like protrusion that intensifies the field, counteracting this effect [31,51].

In the case of ion emission from colloid thrusters, no natural protrusion can form in the transition region where the field reaches a maximum, so the field reduction could affect the ability to extract ions. Figure 3.3.5 shows the field reduction curve given by Equation (3.3.23) for several non-dimensional flow rates as given by Equation (3.1.22) for a formamide solution with $K = 2$ S/m $\rho = 1130$ kg/m^3, $\varepsilon = 111$, and $\gamma = 0.058$ N/m. To compute the parameter ς of Equation (3.3.22) a potential of $\phi_B = 1$ kV and a singly-charged ion of mass 350 amu are assumed. The electric field E is extracted from Equation (3.2.17) and the current density j is obtained from (3.2.15) with $G_0 = 1.5$ eV, assuming full relaxation, so that the surface charge is $\sigma = \varepsilon_o E$.

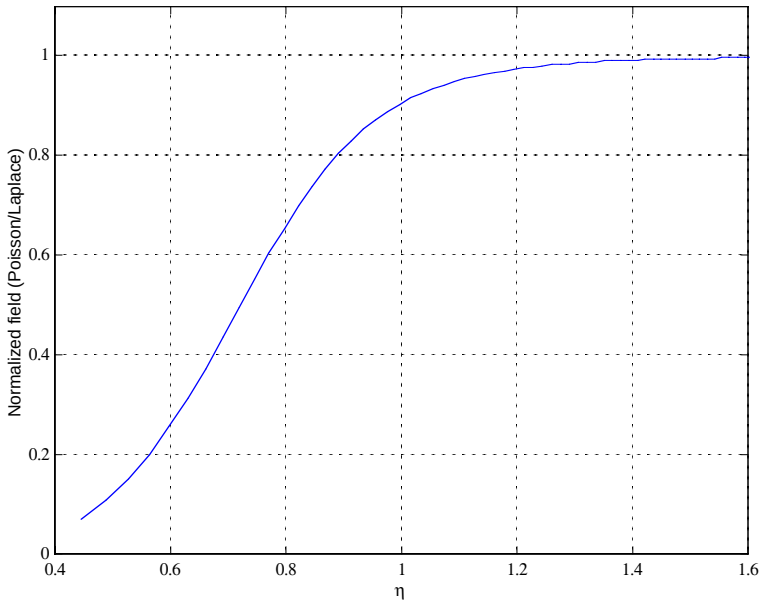

Figure 3.3.5. Field reduction due to space charge for singly charged 350 amu ions with G_0 = 1.5 eV emitted from a formamide solution with K = 2 S/m ρ = 1130 kg/m^3, ε = 111, γ = 0.058 N/m and ϕ_B = 1 kV as a function of non-dimensional flow rate η

It is experimentally known that ion emission starts near minimum flow conditions, when η is of order unity. It is seen from Figure 3.3.5 that the field reduction starts roughly when this flow condition is reached, but it is not too important, at least for $\eta > 1$. In any case, for smaller values, the cone structure becomes unstable and no emission occurs. It has been observed, however, that the flow rate of an ionic liquid can be reduced in such a way that the droplet emission is completely suppressed and a pure ionic regime is reached [52]. For some reason, Taylor cones of ionic liquids and liquid metals (or other highly conductive solutions, like sulfuric acid) do not become unstable for $\eta < 1$, as most organic solvents do [11]. The important point is that for such low flow rates, field reduction could be important, and in fact emission current may reach limitation and obey Child-Langmuir's law (3.3.24).

As mentioned in Chapter 2, one of the features about colloid thrusters is the possibility to micro-fabricate arrays to increase the thrust density. Assume that a large number of emitters are positioned in a 2-D rectangular matrix, as seen in Figure 3.3.6.

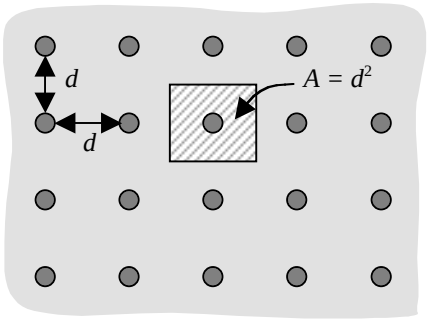

Figure 3.3.6. Two dimensional colloid thruster array

Individual emitters are spaced by a distance *d*, meaning that the current density will be given by,

$$j = \frac{I\,(\text{per jet})}{d^2} \tag{3.3.25}$$

The question arises of whether conditions with this arrangement approach those of a space-charge limited ion thruster (see the introduction). The model described above can be used to obtain a preliminary estimation of how the field is reduced by introducing a cluster of emitters working in the droplet regime. The electrospray definitions of Section 3.1 and the maximum field (3.2.21) are used to write the space-charge parameter in (3.3.22) as a function of flow rate through η,

$$\varsigma = \frac{2\sqrt{2}}{3}\frac{\sqrt{f(\varepsilon)\phi_B}}{d^2}\frac{\varepsilon^{\frac{5}{6}}\gamma^{\frac{1}{3}}\varepsilon_o^{\frac{17}{12}}}{K^{\frac{7}{6}}\rho^{\frac{7}{12}}}\eta^{13/6}. \tag{3.3.26}$$

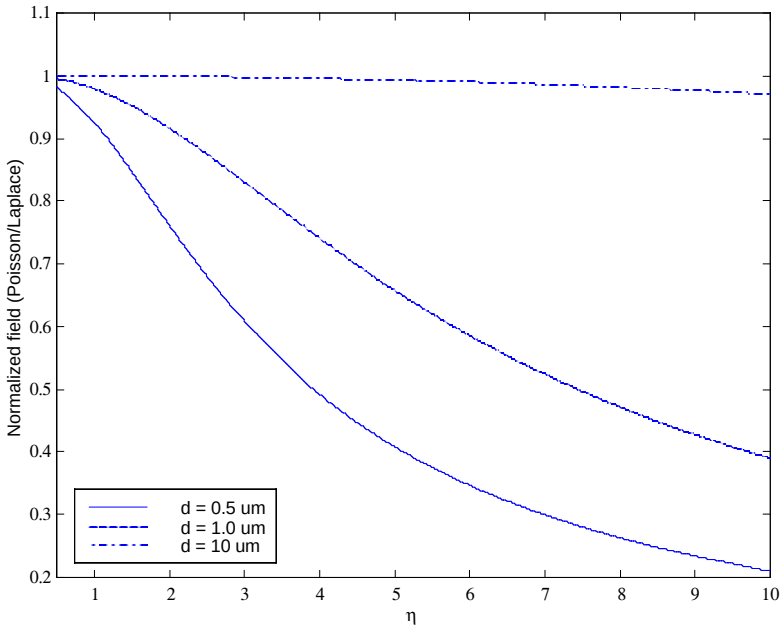

Figure 3.3.7. Field reduction in a colloid thruster array for a formamide solution with K = 2 S/m ρ = 1130 kg/m^3, ε = 111, γ = 0.058 N/m, $f(\varepsilon)$ = 20 and ϕ_B = 1 kV as a function of non-dimensional flow rate η

Figure 3.3.7 shows the field reduction as given by Equation (3.3.23) for a formamide solution with $K = 0.5$ S/m $\rho = 1130$ kg/m^3, $\varepsilon = 111$, $\gamma = 0.058$ N/m, $f(\varepsilon) = 20$, and $\phi_B = 1$ kV, assuming emitter separations of 0.5, 1 and 10 μm. Space-charge is strong for cases with very small separations and relatively high droplet currents, however, it is unlikely that micro-fabricated arrays would have separations smaller than $d = 10$ μm. It appears that space-charge limitation would not be a constraint for operating arrays of colloid thrusters, which could constitute an operational limitation by itself, since it implies that thrust densities as high as to those of ion engines cannot be reached.

As already mentioned, beam spreading is a significant phenomenon, for both ions and droplets. In the design of analytical hardware to study particle beams one is most concerned in estimating the trajectories that such particles will follow, not only under the effects of the beam self-repulsion, but also under the influence of external fields. A more general beam description is required, but given the difficulty that self-consistent problems like this pose, more approximations need to be made.

A very useful approach to the self-consistency is to assume that the particle trajectories remain close to the directional axis (*z*), that externally applied fields are symmetric around this axis and that the beam density profile is uniform. The symmetry can be used to write the equations of motion for the particles in cylindrical coordinates as (with $\phi < 0$, $v = 0$ at $\phi = 0$ and θ lies in the azimuthal direction, no magnetic fields),

$$\begin{aligned} &\ddot{r} - r\dot{\theta}^2 = \tfrac{q}{m} E_r, \\ &r\ddot{\theta} + 2\dot{r}\dot{\theta} = \tfrac{q}{m} E_\theta = 0, \\ &\ddot{z} = \tfrac{q}{m} E_z, \\ &\dot{r}^2 + r^2\dot{\theta}^2 + \dot{z}^2 = -2\tfrac{q}{m}\phi. \end{aligned} \tag{3.3.27}$$

To find the fields, first solve Poisson's Equation for the potential ϕ,

$$\frac{1}{r}\frac{\partial}{\partial r}\left(r\frac{\partial \phi}{\partial r}\right) + \frac{1}{r^2}\frac{\partial^2 \phi}{\partial \theta^2} + \frac{\partial^2 \phi}{\partial z^2} = -\frac{\rho}{\varepsilon_o}, \tag{3.3.28}$$

where ρ is the charge density. Since this is an axially symmetric problem, $\partial/\partial\theta \to 0$. To solve (3.3.28), the potential and the charge density can be expanded in power series,

$$\begin{aligned} \phi(r,z) &= \phi_o + \phi_2 r^2 + \phi_4 r^4 + \ldots = \sum_{k=0}^{\infty} \phi_{2k} r^{2k}, \\ \rho(r,z) &= \rho_o + \rho_2 r^2 + \rho_4 r^4 + \ldots = \sum_{k=0}^{\infty} \rho_{2k} r^{2k}, \end{aligned} \tag{3.3.29}$$

where ϕ_{2k} and ρ_{2k} are functions of *z* only. Substitute back into Poisson's Equation to obtain the following recursion formula,

$$\phi(r,z) = \sum_{k=0}^{\infty} \frac{(-1)^k}{k!^2} \left[\phi_o^{(2k)} + \frac{1}{\varepsilon_o} \sum_{\nu=1}^{k} (-1)^{k-\nu} 2^{2k-2\nu} (k-\nu)!^2 \, \rho_{2k-2\nu}^{(2\nu-2)} \right] \left(\frac{r}{2} \right)^{2k}. \tag{3.3.30}$$

The fields can then be computed with $\vec{E} = -\nabla\phi$. Recalling the assumption that particle trajectories remain close to the *z*-axis, only linear terms in *r* are extracted to obtain,

$$E_r \approx \tfrac{1}{2}\left(\phi_o'' + \tfrac{1}{\varepsilon_o}\rho_o\right) r \qquad \text{and} \qquad E_z \approx -\phi_o'. \tag{3.3.31}$$

Substitution of these fields into (3.3.27) yields the *paraxial ray equation*,

$$r'' + \frac{\phi_o' r'}{2\phi_o} + \frac{\phi_o'' r}{4\phi_o} = \frac{I}{4\pi\varepsilon_o \sqrt{\frac{2q}{m}} r (-\phi_o)^{3/2}}, \tag{3.3.32}$$

in which the uniform beam profile assumption provides a relationship between the axial density ρ_o and the beam current *I*. Notice that Equation (3.3.9) is a particular case of (3.3.32) when $\phi_o' = \phi_o'' = 0$ (the definition of ϕ there is the $-\phi_o$ here, hence the negative sign on the right).

In the paraxial approximation (3.3.32), ϕ_o is the external electrostatic potential along the axis of symmetry (z), while the effects of space charge are lumped together in the right hand side, where the total beam current I and the specific charge q/m appear. The paraxial ray equation with the space-charge term in its RHS can be used to compute laminar beam trajectories only, i.e., there are no crossovers (where $r \to 0$). In Chapter 5 the paraxial theory will reappear in the context of the experimental work.

3.4. Ion-Droplet Interactions

In a thruster application the interest centers around ions born at energies close to that of the emitter and with lives long enough to gain kinetic energy as they fall through the acceleration voltage. If it is assumed that both ions and droplets have a common emission region and travel in the same direction, then some ions could eventually interact with droplets that share similar trajectories.

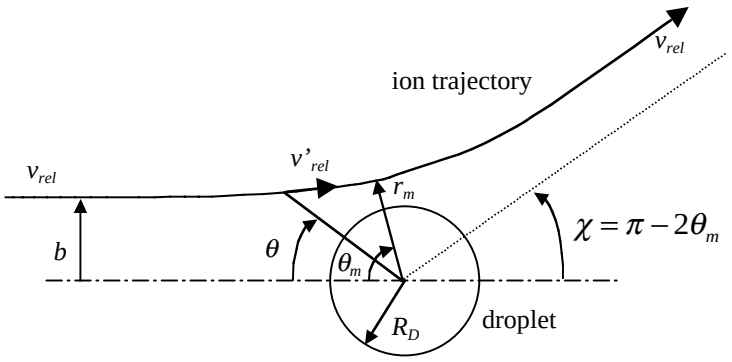

Figure 3.4.1. Geometry for ion-droplet encounter

The concern here, from the experimental point of view, would be to lose the ability of characterizing the ions in the beam because of some perturbing interaction with the

droplets. The possibility of scattering could eventually send ions into trajectories very different from the original ones, hence modifying the measurements. To quantify the amount by which ions are scattered by droplets, a traditional model is used, as shown schematically in Figure 3.4.1. Here it is assumed that the mass of the ions is small when compared to that of the droplets. The reduced mass in the relative system is then the ion mass $\mu_r = m_i m_D / (m_i + m_D) \approx m_i$. The relative velocity is given by $v_{rel} = v_i - v_D$, where *i* and *D* are subscripts for ions and droplets, respectively.

For this analysis, take a single ion moving towards a droplet of radius R_D with an impact parameter *b*. Once inside the droplet's potential sphere of influence, the ion modifies its trajectory and makes its closest approach at a distance r_m from the droplet center corresponding to an angle θ_m. The scattering angle is given by $\chi = \pi - 2\theta_m$. Assume for now that $r_m > R_D$, i.e., ion trajectories do not intersect with the droplet surface. Momentum and energy conservation results in,

$$\begin{array}{c} b v_{rel} = r^2 \dot{\theta} \\ \frac{1}{2}\mu_r v_{rel}^2 = \frac{1}{2}\mu_r v_{rel}'^2 + V(r) \end{array} \qquad \text{with} \qquad V(r) = \frac{q_i q_D}{4\pi\varepsilon_o r}, \tag{3.4.1}$$

where $V(r)$ is the potential energy of interaction at a distance *r* and q_i and q_D are the ion and droplet charges, respectively. Since $v_{rel}'^2 = \dot{r}^2 + r^2\dot{\theta}^2$, the angle of closest approach is, after making $\xi = b/r$,

$$\theta_m = \int_0^{\xi_m} \frac{d\xi}{\left(1 - \xi^2 - 2V(\xi)/\mu v_{rel}^2\right)^{1/2}}. \tag{3.4.2}$$

The value of $r_m = b/\xi_m$ is found by setting the denominator inside the integral symbol equal to zero, thus defining the upper bound that determines the angle θ_m,

$$\xi_m = \frac{b_o}{b}\left(\sqrt{1 + \left(\frac{b}{b_o}\right)^2} - 1\right) \qquad \text{where} \qquad b_o = \frac{q_i q_D}{4\pi\varepsilon_o}\frac{1}{m_i v_{rel}^2}. \tag{3.4.3}$$

Equation (3.4.2) can be integrated to obtain the scattering angle as a function of the impact parameter and, since $r_m > R_D$, the scattering angle is limited to,

$$\tan(\chi/2) < \frac{b_o/R_D}{\sqrt{1-2b_o/R_D}}. \tag{3.4.4}$$

If ions and droplets are accelerated through the same potential ϕ_B, then the relative kinetic energy can be written as,

$$\tfrac{1}{2} m_i v_{rel}^2 = \tfrac{1}{2} m_i v_i^2 \left(1-\sqrt{\zeta}\right)^2 \qquad \text{with} \qquad \zeta = \frac{(q/m)_d}{(q/m)_i}. \tag{3.4.5}$$

Assuming that the droplets are charged to the Rayleigh limit (3.1.12), an expression for the size of the impact parameter with respect to the droplet radius R_D can be found after some manipulations,

$$\frac{b_o}{R_D} = \left(\frac{6\gamma^2}{\varepsilon_o \rho (q/m)_D}\right)^{1/3} \frac{1}{\phi_B\left(1-\sqrt{\zeta}\right)^2}, \tag{3.4.6}$$

where $(q/m)_D$, the droplet specific charge, can be put in terms of the non-dimensional flow rate by using (3.1.22-23),

$$\left(\frac{q}{m}\right)_D = \frac{f(\varepsilon)K}{\varepsilon\eta\sqrt{\varepsilon_o\rho}}. \tag{3.4.7}$$

For a concentrated formamide solution with $K = 2$ S/m $\rho = 1130$ kg/m^3, $\varepsilon = 111$, $\gamma = 0.058$ N/m, $f(\varepsilon) = 20$, and $\phi_B = 1$ kV, close to the minimum flow rate condition $\eta = 1$, the following can be computed: $b_o/R_D = 0.01$ for $(q/m)_D = 3.6$ C/gr and $\zeta = 0.013$. From Equation (3.4.4), the upper bound for the scattering angle is then

$\chi_{\max} = 1.16^{\circ}$. This is an important result, which shows that absorption, or collision, is much more likely than scattering.

To obtain an idea of the collision probability, the same model is used to estimate the mean free path of ions in a droplet beam. Collisions will occur, for values of the impact parameter smaller than the one that would make $r_m = R_D$,

$$b_{\max} = R_D \sqrt{1 - 2\frac{b_o}{R_D}}. \tag{3.4.8}$$

The collision cross section is given by $Q_{iD} = \pi b_{\max}^2$, the area delimited by this critical impact parameter. Therefore,

$$Q_{iD} = \pi R_D^2 \psi \qquad \text{with} \qquad \psi = 1 - 2\frac{b_o}{R_D}. \tag{3.4.9}$$

The parameter ψ will usually be very close to unity, as shown in the example given above. The mean free path for ion-droplet collisions is,

$$\lambda_{iD} = \frac{1}{n_D Q_{iD}}. \tag{3.4.10}$$

The droplet density n_D can be related to the droplet current *I* given by (3.1.21),

$$n_D = \frac{I}{v_D q_D A_b} \qquad \text{with} \qquad v_D^2 = 2\left(\frac{q}{m}\right)_D \phi_B, \tag{3.4.11}$$

where A_b is the droplet beam cross sectional area. Considering that the beam diverges at an angle θ due to the space-charge repulsion while moving along the axial distance *z*, the beam area can be modeled as,

$$A_b = \frac{\pi d_b^2}{4} = \pi z^2 \tan^2\theta. \tag{3.4.12}$$

For a fixed collision cross section, the mean free path (3.4.10) will depend on the droplet density (3.4.11). A way to assess the probability of collision would be to compute the ratio of the mean free path to the axial distance *z*. If this relative mean free path is close to unity, the probability of collision will increase. If, on the other hand, the ratio is large, collisions will be rare. Again, using the assumptions already discussed, an expression for the mean free path to axial distance ratio in terms of the non-dimensional flow rate η is written as,

$$\frac{\lambda_{iD}}{z} = \pi\left(256\sqrt{8/9}\right)^{1/3}\left(\frac{K^5}{\varepsilon^5\gamma^4 f(\varepsilon)}\right)^{1/6}\left(\frac{\rho^5}{\varepsilon_o^7}\right)^{1/12}\frac{\phi_B^{1/2} z\tan^2\theta}{\eta^{11/6}\psi}. \tag{3.4.13}$$

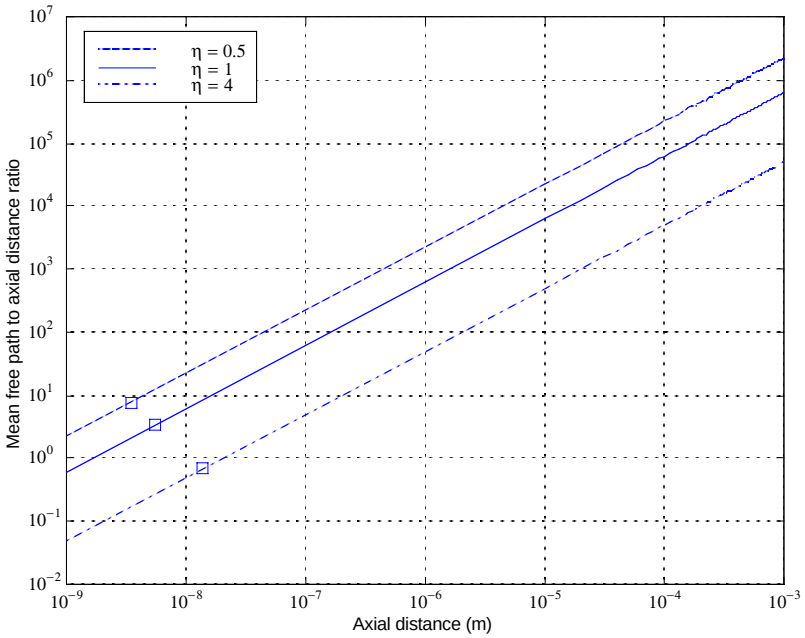

Figure 3.4.2. Relative mean free path vs. axial distance for a formamide solution with K = 2 S/m ρ = 1130 kg/m^3, ε = 111, γ = 0.058 N/m, $f(\varepsilon)$ = 20, ϕ_B = 1 kV and θ = 20° as a function of axial distance z

Figure 3.4.2 shows a plot of Equation (3.4.13) for three different values of η. A spreading angle of $\theta = 20^\circ$ is used and $K = 2$ S/m $\rho = 1130$ kg/m^3, $\varepsilon = 111$, $\gamma = 0.058$ N/m, $\phi_B = 1$ kV and $f(\varepsilon) = 20$. It can be seen that, for small flow rates, the relative mean free path is close to unity only when the axial distance is of the order of 1 nm. For larger flow rates, the ratio is unity for distances slightly larger than 10 nm. These dimensions are very small and comparable to the jet size. The jet radius can be calculated with the same set of tools already presented and by considering that droplets are 1.89 times larger,

$$R_J = \frac{1}{1.89}\left(\frac{6}{f(\varepsilon)} \sqrt{\frac{\gamma}{\rho}} \frac{\varepsilon \varepsilon_o}{K} \eta \right)^{2/3}. \tag{3.4.14}$$

Under the above conditions, the jet radii (3.4.14) for three values of η are also shown in Figure 3.4.2 as the three squares superimposed on their respective lines. Their values can be read in the abscissa. This means that only those values to the right of the squares can be considered in this analysis, since no droplets could exist at smaller distances. This argument does not take into account that the jet length may be considerably longer than the axial dimensions shown. This would effectively move the squares in Figure 3.4.2 further to the right.

Of the three cases shown, only the one with $\eta = 4$ makes the relative mean free path close to unity for small axial distances. This makes sense, since for that flow rate the droplet is bigger and therefore presents a relatively large cross section to incoming ions. But, as seen in Figure 3.2.2, such a high flow rate does not generate a sufficiently large electric field to meet the required conditions for ion emission.

For cases where ion emission is possible, the collision probability is small as shown in Figure 3.4.2, which is a worst-case scenario, in the sense that, because the emission mechanisms of ions and droplets are very different, the trajectories of ions and droplets

are unlikely to overlap in regions near the Taylor cone apex. If they do, it will occur relatively far away where the droplet density is low and the relative mean free path is extremely large. For example, note in the figure that only one mm downstream of the emission point, this ratio is about 10^6 for $\eta = 1$, almost zero collision probability if the ion trajectories intersect the droplet beam at this point.

3.5. Neutralization

Most electric propulsion thrusters eject charged particles, thus transferring opposite charge to the vehicle's components. If no action is taken, extremely high potentials can be reached, disturbing the payload and system components, or in the worst case, causing catastrophic failures. To avoid this situation, electric propulsion devices make use of charged particle sources (usually electron sources, if the particles emitted are positive) to dispose of the extra charge and neutralize the thruster exhaust. The problem of neutralizing positive droplets with electrons is different from ion neutralization since droplets are large enough to be considered an electron sink, i.e., there is no need for three-body recombination.

For a preliminary quantification of the neutralization process, assume a colloid thruster emitting a beam of monodisperse positively-charged droplets that spreads at a semi-angle θ along the *z*-axis. A flux of electrons,

$$\Gamma_e = \int f(\vec{v}) v d^3\vec{v}, \tag{3.5.1}$$

with maxwellian distribution,

$$f(\vec{v}) = n_e \left(\frac{m_e}{2\pi k T_e} \right)^{3/4} e^{-\frac{W}{kT_e}}, \tag{3.5.2}$$

is applied and encounters the droplets at the axial distance where the beam has a radius r_o. W is the electron's total energy and m_e its mass. The orbital motion limit for the electrons can be assumed, as long as the Debye length,

$$\lambda_D = \sqrt{\frac{\varepsilon_o k T_e}{n_e e^2}}, \tag{3.5.3}$$

(where T_e and n_e are the electron temperature and number density) is large compared to the droplet radius, which is 1.89 times the jet size (3.4.14),

$$\frac{\lambda_D}{R_D} >> 1. \tag{3.5.4}$$

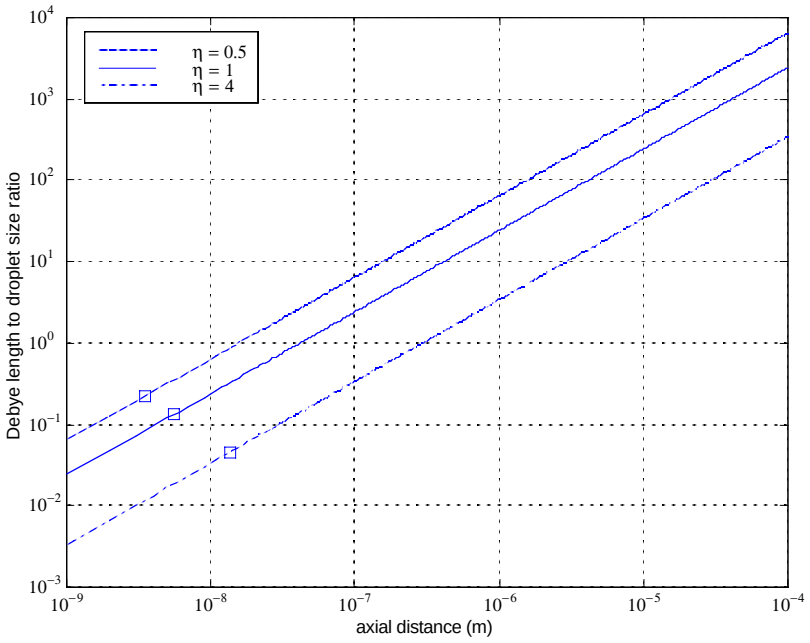

Figure 3.5.1. Debye length to droplet radius ratio for a formamide solution with K = 2 S/m ρ = 1130 kg/m^3, ε = 111, γ = 0.058 N/m, $f(\varepsilon)$ = 20, ϕ_B = 1 kV and θ = 20° as a function of axial distance z

Figure 3.5.1 shows a plot of the ratio of the Debye length to droplet radius as a function of axial distance z using the same values of the previous section (taking $r_o \to 0$) and assuming quasi-neutrality, so that the electron density is given by,

$$n_e = \frac{q_D}{e} n_D. \tag{3.5.5}$$

The droplet density n_D is computed from (3.4.11-12). The droplet beam is also assumed to spread according to (3.4.12). In the same sense as in Figure 3.4.2, the small squares superimposed on the lines represent the jet radii for the three conditions. Given this, the analysis can only be applied for values to the right of them, where droplets exist.

It is evident that condition (3.5.4) only applies for axial distances roughly larger than one micron. This means that there is a small region adjacent to the emitter where this analysis cannot be applied. But, as will be discussed below, electrons will most likely be forced to stay away from the emitter, thus increasing the local value of the Debye length in an important way. With no more considerations, it is assumed that electron-droplet interactions can be described using the orbital motion limit.

Since $W = \frac{1}{2} m v^2 + e\phi_D$ (ϕ_D is the droplet potential), the integral (3.5.1) can be evaluated to find the current density of electrons into the attractive droplets,

$$j = \frac{e n_e \bar{v}_e}{4} \left(1 + \frac{e\phi_D}{kT_e} \right), \tag{3.5.6}$$

where the droplet potential ϕ_D is given by (3.4.8) as a function of the droplet charge q_D and the thermal velocity for the maxwellian electrons is,

$$\bar{v}_e = \left(\frac{8kT_e}{\pi m_e} \right)^{1/2}. \tag{3.5.7}$$

Given a fixed volumetric flow rate Q, the droplet density can be written as $n_D = Q\left[\frac{4}{3}\pi R_D^3 v_D \pi\left(r_o + z\tan\theta\right)^2\right]^{-1}$. Equation (3.5.6) can be used to compute the rate at which electrons neutralize a droplet, therefore a differential equation can be set up for the droplet charge. Using (3.5.5-7), this can be written as,

$$\frac{dq_D}{dz} = -\xi q_D \frac{1+\psi q_D}{\left(z\tan\theta + r_o\right)^2}, \tag{3.5.8}$$

where the parameters ξ (a distance) and ψ (an inverse charge) are written in terms of the non-dimensional flow rate η,

$$\xi = \frac{\bar{v}_e}{8\pi\phi_B}\left(\frac{3\gamma^2\varepsilon^4\eta^7}{4f(\varepsilon)K^4}\right)^{1/3}\left(\frac{\varepsilon_o^5}{\rho}\right)^{1/6} \qquad \text{and} \qquad \psi = \frac{e}{4\pi\varepsilon_o kT_e}\left(\frac{f(\varepsilon)}{6}\sqrt{\frac{\rho}{\gamma}}\frac{K}{\varepsilon\varepsilon_o\eta}\right)^{2/3}. \tag{3.5.9}$$

Equation (3.4.8) can be integrated directly, resulting in,

$$q_D = q_{D_0}\frac{e^{-\xi/z^*}}{1+\psi q_{D_0}\left(1-e^{-\xi/z^*}\right)}, \tag{3.5.10}$$

where the variable z^* is,

$$z^* = \frac{r_o^2}{z} + r_o\tan\theta, \tag{3.5.11}$$

and the initial droplet charge q_{D_0}, at the Rayleigh limit, in terms of η is,

$$q_{D_0} = 48\pi\sqrt{\frac{\varepsilon_o^3}{\rho}}\frac{\gamma\varepsilon}{f(\varepsilon)K}\eta. \tag{3.5.12}$$

By analyzing the asymptotic behavior of (3.5.10) some useful information about the neutralization mechanics of liquid droplets by electrons can be extracted. Take a look at the limit when $z >> r_o/\tan\theta$, the case far downstream from the beam source. It can be seen by (3.5.11) that $z^* \approx r_o \tan\theta$. The droplet charge stops decreasing, reaching a constant value given by,

$$q_D = q_{D_0} \frac{e^{-\xi/(r_0 \tan\theta)}}{1+\psi q_{D_0}\left(1-e^{-\xi/(r_0 \tan\theta)}\right)}. \tag{3.5.13}$$

After this limit charge is reached, the jet continues as a "dusty plasma", i.e., it is still quasineutral, but with a finite electron density balancing the residual spray charge.

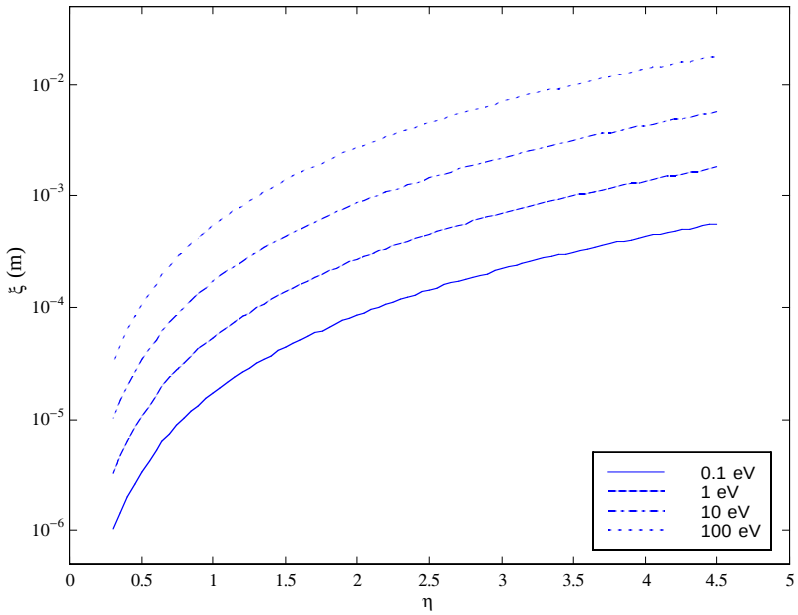

Figure 3.5.2. Characteristic dimensions for droplet neutralization for a formamide solution with K = 2 S/m ρ = 1130 kg/m^3, ε = 111, γ = 0.058 N/m, $f(\varepsilon)$ = 20, ϕ_B = 1 kV and θ = 20° as a function of the non-dimensional flow parameter η

Since the spreading angle is relatively fixed, the amount by which the droplet charge decreases is given by the ratio ξ/r_o. If this ratio is close to unity, then *droplets* are almost fully neutralized. If on the other hand, the ratio is small, the droplet neutralization process is incomplete, although the *jet* is still fully neutralized, both by charge and by current. As a result, the parameter ξ introduced in (3.5.9) can be considered as the characteristic dimension for droplet neutralization. Figure 3.5.2 shows curves of the parameter ξ as a function of the non-dimensional flow rate η for different electron energies with $\theta = 20^\circ$, $K = 2$ S/m $\rho = 1130$ kg/m^3, $\varepsilon = 111$, $\gamma = 0.058$ N/m, $\phi_B = 1$ kV and $f(\varepsilon) = 20$.

The way in which the initial beam radius r_o modifies the final value of the droplet charge can be seen in Figure 3.5.3. The terminal droplet charge as given by (3.5.13) is shown, normalized by the initial charge q_{D_0} as a function of η for 1 eV electrons, for different values of the ratio ξ/r_o.

Finally, note that the terminal value of the droplet charge (3.5.13) will be reached once the axial distance becomes a few times larger than r_o. Since in general r_o is a small number, the neutralization, complete or incomplete, occurs very quickly. This increases the concerns about possible electron bombardment of the emitter or the neutralization of charges still within the accelerating region that have not reached their maximum velocity, thus decreasing the thruster performance. Of course, this analysis assumed overlapping droplet-electron sources. In a real design, electrons could be maintained away from the emitter by biasing the extractor negatively with respect to the electron emitter cathode, and placing it downstream of the extractor. This situation could effectively reduce the ratio ξ/r_o to the point that no direct neutralization may occur. What would happen is something similar to ion “neutralization” in other electric thrusters, where charges do not physically recombine, but they leave the spacecraft vicinity in an intermixed plasma cloud that is basically neutral, macroscopically speaking.

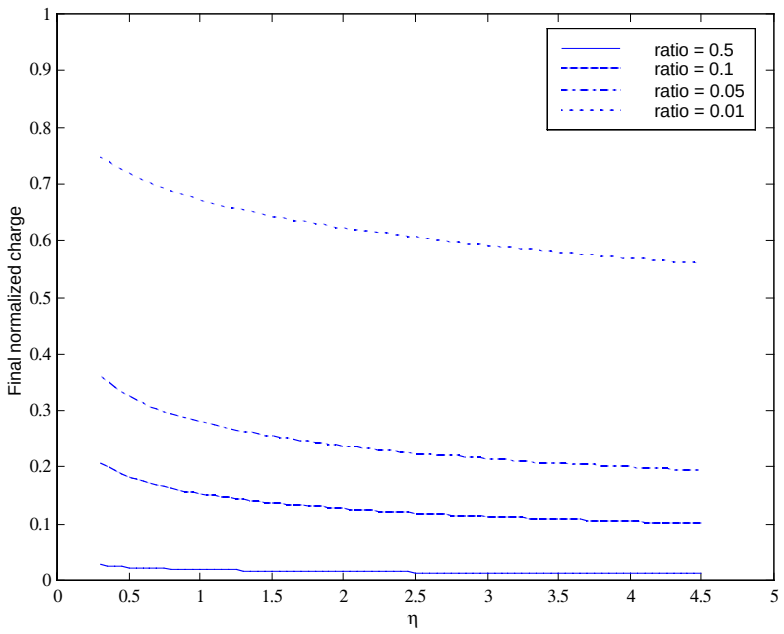

Figure 3.5.3. Droplet terminal charge - 1eV electron neutralization (ratio = ξ/r_o) for a formamide solution with K = 2 S/m ρ = 1130 kg/m^3, ε = 111, γ = 0.058 N/m, $f(\varepsilon)$ = 20, ϕ_B = 1 kV and θ = 20° as a function of the non-dimensional flow parameter η

On a related note, it is not clear what happens with the neutralized counter-ions in the solution when only one polarity is emitted. One possibility is that the counter-ions travel to the attractive electrode, where they neutralize and then leave with the liquid droplets. On the other hand they could react on the electrode surface (anodic oxidation), degrading its properties. A third possibility is that the neutralized counter-ions pass into solution, but stay in the capillary or its supply plenum, changing the liquid's chemistry. A way to test these ideas would be to run with a measurable liquid sample until completion and then analyze any residues. Given the small flow rates, this study could take long times

and has not been performed so far. The performance of colloid thrusters depends on the liquid properties. It is then of primordial importance to clarify this *chemical neutralization* issue.

A very interesting way around the problem of both electrical and chemical neutralization can be achieved by noting that it is possible, at least in principle, to operate colloid thrusters in a bi-polar mode by merely switching the polarities of the emitter-extractor assembly.

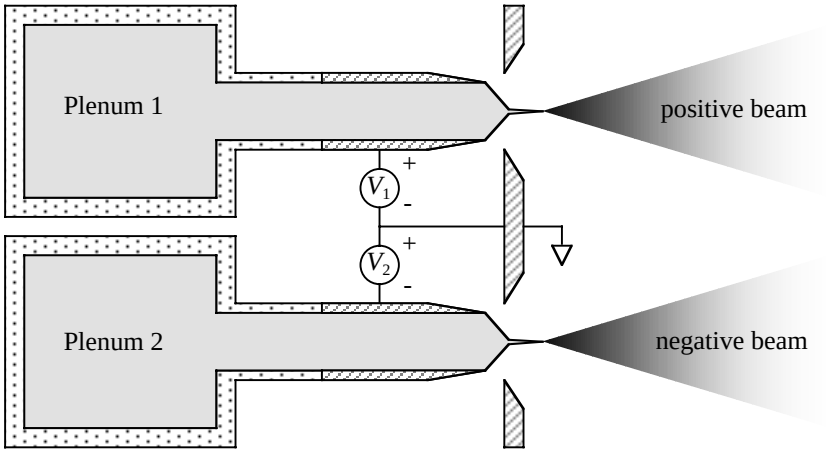

Figure 3.5.4. Conceptual bi-polar operation mode

Figure 3.5.4 conceptually shows how a bi-polar colloid thruster might work. In the picture are two separate plenums containing the propellant and each feeding a thruster capillary (could be an array of emitters). Charged particles are extracted by two separate

power supplies V_1 and V_2 and a single extractor grounded to the spacecraft. If $V_1 > 0$ then positive charges will be extracted from this emitter. To establish electrical neutrality, the second power supply should be set to $V_2 < 0$, thus emitting negative charges. It is clear that chemical neutrality is not guaranteed with this arrangement (counter-ions will be accumulated in each plenum) unless the supply voltages are alternated periodically. The frequency of voltage switching would be determined by factors such as the speed of counter-ion accumulation/reaction in the thruster materials among other engineering considerations.

Voltage alternation could be avoided by using an arrangement in which a single plenum is used to feed both emitters, set to ground potential. Charge extraction would then be achieved after biasing separate extractors to negative and positive voltages. This device would keep electrical and chemical neutrality since both ions and counter-ions are emitted simultaneously. On the other hand, it could not be used as a thruster, since charged particles are originally at the same potential inside the plenum and they end up at the same potential at infinity after being emitted, thus no work is done.

3.6. Summary

This chapter provides a general review about the relevant features in colloid thruster emission physics. In Section 3.1, the basic phenomena involved in the formation of the cone-jet structure are outlined. Relevant results are cited and some of them are reproduced in light of their usefulness for the discussions to follow. In Section 3.2 a link is created between the cone-jet description and the mechanics of ion emission. These two sections provide the theoretical background required to understand the nature of the ion-droplet mixed regime.

In the rest of the sections in this chapter, further theoretical analyses are developed to investigate the way in which ion-droplet emissions can interact either with themselves or

with electrons. The problem of space-charge limitation is reviewed in Section 3.3 through a 1-D model. It could be argued that the lack of dimensionality could yield some inaccurate results. Nevertheless, as in other examples in plasma physics, these simple models provide an adequate estimation of the magnitude of these effects. It is found that space-charge limitation is not significant unless the non-dimensional flow parameter η is less than unity (abundant ion emission). Most solutions, however, become unstable before this condition is reached. Another important result, that may have a technological impact, suggests that space-charge limitation is negligible for droplet emission from emitter arrays, unless they are extremely dense. As explained in this section, the most relevant effect of space-charge appears to be the initial beam spreading due to self-repulsion forces among charged particles. A simple model in which charged particles repel each other while drifting at constant velocity is used to find the *terminal* beam spreading angle. It is important to note that this model can be considerably improved by allowing acceleration in the axial direction, thus reflecting more accurately what actually occurs under circumstances where the local potential is still very different from the extractor potential at the point where the jet breaks up into a droplet spray. This improvement, however, is difficult to implement analytically, instead, a version of the paraxial ray equation (3.3.32) should be solved numerically with the Taylor potential (3.1.11) to obtain the complete set of trajectories between the emitter and the extractor.

In Section 3.4, the possibility of interaction between ions and droplets is analyzed. From an experimental point of view, this analysis is of great relevance since measurement of individual properties of droplets or, in particular ions, would be extremely difficult if these particles interact with each other, such that the relative magnitude of the signals becomes function of the cone-jet operational parameters. Fortunately, the theoretical analysis estimates that such interactions are small enough and can be neglected. This has an implication for space propulsion as well; for example, for a colloid thruster operating in the ion-droplet mixed regime, the performance gains due to the presence of ions in the beam depend on their unaffected acceleration by the local potential generated by the cone-jet structure and the external electrodes. If these ions collide with neighboring

droplets before they fully accelerate, their contribution to the total thrust would be lost, decreasing the overall efficiency.

Another important consideration for actual colloid thrusters is the way in which neutralization will be provided. Two alternatives are mentioned in Section 3.4. In the first one, externally supplied electrons ejected from a cathode are considered. As shown, these electrons will move very quickly to regions close to the emitters and could neutralize the liquid even before it fully accelerates. It is suggested that external electrodes should be biased to lower potentials than the one from the cathode to keep the electrons at some safe distance from the emitters. The second alternative is to operate colloid thruster arrays in bi-polar mode. This has the advantage of eliminating the additional complexity of electron sources and provides additional thrust while generating a quasineutral beam.

4. Experimental Methods

The fundamental objective of this work is to provide a description of the behavior and characteristics of colloid thruster emissions. For this description to be as complete and accurate as possible, different experimental observations are required for properties in every regime of electrospray operation.

The experimental hardware is designed to provide several important pieces of information about the charged beam, by being able to:

- **Measure the spreading angle.** It is expected, from the discussion in Section 3.3, that the dominant effect of space-charge emission is the initial self-repulsion of charged particle beams.
- **Verify the applicability of electrostatic focusing.** Given the beam spreading, the resolution of time-of-flight measurements is limited by the drift distance in the analytical device. By being able to counteract this initial divergence using ion optical elements, longer distances are possible, thus higher resolutions.
- **Operate at low flow rates, down to cases with $\eta \approx 1$.** Ion emission from the liquid cone-jet structure occurs when the flow rate reaches this condition.
- **Measure the beam energy.** The specific impulse and the thrust are determined in part by the energy of particles in the beam. From a scientific point of view, these

measurements would provide useful information to understand the mechanics of droplet and ion emission from electrospray sources.

- **Determine whether ion emission occurs or not.** Time-of-flight spectrometry techniques are ideal to study the beam composition, thus distinguishing ions from droplets. Together with the beam energy, these measurements characterize completely the emissions from colloid thrusters, thus determining the specific impulse and thrust.
- **Measure the beam ion fraction.** The performance of the thruster in terms of the efficiency is established by measuring the individual contributions of ions and droplets to the total current.
- **Identify the ion or ions emitted.** High-resolution time-of-flight measurements can be used to establish the nature of the ions emitted from colloid thrusters.

In order to accomplish these tasks, a number of experimental techniques are evaluated. A brief description of each one of them is given in this chapter.

4.1. Basic Techniques

Besides the experimental determination of the spreading angle, every aspect of colloid thruster beam characterization requires information about the particles emitted, the relevant quantity being the specific charge, or charge per unit mass. The reason for this is that once known, the specific charge q/m can be used to determine the exhaust velocity and therefore the specific impulse. This can be seen from Equation (3.3.3), which is rewritten here:

$$v_z = \sqrt{2\frac{q}{m}\phi_B}\,. \tag{3.3.3}$$

Complete determination, however, cannot be made unless the beam accelerating potential ϕ_B is also available. Assuming that these quantities are known, in addition to the beam current *I*, the thrust can be calculated directly,

$$F = I\sqrt{\frac{2\phi_B}{q/m}}. \tag{4.1.1}$$

In a space mission, it is likely that the only available information for thruster operation will be the current *I* and the applied voltage ϕ_a. The specific charge should be known a priori, from experimental tests. As for the beam potential ϕ_B, though closely related to the applied potential ϕ_a, the two are not identical because loss mechanisms such as the energy spent to create the cone-jet, make $\phi_B < \phi_a$. The beam potential, and its relationship to the applied voltage also need to be obtained experimentally. Furthermore, both the specific charge and the potential are usually distributed quantities, as opposed to being fixed numbers.

The inverse procedure can be used in the laboratory to determine the distribution of specific charges from the beam potential and the velocity distribution. A common way of doing this is by the time-of-flight (TOF) technique [53,54,55,56,57,58].

The basic idea behind the TOF method is that one can measure the time required for a charged particle to traverse a certain distance in a region free of external fields thus giving enough information to calculate the particle's velocity. If that velocity is acquired by an initial acceleration through a known potential, then (3.3.3) can be inverted to compute the specific charge. There are many ways to perform TOF measurements. Three methods have been used in this study, as follows.

Single gate continuous TOF

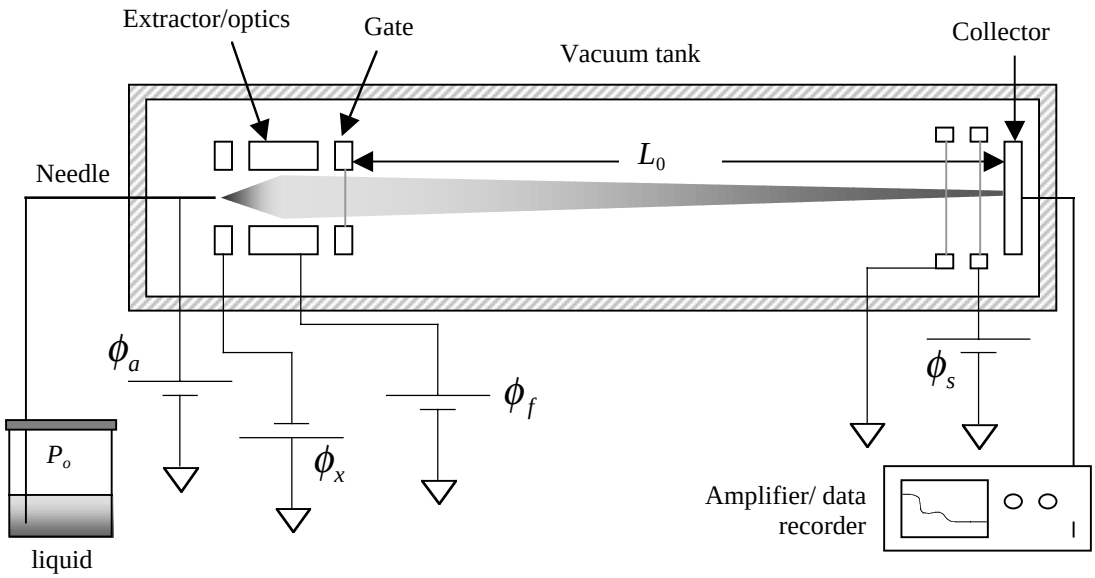

Figure 4.1.1. Schematic of the single gate TOF

In this approach, the needle electrospray source (Section 4.3) is operated continuously at a specific flow rate Q, applied beam voltage ϕ_a, extractor voltage ϕ_x and focusing potential ϕ_f. In front of the emitter, there is an electrostatic gate that allows particles to flow out of the emitter when it is open or stops them when the gate is closed. A schematic of this system is shown in Figure 4.1.1.

At a distance L_0 from the gate a metallic plate measures the beam current in time. The signal from the plate is taken through an amplifier and displayed on an oscilloscope screen. If the gate remains open, the recorded signal is a single flat line displaying the magnitude of the total current, as shown schematically in Figure 4.1.2.

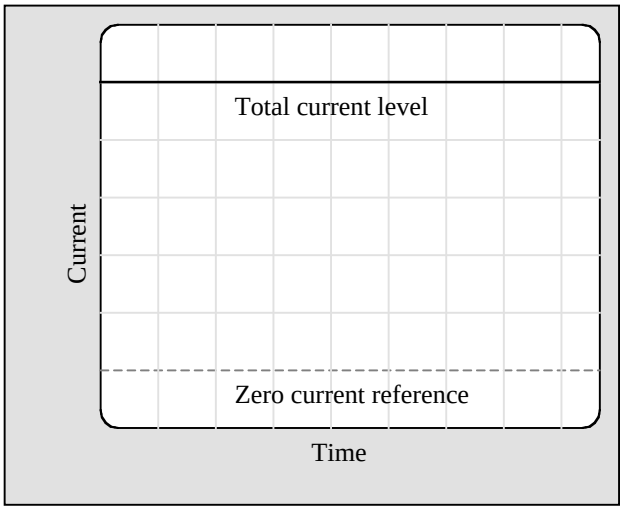

Figure 4.1.2. Schematic of the scope screen with opened gate

On the other hand, if the gate is closed, the current goes to zero on the scope screen, as shown in Figure 4.1.3.

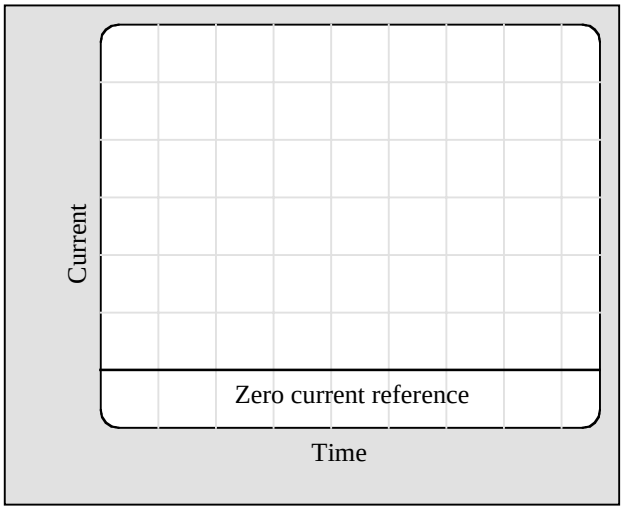

Figure 4.1.3. Schematic of the scope screen with closed gate

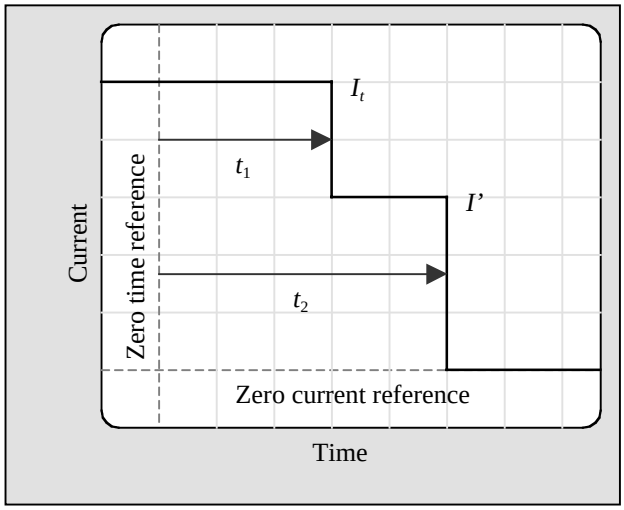

Figure 4.1.4. Schematic of the scope screen with synchronized closed gate

If the closing of the gate is synchronized with the zero time reference of the oscilloscope, the variation of the measured current as it changes from its total value to the zero reference is obtained. If the gate closing is instantaneous, the scope will continue to measure the current until the last set of particles reaches the collector, thus determining their time of flight. For example, Figure 4.1.4 shows the TOF signal curve for a particle beam, where the indicated zero time reference coincides with the moment at which the gate is closed.

Assuming that the beam potential ϕ_B is known and is the same for every particle in the beam, from the curve shown it is found that there are two families of particles with different specific charge,

$$\left(\frac{q}{m}\right)_1 = \frac{(L_0/t_1)^2}{2\phi_B} \quad \text{and} \quad \left(\frac{q}{m}\right)_2 = \frac{(L_0/t_2)^2}{2\phi_B}. \tag{4.1.2}$$

Furthermore, the contribution of each particle family to the total beam current can also be calculated. From the figure, the current fractions are simply given by,

$$f_1 = \frac{I_t - I'}{I_t} \qquad \text{and} \qquad f_2 = \frac{I'}{I_t}. \tag{4.1.3}$$

Figure 4.1.4 is of course an ideal representation in which the TOF steps are located at precise moments in time. In reality one would measure time distributions, i.e., the fall time is not zero. The origin of the time spread can be attributed to two sources:

- Experimentally induced spreads:
    - Gate voltage: The power supply used to control the voltage to the gate has finite rise and fall times that propagate in the measurements.
    - Gate non-idealities: As will be described in Section 4.4, the way in which the gate is constructed introduces some time perturbations that also affect the measurements.
    - Detector speed: The amplifier used to magnify the signal prior to connection to the oscilloscope has an associated time constant.
- Intrinsic spreads:
    - Beam potential: Instead of being a fixed quantity, ϕ_B has an associated energy distribution that modifies the flight time via (3.3.3).
    - Specific charge: It is possible that particles, in particular droplets, are not monodisperse, thus having different sizes or charges distributed around a particular value.

The first type of source will be explored in more detail in following sections, while the second will become a point of discussion when the experimental results are presented.

In any case, a sensitivity analysis for the time resolution, defined here as the time spread Δt divided by the nominal time of flight t_f, can be easily done in terms of the beam potential and specific charge resolutions,

$$\frac{\Delta t}{t_f} = -\frac{1}{2}\left(\frac{\Delta(q/m)}{q/m} + \frac{\Delta\phi_B}{\phi_B}\right). \qquad (4.1.4)$$

This equation will be very helpful in determining the actual distributions in the experiments, assuming that each possible source of time spread can be individually explained.

Dual gate pulsed TOF with charge accumulation

Also tested in the laboratory is a TOF system analogous to the classic Fizeau experiment for measuring the speed of light. This involves the use of two gates, one located in front of the emitter, as in the previous case, and one just before the collector plate. This configuration is shown in Figure 4.1.5.

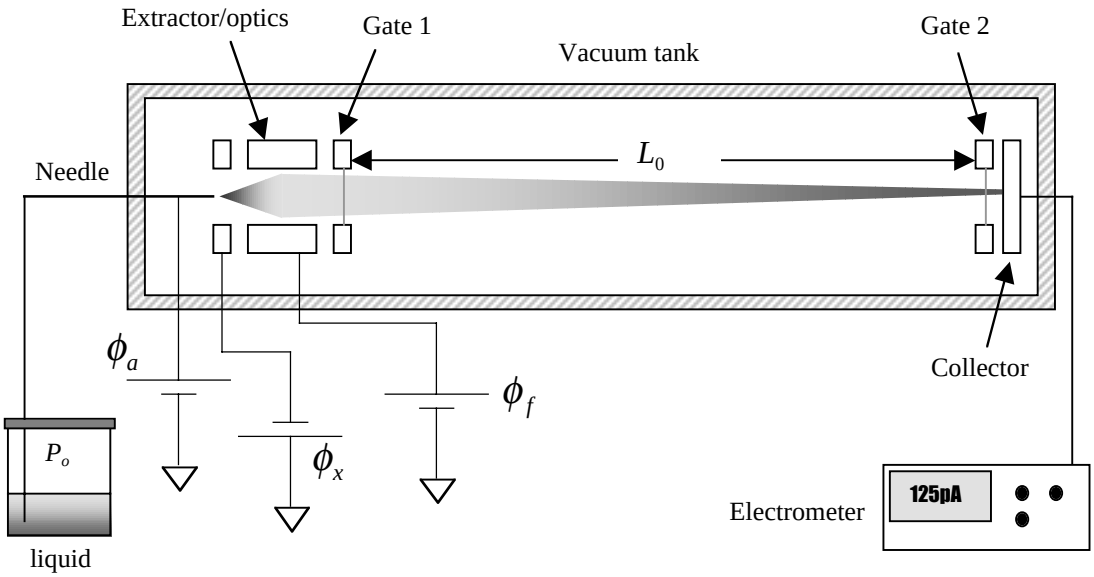

Figure 4.1.5. Schematic of the dual gate TOF

In this configuration, both gates are normally closed and open only for a very short time with a relative delay between the gates. The delay is selected to accept a specific narrow range of flight times. The width of the pulses that open the gates determines the spread of the observed specific charge assuming that no other spreading mechanism exists. The pulse sequence is repeated, with a period long enough to avoid intermixing of particles with different velocities, until enough charge accumulates at the collector. The current is then measured using a sensitive electrometer. The spectrum of the beam is constructed by sweeping the opening delay time between the gates. The advantage of this technique is its potential for wide dynamic range, since the delay can be controlled to almost any value without any constraint. Another virtue of this approach is that it avoids the requirement of high-speed amplifier electronics in the detector. As long as the current is measurable, it is possible to extract time of flight information. The resolution of this technique is limited to the pulse width Δt used to open the gates and can be calculated directly from (4.1.4). The specific charge resolution increases linearly as the pulse width decreases. The current collected, however, decreases with smaller pulses.

Single gate continuous/pulsed TOF with fast ion detection

Finally, a third technique is tested. The configuration is essentially the same as the one shown in Figure 4.1.1, the only difference being the detector type. Since the application is mainly to study fast ions and not droplets, a fast electron multiplier (Channeltron) is installed in the system instead of a metallic collector.

A complete description of this type of detector will be provided in Section 4.2. Suffice it to say for now that an electron multiplier significantly reduces the burden on the amplifier electronics, since they provide formidable gains and extremely short response times.

As for the gate operation sequence, two types are used. The first one is the same as the one shown in Figure 4.1.4, operating in a continuous mode. The second one is pulsed

operation in which the gate is normally closed and only opens for a short time in a single pulse with a repetition period large enough to avoid re-measuring ions. Every time an opening pulse is sent to the gate, a small sample of all particles is allowed to drift towards the electron multiplier detector. The signal is then conditioned and displayed on the oscilloscope screen. Figure 4.1.6 shows the spectrum that would be obtained using this method under the same ideal conditions established for Figure 4.1.4.

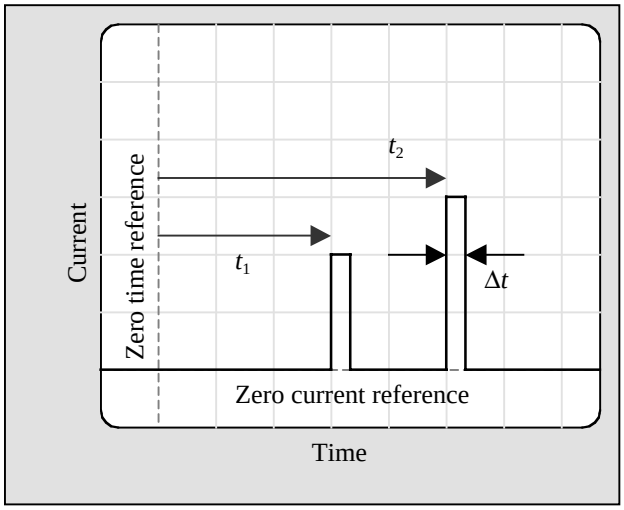

Figure 4.1.6. Schematic of the scope screen: opening pulses, fast detector

The signal peak width shown in Figure 4.1.6 is the same as the pulse width in the ideal situation where there are no other spreading sources. Given this, the resolution can also be computed with (4.1.4). The advantage of this gate operation mode is that the spectrum can be directly displayed on the scope screen and the peak widths and positions can be clearly detected. Of course, another method of obtaining the spectrum would be to take the derivative of the signal shown in Figure 4.1.4. But the signal is often noisy and taking numerical differences in the data produces more noise in the final spectrum, outweighing the advantage of infinite resolution in the ideal case where the derivative of the step yields a delta function.

Stopping potentials

As mentioned before, it is not enough to know the velocity distribution in the particle beam to obtain the distribution in specific charge. So far, it has been assumed that the beam potential ϕ_B is known, but as was briefly discussed above, this is not usually the case. Although there is a relationship between the beam and the applied potentials, the real potential distribution needs to be experimentally measured.

The potential of the beam is measured directly by introducing a controlled potential difference to retard the motion of the particles. Varying the retarding potential while measuring the beam current provides the means to measure the potential distribution. This potential is set by applying a voltage ϕ_s to a set of parallel grids located near the detector, as shown in Figure 4.1.1.

It is possible to combine the TOF experiments with this stopping potential (SP) technique to measure the energy of individual particle families. This will prove to be extremely useful in establishing some important properties of the emission physics of colloid thrusters.

4.2. Hardware and Electronic Setup

Vacuum chamber

It is highly desirable to study colloid thruster emissions under conditions similar to those expected in space. It is very difficult, however, to simulate the same levels of high vacuum that exist in earth orbit. Because of the large difference in pressures between an earth-bound vacuum chamber and outer space, it is important to determine how non-ideal laboratory conditions modify experimental outcomes. As long as the charged particles do not interact with the residual gas inside the vacuum chamber, it can be safely assumed that ground testing is representative of actual thruster operation. The best parameter to

quantify this effect is the mean free path of emitted particles, which is roughly proportional to $1/nQ_c$, where n is the residual gas number density and Q_c is its collision cross section. The density can be estimated assuming an ideal gas from $P = nkT$, where P is the gas pressure, T is its temperature and k is Boltzmann's constant. The cross section can be related, to first order, to the individual projected area of each gas molecule and it decreases with increasing incoming particle energy. Assuming $Q_c = 3\times10^{-19}\text{m}^2$ (relatively large residual molecules) and a minimum mean free path of 3 m, the pressure inside the vacuum chamber must be below 3.5×10^{-5} Torr to avoid interactions [59].

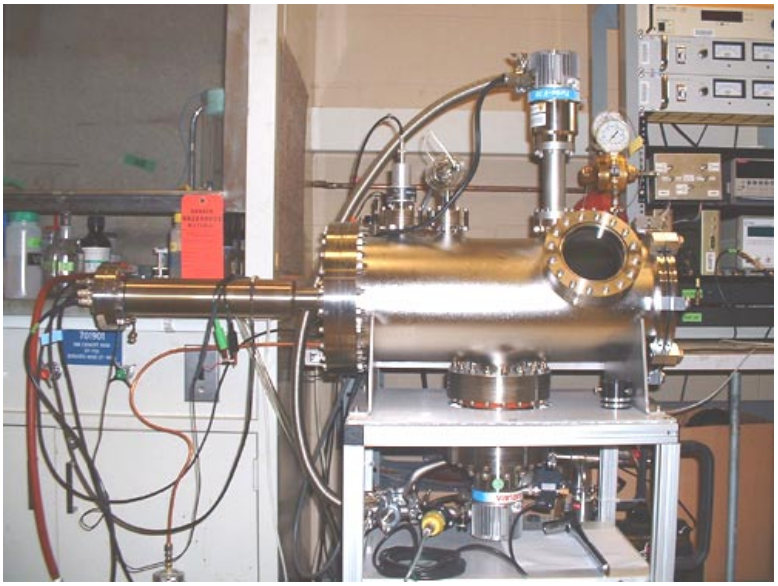

Figure 4.2.1. Vacuum chamber

The vacuum system (Varian Inc) installed in the laboratory consists of a stainless steel cylindrical chamber with an inner diameter of 19.7 cm and a length of 49.5 cm. A cylindrical stainless steel extension with 5.6 cm ID and 36.5 cm in length is attached at the rear end of the main chamber. The total volume of the vacuum system is about 16 liters. The chamber is evacuated by a couple of small turbo pumps (Varian V-70) with a pumping capacity of 68 liters/s (N_2) each. A primary mechanical pump (Varian SD-40) is used to provide the required foreline pressure for both turbo pumps. Ultimate pressure,

with no volatile substances inside the chamber and leak tested, is about 6×10^{-8}torr. The vacuum system is pictured in Figure 4.2.1.

High voltage power supplies

A total of 6 regulated high voltage power supplies are used in the experiments, as can be seen in Figure 4.1.1. Not shown are the two supplies dedicated to the channeltron operation. Their functions and models are:

- Needle emitter: Bertan 205B-05R, 5 kV max.
- Retarding grid: Bertan 205B-10R, 10 kV max.
- Extractor electrode: Acopian P03.5HP17, 3.5 kV max.
- Lens electrode: Acopian P03.5HN17, -3.5 kV max.
- Channeltron: Two Keithley 246, 3 kV max.

Oscilloscope

The data are acquired and displayed using a four-channel digitizing oscilloscope (Agilent 54835A) with 4 GSa/s sample rate in 2-channel mode and 2 GSa/s sample rate in 4-channel mode. The bandwidth of the system is 1 GHz. Rise time into the 1MΩ inputs is 700 ps, while it decreases to 350 ps if 50Ω inputs are used instead. The scope is fully programmable and can be used to analyze and store data in a number of ways. Its memory depth feature is particularly useful in performing average analysis over the observed data. The bandwidth characteristic of this system exceeds any other used in the experiments. The contribution of the oscilloscope to the overall time spreads discussed in the previous section is negligible.

Gate signal and connections

A programmable four-channel pulse/delay generator (BNC 555) is used to produce the gate signal. This device has the ability of generating square pulses from 10 ns to 100 s in width with a 1 ns resolution. The output signal can be either TTL or adjustable up to 12 V with a slew rate of 1 V/ns. The gate voltage needs to be higher than the beam potential ϕ_B in order to stop every particle on its way towards the detector. Typical beam experimental potentials vary from 500 to 1500 V. Obviously, the pulse generator output voltage is not enough to meet this requirement.

To increase the voltage from the generator output, a pulse amplifier module is used (DEI PVM-4210). This module provides two simultaneous differential voltage pulses of up to ±950V (1900 V differential), with pulse rise and fall times <15 ns, and pulse widths adjustable from <40 ns to DC.

Many of the measurements are performed using a metallic collector plate as the particle detector. There is, however, a continuous problem with capacitive coupling between the high voltage pulse generated in the gate and the collector. This coupling manifests as induced noise with a certain time constant that often is longer than the time of flight of the fastest particles. The magnitude of the noise increases as the distance between the gate and the collector decreases. This eventually transforms into a severe limitation for cases where the signal is very small in magnitude, in particular for the dual gate TOF method discussed in Section 4.1.

This capacitive coupling is mainly induced by the high frequency harmonics that give shape to the square pulse generated by the high voltage amplifier. A solution to this problem is to filter out these high frequency harmonics from the gate signal. Since the gate is basically a capacitive load, a low pass filter can be directly applied by adding a resistor in series between the amplifier and the load. The cut-off frequency is determined by the size of the resistor - the smaller its value, the higher the number of high frequency harmonics allowed through the transmission line. Measuring the capacitance of the gate-collector system is not done, but several resistor values are tried until the noise is reduced

well below the weakest signals from the emitter. A resistor value of 2.3 kΩ is finally selected. The result is an amplified signal with slower characteristic times than the original square wave.

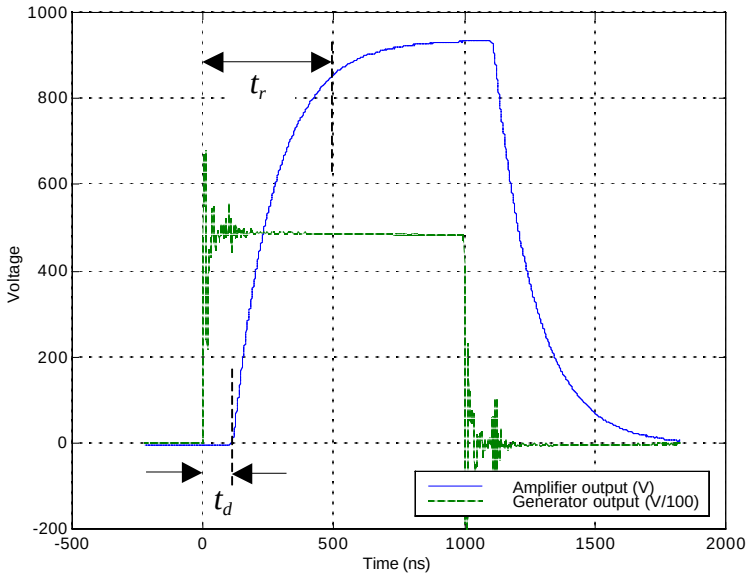

Figure 4.2.2. Pulse amplifier response with *R* = 2.3 kΩ and 1 μs pulse

Figure 4.2.2 shows direct measurements from both the pulse generator and the amplifier module for a 1 μs pulse. The first thing to note is that there is a delay between the rise of the reference signal and the amplifier response. This delay is very close to $t_d = 100$ ns and is intrinsic to the amplifier, i.e., has nothing to do with the applied filter. This means that, using (4.1.4) and assuming zero energy spread, the specific charge spread due to the amplifier delay is about 1% for a typical 20 μs time of flight for the fastest ions observed.

The effect of eliminating high frequency harmonics in the amplified signal is to slow down its rise and fall times as shown in Figure 4.2.2. The rise time is actually slightly less than 500 ns, meaning that, again for a baseline 20 μs time of flight particle, the induced spread in specific charge will be less than 5%.

When working with fast signals it is also important to avoid reflections in the transmission line. Reflection is the main cause of ringing, which results in signal degradation to the point that no measurements can be obtained at all. The way to avoid reflections is to use a homogeneous line (matched impedances) between the signal source and the capacitive load. Ringing is eliminated completely after isolating the amplifier module ground from the global ground inside the chamber. This is done by connecting every grounded element in the vicinity of the gate (third lens electrode, described in Section 4.3 and the gate's grounded apertures, seen in Figure 4.4.4) to the module ground through a separate, isolated cable.

One final word about capacitive coupling: it is important not to neglect it under any circumstances, even with the application of a low pass filter. The larger the exposed area of the gated electrode, the larger the effects of this coupling. This is particularly important for the transmission lines, which need to be shielded and grounded as well as possible, outside and inside the chamber. The use of shielded coaxial cable is strongly recommended, and it is always a good practice to remove the external insulation when exposing the cable to vacuum, thus avoiding air traps that would degrade the pumping performance. It must be kept in mind, however, that the shield should not make contact with any conductive part of the setup besides its ground connection. Shielded vacuum feedthroughs should also be used to further reduce any possibility of interference.

Electron multiplier (Channeltron)

The principles of operation of the electron multiplier are simple to understand. Whenever a sufficiently energetic particle collides with a low work function material (a 200 Å layer of SiO_2 for the one used in these studies), it can extract electrons from it. If there is an electric field that now redirects those electrons towards the material surface, then each one of them could detach many electrons in a new collision. This chain of events would eventually produce a cascade of electrons that could then be collected at an appropriate electrode. These detectors have the formidable property that a single ion can multiply its

charge by many orders of magnitude when detected - gains around 10^6 are typical and larger ones are possible. The other important feature about electron multipliers is their response time that lies in the sub nano second level. This is due to the large voltages used (1.5 to 1.8 kV, negative) to accelerate the electrons towards the anode. In The electron multiplier installed in the experimental arrangement (Channeltron from Burle Electro-Optics Inc.) is similar to the one shown in Figure 4.2.3.

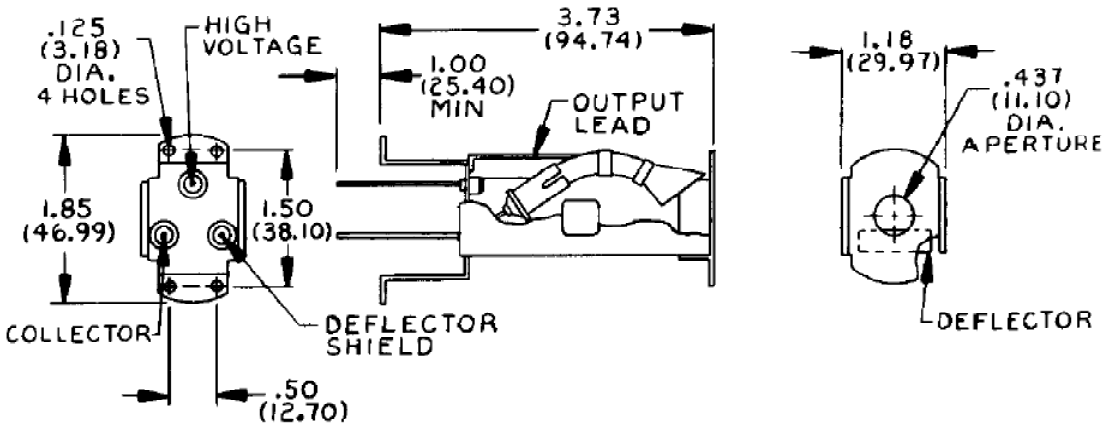

Figure 4.2.3. Off-axis Channeltron (from Burle handbook)

This is an off-axis electron multiplier. The ion beam is detected by the channeltron after biasing a deflector plate located near the casing aperture with a positive voltage between 100 and 300 V. This potential, together with the negative voltage applied to the cone surface, generates an electric field that bends the ion trajectories towards the cone. Figure 4.2.4 shows a schematic with the connections and parts of this type of detector.

The advantages of using an off-axis detector are twofold. First, the deflector plate can also be used as an independent collector plate to monitor the beam current. Second, the emissive channeltron surface is not constantly bombarded, thus extending the device lifetime, especially when beams in the mixed ion-droplet regime are explored. It is also interesting to note that it seems that droplets do not have enough energy to extract electrons from the sensor surface material. However, they can impinge over the sensor

surface and degrade it, especially if the vapor pressure of the liquid is very small. One disadvantage of these detectors is that they only provide “event detection”, i.e., no absolute current measurement. In other words, they are excellent for ion identification purposes, but not to determine relative fluxes.

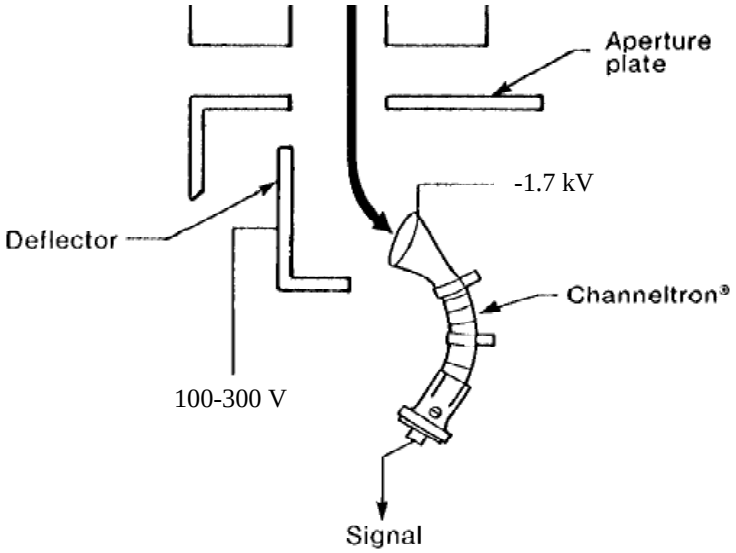

Figure 4.2.4. Off-axis Channeltron schematic (from Burle handbook)

Signal conditioning and amplification

There are different approaches to signal management depending on the type of detector used and the kind of measurement desired. For example, if monitoring the beam current is required, an electrometer operating in the current mode is the ideal solution. The electrometer used (Keithley 6514) has extremely high sensitivity and can measure currents down to a fraction of a pico amp, with resolution in the femto amp level. Such unique specifications are well suited for doing experiments in the dual-gate scanning mode described in Section 4.1. Unfortunately, induced DC noise from capacitive coupling due to the proximity of the second gate to the collector plate produces spurious signals, often in the nA level, high enough to bury the small signals from the TOF measurements.

Nonetheless, the electrometer is a very valuable tool to monitor the behavior of the beam. This is particularly true for the startup process in which a stable cone operation is sought and also when operating for long periods of time, since the electrometer is able to measure the stability of the current signal.

It is usually the case that high speed and high sensitivity is a difficult combination to achieve. In this case the electrometer, operating with relatively slow response times, of the order of milliseconds or higher, has an outstanding sensitivity to very low currents. If high speed is desired, then some sensitivity must be compromised.

In the market today there is an abundant source of discrete electronic components that have extraordinarily high bandwidths. For any given electronic device, the bandwidth decreases as more sensitivity is demanded. TOF measurements represent one of those particular applications in which high sensitivity and high speed are simultaneously required.

In these experiments, operational amplifiers, or op-amps, which are considered among the most useful and flexible discrete electronic components in terms of fast response speeds and high sensitivities, were used. To take advantage of the raw speed characteristics of op-amps, some of the most basic configurations are used to analyze the signals from the TOF detectors: the non-inverting amplifier, the trans-impedance amplifier and the follower or buffer. These configurations are shown in Figure 4.2.5.

The type of signal generated by the detectors is a current i_c varying with time. In the case of the metallic collector plate this current is the same as the beam current, while for the channeltron the current is composed of electrons generated inside the device. Op-amps draw virtually no current at their inputs. This very high impedance makes them ideal to work with voltage signals. In all cases, the current needs to be converted to a voltage in order for the op-amp to work with appropriate sources.

(a)

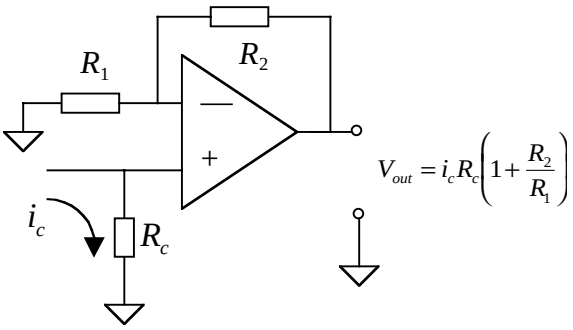

(b)

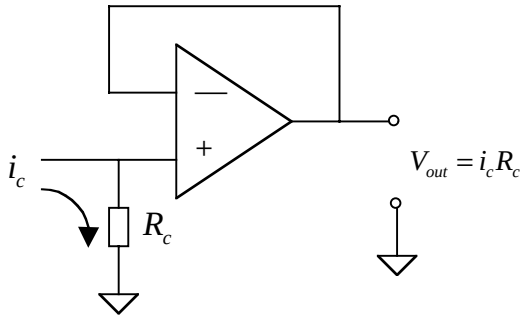

(c)

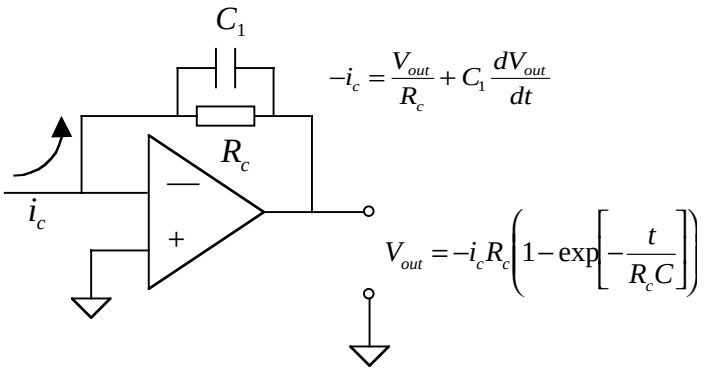

Figure 4.2.5. Op-amp configurations: (a) Non-inverting amplifier, (b) follower or buffer and (c) trans-impedance amplifier

To measure weak signals, the most useful operation modes are the non-inverted and the transimpedance amplifier shown in Figure 4.2.5(a, c). The gain is determined by the relative values of the resistors shown. The larger the gain, the lower the response speed of the circuit. The follower, or buffer, shown in Figure 4.2.5(b) is ideal for signals that do

not require amplification. This unity gain configuration has the advantage of transforming the current source to a voltage source, and the low impedance from the R_c resistor to a high impedance determined by the op-amp inverting input. Two high-speed op-amp components are used in the experiments (TI's OPA602 and OPA655). Their typical responses to small and large signals are shown in Figs. 4.2.6(a) and (b) along with the gain variation with bandwidth.

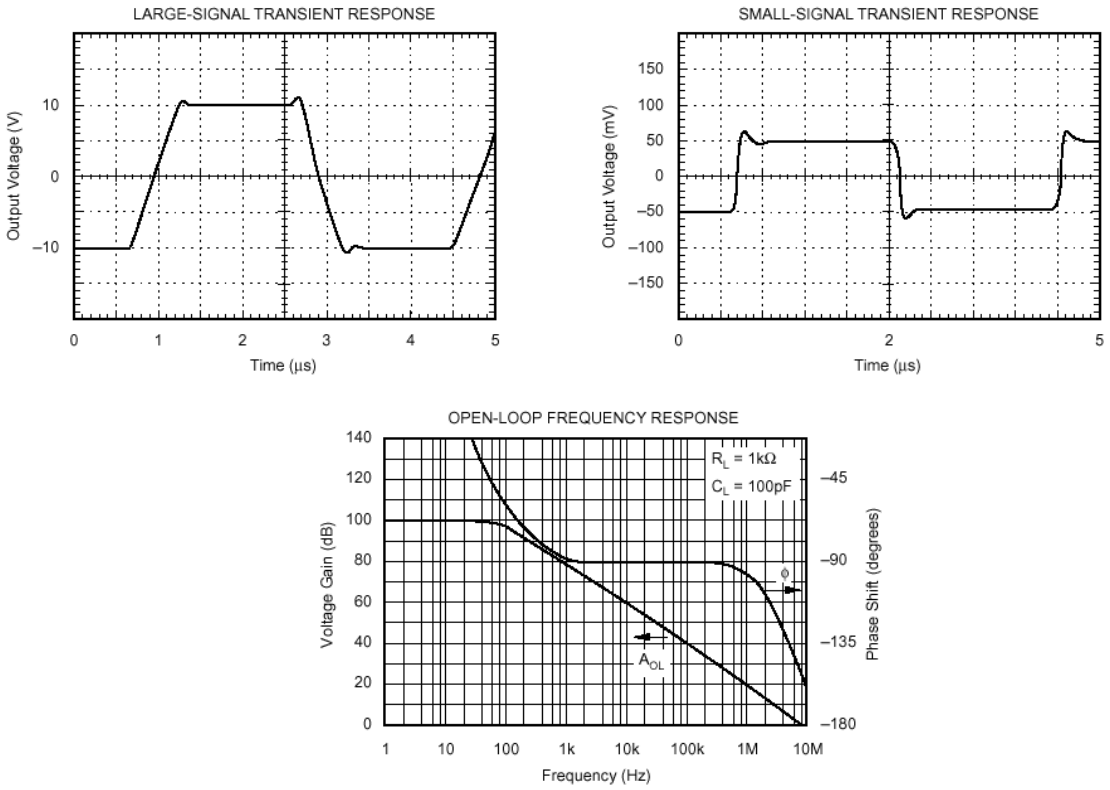

Figure 4.2.6(a). OPA602 - Gain and response characteristics

The OPA602 has similar time characteristics to the filtered pulse generator shown in Figure 4.2.2, while the OPA655 is considerably faster, at small gains. The errors associated with the use of these devices at unity gain will be similar to the 5% time spread induced by the pulse generator. These error sources apply simultaneously and

their contributions are not additive, i.e., the dominant source is the one that gets reflected in the measurements. Op-amp errors will increase if higher gains are used.

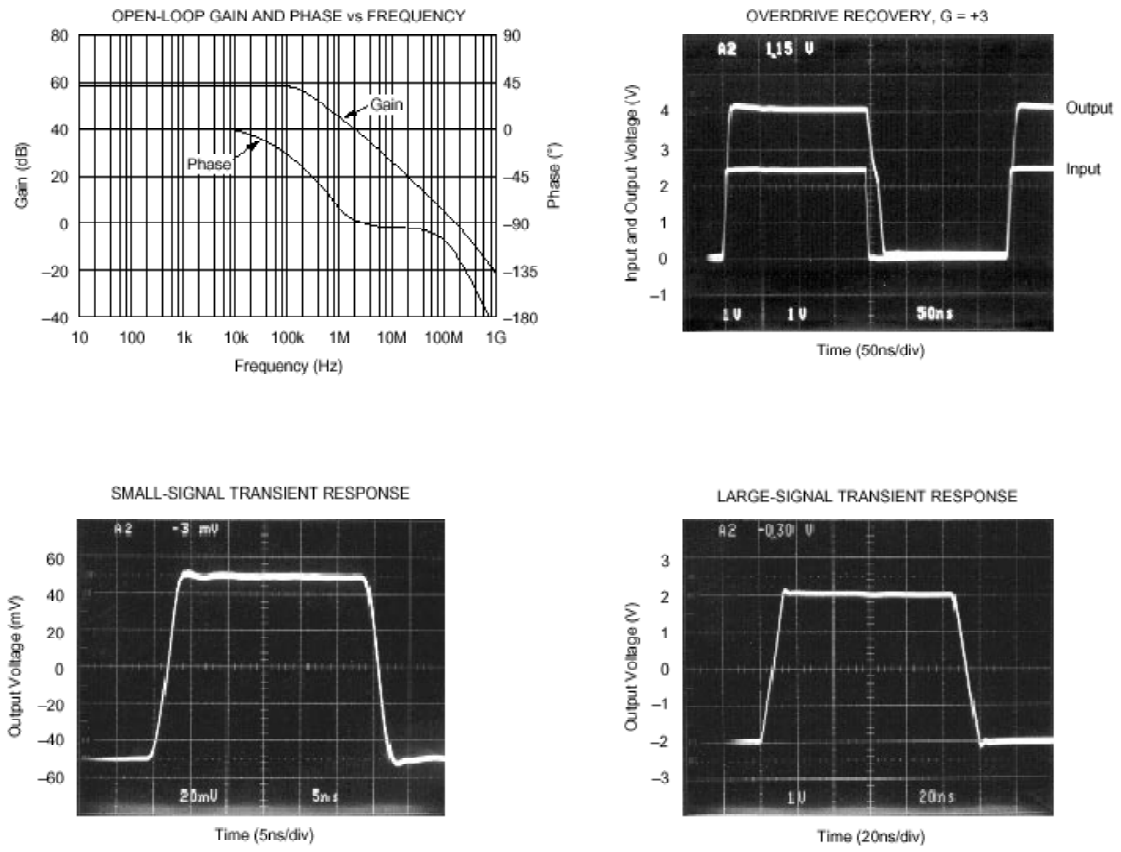

Figure 4.2.6(b). OPA655 - Gain and response characteristics

4.3. Emitter and Optics Design

The emitter is perhaps the most important part of the system. It is designed to produce droplets or ions in a suitable way for the detector to measure them. Since its introduction a few years ago, electrospray science has evolved and grown in considerable ways. Presently there is a well-established industry tailored for the chemical analyst who uses electrosprays to extract macromolecules from liquid solutions [16]. The needle emitters

used in this study are commercially available (New Objective Inc). They consist of a fused silica capillary 5 cm in length, 20, 50 or 75 µm ID and 360 µm OD. One end of the capillary is gradually tapered to the final tip diameter of 5, 10, 15 or 30 µm. The capillary needle is covered with a noble metal conductive layer, except for the tip, which is left uncoated. Needle description, connections and a close-up of the tip section can be seen in Figure 4.3.1.

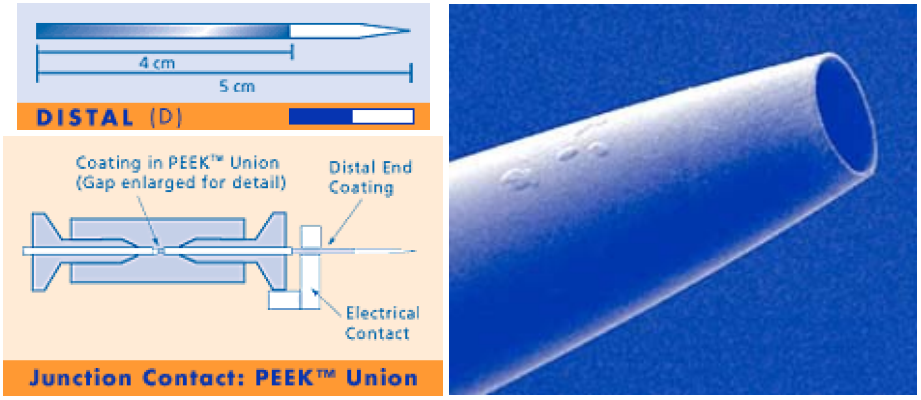

Figure 4.3.1. Distal coated needle emitter, from New Objective Inc.

A modified capillary union (Upchurch Scientific) is used to make the electrical contact between the power supply and the liquid. This contact actually occurs between capillary connections, where the distal end of the coated needle meets the liquid, as seen also in Figure 4.3.1. As explained before, the liquid is injected into the needle at a certain rate while a potential between the emitter and a downstream electrode (extractor) provides the electric field that deforms the meniscus in the tip into a Taylor cone, from which a spray of charged droplets is emitted and diverges as it moves downstream.

There are two advantages of leaving the tip section uncoated: (1) fused silica is transparent and with the aid of a microscope one can troubleshoot the system for trapped bubbles and (2) there is no coating that can be damaged because of unintentional arcing between the tip and the extractor electrode, so the electrical contact remains intact.

Another important aspect of the emitter is that a higher voltage is required to form the cone and start the emission than that required to keep the conical shape in steady state. This hysteresis behavior indicates that it takes more energy to produce the initial instability than to maintain it. A geometrically sound model has been used [60] to estimate the starting voltage as a function of the needle tip ID d_c, the surface tension of the liquid γ and the distance from the extractor electrode D,

$$V_{start} = \sqrt{\frac{d_c \gamma}{2\varepsilon_o}} \ln\left(\frac{4D}{d_c}\right). \tag{4.3.1}$$

Figure 4.3.2 shows the starting voltage for three different tip-extractor separation distances as a function of needle tip diameters for $\gamma = 0.058$ N/m (formamide).

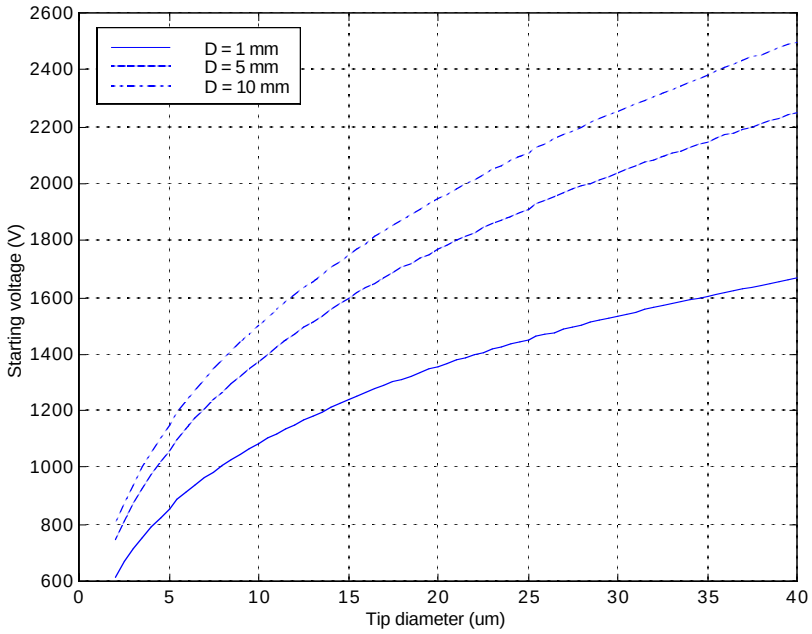

Figure 4.3.2. Starting voltage vs. needle tip diameter for γ= 0.058 N/m (formamide)

Since the steady-state operation voltage is only slightly less than the starting voltage, it is desirable to operate with small tips and separation distances, in order to keep the beam potential lower than the gate potential, as discussed in Section 4.2.

Once emitted, charged particles travel towards the detector. It is clear from (4.1.4) that the longer the flight time t_f, the better the resolution in specific charge. There are only two ways of increasing the time of flight for fixed particle properties. One is simply by increasing the flight distance between the gate and the detector plate. The second is to slow the particles down so they arrive at a later time. In either case, the initial beam spreading can be quite large, thus reducing the amount of charge density with distance considerably.

To obtain measurable signals at long distances, with relatively small detectors, a way of focusing the beam to counteract the initial spreading is needed. The theory of focusing charged particles is well developed [48,49]. In fact there is a complete analogy between light optics and ion optics, to the point where the same models can be used indistinguishably if the ion beams meet the conditions that lead to the homogeneous version of the paraxial ray Equation (3.3.32). As discussed in Section 3.3, space charge effects are important if the perveance is high. If that is the case, the RHS of (3.3.32) becomes important, possibly dominating the behavior of the beam, especially for trajectories very close to the propagation axis.

The use of external electromagnetic fields is the only way in which charged particles can be forced to modify their trajectories. Instead of building lenses out of materials with different indices of refraction as in the case of light optics, ion optics make use of electrodes set at different potentials, and of magnets. Assuming, as in Section 3.3, that the beams are axisymmetric, it is logical to use fields with the same symmetry to construct optical devices. This restricts the type of elements for electrostatic focusing to conductive apertures and cylinders.

In particular, one could make use of a focusing device commonly known as an *einzel* or equipotential lens. In a lens of this type, a potential gradient is generated in the path of the charged beam, followed by a second opposite gradient that leaves the particles with the same axial kinetic energy they had before entering the device, while providing a net focusing effect in the radial direction.

The most widely-used einzel lens configuration is comprised of three cylindrical electrodes as shown in Figure 4.3.3(a). The first and third electrodes share the same potential, usually ground, while the second is biased either up or down with respect to the other two.

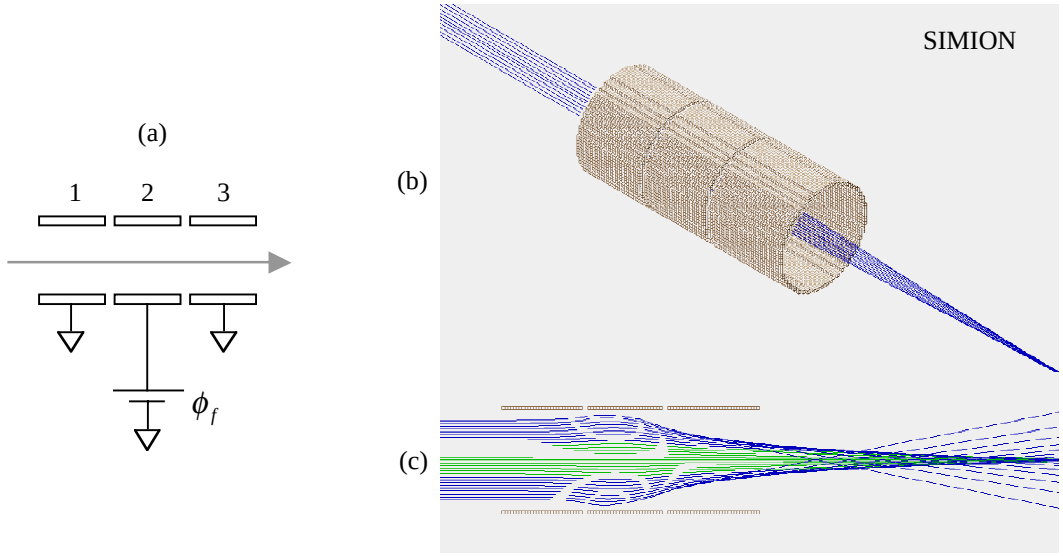

Figure 4.3.3. (a) Einzel lens configuration, (b) focusing property and (c) radial effect: spherical aberration

Figure 4.3.3(b) shows a result from ion simulation software (Simion) able to trace charged particle trajectories as they travel through the lens. As can be seen in Figure 4.3.3(c), an important effect that needs to be considered is that near the electrodes, the electric fields are distorted considerably with respect to the fields at the propagation axis,

thus changing the focusing properties of those particles that move too close to the electrodes. A good design avoid this form of *spherical aberration* by using cylinder diameters at least twice as large as the expected beam size inside the lens. Of course, the larger the lens, the higher the focusing voltage. The best design results from a compromise among all these factors.

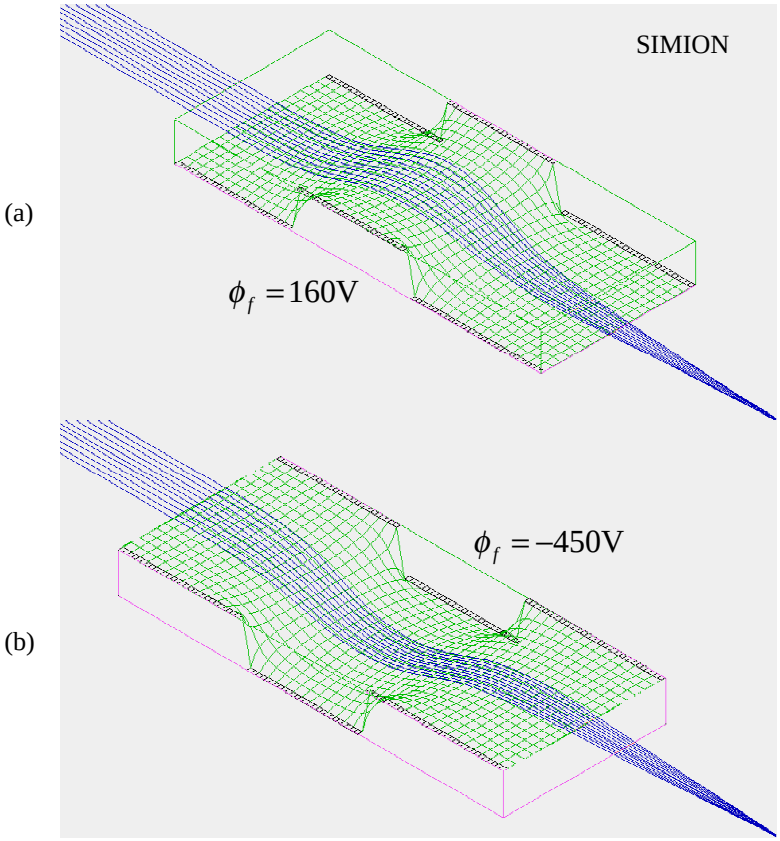

Figure 4.3.4. Einzel lens focusing with (a) positive and (b) negative voltage

An interesting property of the einzel lens is that it always has a focusing effect on charged particles, regardless of the charge sign or of the focusing voltage polarity for a given particle charge. Figure 4.3.4 exemplifies this situation. Shown is a trajectory simulation in the electric potential space of 200 eV positive singly-charged ions passing through an einzel lens in the cases where (a) the focusing potential is positive and (b)

where it is negative. As can be seen, similar optics properties are obtained despite the applied voltages being quite different. The reason is simple; in case (a) the positive potential retards the axial motion of the particles, thus allowing more time for radial movement before they accelerate again to their original speed. The opposite occurs in (b) where the negative field accelerates the beam, considerably decreasing the residence time inside the lens and therefore limiting the perpendicular movement of charged particles.

For the experiments, two einzel lenses using different approaches are designed. In the first design the paraxial ray approximation described in Section 3.3 is used. With the help of an elliptic solver (Matlab's PDE toolbox), the electric potential can be obtained after solving Laplace's Equation for a given electrode geometry and boundary conditions. Figure 4.3.5 shows the geometry of the emitter, extractor and the lens, superimposed on the mesh and the solution itself. It is clear how the grounded electrodes effectively shield the strong negative potential in the middle region of the lens.

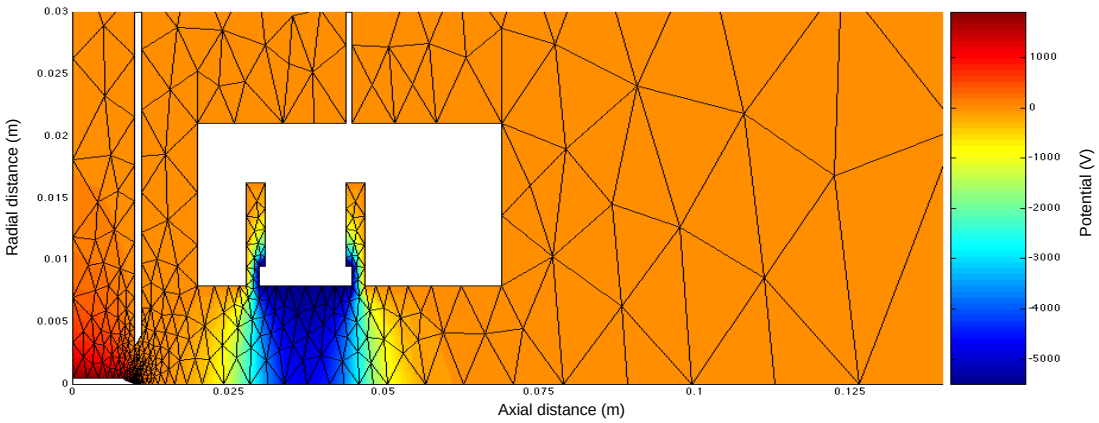

Figure 4.3.5. Computational domain – emitter, extractor and einzel lens

The next step is to extract the axial potential from this configuration and use it to solve (3.3.32) with the conditions expected during the focusing experiments. Figure 4.3.6 shows the result of the calculation. This particular beam shape is obtained with a negative

potential $\phi_f = -5.5\text{kV}$. The rest of the required parameters are extracted from experimental conditions (Section 5.2).

It is interesting to note from Figures 4.3.5-6 that trajectory changes occur precisely at regions with large potential gradients. It is also worthwhile to mention that this solution retained the space charge term on the RHS of (3.3.32). The most important effect of this term is the initial spreading of the particle beam observed close to the emitter.

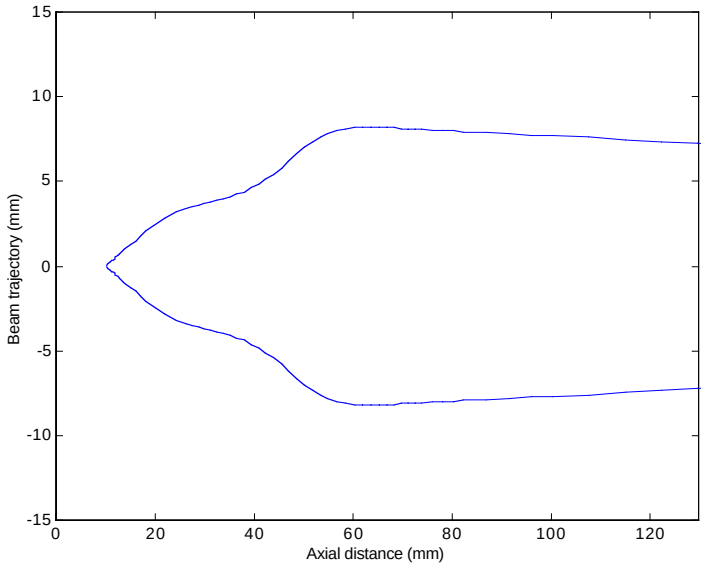

Figure 4.3.6. Trajectory calculation from the paraxial ray equation

This design was the first to be tested in the laboratory. Its main purpose was to validate the use of an einzel lens to focus charged particles from colloid beams. The experimental arrangement is pictured in Figure 4.3.7, where the needle emitter with its electrical connection and the extractor aperture can be seen.

Note from Figs. 4.3.5-6, that some of the computed trajectories suffer from a problem mentioned a few paragraphs above, namely, they get too close to the electrode surface, therefore introducing spherical aberration like that of Figure 4.3.3(c).

In order to prevent the signal from being deteriorated by the lens, a new design was made using commercially available simulation software (Simion). Figure 4.3.8 shows a design view of the emitter-lens components along with some particle trajectories. Only conductive materials are shown in this representation.

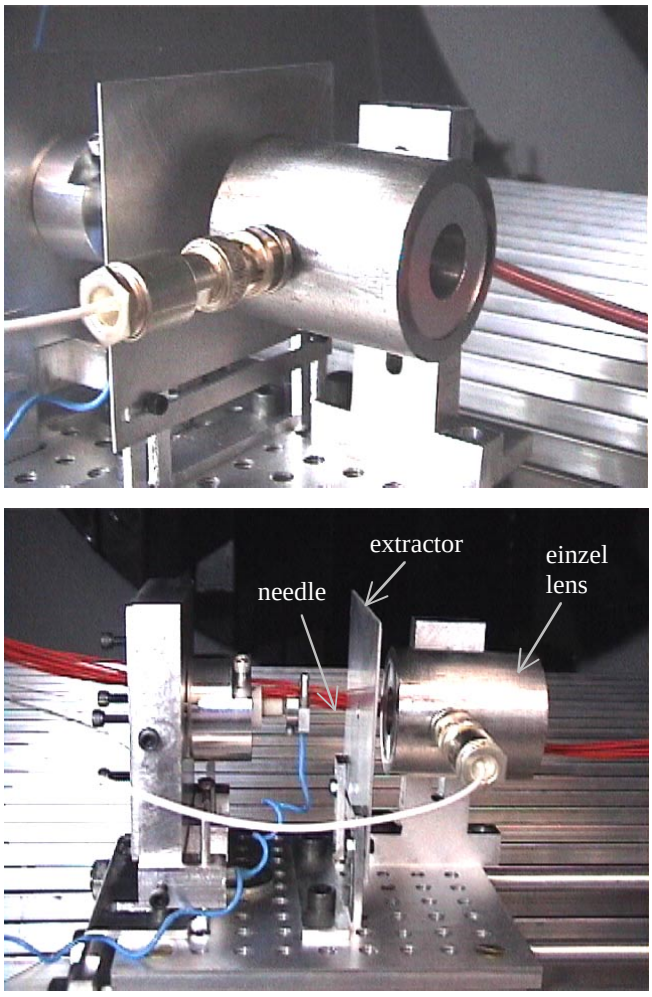

Figure 4.3.7. Needle emitter and einzel lens

Labeled number 1 in Figure 4.3.8 is the needle emitter, which is distal coated, and therefore abruptly ends between electrodes 2 and 3, although its uncoated tip is very close to the extractor aperture 3. As seen in the previous design shown in Figure 4.3.7, the needle was mounted on a movable device. Centering the tip with respect to the extractor was manually done, a difficult task. Instead of this manual approach, a simpler way is to introduce the needle into a self-centering pinhole slightly larger than the 360 μm needle OD, drilled in the center of plate 2, which is kept at the same potential ϕ_a as the emitter. Fused silica needles are extremely fragile, especially in the tip section. To avoid damage, the needle insertion is made with the help of a microscope. The extractor plate 3 has a small aperture in its center and is connected to its own power supply set at a potential ϕ_x. The net extraction voltage is then $\phi_{ex} = \phi_a - \phi_x$, while the beam potential is $\phi_B < \phi_a$.

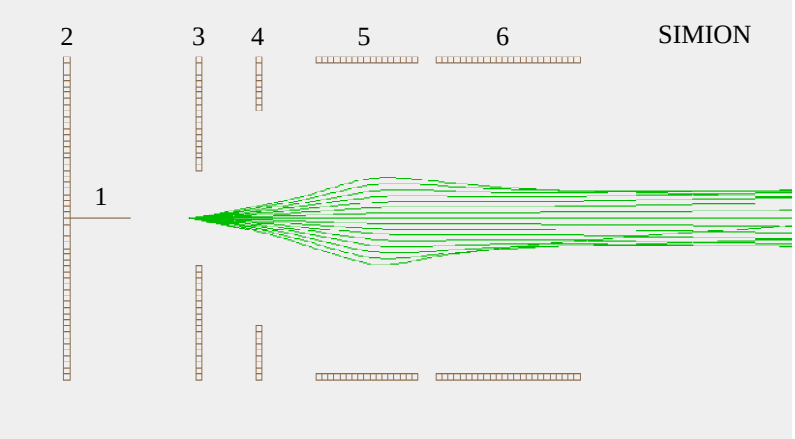

Figure 4.3.8. Configuration of the colloid emitter

Electrodes 4, 5 and 6 form a non-symmetric einzel lens [61]. The reason it is called non-symmetric is because grounded electrodes 4 and 6 have very different shapes; electrode 4 is an aperture, while number 6 is a cylinder. This configuration is selected to minimize the axial distance, and therefore, the beam spreading, before the region of high potential

gradients is reached in electrode 5, which is also a cylinder and is connected to a power supply set at a voltage ϕ_f.

Figure 4.3.9 shows a view in electric potential space of the simulated emitter. In this case $\phi_a = 900\text{V}$ and $\phi_x = -200\text{V}$, so that $\phi_{ex} = 1100\text{V}$. The lens voltage is $\phi_f = 1200\text{V}$.

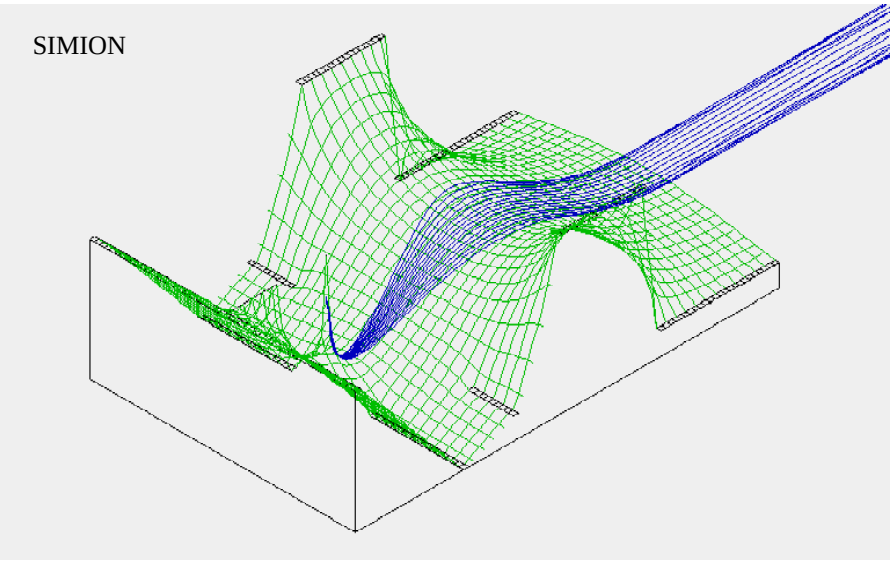

Figure 4.3.9. Emitter design in electric potential space with ϕ_a = 900 V, ϕ_x = -200 V, ϕ_{ex} = 1100 V and ϕ_f = 1200 V

By setting the extractor voltage to a negative value, the emitter potential and therefore the beam potential can be decreased proportionally, thus allowing the use of the gate amplifier discussed previously. As pointed out, this has the advantage of improving the time resolution by increasing the time of flight. The problem is that this advantage could be canceled out since energy resolution is lost via (4.1.4) at lower beam potentials. The dimensions of the emitter are shown in Figure 4.3.10

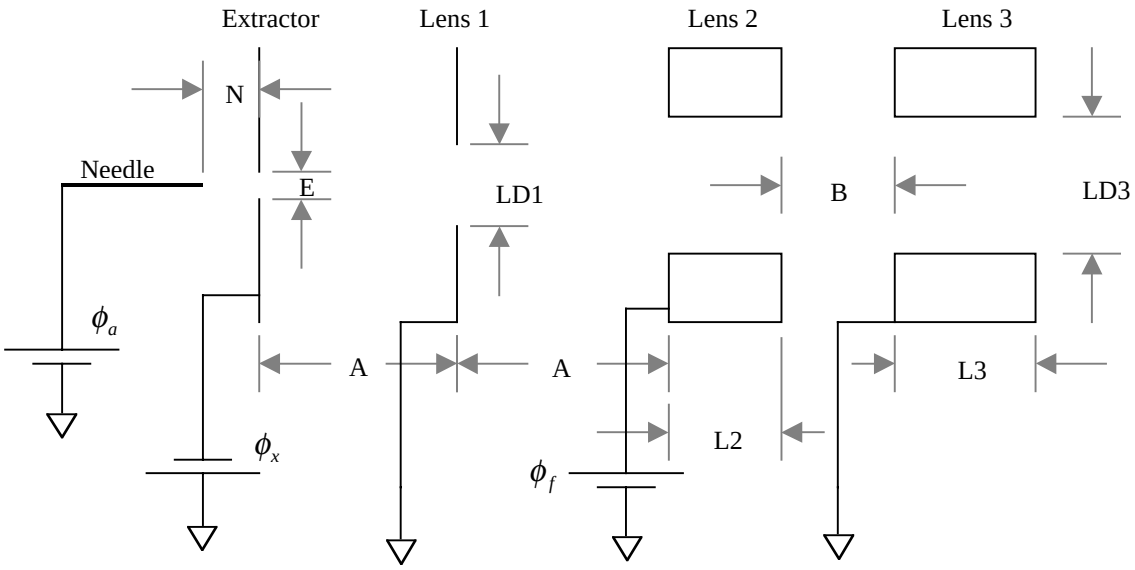

Thickness of the Extractor and Lens 1 plates is 0.025” = 0.635 mm

Longitudinal separations:	Cylinder lengths:	Aperture diameters:
N = 0.3 mm	L2 = 5.59 mm	E = 5.08 mm
A = 2.54 mm	L3 = 7.87 mm	LD1 = 11.4 mm
B = 0.64 mm		LD3 = 16.25 mm

Figure 4.3.10. Emitter dimensions

Figure 4.3.11 shows a picture of the assembled emitter and lens. Most of the components used to put the emitter together are commercially available (Kimball Physics Inc). Stainless steel is the material used for every conductive component. The cylinders are spot-welded to appropriate apertures. Alumina tubes and spacers are used to separate individual electrodes. Also shown in this picture are a set of deflection plates used to steer the beam into the detector and the electrostatic gate.

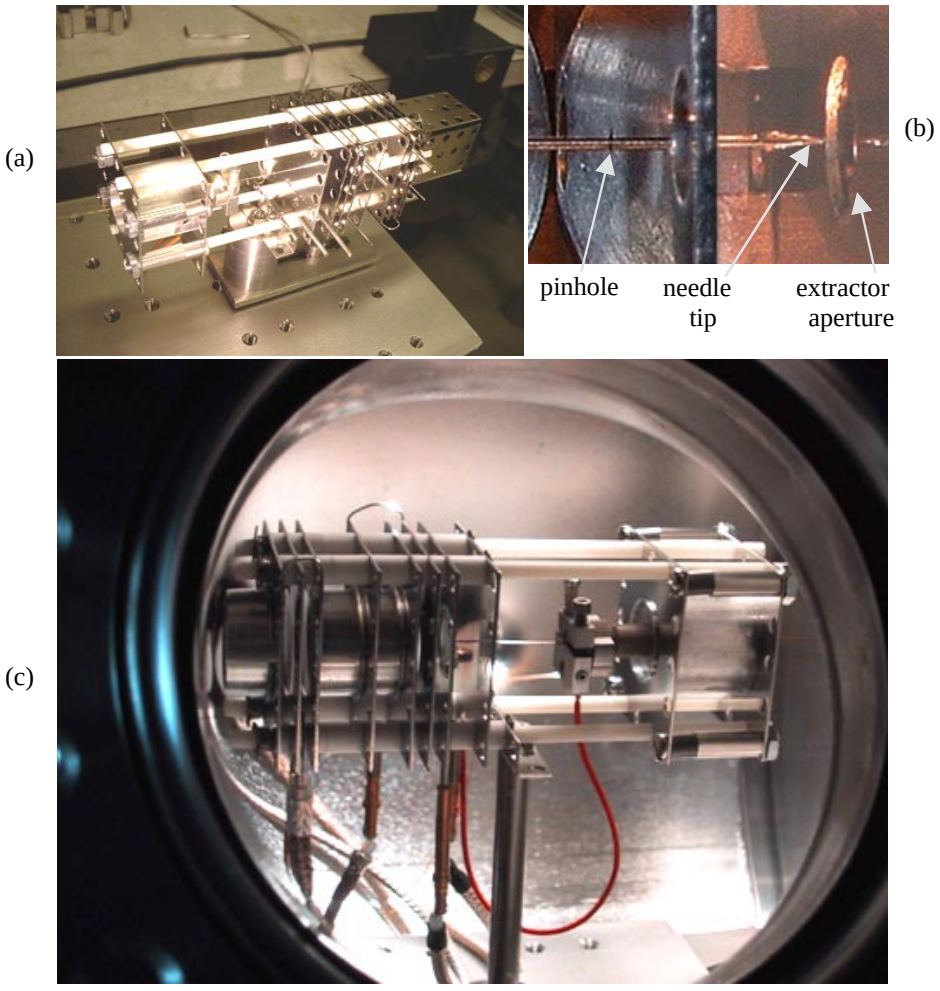

Figure 4.3.11. (a) Assembled emitter with einzel lens, electrostatic gate and deflection plates, (b) close-up of the needle and (c) emitter inside the vacuum chamber with electrical connections.

4.4. Electrostatic Gates

A common part of many TOF spectrometers is the electrostatic gate, which stops the flow of particles when activated. The gating mechanism introduces electric fields in the direction of motion of the particles that could modify the velocity, and therefore the

energy level of those that are not stopped because of the gate non-idealities [62]. The perfect gate would present symmetric potentials upstream and downstream along the particle's path when active and therefore no electric forces would show up in the direction of motion. The interleaved comb gate is an example. It is constructed from very thin, closely-spaced conducting filaments having alternating positive and negative potentials [63,64]. The most elementary type of symmetric gate would be a set of parallel plates. The problem with these is that they behave non-ideally near the plates, and also require very high voltages to produce important deflections.

Very fine interleaved comb gates may be unsuitable for colloid experimentation since liquid could deposit in the filaments, causing possible short-circuits. If non-ideal devices need to be used, gate effects that would modify the measurements can be expected. In this section, a model to describe these effects is presented.

The electrostatic non-ideal gate used in the experiments introduces a potential barrier that allows particles to reach the current collector or be stopped and reflected. The simplest model (which could also be the correct one in a charge-free region) for the gate is a linear barrier grounded at its extremes as shown in Figure 4.4.1. The parameters that completely describe this barrier are the positions of the pulsed and grounded grids; x_m and x_∞ respectively, and the grid voltage ϕ_m. Shown also is the potential level ϕ_B of the particle beam. It is clear that, since $\phi_B < \phi_m$, all particles are stopped when the barrier is up.

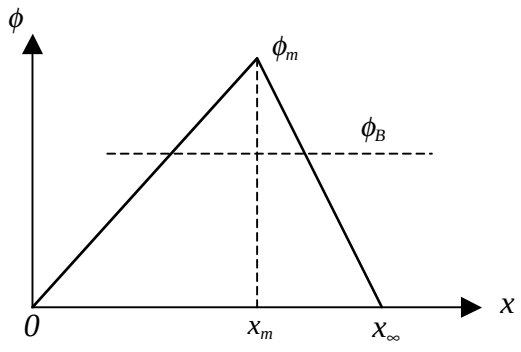

Figure 4.4.1. Electrostatic gate potential barrier

In some of the experiments, the barrier is normally closed and opens only for a small time *T*. Defining x_0 as the position of a particle at the time when the barrier is opened, the position of the particle at the moment when the barrier closes is,

$$\begin{aligned} x_T &= x_0 + T\sqrt{2\frac{q}{m}\left(\phi_B - \phi_m \frac{x_0}{x_m}\right)} \quad \text{for} \quad x_0 > 0, \\ x_T &= x_0 + T\sqrt{2\frac{q}{m}\phi_B} \qquad\qquad \text{for} \quad x_0 < 0. \end{aligned} \tag{4.4.1}$$

If the particle has enough energy to pass the potential barrier by the time it closes, it will in general leave with a different energy than it had prior to entering the barrier influence zone. This is evident since the fields generated by the potential distribution are axially directed and they either accelerate or decelerate charged particles depending on their positions. The different regions that share an energy level in the exit plane are shown in Table 4.4.1 in terms of the non-dimensional parameters,

$$\begin{aligned} &\xi_0 = \frac{x_0}{x_m} \quad \xi_\infty = \frac{x_\infty}{x_m} \quad \xi_T = \frac{x_T}{x_m} \quad \alpha_v = \frac{\phi_B}{\phi_m}, \\ &\alpha_T = \frac{q}{m}\phi_m (T/x_m)^2. \end{aligned} \tag{4.4.2}$$

Region	ξ_0	ξ_T
A1	$\xi_0 < 0$	$\xi_T < 0$
A2		$0 < \xi_T < 1$
A3		$1 < \xi_T < \xi_\infty$
A4		$\xi_T > \xi_\infty$
B1	$\xi_0 > 0$	$\xi_0 < \xi_T < 1$
B2		$1 < \xi_T < \xi_\infty$
B3		$\xi_T > \xi_\infty$

Table 4.4.1. Regions with different energy characteristics

For each of these regions the non-dimensional energy gain (or loss) is given by,

$$\Delta\varepsilon = \frac{(\phi_T - \phi_0)}{\phi_B}, \tag{4.4.3}$$

where ϕ_0 and ϕ_T are the local potentials corresponding to x_0 and x_T respectively. Table 4.4.2 shows the energy level for each region and whether it contains particles that pass through or bounce from the potential barrier.

R	$\Delta\varepsilon$	**Pass the barrier?**
A1	0	No
A2	$\frac{\xi_0 + \sqrt{2\alpha_v\alpha_T}}{\alpha_v}$	If ξ_0 is larger than $1-\alpha_v-\sqrt{2\alpha_v\alpha_T}$
A3	$\frac{\xi_\infty - \xi_0 - \sqrt{2\alpha_v\alpha_T}}{\alpha_v(\xi_\infty - 1)}$	Yes
A4	0	Yes
B1	$\frac{\sqrt{2\alpha_T(\alpha_v - \xi_0)}}{\alpha_v}$	If ξ_0 is less than $\alpha_v - \frac{(1-\alpha_v)^2}{2\alpha_T}$
B2	$\frac{\xi_\infty - \xi_0 - \sqrt{2\alpha_T(\alpha_v - \xi_0)}}{\alpha_v(\xi_\infty - 1)} - \frac{\xi_0}{\alpha_v}$	Yes
B3	$-\frac{\xi_0}{\alpha_v}$	Yes

Table 4.4.2. Energy change of particles

The velocity at which particles leave the gate is then,

$$v_\infty = v_s\sqrt{1+\Delta\varepsilon} \qquad \text{with} \qquad v_s = \sqrt{2\frac{q}{m}\phi_B}, \tag{4.4.4}$$

where v_s is the original particle velocity. Plotted in Figure 4.4.2 are lines of v_∞ / v_s with respect to the initial position ξ_0 for three cases with $T = 30\mu\text{s}$, $x_m = 10\text{mm}$, $x_\infty = 15\text{mm}$, $\phi_B = 700\text{V}$ and $\phi_m = 950\text{V}$. In the first case ($q/m = 100$ C/kg), all particles exit the gate with a velocity $v_\infty > v_s$. The net effect for these conditions would be a shift and broadening of the measured spectrum. In the second and third cases, particles start to fall into region A4, in which their velocity remains unchanged. Also for these cases, a fraction of the particles leave the gate with velocities lower than the source velocity.

Figure 4.4.2 gives a preliminary indication that the fraction of particles that leaves the gate with a different velocity than the original will be smaller for larger values of specific charge, i.e., for larger particle velocities. The reason for this is that the larger the particle velocity, the smaller the residence time inside the gate, and therefore the smaller the time for interactions.

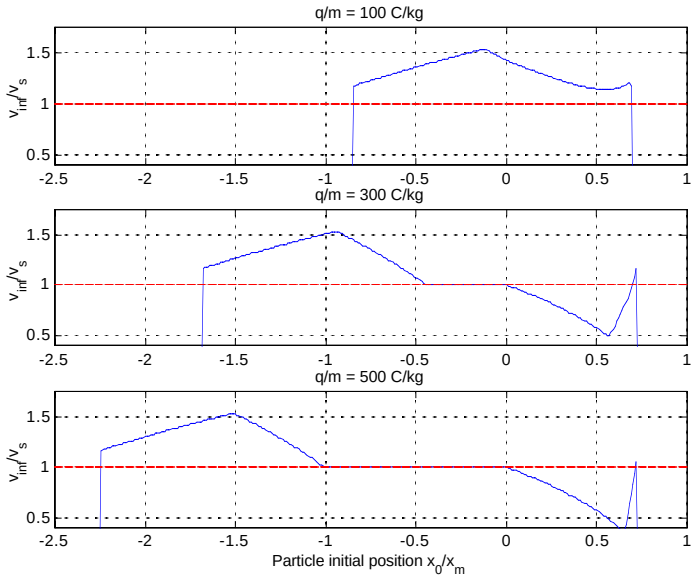

Figure 4.4.2. Velocity maps for different specific charge

The fraction of total current $f_{v_\infty} dv_\infty$ contributed by particles in $[v_\infty, v_\infty + dv_\infty]$ is written in terms of $f_{x_0}(x_0)dx_0$, the fraction of passing particles in the range $[x_0, x_0 + dx_0]$ and $f_{q/m}(q/m)d\frac{q}{m}$, the fraction of current emitted by the source in $[\frac{q}{m}, \frac{q}{m} + d\frac{q}{m}]$,

$$f_{v_\infty} dv_\infty = \int_{-\infty}^{\infty} f_{x_0}(x_0)dx_0 f_{q/m}\left(q/m(v_\infty, x_0)\right)d(q/m). \tag{4.4.5}$$

Note that $q/m = q/m(v_\infty, x_0)$ through Table 4.4.2 and Equation (4.4.4), since v_∞ depends on location x_0 at gate opening and particle q/m. If x_0 and v_∞ are fixed, this determines q/m, although maybe non-uniquely. For a line of constant q/m,

$$dv_\infty = \frac{\partial v_\infty}{\partial x_0} dx_0 + \frac{\partial v_\infty}{\partial (q/m)} d(q/m) = \left(\frac{\partial v_\infty}{\partial x_0}\right)_{q/m} dx_0, \tag{4.4.6}$$

and the exit velocity distribution function is,

$$f_{v_\infty}(v_\infty) = \int_0^{\infty} f_{q/m}(q/m) f_{x_0}\left[x_0(v_\infty, q/m)\right] \frac{d(q/m)}{\left(|\partial v_\infty / \partial x_0|\right)_{q/m}(v_\infty, q/m)}. \tag{4.4.7}$$

Defining $n(x_0)$ and $v(x_0)$ as the number of particles per unit length and particle velocity at x_0, the fraction of passing particles per unit length dx_0 in the interval between x_0 and $x_0 + dx_0$ is,

$$f_{x_0}(x_0) = \frac{n(x_0)}{\int_{x_{0\,\min}}^{x_{0\,\max}} n(x_0')dx_0'}, \tag{4.4.8}$$

where $[x_{0\min}, x_{0\max}]$ defines the interval in which particles pass the barrier. Since the particle flux Γ must be conserved,

$$\Gamma = nv = n(x_0)v(x_0). \tag{4.4.9}$$

Substituting (4.4.9) into (4.4.8) and using Tables 4.4.1 and 4.4.2, the passing particle fraction is,

$$f_{x_0}(x_0) = B^{-1}\begin{cases} 1 & \text{for} \quad \xi_0 < 0 \\ (1-\xi_0/\alpha_v)^{-1/2} & \text{for} \quad \xi_0 > 0, \end{cases} \tag{4.4.10}$$

in which the coefficient B is given by,

$$B = x_m\left(\alpha_v + \sqrt{2\alpha_v\alpha_T} - 1\right)\left(1 + \sqrt{2\alpha_v/\alpha_T}\right). \tag{4.4.11}$$

Equations (4.4.1-4, 4.4.10-11) and tables 4.4.1 and 4.4.2 can be used to compute the elements of (4.4.7) for a given set of physical parameters, with the exception of those particles contained in region A4 for which a special treatment is required.

Since all particles in region A4 pass the barrier without energy change, the function $f_{x_0}(x_0)$ is a constant and the partial derivative in (4.4.7) is zero. This means that,

$$\frac{f_{x_0}[x_0(v_\infty)]}{\partial v_\infty/\partial x_0} \to \infty, \tag{4.4.12}$$

is a Dirac delta function whose contribution can be added to the rest of the terms in (4.4.7). The delta function can be written as,

$$\left.\frac{f_{x_0}[x_0(v_\infty)]}{\partial v_\infty/\partial x_0}\right|_{\text{A4}} = C\delta(v_\infty - v_s). \tag{4.4.13}$$

Using (4.4.10) and performing the integral in the A4 region, the value of C is computed,

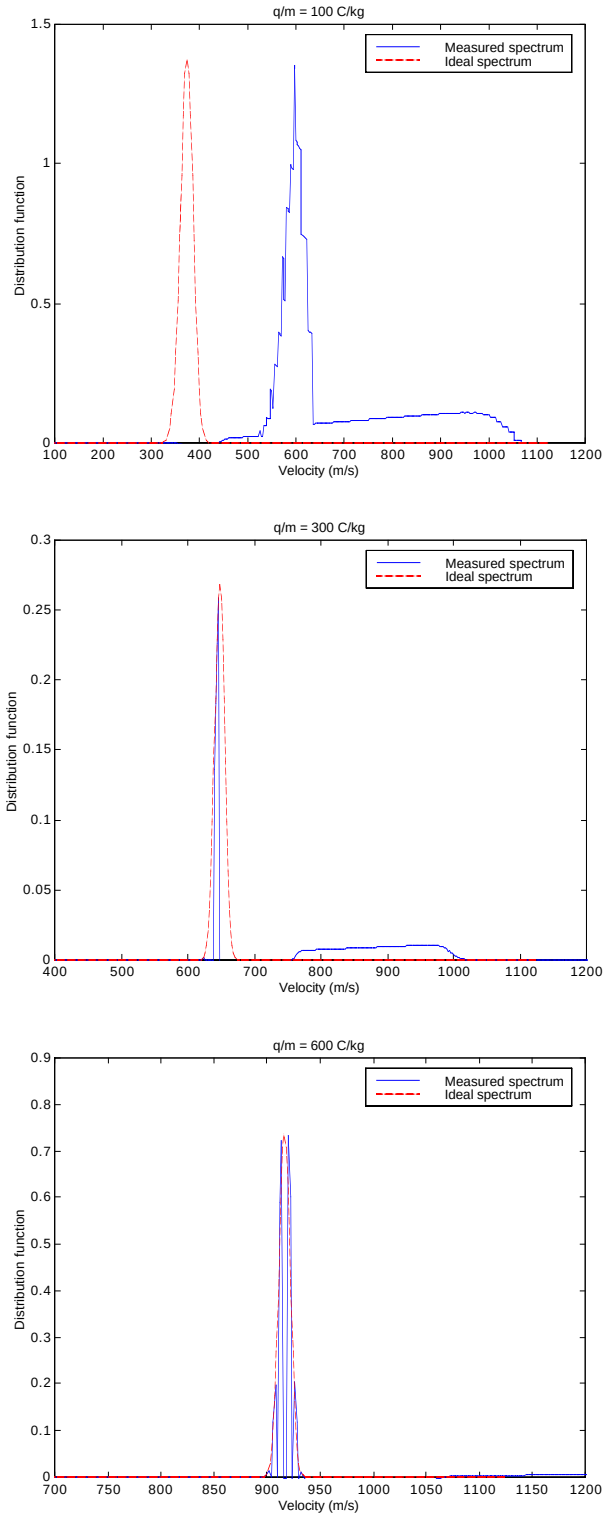

Figure 4.4.3. The effects of using non-ideal gates for increasing particle velocity

$$C = \frac{\sqrt{2\alpha_v\alpha_T} - x_\infty}{\left(\alpha_v + \sqrt{2\alpha_v\alpha_T} - 1\right)\left(1 + \sqrt{2\alpha_v/\alpha_T}\right)}. \tag{4.4.14}$$

Equation (4.4.14) depends on q/m through α_T. The additive contribution of region A4 for the distribution function (4.4.7) is,

$$\Delta f_{v_\infty}\Big|_{\text{A4}} = f_{q/m}[q/m(v_\infty)]C[q/m(v_\infty)]\sqrt{2\frac{q/m}{\phi_B}}, \tag{4.4.15}$$

after noting that $\delta(v_\infty - v_s)dv_\infty = \delta(q/m(v_\infty))d(q/m)$. This analysis can be used to improve the design of non-ideal gates by assessing how the experimental parameters modify the outcome of the measurements. For the same set of values used for Figure 4.4.2, the velocity distributions, as calculated with (4.4.7), are shown as the continuous line in Figure 4.4.3. The dashed line represents the assumed source gaussian-shaped q/m distribution. The normalized area under the curve is proportional to the probability of having particles with such velocities.

For the three cases shown in Figure 4.4.3, the fraction of particles that leave the gate with different energy is smaller for larger source velocities. In particular it is seen that for $q/m = 600$ C/kg, the fraction of particles leaving with higher velocities is very small.

Most the experiments in this study involve the use of highly doped solutions with relatively large conductivities, thus yielding specific charges about one order of magnitude higher for the droplets and almost three orders of magnitude for the ions when compared with the largest number used in the previous example. It can be concluded that the effects of using this type of gate will be negligible in the measurements.

The final design of the gate is schematically shown in Figure 4.4.4. The gate is composed of three stainless steel plates with apertures separated by alumina tubes. A tungsten mesh

with a transparency of about 90% covers the inner aperture. Practically all experiments were performed with $x_m = 2.5$ mm, $x_\infty = 5$ mm, and $\phi_m = 950\text{V}$. This gate size is smaller than the one shown in the examples above, further reducing the residence time of particles inside it and therefore the effects on their energies.

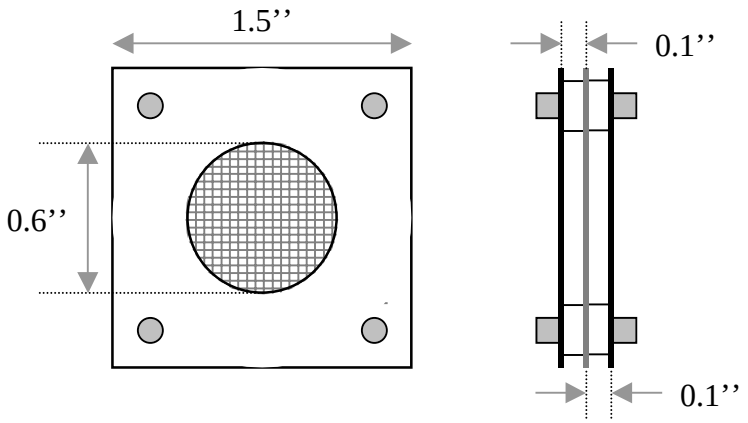

Figure 4.4.4. Diagram of the electrostatic gate used for the TOF experiments

4.5. Colloid Thruster Liquids

Perhaps one of the most relevant issues having an impact in thruster development is the propellant selection. If high specific impulse is desired, then liquids with relative high conductivities are necessary. In other words, good polar solvents with high dielectric constants are required. These type of solvents can be doped with salts very close to saturation, to reach conductivities larger than 1 S/m. It is also desirable to work with low volatility liquids, since operation in space would cause large evaporation losses unless very small emitters are used - difficult since clogging problems increase as inner diameters decrease.

F. de la Mora [11] and Gamero [58] performed an extensive search for propellants and found there are several liquids that meet the criteria. In particular, formamide (CH_3NO) seems

to be an ideal solvent for this application. It has both high dielectric constant and low volatility. This formidable solvent is used to obtain measurements in the ion-droplet mixed regime. Experiments are also done with Tributyl Phosphate or TBP [58], which has a much smaller dielectric constant. This provides a relatively low conductivity, ideal to explore pure droplet beams.

Even though solvents such as formamide appear to be ideal for colloid thrusters, their non-zero vapor pressure is still problematic when considering in-space operation. If the thruster is required to stop during any period of time, liquid remaining in the emitter tip will evaporate, leaving behind salts that could block the flow when a re-start is attempted. One solution would be freezing the liquid while the thruster is not working and then thawing it moments before a re-start. However, phase changes like this modify the material volume and lead to a possibility of structural failure as well as the additional complexity required to perform this thermal cycling.

Romero, Bocanegra and F. de la Mora [52] have also explored the possibility of using pure ionic liquids as colloid thruster propellants. Ionic liquids [65,66,67,68] have the important property of remaining in the liquid state down to ambient temperature (organic molten salts). They were discovered recently and new ones with different properties are continually being developed, potentially the ideal liquids for space propulsion. Ionic liquids have relatively high conductivity, which increases dramatically with temperature. Their viscosity also depends strongly on temperature. The controlling parameter in a colloid thruster using this type of propellant could then be the liquid temperature. Perhaps the most important aspect of ionic liquids is that they have practically zero vapor pressure, thus eliminating the problems associated with volatile liquids.

The final liquid used in this study is an ionic liquid 1-Ethyl-3-Methyl-Imidazolium Tetrafluoroborate ($C_6H_{11}BF_4N_2$), or EMI-BF_4, first used by Romero et al. [52] for this purpose.

All the liquids used in the experiments share the property of being hydrophilic, so they need to be dried prior to introducing them into the vacuum chamber by:

- Exposing them to vacuum
- Increasing the temperature
- Providing an ultrasonic bath

It is found that it is very important to follow these steps with care, since any quantity of gas or water dissolved in the liquid will evaporate as the pressure in the line decreases, creating bubbles that would make thruster operation very difficult, if not impossible. Table 4.5.1 shows the physical properties of the liquids used in this study.

Solvent	Solute	Concentration	K (S/m)	ε	ρ (kg/m^3)	γ (N/m)	μ_l (cP)	P_v (Pa)
Formamide	LiCl	5%W	1.02	111	1130	0.058	3.8	~1.9
Formamide	NaI	28%W	2.15	111	1130	0.058	3.8	~1.9
TBP	EMI-BF_4	7%W	0.05	8.91	976	0.027	3.4	0.58
EMI-BF_4			1.3		1294	0.052	43	0

Table 4.5.1. Liquid properties at room temperature (25 °C)

4.6. Flow Rate Control

Delivering the correct amount of liquid to the emitter is very important, experimentally speaking. As explained in Chapter 3, the relevant parameter, which controls almost every aspect of droplet and ion emission, is the flow rate. The magnitude of the flow rate for single emitter operation, at the levels aimed to achieve, is extremely small. For example, for the formamide + NaI solution, it is desirable to deliver flow rates close to $\eta = 1$, which translates to $Q = 2.5 \times 10^{-14}\ \mathrm{m^3/s}$, or 25 pico-liters per second. To put this in perspective, a 1 ml liquid sample would last for 15 months of continuous operation.

Two methods of injecting the liquid are evaluated and used in this study. The first one consists of a positive displacement programmable syringe pump (Cole-Parmer model A-74900-10). This pump delivers liquid in a wide range of flows and is easy to install in the system. According to the model specifications, the lowest flow rate that can be achieved by the syringe pump is 0.28 pico-liters per second, or about $\eta = 0.1$ for the formamide + NaI solution described in Table 4.5.1.

In spite of these formidable specifications, operating the syringe pump is very difficult for a sample injection into vacuum. The main problem is to match the flow rate delivered by the pump to the hydraulic impedance given by the tubing line and the fact that there is a positive pressure constantly pushing the syringe piston, due to the pressure differential (1 atm) between the inside and the outside of the chamber. The hydraulic impedance of the line sets the minimum flow rate that can be achieved, while the syringe piston is required to move faster than this flow. This increases the pressure of the line to very high values, sometimes causing leakages, particularly in the interface between the syringe and the tubing. This pressure accumulation in the syringe piston also causes flow rate oscillations that are very difficult to eliminate, and in the end, there is a large uncertainty of whether or not the programmed flow rate is actually delivered. All these problems multiply for lower flow rates. It is quite obvious, after using the pump for a while, that if low flow rates are desired, a different approach is needed. Nevertheless, some very useful data were obtained using this system at larger flow rates, as will be shown in the next chapter.

The second method consists of a gas pressurization system to control the flow rate, similar to that used by Gamero [58]. This is the selected technique for most experiments. Given the importance of flow rate, a full description of this pressurization system is presented. A schematic showing the different components and connections can be seen in Figure 4.6.1.

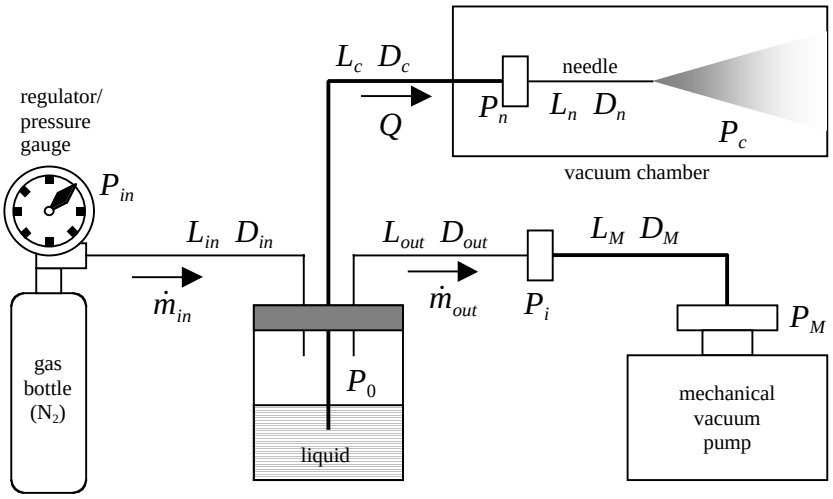

Figure 4.6.1. Gas pressurization system for liquid injection

The basic idea is to control the pressure P_0 inside the liquid container by using a gas tank (delivery pressure = P_{in}) and a mechanical vacuum pump. Once the pressure P_0 is known, the liquid (laminar, Poiseuille) flow rate is given by,

$$Q = \frac{\pi D_c^4}{128\mu_l}\frac{(P_0 - P_n)}{L_c} = \frac{\pi D_n^4}{128\mu_l}\frac{(P_n - P_c)}{L_n}, \tag{4.6.1}$$

where μ_l is the liquid viscosity. The rest of the quantities can be read in Figure 4.6.1. *P* relates to pressures, *D* is for tube diameters, and *L* represents tube lengths. The gaseous mass flow rates are also modeled as laminar flows,

$$\begin{aligned} \dot{m}_{in} &= \frac{\pi D_{in}^4}{256\mu_g RT}\frac{\left(P_{in}^2 - P_0^2\right)}{L_{in}}, \\ \dot{m}_{out} &= \frac{\pi D_{out}^4}{256\mu_g RT}\frac{\left(P_0^2 - P_i^2\right)}{L_{out}} = \frac{\pi D_M^4}{256\mu_g RT}\frac{\left(P_i^2 - P_M^2\right)}{L_M}, \end{aligned} \tag{4.6.2}$$

where μ_g is the gas viscosity, R is the gas constant, and T is its temperature (assumed constant). The exit choking has been neglected.

In steady state, there should be no mass depletion or accumulation inside the liquid container, and therefore $\dot{m}_{in} = \dot{m}_{out}$. Using this condition and (4.6.2) an expression for the container pressure is obtained,

$$P_0 = \sqrt{\frac{P_M^2 + \beta P_{in}^2}{1+\beta}} \qquad \text{with} \qquad \beta = \frac{D_{in}^4}{L_{in}}\left(\frac{L_{out}}{D_{out}^4} + \frac{L_M}{D_M^4}\right). \tag{4.6.3}$$

In general, the mechanical pump pressure P_M is much lower than the inlet gas pressure P_{in} or even the container pressure P_0. This depends of course on the pumping capacity of the mechanical vacuum pump. A more complete analysis can be used to compute P_M as a function of the gas flow and the pumping speed S_P,

$$P_M = RT\frac{\dot{m}_{out}}{S_P}. \tag{4.6.4}$$

$\dot{m}_{out}$ is given by (4.6.2), then substituted into (4.6.4) and back into (4.6.3) to obtain an algebraic equation for P_0. If S_P is large enough, then P_M can be neglected in (4.6.3). For example, for a vacuum pump (Varian SD-201) with $S_P = 3.25$ l/s, the pump pressure P_M is more than two orders of magnitude smaller than P_0, even for the largest values of P_{in}. Under these conditions, (4.6.3) can be written simply as,

$$P_0 = \sqrt{\frac{\beta}{1+\beta}}P_{in}. \tag{4.6.5}$$

Finally, the pressure at the needle inlet can be computed with (4.6.1),

$$P_n = \frac{P_c + \beta_n P_0}{1 + \beta_n} \qquad \text{with} \qquad \beta_n = \frac{L_n}{L_c}\left(\frac{D_c}{D_n}\right)^4. \tag{4.6.6}$$

The chamber pressure P_c is known and is much smaller than any other pressure in the system by at least 4 orders of magnitude, therefore its contribution to (4.6.6) is negligible. Table 4.6.1 contains the model parameters used for the experiments with formamide + NaI. Figure 4.6.2 shows a plot of flow rate (4.6.1) and the container pressure (4.6.5) as functions of the gas inlet pressure P_{in} for the parameters of Table 4.6.1.

Tube ID	μm		Tube length	cm
D_n (needle)	20		L_n	4.5
D_c	50		L_c	70
D_{in}	63.5		L_{in}	100
D_{out}	381		L_{out}	20
D_M	3680		L_M	100

Table 4.6.1. Pressurization system parameters for formamide + NaI

These values were obtained by the following procedure. (1) An initial set of values is determined from the actual dimensions of the system's connections. (2) Three calibration measurements of the flow rate at different inlet pressures are then conducted. Measuring the flow rate with macroscopic tools is difficult and time-consuming, so it is attractive to make a model that provides a one-to-one correlation between the easily measurable inlet pressure and the flow rate. To measure the flow rate for this calibration, a small bubble is injected into the 50 μm fused silica tubing used to transport the liquid from the container to the needle. Given the small dimensions and low flow rates, the bubble has to be tracked using a microscope. Knowing the time it takes the bubble to move a certain distance, the flow rate can be estimated. The three experimental measurements are shown as the diamonds in Figure 4.6.2.

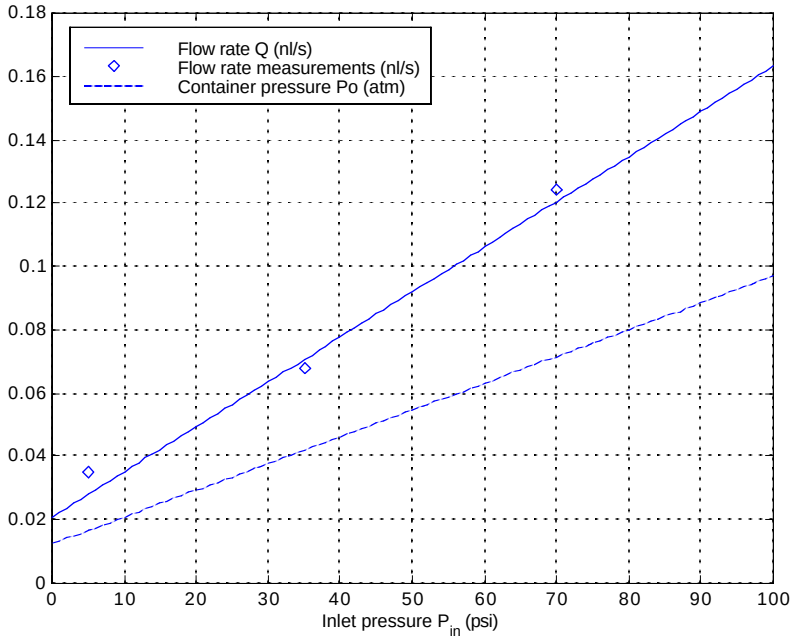

Figure 4.6.2. Flow rate and container pressure vs. inlet pressure, for formamide with μ_l = 3.8 cP. Experimental measurements were performed with a needle emitter tip with ID = 5 μm and ϕ_{ex} = 1250 V

(3) The tube length model values are finally tuned (tubing diameters are kept fixed) to obtain the best fit with respect to the measurements, as shown by the solid line in Figure 4.6.2. For this calibration, a 5 μm needle-emitter ID tip was used, working with an extractor voltage of $\phi_{ex} = 1250$ V.

As can be expected, there are several sources of uncertainty in this approach. One is the measurement error when determining the time and distance while following the bubble. Another is the neglect of the pressure drop in the cone, even though it should be small since the surface tension is closely balanced by the electric pressure, but still might depend on the applied voltage.

5. Experimental Characterization

5.1. Needle Emitter Test

The first experimental run was aimed at testing the performance and reliability of the needle emitters selected for this study. The system setup consisted of the syringe pump to inject the liquid through a 100 μm capillary that ran into the vacuum chamber and then was connected to a higher flow impedance line of 20 μm, finally arriving to a 75 μm needle emitter with a tip diameter of 30 μm. The extractor plate was positioned at about 3 mm from the tip. For these conditions and from Figure 4.3.2, a starting voltage of about 2 kV was expected. The tip of the needle could be directly monitored with the help of a 450x video microscope. A metallic collector plate was positioned 5 cm away from the extractor, and its current was continuously monitored with an electrometer.

The purpose of this test was to determine the lifetime of the needle emitter and to observe if flow control could be obtained with the syringe pump. An initial voltage of $\phi_a = 1913\text{V}$ was applied to the needle and a stable cone was obtained after reducing the voltage to $\phi_a = 1850\text{V}$. The pump was initially programmed to deliver a flow rate of 0.1 μl/min (1.7 nl/s) and an initial current of 800 nA was detected. The chamber pressure at start-up was 9×10^{-6} Torr. The liquid used for this test was formamide + LiCl - its properties can be found in Table 4.5.1.

The current was monitored with time for the 117 hours that the system was in operation and is shown as the solid line in Figure 5.1.1. The dashed line in the same plot results from calculating the current from Equation (3.1.21), using the flow rate programmed into the syringe pump, which was varied at different times in order to observe how the current responds to flow rate variations.

Note that the magnitude of the measured current differs from the calculated current by about a factor of 2. It, however, roughly follows the same shape as the calculated current. This is an indication that the syringe pump is delivering higher flow rates. Of course, some calibration could be performed to correlate the indicated and the real flow rate.

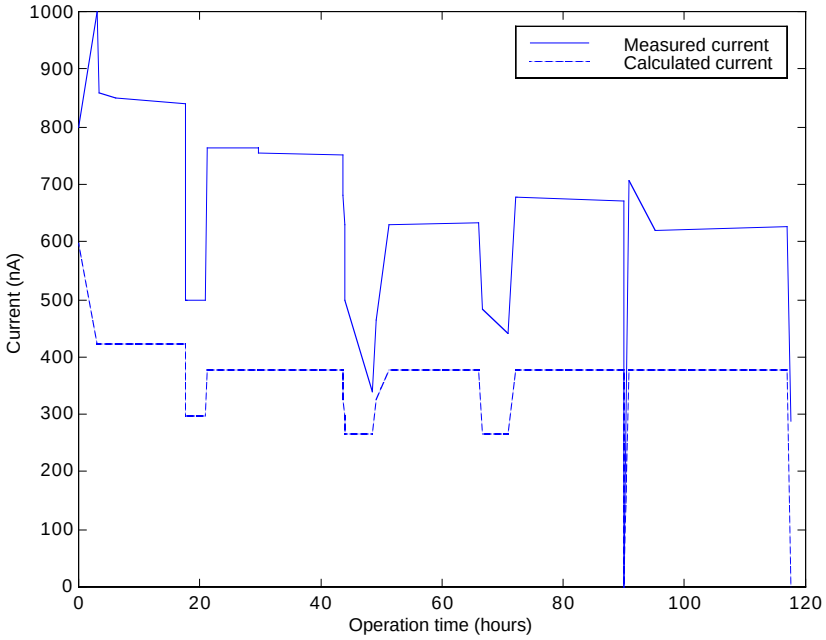

Figure 5.1.1. Current profile for the needle emitter test

The real problem with the pump is reflected in some of the transients. At startup, the flow rate is decreased but the current increases and then decreases until reaching a steady value. After that, every time the flow rate is changed the current changes accordingly but

in general, do not reach a consistent value. This is apparent in the time ranges 20-40, 50-65, 70-90 and 90-116 hours. Not only the reading of the flow rate from the syringe pump is incorrect, but also the real flow delivered is different after a transient, though the reading is the same. These inconsistencies are the main reason why the syringe pump was substituted by a gas-pressurized system, as discussed in Section 4.6.

On the other hand, this test was extremely useful to characterize the general behavior of the needle emitter. It was observed that, except for the transients, the current lines were stable in time. Under the microscope the cone appeared stable as well. The needle ran continuously without any problems. In fact, the only contingency happened at about 90 hours into the sequence. For some reason, the syringe pump stopped working and therefore the current decreased until reaching minimum flow conditions. The cone disappeared and the residual meniscus evaporated, leaving some LiCl salts that accumulated on the needle tip. Increasing the voltage momentarily to $\phi_a = 2300\text{V}$ while resetting the syringe pump solved the problem. The salts accumulated were extracted from the tip and the cone formed again.

The test was intentionally stopped after 117 hours of operation. Once the system was disassembled, the needle was inspected and no damage was observed to either the tip or the conductive coating.

5.2. Beam Spreading and Focusing

Given the interest in performing reliable TOF measurements of colloid beams and, since electrospray emissions suffer from space-charge effects (the most noticeable being the initial spreading), it is decided that measuring the terminal angle at which particles diverge is important to determine whether ion optics are necessary for improving the overall resolution of TOF experiments [69].

The colloid beam source consisted of a single fused silica needle with ID of 75 μm and final tip ID of 30 μm. As in the previous experiment, the syringe pump was used to inject and monitor the liquid flow rate. The liquid solution was also formamide + LiCl. As already discussed, capacitive effects due to pump operation under vacuum did not allow a precise determination of the flow rate from the setting of the pump alone. Nevertheless the results from Section 5.1 are used to estimate $Q = 2 \times 10^{-12} \mathrm{m}^3/\mathrm{s}$ (2 nl/s).

For this experiment, the emitter design shown in Figure 4.3.7 was used. The needle tip was positioned at the center of a circular aperture of 6 mm in diameter that served as the grounded extractor electrode. For the focusing experiments, the electrostatic lens was positioned close to the extractor and was biased negatively with respect to ground by using a high voltage power supply.

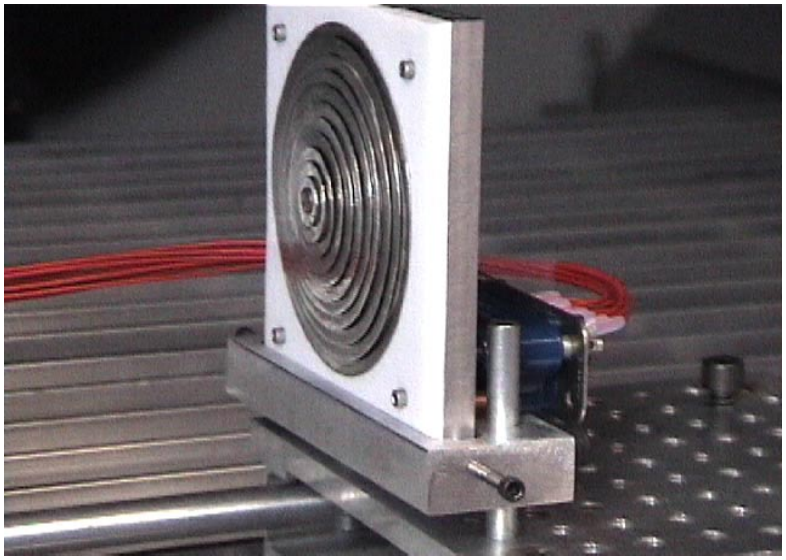

Figure 5.2.1. Current collector

The current collector (Figure 5.2.1) is comprised of a single circular plate, 1 cm in diameter, surrounded by a series of 10 concentric metallic rings, each with a width of 3

mm and a maximum radius of 3.5 cm. Each ring is electrically isolated from the rest and has an individual connection to a chamber feed-through.

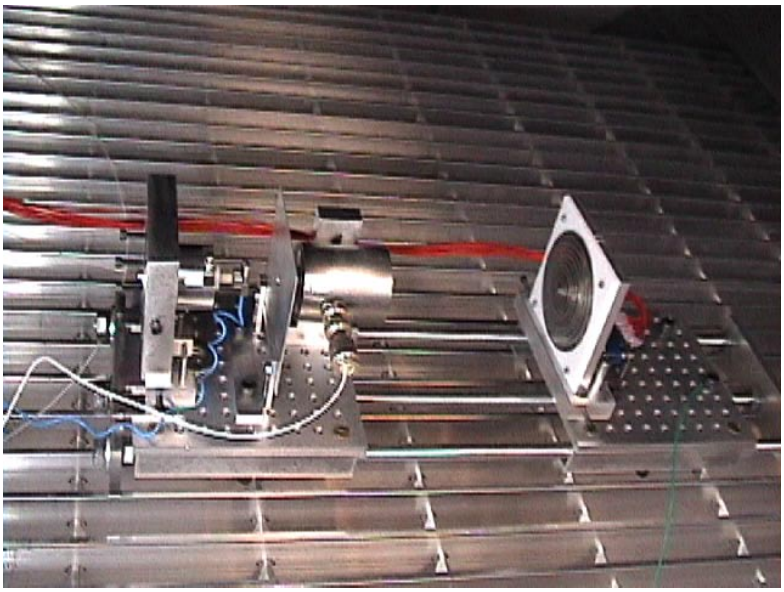

Figure 5.2.2. Experimental setup for the beam spreading, focusing experiments

With this setup, the collected current can be measured at different angles from the centerline with a radial resolution given by the number of rings. The electrometer is used to record the signal from each ring while the emitter is in operation. It is assumed that the beam angle is basically constant, except for regions very close to the needle tip, as discussed in Section 3.3. By measuring the current profiles for each ring at different distances L from the extractor to the collector and without using the lens, the beam profile can be built, assuming good alignment with the detector centerline. If the lens is used, the effect of different focusing potentials on the recorded current can be obtained. The experimental arrangement, including the lens and the collector, is shown in Figure 5.2.2. The background pressure during tests was about 5×10^{-6} Torr. The emitter to extractor

potential was held at 1.9 kV. This value was determined by visual inspection of a stable cone at the needle tip and measurement of a stable current.

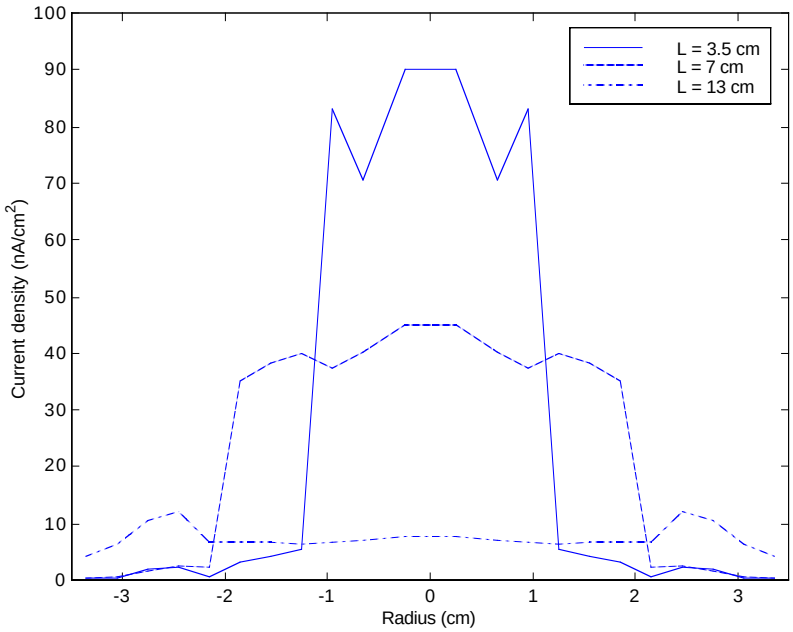

Figure 5.2.3. Current density distributions from experiments with formamide + LiCl and Q = 2 nl/s, P_c = 5×10^{-6} Torr and ϕ_a = ϕ_{ex} = 1.9 kV for a 30 μm ID emitter

The amount of spreading of the charged beam was determined first. The lens was taken out from the system and current density measurements were performed at three different axial positions from the extractor/emitter plane. The results are summarized in Figure 5.2.3. It is interesting to note that for the first two measurements ($L = 3.5$ and 7 cm), a more or less uniform charge density profile can be observed. For the third measurement ($L = 13$ cm), the profile is roughly uniform but spreads out covering the whole area of the detector. From the cutoff values of the current and the distances involved, a semi-angle of about 18° can be estimated.

The non-dimensional flow rate for this case, from the liquid properties of Table 4.5.1 and Equation (3.1.22) is $\eta \approx 6.36$. Substituting this value into (3.3.19), a spreading semi-angle of 19.06° can be calculated, using $f(\varepsilon) = 20$. These measurements prove that the divergence semi-angle is usually large, and unless very large collectors are used at relatively short distances, TOF measurements would not be able to reach high resolution. As will be shown later in this chapter, divergent beams introduce an additional energy spread in the measurements. This means that the larger collector, longer distance solution is not ideal at all. Ion optics is a necessity for analysis of colloid thruster emissions. The next experiment was done to determine if colloid beams, made out of charged droplets, could be electrostatically focused.

The einzel lens was installed in the system, as shown in Figure 5.2.2 and the current collector was positioned at a distance $L = 13$ cm from the extractor plate. If the lens works as expected, then the current collected in the inner circular electrode at the detector will increase as more trajectories are directed towards it by the focusing effect.

Figure 5.2.4 shows the current collected by this electrode as a function of various negative lens potentials. A maximum in current (72 nA) is obtained when $\phi_f \approx -5.5$ kV. It is interesting to observe that for higher negative values the current starts to decrease. The reason for this might be related to space charge itself, since the self-repulsion forces get stronger as the local charge density increases, which happens when the beam becomes too concentrated near the propagation axis (focused ahead of the collector).

The einzel lens behaves as designed, but it also suffers from the anticipated problem (see Section 4.3) regarding the closeness of some trajectories to the electrode surface. The total current collected by the detector can be extracted by integrating the curves in Figure 5.2.3. It can also be calculated with F. de la Mora's law (3.1.21). In both cases, the current is close to 400 nA. The current collected in Figure 5.2.4, however, is about 1/4 of the emitted current, including the measurements of adjacent electrodes at $\phi_f \approx -5.5$ kV. This means that most of the current is lost in the lens itself. This is the reason why the focusing system is re-designed, as explained in Section 4.3.

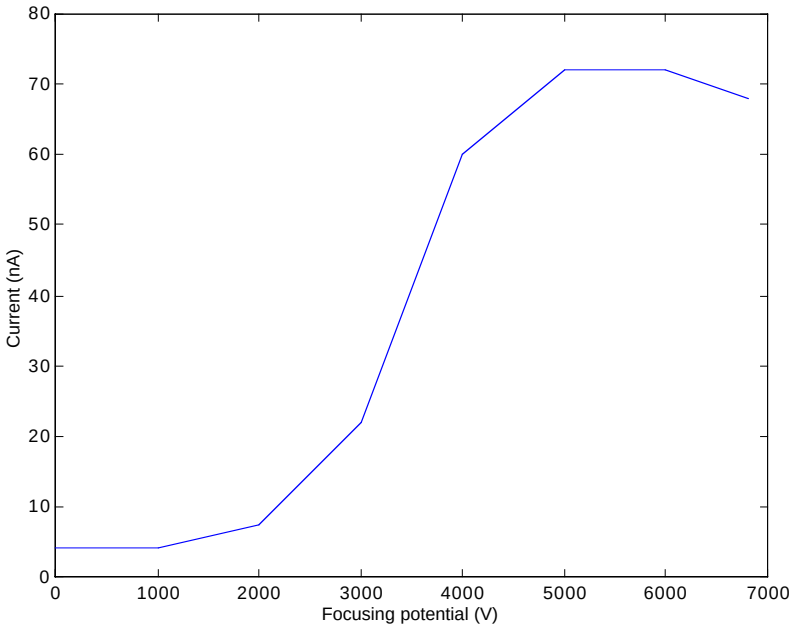

Figure 5.2.4. Electrostatic focusing – collected current vs focusing potential ϕ_f with formamide + LiCl and Q = 2 nl/s, P_c = 5×10^{-6} Torr and $\phi_a = \phi_{ex}$ = 1.9 kV for a 30 μm ID emitter and L = 13 cm

5.3. Dual Gate TOF

The idea behind this method, as described in Section 4.1, is to design a TOF technique well suited to measure specific charge distribution in electrosprays when ions and droplets are simultaneously present in the beam. It would be desirable to obtain at least 1-Dalton resolution for the ions, so as to be able to identify them and their solvatants. The very precise methods used in analytical chemistry for the detection of trace impurities, where small fractions of 1 Dalton resolution are possible, suffer from one defect: the dynamic range will not extend to the droplets.

In addition to specific charge, a measurement of the acceleration potential of each particle type is needed for a complete diagnosis. As explained in Section 4.2, this is typically done through stopping potential analysis. An alternative, which does not require differentiation of the data, is to use some form of an electrostatic reflector, which will segregate an incoming beam into emerging beams at angles dependent on the potential, but independent of specific charge. The goal is to design an apparatus with these considerations in mind. A schematic of such system is shown in Figure 5.3.1.

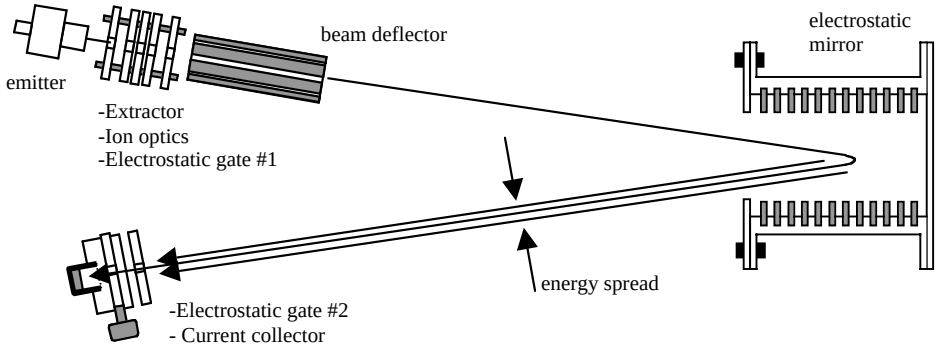

Figure 5.3.1. Conceptual design of a dual gate, high resolution TOF

In this design the single-needle emitter/extractor is followed by an einzel lens, which has the dual purpose of beam focuser (as already demonstrated) and beam decelerator for increased flight time. For centering of the beam in its target, a charged particle deflector is required. The drift length is split into two halves by the use of an electrostatic mirror, which accomplishes three objectives: (a) it increases the TOF working distance, (b) it de-sensitizes the TOF measurements to variations about a nominal accelerating voltage, and (c) it provides lateral separation of the beam into components of different energy.

As discussed in Chapter 4, the TOF determination is analogous to the classic Fizeau technique for measuring the speed of light. A systematic rejection of the much slower droplets must be made in order to individually analyze the faster species in the beam. To

accomplish this, opening pulses for both gates are synchronized in such a way that ions with a narrow specific charge range will reach the detector before the fastest droplet from the first opening of gate 1 reaches the second gate. The sequence is repeated after the slowest droplets have cleared the drift length. This process is illustrated in Figure 5.3.2.

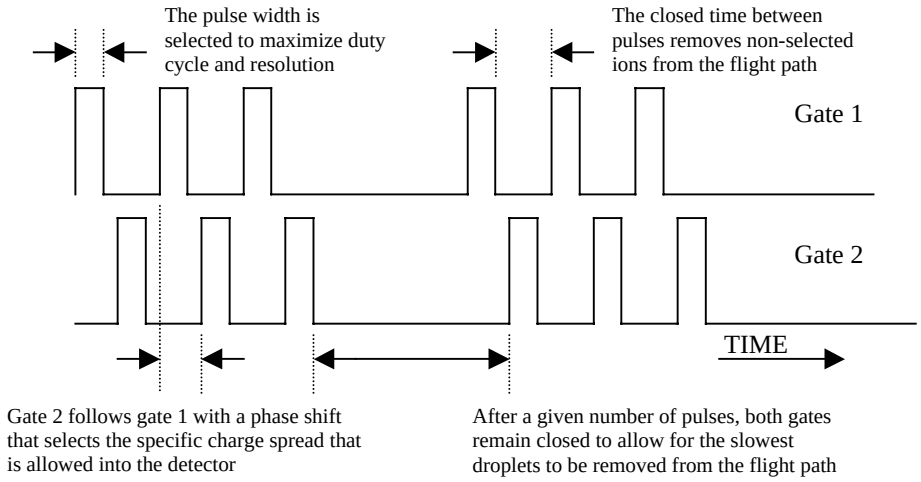

Figure 5.3.2. Functioning of the TOF spectrometer in the ion-scanning mode

Before building the complete system, a validation experiment was performed, in which the mirror was omitted and only droplets were present in the beam, which allowed use of less rapid pulses [70].

For this experiment, the TBP solution described in Table 4.5.1 was used. As pointed out earlier, its conductivity of 0.05 S/m is insufficient for ion emission and therefore is ideal to investigate pure droplet beams. The fused silica needle emitter was 75 μm ID in the body and 15 μm ID in the tip. Unlike every other experiment, the whole needle was coated with a metallic multi-layer (New Objective Inc). As in Section 5.2, the syringe pump controlled the liquid feed. Including the associated uncertainties, the flow rate is estimated to be close to $Q = 5 \times 10^{-13}$ m^3/s (0.5 nl/s), which is about 11 times the minimum stable flow for cone-jet formation as given by $\eta = 1$ in (3.1.22).

As mentioned in Section 4.2, capacitive coupling induces electrostatic noise in the detector, which is anticipated to be a problem since the detector is required to be relatively close to the second gate. To minimize these effects in this experiment, a shielded Faraday cup was used as the detector, and was placed 2 cm from the second gate. A 15 mm diameter grounded stainless steel tube was placed between gates, to provide a zero-field drift region. The distance between gates was set at $L = 15$ cm. The high-voltage lines connecting the pulse generators were shielded using coaxial cable, and were routed as far apart as possible from the detector lead, which was also shielded using low-capacitance cable. Despite this, the 1 sq. inch plate supporting the gate grid in front of the collecting Faraday cup was found to interact strongly with the output signal during fast pulses. Two grounded shields were interposed, one physically identical to the pulsing plate, at about 3 mm from it, and an open mesh covering the 10 mm open area of the Faraday cup itself. After these additions, the input capacitance (10 pF) of the electrometer somewhat reduced the spurious signals during pulses. The general arrangement is shown in Figure 5.3.3, where the emitter needle would be on the left side, and the collector is seen on the right.

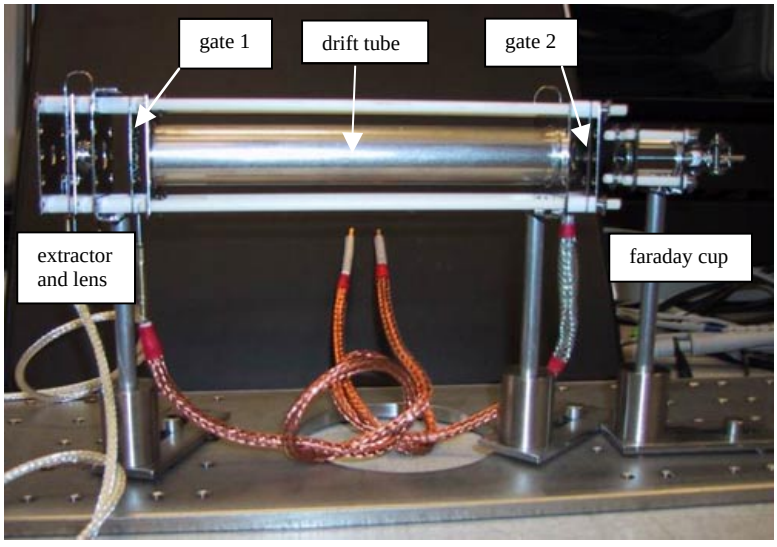

Figure 5.3.3. Apparatus configuration for validation experiment

The emitting needle was biased with respect to ground at +700 V, while the extractor was set at –500 V. The detector was grounded. The focusing potential was biased at increasingly negative voltages, until the current reading was maximized at about –6 kV.

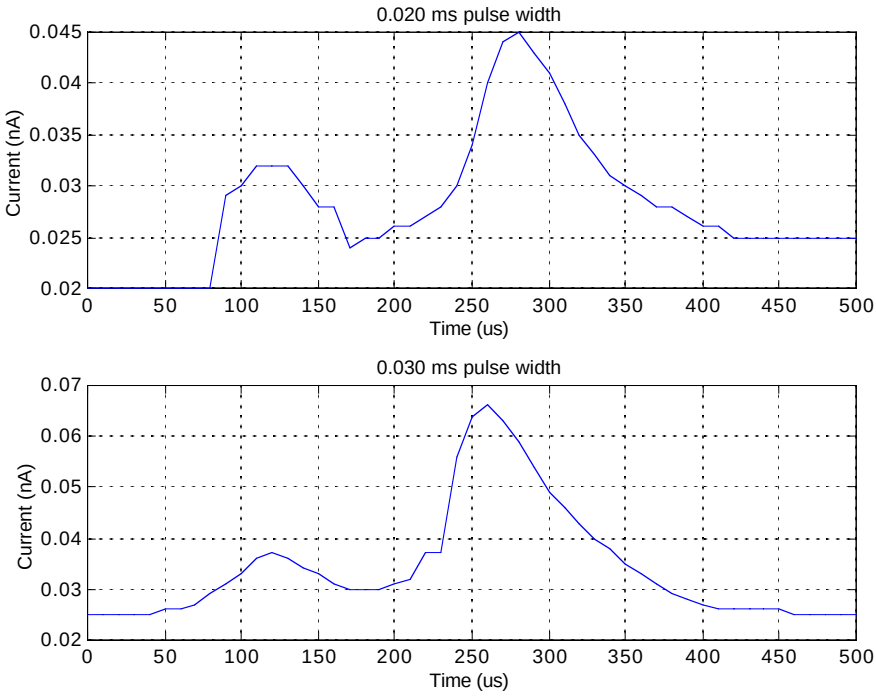

Figure 5.3.4. Time of flight spectrum taken with two different pulse widths for TBP and Q = 0.5 nl/s, ϕ_a = 700 V, ϕ_{ex} = 1.2 kV, and ϕ_f = -6 kV for a 15 µm ID emitter. Pulse repeating period is 500 µs

Figure 5.3.4 shows experimental results under these conditions. Two droplet population distributions are apparent, centered at flight times of 120 µs and 270 µs, corresponding to speeds of 1250 m/s and 560 m/s. The faster population constitutes approximately 17-20% of the total current. A background current of 25 pA, due in part to the remaining capacitive coupling and gate leakage, is also present. In both cases, the pulse repetition

rate was 2 kHz (500 μs between pulses for each gate). Comparison of results with two pulse widths of 20 μs and 30 μs shows that the current level is higher with longer pulses, while introduction of time spread causes a shift towards lower times. The peak widths, however, appear to be insensitive to pulse size, which suggests that the observed broad time distribution may be related to some intrinsic distribution in either the specific charge or the beam potential.

The electrospray current can be estimated by using Equation (3.1.21). Gamero [71] has used various TBP solutions, and a value of $f(\varepsilon) \approx 7$ is extracted from his data. Using the properties in Table 4.5.1, a total droplet beam current of $I = 62$ nA is computed. However, with both gates open, a current of only 8.2 nA, or about 13% of *I* was detected. The discrepancy may be due to a number of reasons, such as the 85-90% transparency grids installed in the gates and shields. Since four of them are used in series, a 50-65% transmission can be expected. Other losses may be due to the $\sim 16^\circ$ spray angle computed from (3.3.19), which is larger than the 13° acceptance angle of the einzel lens and account for an additional 20% loss. But as explained in Section 4.3 and as seen in Figure 4.3.3(c), the loss effect is magnified by the aberrations introduced by the proximity of the outer trajectories to the electrode surface.

The expected droplet charge/mass ratio can be computed using (3.1.23). This gives $q/m = 127$ C/kg. Assuming that the net acceleration potential for these droplets is the same as the needle voltage, a speed of 422 m/s is calculated, which corresponds to a TOF of 355 μs. This time is larger than the 270 μs observed for the slow component in Figure 5.3.4. In fact, these experimental data indicate a specific charge $q/m = 224$ C/kg for the slow component and $q/m = 1120$ C/kg for the fast.

The reason for this inconsistency was traced to what was already explained in Section 4.4. As can be seen in the first plot of Figure 4.4.3, when working with particles with relatively low specific charge, the gate non-idealities will have the undesired effect of increasing the net velocity of all particles, and in this particular case, creating a second family at much higher velocities.

To validate this assumption, the effect the gate has on a specific charge distribution function was calculated using the set of tools presented in Section 4.4. The source distribution was assumed to be gaussian with a single peak centered at the expected $q/m = 127$ C/kg, or a TOF of 355 μs. The result of this calculation is shown in Figure 5.3.5. The dashed line represents the experimental data for the 30 μs pulse, from Figure 5.3.4.

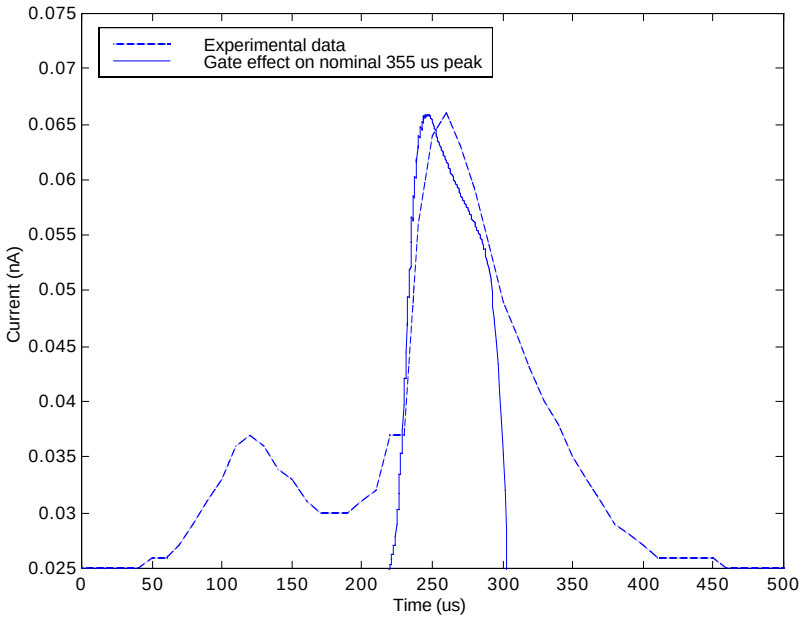

Figure 5.3.5. Effect of the electrostatic gate on a gaussian peak centered at a TOF of 355 μs

As explained in Section 4.4, the effects of the gate on faster particles (larger specific charge) would be very small, as evidenced by Figure 4.4.3. The same setup can be used to validate this assumption by changing the fluid to one with higher conductivity. With this in mind, a set of experiments were made using the formamide + NaI solution with its properties outlined in Table 4.5.1. The flow rate in this case was estimated to be close to

$Q = 8 \times 10^{-13}$ m^3/s (0.8 nl/s). The result from sweeping the time delay between gates is shown in Figure 5.3.6. Error bars have been included in the plot, showing the stability of the current during operation.

From (3.1.23) the specific charge is $q/m = 660$ C/kg, which corresponds to a velocity of 961 m/s, or a TOF of 156 µs. This value is very close to what is observed in the measurements of Figure 5.3.6, thus validating the assumption that the effect of the gates is negligible for sufficiently fast charged particle beams.

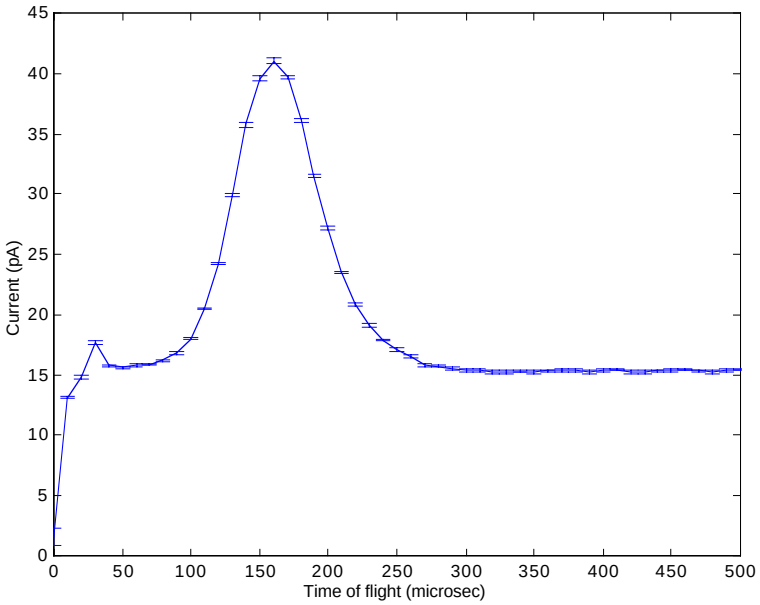

Figure 5.3.6. Dual gate TOF measurements with formamide + NaI

Similar to the measurements done with TBP, the peak FWHM (full width at half maximum) is about 80 µs in Figure 5.3.6, or about 50 µs larger than the pulse used to create the spectrum, thus revealing that the time spread cannot be attributed to the gate width alone, but also to an energy distribution and a specific charge polydispersity centered around the nominal value of 660 C/kg. Unfortunately, no stopping potential

measurements were performed to identify the relative contributions of these spreads. The small peak precisely centered at 30 μs is artificially introduced by a gate resonance mechanism.

Given these results, it is not difficult to understand why this method was eventually abandoned before implementing it to obtain high-resolution TOF spectra of fast ions. Among the drawbacks are extremely weak current signals, just above the capacitive coupling and gate leakage levels. As faster species are analyzed, shorter pulses are required for the resolution to remain constant. The distance between pulses, however, is dictated by the speed of the slowest droplets, and therefore the duty cycle, i.e., the current throughput, decreases. Furthermore, faster pulses increase the amount of capacitive coupling. This reduction of the signal to noise ratio is more than the system can handle, and practically no current was detected in the trials with faster particles. Despite this, the experiments presented in this section are useful to characterize the properties of the electrostatic gates.

5.4. Flow Rate and Ion Emission

As mentioned in Section 3.2, ion emission from a colloid thruster will occur whenever the ratio K/Q exceeds a certain value. The extreme case is pure ion evaporation in liquid metals, where the conductivity is orders of magnitude higher than in either organic-based or ionic colloid thruster liquids. The two quantities in this ratio play a role in the onset of ion emission. As the flow rate is decreased, the surface curvatures induced by the external voltage in the Taylor cone tip become very high and with enough charge transport from a high conductivity solution, the normal electric field can reach values sufficiently large to start surface evaporation of ions. But as explained in Section 3.1, the flow rate cannot fall below a minimum value or else the cone goes unstable. Above this value, the current follows the F. de la Mora's law (3.1.21) down to almost all values of Q, except for cases when sufficiently large liquid conductivities induce ion emission. In such cases, the

current increases with decreasing flow rate. This behavior was first reported by Gamero and F. de la Mora [41] for several formamide + NaI solutions with different conductivities.

For this experiment the syringe pump was substituted by the more reliable gas pressurization system described in Section 4.6. The flow rate was estimated using the calibration lines of Figure 4.6.2. The distal coated needle emitter had a 20 μm ID body section followed by a 5 μm ID tip. This small size is particularly useful for minimizing evaporation losses, for reducing the starting voltage (as seen in Figure 4.3.2) and for working with the small flow rates required for ion emission. The applied voltage was set to $\phi_a = 1250\text{V}$ with respect to the grounded extractor. No lens is installed in the system and a sufficiently large detector plate is placed 2 cm from the extractor, close enough to contain the whole beam.

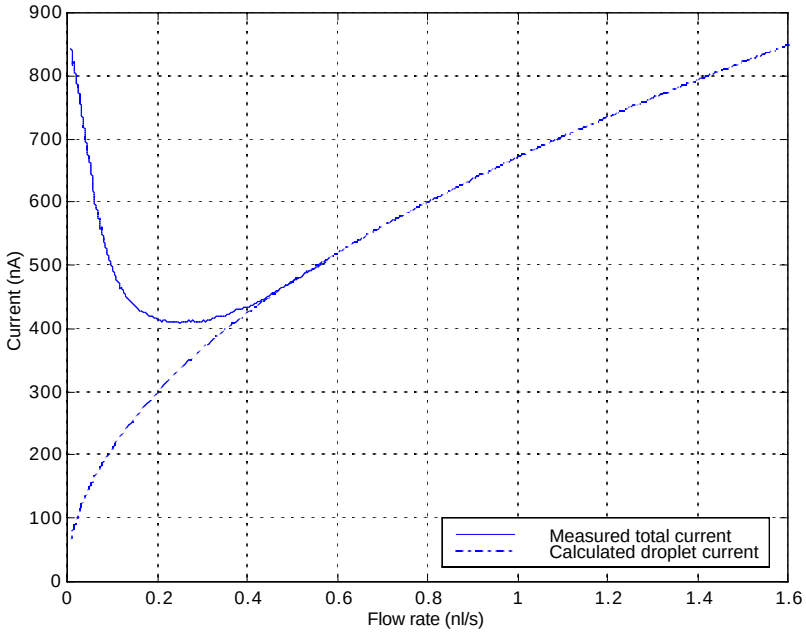

Figure 5.4.1. Variation of current with flow rate with formamide + NaI and $\phi_a = \phi_{ex}$ = 1250 V for a 5 μm ID emitter. Detector distance from the extractor = 2 cm

The solid line in Figure 5.4.1 shows measurements made at different flow rates with the formamide + NaI solution described in table 4.5.1. The segmented curve represents Equation (3.1.21) with $f(\varepsilon) = 20$. This particular formamide mixture has a high ion yield. Almost every possible ion fraction is covered for the range of flow rates shown.

Assuming that the $I(Q)$ law valid for droplets alone continue to be valid in the presence of ion emission, the droplet current, as given by (3.1.21), can be subtracted from the measured total current in this experiment to find the ion current as a function of flow rate. The result of this operation can be seen as the solid line in Figure 5.4.2. The relationship between the flow rate and the non-dimensional parameter η (3.1.22) is depicted in the same figure as the dashed line.

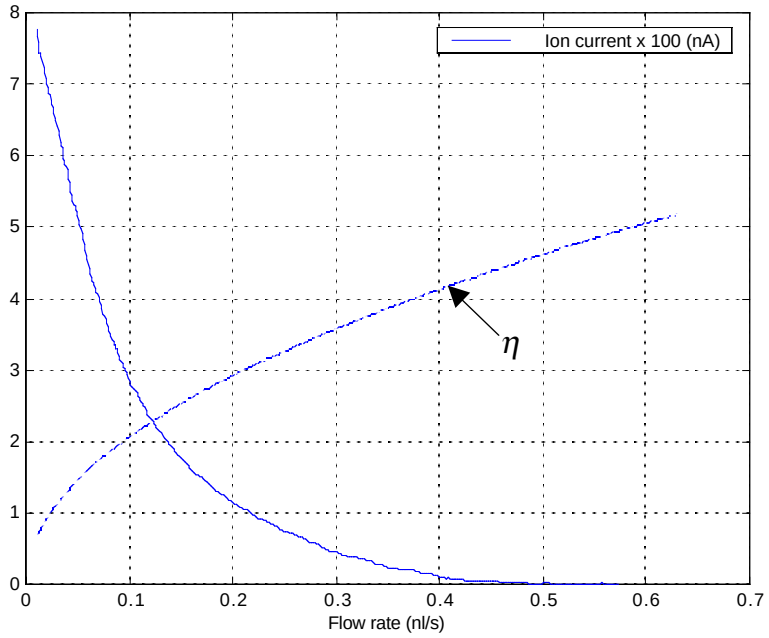

Figure 5.4.2. Ion current vs. flow rate. formamide + NaI. The dashed line corresponds to the value of the non-dimensional flow parameter η

5.5. Energy Properties of Colloid Beams

For measurements of the energy properties of colloid beams, the same setup as the one described in the previous section was used (including voltages and distances), except for a pair of metallic grids positioned close to the detector surface. As described in Section 4.1, one of these grids is grounded while the one closer to the detector is biased to a potential varying from zero to slightly above the beam potential, thus retarding the motion of the charged particles and allowing a determination of their energy distribution.

Many measurements of current as a function of flow rate are done for different stopping potentials (SP). Several of those curves are plotted in Figure 5.5.1.

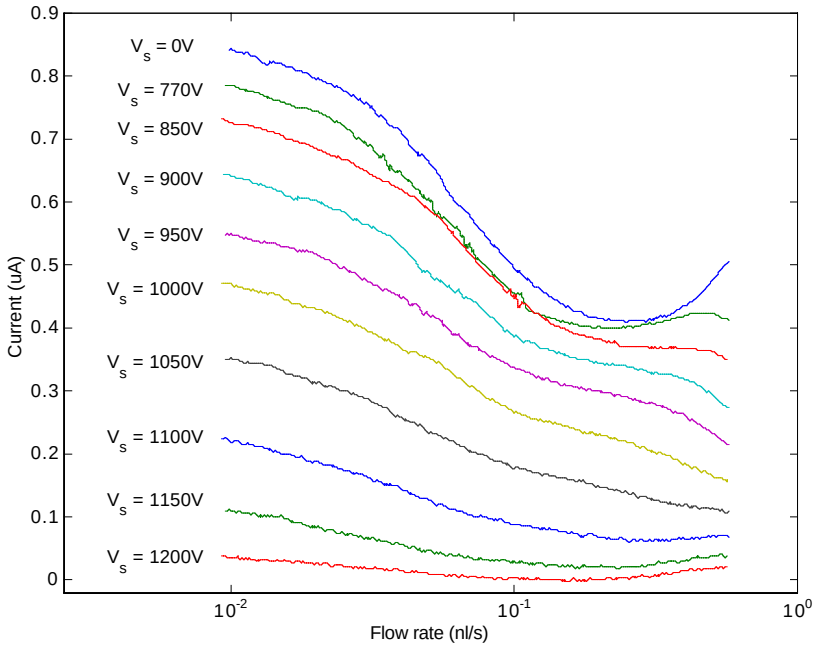

Figure 5.5.1. Variation of current vs. flow rate for different stopping potentials, with formamide + NaI and $\phi_a = \phi_{ex}$ = 1250 V for a 5 µm ID emitter. Detector distance from the extractor = 2 cm

Note that the stopping potential effect is generally different for the range of flow rates shown. To illustrate this, SP data from three flow rates are extracted and plotted in Figure 5.5.2: curve (a) is for the highest Q shown in Figure 5.5.1, or about 0.6 nl/s, curve (b) is for the flow rate where the current value is close to its minimum, or about 0.2 nl/s, and (c) is for the smallest flow rate shown, near 10 pl/s, which is very close to the instability limit, corresponding to a value of the non-dimensional flow rate of $\eta \approx 0.5$. The curves have been normalized to show them on the same scale.

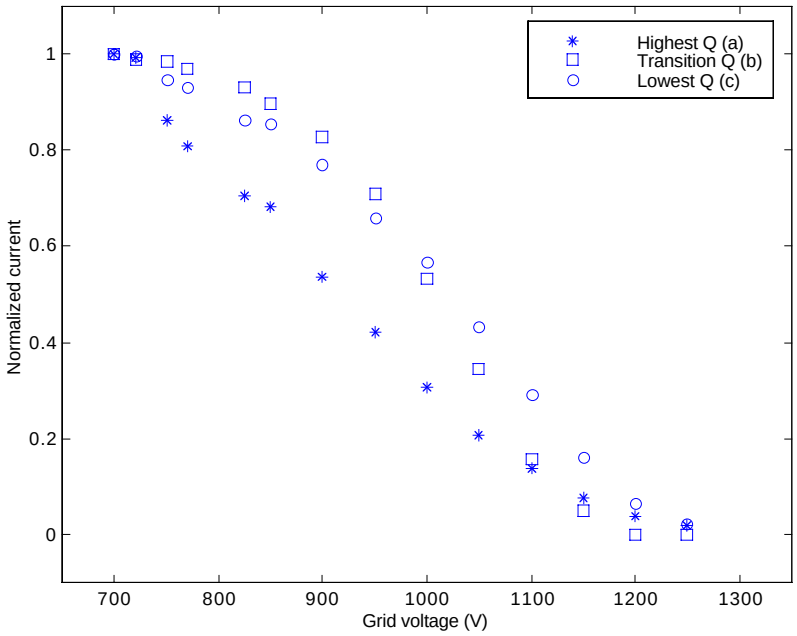

Figure 5.5.2. Stopping potential measurements for 3 different flow rates: (a) Q = 0.6 nl/s, (b) Q = 0.3 nl/s and (c) Q = 0.02 nl/s with formamide + NaI and $\phi_a = \phi_{ex}$ = 1250 V for a 5 µm ID emitter. Detector distance from the extractor = 2 cm

The shape of curves (a) and (b) reflects the previously reported [71] behavior of electrospray emissions at comparable flow rates; for high *Q*, curve (a), the beam is composed of multiple-sized droplets, some of which are ejected at different (lower) potentials, thus the relatively fast current decline between 700 and 800 V. For lower *Q*, curve (b), the current decreases gradually, starting at higher voltages than in (a), and therefore suggesting that particles are emitted from regions where the potential does not change as much. For lower flow rates, curve (c), ion current dominates and the structure of the remaining droplets becomes richer and more difficult to characterize.

In any case, what is most noticeable about these results is the fact that electrospray emissions, particularly in the ion-rich regime, show a relatively broad energy distribution.

It is virtually impossible to find a charged particle source with zero energy spread. Even if the source spread is very small, a number of possible mechanisms could magnify the intrinsic energy distribution once the particles drift away. For example, space charge forces could modify the axial speed of particles (Boersch effect) by individual charged particle interactions. In this case, statistical/numerical analyses are required to determine the energy broadening and are usually very difficult to come by if the charge density is very high, as in focused ion or electron beams. In fact, mechanisms such as these are the main cause of the observed energy spread in liquid metal ion sources (LMIS).

As mentioned before, LMIS work in a very similar way as electrosprays. Identical Taylor cone mechanics explain the deformation of a liquid metal meniscus. The difference between the technologies lies mainly in the fact that LMIS eject only ions, at least for moderate currents. As mentioned in Section 3.3, the LMIS emission surface is a hemispherical cap at the end of a small protrusion located at the tip of the Taylor cone. This metallic surface is practically an equipotential and therefore, ions leave it with extremely small energy differences, if any. Experimental measurements [43] of LMIS energy spreads in terms of the FWHM for several metals at different temperatures as a function of current can be seen in Figure 5.5.3.

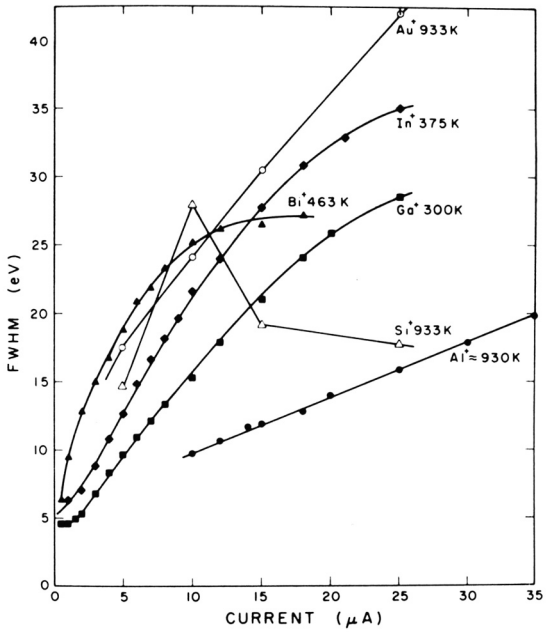

Figure 5.5.3. Energy distribution of LMIS, from [30]

It can be observed that, for the smallest currents, the FWHM of the energy distribution is below 5 eV, assuming singly charged ions emitted with potentials of a few kV. This is drastically different from the hundreds of volts in spread for the ion-rich electrospray measurements shown in Figure 5.5.2.

In addition to the intrinsic energy spread in particle beams, an additional broadening mechanism is introduced as the particles diverge from the propagation axis. The larger the angle, the less axial direction energy the particles carry.

To see this, assume all particles, originating from a common potential ϕ_B, leave the needle with a speed *v* and are distributed over a semi-angle θ as shown in Figure 5.5.4.

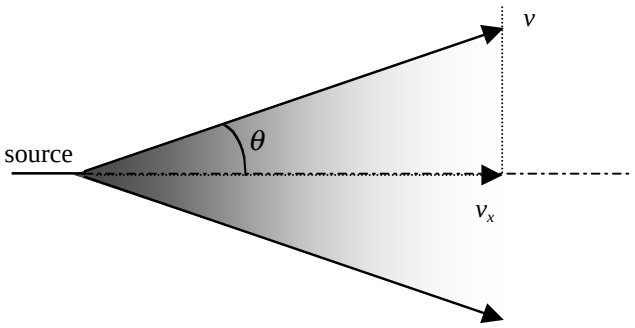

Figure 5.5.4. Beam divergence

For any given diverging "ray", its velocity component in the *x* direction is $v_x = v\cos\theta$. The energy associated with this component is $E_x = \frac{1}{2}mv_x^2 = \frac{1}{2}mv^2\cos^2\theta$. Since the retarding electric field lies in the *–x* direction, particles under its influence will only lose this component of the kinetic energy while climbing the potential barrier ϕ_s. Defining $E_o = \frac{1}{2}mv^2 = q\phi_B$ as the nominal (on-axis) energy of the beam and taking variations of the stopping potential with respect to the beam potential $\Delta\phi_s = \phi_s - \phi_B$,

$$\frac{\Delta\phi_s}{\phi_B} = -\sin^2\theta. \tag{5.5.1}$$

As a test for Equation (5.5.1), an experiment was performed in which the detector was segmented into two concentric plates isolated from each other. The inner collector was circular in shape with a radius of 10 mm while the outer collector was annular with inside and outside diameters of 10 mm and 20 mm. The detector was positioned 20 mm from the extractor-needle assembly. These dimensions were chosen such that the inner electrode would collect all trajectories with $\theta < 20^\circ$. The flow rate was 0.05 nl/s (ion-rich spray). The beam needle potential was set at $\phi_a = 1650\text{V}$ and the needle emitter had a 15

μm ID tip. The results of making SP measurements with this arrangement are shown in Figure 5.5.5.

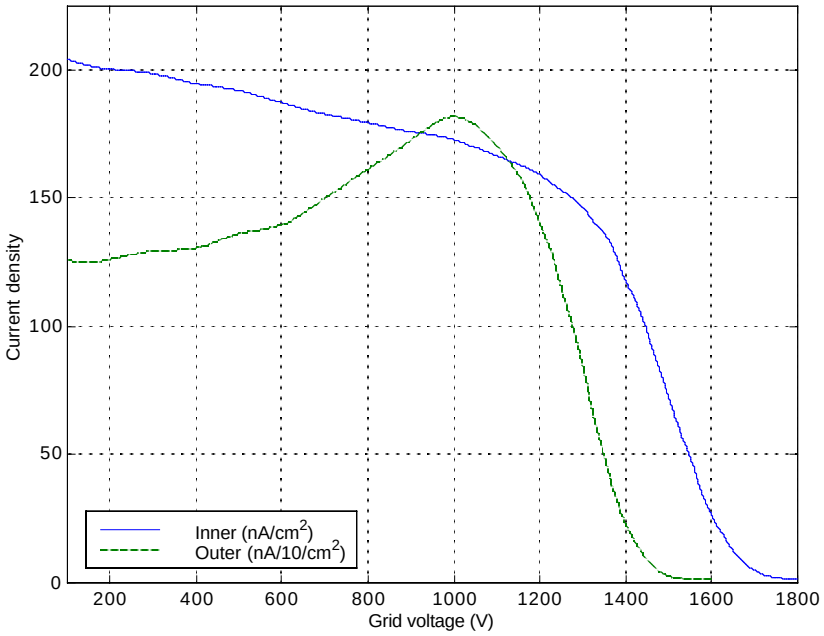

Figure 5.5.5. Energy distributions for the segmented detector with formamide + NaI and Q = 0.05 nl/s and $\phi_a = \phi_{ex}$ = 1650 V for a 15 μm ID emitter. Detector distance from the extractor = 2 cm

The plot shows current density values, so the difference in collector areas is already taken into account. Note also that, as planned, most of the current is measured in the inner electrode. The decrease/increase of current density for the first 1000 V applied to the grid voltage is due to the change in particle trajectories while climbing and descending the stopping potential barrier, i.e., particles that were moving directly into regions close to the edge of the inner electrode got deflected enough to end up in the outer electrode.

It is observed that the potential curve of the outer electrode is shifted about –190V with respect to the inner potential curve. Taking $\theta = 20^\circ$ and $\phi_s = 1500\text{V}$, $\Delta\phi_s = -175\text{V}$ can be

computed from (5.5.1), which is close to the observed shift. This suggests that the intrinsic energy spectrum of the particles collected in both angular ranges is actually the same, the shift being an artifact due to the lack of beam collimation.

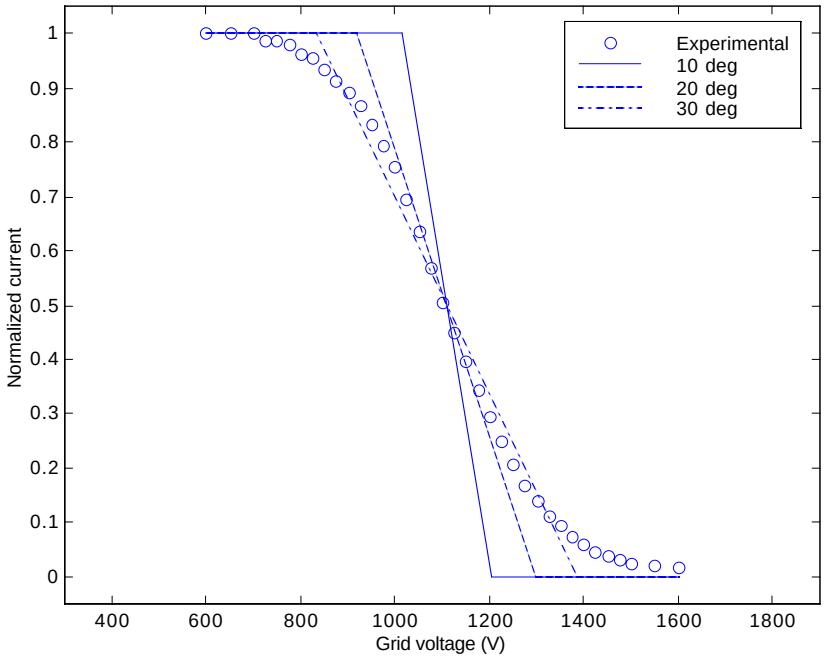

Figure 5.5.6. Comparison between experimental SP measurements and energy spreads calculated from an initially monoenergetic beam at different divergence semi-angles

The question now is to figure out how much of the observed energy spread can be attributed to this beam divergence effect. The energy spread $\Delta\phi_s$ depends strongly on the divergence angle. This can be seen in Figure 5.5.6, where the experimental curve of an energy distribution centered at about $\phi_B = 1110\text{V}$ is superimposed with calculations using (5.5.1), where initially monoenergetic beams have been assumed for three different divergence semi-angles.

Since the divergence angle is fixed at $\sim 20^{\circ}$, it is seen from Figure 5.5.6 that beam spreading explains part, but not all of the observed energy distribution. The logical step towards understanding this issue would be to explore the energy distribution of focused beams.

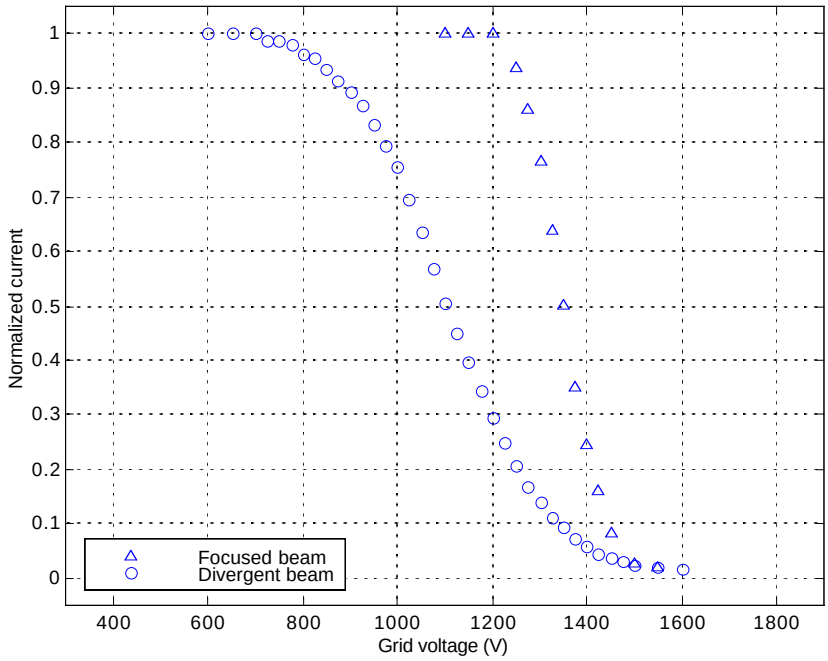

Figure 5.5.7. Effect of beam focusing on the energy distribution

To do this, the einzel lens was installed in the emitter, as shown in Figure 4.3.11 and the working distance was increased from 2 cm to 74 cm. The detector active surface was also smaller; a 1.5 cm radius circular plate was used. The maximum energy spread due to the difference in TOF of particles that travel close to the axis with those that travel in trajectories near the focusing electrode can be estimated from the diagram in Figure 4.3.10 and is just 0.6%. Figure 5.5.7 shows the difference between the focused beam energy spread and the divergent beam of Figure 5.5.6.

The energy distributions shown in Figure 5.5.7 are quite different. In particular it is evident that the focused version has a significantly smaller energy spread than the divergent beam. In fact, the energy distribution FWHM is about 122 V, still large compared to what is observed in LMIS, but definitely smaller than the 300 V of the divergent beam.

The use of the einzel lens reduces the amount of energy spread of an otherwise divergent beam. It would be tempting to think that this is a consequence of beam collimation alone, but in reality the electrostatic lens is an energy sensitive device; it brings into focus charged particles independent of their specific charge as long as they share the same energy level.

This brings up an important aspect about the ability to focus ion beams. It turns out that the size of the *disc of least confusion*, or *spot* generated by a focused ion beam will depend strongly on the energy distribution. In lithography applications tailored to micro-fabrication, it is highly desirable to work with beam sizes smaller than the features to be generated. This is one of the reasons why LMIS are well suited for this sort of application. Given the relatively large energy spread in the colloid beam, it can be anticipated that the einzel lens would not be able to focus every particle on a single spot, but rather would introduce *chromatic aberration,* thus scattering away those particles with energies different from the nominal focusing potential, set by the characteristics of the lens and the applied voltage.

To analyze this in detail, it is required to have a complete knowledge of the structure of the beam. To obtain it, TOF experiments were performed at different flow rates with the formamide + NaI solution of Table 4.5.1 using the single-gate continuous TOF apparatus described in Section 4.1 and shown schematically in Figure 4.1.1. Depicted in Figure 5.5.8 is a typical measurement with this device using $\phi_a = 1000\text{V}$, $\phi_x = -250\text{V}$, $\phi_f = 1100\text{V}$, and $\phi_s = 0\text{V}$. The flow rate was set to 0.1 nl/s. The flight length was $L_0 = 74.2$ cm and the needle-emitter had an ID of 5 μm. The signal was amplified using

the OPA602 op-amp (described in Section 4.2) with a gain of 100, thus limiting the bandwidth response, as seen in Figure 4.6.2(a).

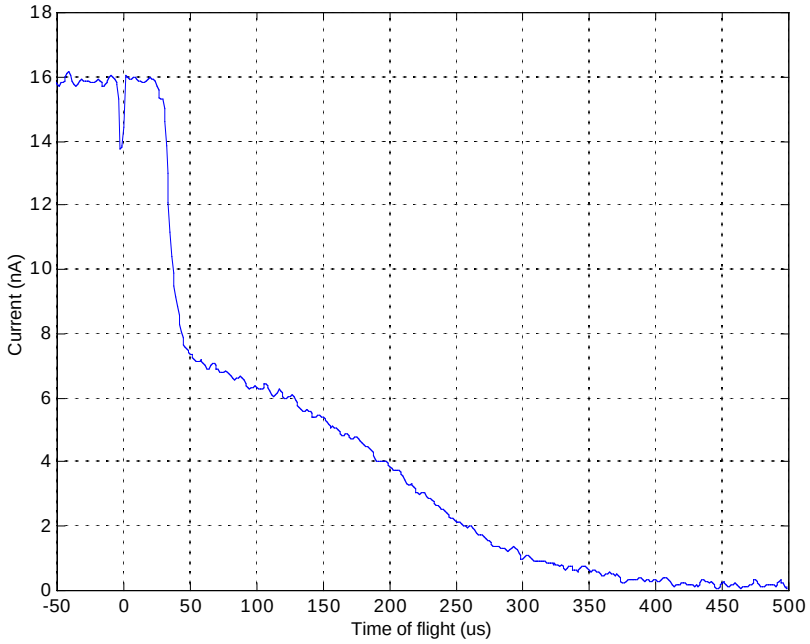

Figure 5.5.8. TOF measurement for formamide + NaI with Q = 0.1 nl/s, ϕ_a = 1 kV, ϕ_{ex} = 1.25 kV, and ϕ_f = 1100 V, for a 5 µm ID emitter and L_0 = 74.2 cm

The significance of this plot can be better understood by comparing it with the ideal TOF shape presented in Figure 4.1.4. As mentioned in Section 4.1, the current drop in real measurements is not abrupt, denoting a distribution, either in specific charge, energy or electronic equipment response.

There are two current drops in the figure. One is relatively sharp and centered at about 30 µs, while the second is very wide and centered at about 190 µs. Each current drop represents a charged particle family. The first one is fast, almost monodisperse. The specific charge, as estimated by Equation (4.1.2), is orders of magnitude higher for these

particles than what would be expected from the F. de la Mora's law (3.1.23) for droplets charged to the Rayleigh limit (3.1.12). These fast particles must be ions. The second current drop occurs at much longer times, and the specific charge is now in agreement with (3.1.23) and the Rayleigh limit, thus suggesting that droplets are also emitted.

The difference in relative time spreads of both species is clear. If it is assumed that both families have similar energy spreads, then the wide time distribution of the droplet component can only be explained if they have been formed with different physical properties, i.e., size and charge [18,19].

Perhaps the most intellectually appealing question that can be posed about the results shown in Figure 5.5.8 is whether ions and droplets share the same emission energy and the same energy spread [72]. To investigate this further, several TOF measurements were performed at different stopping potentials. This technique and some of its results have also been performed and corroborated by Gamero [73].

Figure 5.5.9 shows a typical example of these measurements. The inset in the top right corner of this figure represents the stopping potential measurements for the ion component. The applied voltage was set at $\phi_a = 970$ V. There is much useful information that can be extracted from this plot alone. To clarify the matter, some labels have been added to the figure. $\Delta\phi$ is the stopping potential change between two given curves, and ΔI is the corresponding percent change in ion or droplet current with respect to their totals. Here are the relevant aspects:

- There is a slight decrease of about 8% in the ion current for $\phi_s < 500$ V. Meanwhile, the droplet current remains practically constant.
- From 700 to 840 V, or $\Delta\phi = 140$ V, the ion current decreases 46% from its nominal value, while the droplet current decreases only by 15%.
- From 840 to 950 V, or $\Delta\phi = 110$ V, the ion current goes close to zero, losing 42% of its total value, while the droplet current vanishes, losing 85% of its total in this voltage range.

- Changes in ion and droplet currents in the range from 840 to 950 V are nearly proportional, i.e., they decrease at the same rate.
- The change in ion current in the overall range from 700 to 950 V is smooth, i.e., there are no steps in the inset shown in Figure 5.5.9.

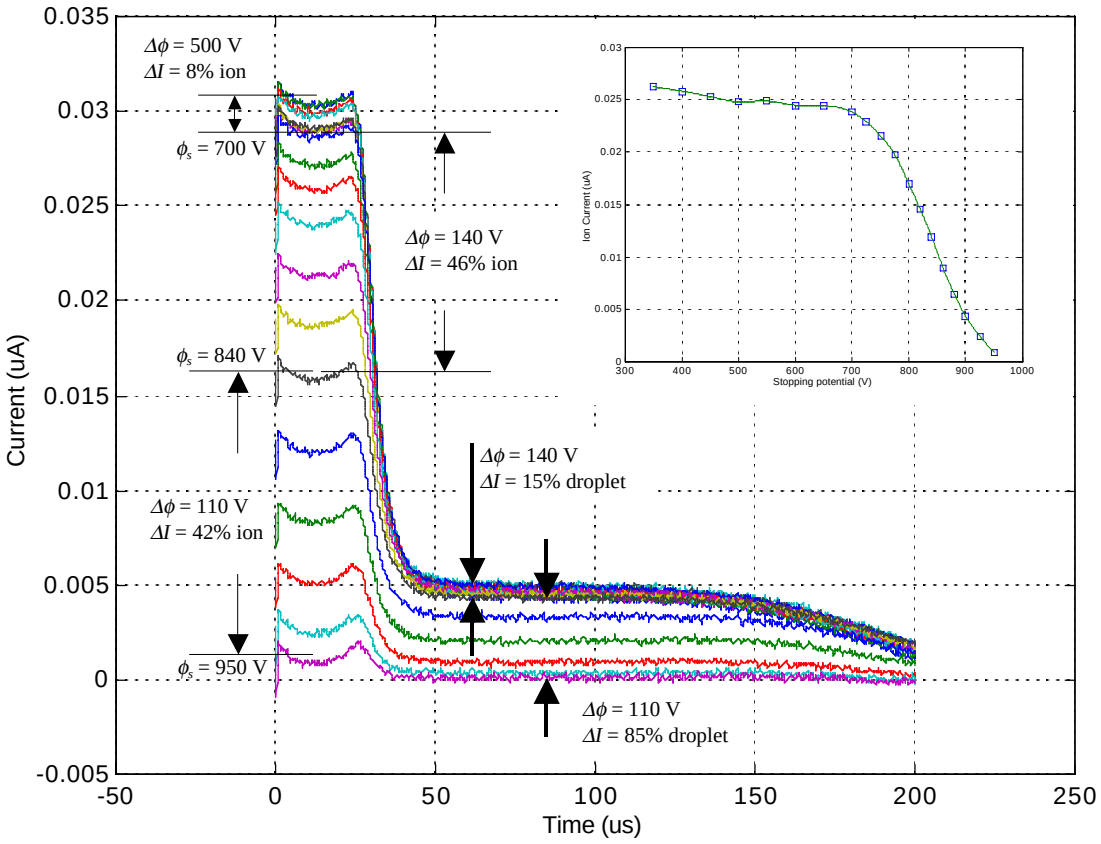

Figure 5.5.9. TOF measurements at different stopping potentials for formamide + NaI with Q = 0.06 nl/s, ϕ_a = 970 V, ϕ_{ex} = 1.2 kV, and ϕ_f = 1065 V, for a 5 µm ID emitter and L_0 = 74.2 cm

The first conclusion that can be extracted from these observed facts is that ions and droplets have different energy. In the particular case of Figure 5.5.9, more than half of the

ions have smaller energies than most of the droplets, while the remainder 42% has roughly the same energy as most of the droplets.

The second conclusion is that the energy spreads are very different, mainly because of the difference in emission energies cited above. In general terms it is observed that about 85% of the droplet current has an equivalent energy spread of 110 V, while the energy distribution of roughly the same fraction of ion current spans 250 V.

As cited above, and in more detail in Section 3.2, the normal electric field reaches a maximum near the transition region. Ion emission then occurs if this field is large enough to overcome the potential barrier given by the ion solvation energy. Those ions that leave the liquid surface do it with practically zero kinetic energy. Once extracted, they accelerate under the local potential gradient outside the liquid, which is closely related to the surface potential distribution.

Numerical simulations of the cone-jet structure performed by several authors [30,35,36] provide a plausible explanation for the energy spread observed in ions. These electro-hydrodynamic models describe the liquid behavior through a system of differential equations that include force balances and conservation laws. Some results from Carretero [35] are shown in Figure 5.5.10, where the grounded collector has been placed 300 μm from the emitter tip.

These results were computed for a formamide solution with a conductivity of only $K = 0.001$ S/m. This was chosen to keep the relaxation time $\varepsilon\varepsilon_o/K$ from being too small, since this time dictates the size of the simulation's discrete increments. As it turns out, high conductivities, such as those found in the experiments, would make these models take 2000 times longer to converge. This is why most of the numerical results show examples with low conductivities. Despite this difference, it is relevant to observe the general shape and scales of these plots.

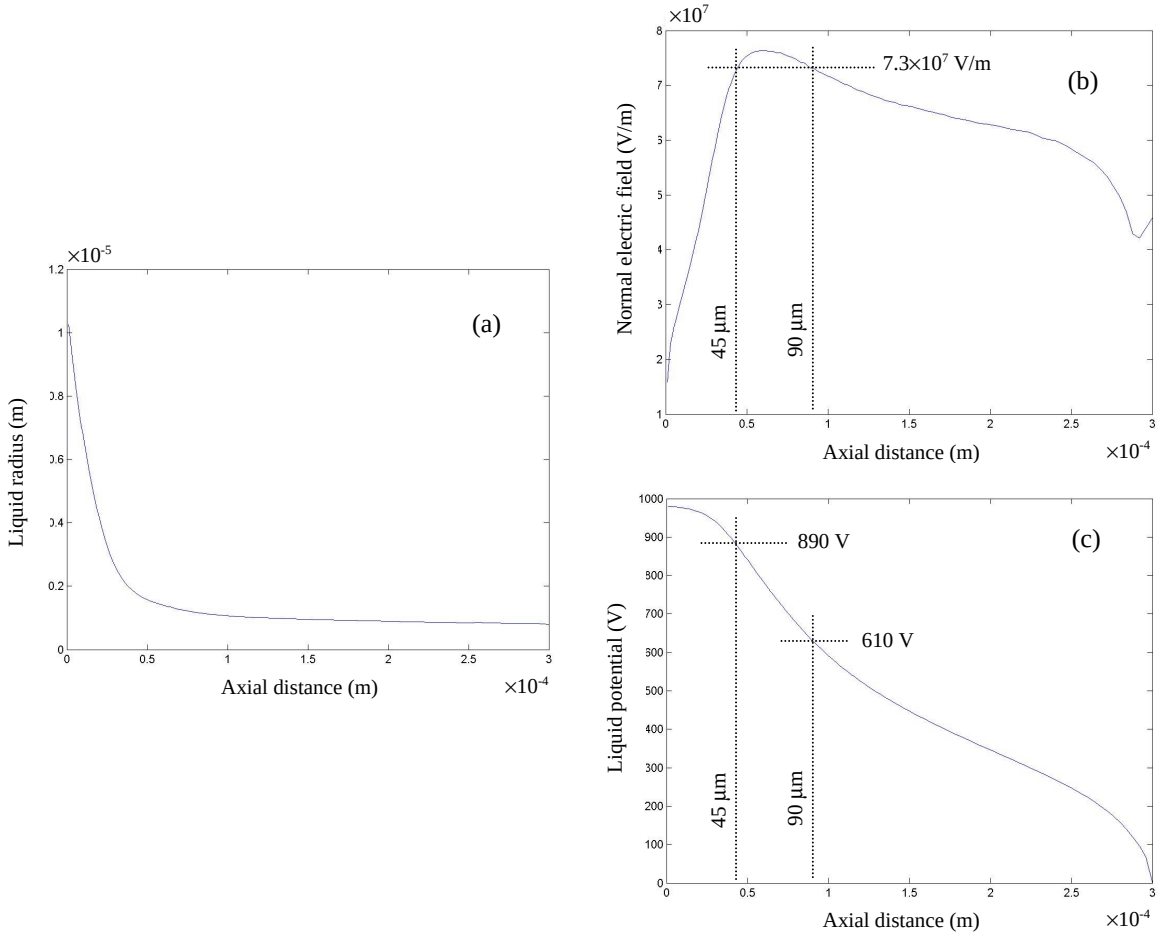

Figure 5.5.10. Numerical results from [35]: (a) liquid surface shape, (b) normal electric field and (c) electric potential as functions of axial distance

Figure 5.5.10(a) represents the liquid surface as it changes from a conical shape to a cylindrical jet. The normal electric field in Figure 5.5.10(b) increases towards the transition region, reaching a maximum value that is not sharply defined, i.e., the field can be relatively intense along the liquid surface. The electric potential in Figure 5.5.10(c) is roughly constant close to the origin (as assumed in Taylor's theory) and then decreases relatively fast within the transition region. Assuming that an electric field of

7.3×10^7 V/m is enough to extract ions, it is observed that there is a range of axial distances (~45 to 90 μm) in which ions can be emitted. In this same region, the electric potential changes from about 890 to 610V. This means that ions will have a potential distribution at least a few hundred volts, thus possibly explaining what is experimentally observed.

Gamero [73] has postulated that low energy ions are emitted from the region where the jet breaks up into droplets, while high energy ions come from the transition region where the cone turns into a cylindrical jet. However, these *low energy* ions actually have at least 80% of the emission potential of the droplets and the most energetic ions. This fraction is almost identical to the one observed in measurements for the ions in the stopping potential range from 700 to 840 V in Figure 5.5.9.

As discussed in Chapter 3, the strongest gradients of the pertinent quantities (fluid velocity, electric fields, potential, curvature, pressure, etc.) occur in the cone-jet transition region. Therefore, the electric potential near the end of the jet, where it collapses forming droplets, must be smaller than the potential levels near the transition region. This is also suggested by numerical calculations, such as the one shown in Figure 5.5.10(c). It is possible that the amount by which the potential decreases along the jet depends on parameters such as the liquid viscosity and the flow rate. This is still a matter of current research and more work needs to be done to fully characterize these dependences and therefore estimate the surface potential at the jet breakup region.

In the extreme case where the jet breakup occurs so far away that the potential practically vanishes, the ions, if emitted, will have a velocity similar to that of the droplets, and therefore a significantly smaller energy. If this is the case, the potential of such ions ϕ_{ion} compared with the potential of the energetic droplets $\phi_{droplet}$ will be,

$$\frac{\phi_{ion}}{\phi_{droplet}} = \frac{(q/m)_{droplet}}{(q/m)_{ion}}. \qquad (5.5.1)$$

In general, as seen in the previous examples, the specific charge of ions is very large compared with that of even the most heavily charged droplets. This means that the ratio given by (5.5.1) is in most cases less than 3%, definitely smaller than the 80% observed in the experiments.

One could argue that the potential level in the breakup region may not be exactly zero, but a finite value. Regardless, the potential there must be small since its variation along the jet is slow compared with the drastic changes that occur in the transition region [32,33,34]. Unless the potential in the breakup region is relatively large (~80% of the most energetic droplets' emission potential), the argument that every ion with lower energy is emitted from the breakup region is not complete.

This conclusion is reinforced by the fact that the stopping potential curve for ions, shown in the inset of Figure 5.5.9, is continuous in the range of stopping potentials from 700 to 950 V. On the other hand, it is observed in Figure 5.5.9 that there is a relatively small fraction of ions (about 8%) that have significantly less energy than any other component in the beam. Furthermore, the inset in the same figure shows what appears to be a relatively broad step for stopping potentials of less than 500 V. It is possible that these less energetic ions are in fact emitted from the breakup region. This will become clearer in Section 5.7, where the problem of ion identification is discussed.

The fact that ions and droplets have different energies has an important implication regarding the focusability of colloid beams. As mentioned above, the einzel lens is sensitive to energies, although not to specific charge. It must be possible then to use the lens to physically segregate the ion flux from the droplets in order to analyze them separately.

Figure 5.5.11 shows trajectory simulations using the emitter design used to obtain the results in this section. In agreement with the TOF-SP measurements shown in Figure 5.5.9, two particle families with different energies are injected from the needle. The high-energy component has a mean potential of $\phi_B = 895\ \mathrm{V}$, while the low-energy has

$\phi_B = 770$ V. The difference between the two cases is the focusing voltage for the lens. In (a), the lens voltage is set to $\phi_f = 1350$ V, bringing the low-energy beam into focus on the plane located in the far right side of the figure. The high energy component is also focused, though much less efficiently. In (b), the lens potential is increased to $\phi_f = 1570$ V, thus overfocusing the low energy component and effectively scattering it away. Under these conditions, if the plane was a collector plate, it would pick up a very small contribution from this particle family. Conversely, the high-energy component is brought into focus with the higher lens potential.

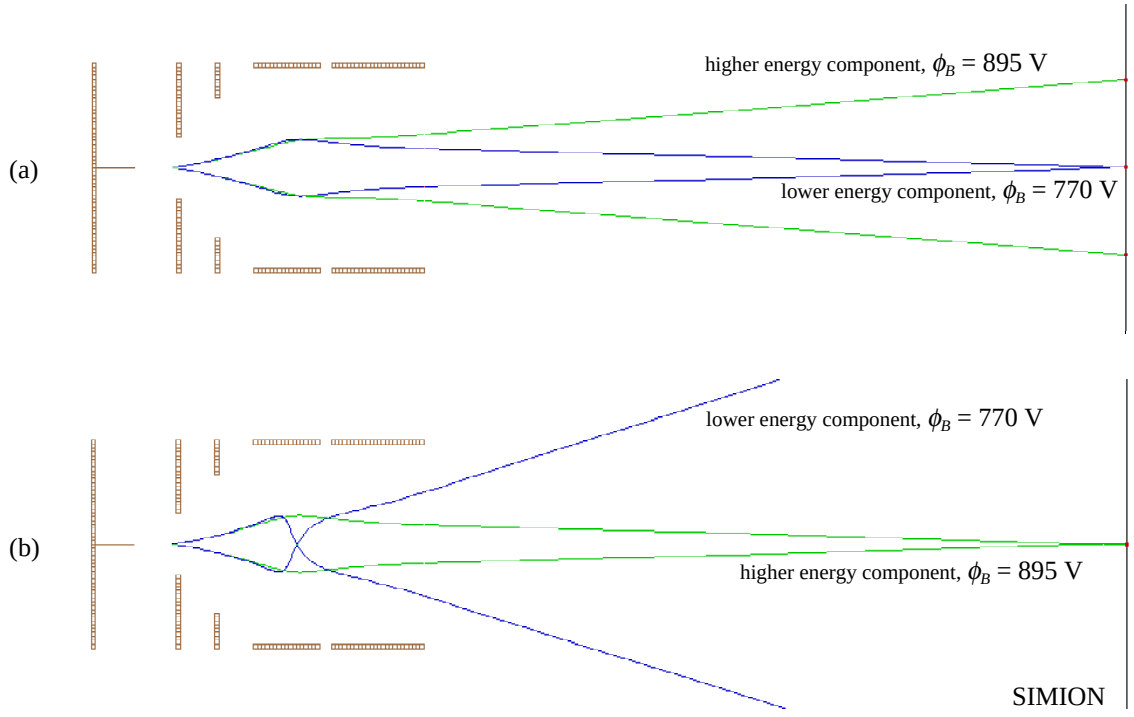

Figure 5.5.11. Trajectory simulations of two beams with different energy. (a) ϕ_f = 1350 V and (b) ϕ_f = 1570 V

As previously discussed, the low-energy component is made out of ions, while the high-energy component is comprised of both ions and droplets. As long as there is a mixed beam, the best configuration for separating the ion component from the droplet component is what is shown in Figure 5.5.11(a), thus leaving a droplet background in the measurements.

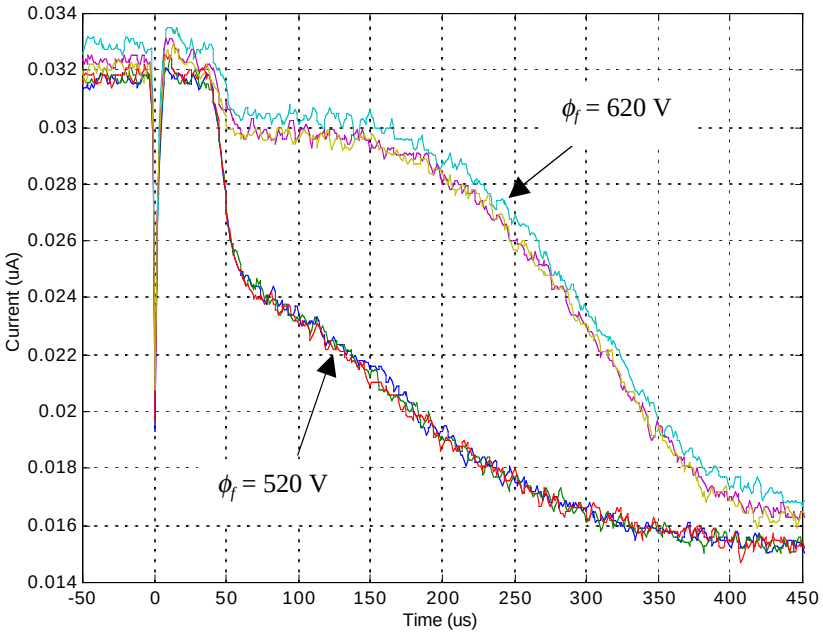

Figure 5.5.12. Effect of varying the focusing potential on measured particle distribution for formamide + NaI with Q = 0.1 nl/s, ϕ_a = 500 V, and ϕ_{ex} = 1.2 kV, for a 5 µm ID emitter and L_0 = 74.2 cm

To test this hypothesis, a set of experiments was performed combining TOF with variations in the focusing potential ϕ_f. Figure 5.5.12 is an example of measurements with $\phi_a = 500$ V and $\phi_x = -700$ V. Several curves taken at different times for a given ϕ_f are superimposed to show the repeatability of the experiment. It is observed that there are both ions and droplets in this beam. The less energetic ions are brought into focus along with some droplets by applying a focusing potential of $\phi_f = 520$ V. When this potential

is increased to 620 V, the signal from the higher energy component, i.e., droplets and some ions, increases, in agreement with the explanation given above. This separation technique is very useful in performing a detailed analysis of the ion component.

Another interesting effect of using the lens with particles of different energies is revealed when bringing into focus the high-energy beam component as the lens potential could virtually reflect some of the lowest energy particles, sending them into trajectories in the opposite direction as the original. Figure 5.5.13 shows a computer simulation in which the lens potential is increased to $\phi_f = 1670$ V for a beam of two families with energies of $\phi_B = 770$ V and $\phi_B = 895$ V, identical to those used in the previous example, shown in Figure 5.5.11.

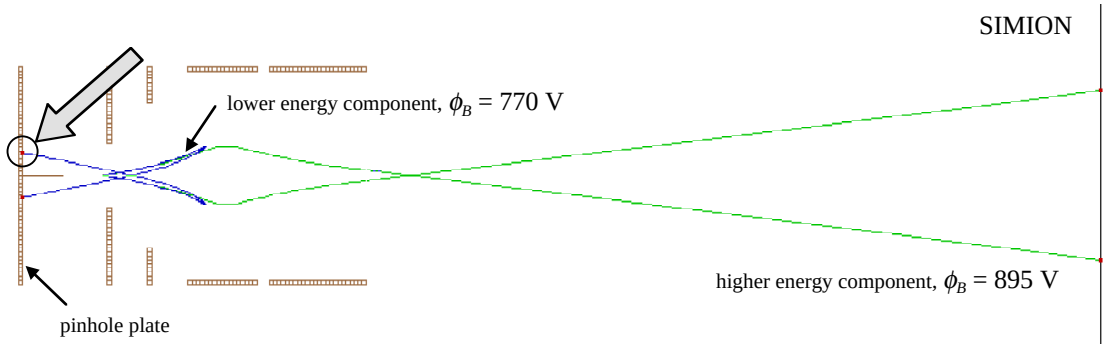

Figure 5.5.13. Trajectory simulations of two beams with different energy with ϕ_f = 1670 V. The 770 V component is deflected and hits the pinhole electrode held at a potential ϕ_a = 970 V

The potential field generated by the focusing electrode is large enough to make the low energy component in this simulation to collide with the pinhole electrode plate used to keep the needle emitter aligned with the setup centerline. The effect would be more noticeable for particles with smaller energies, such as ions emitted from the jet breakup region, as described above. If such collisions actually occur, then there should be some

physical evidence on the pinhole plate. After operating the emitter assembly for several hours with different focusing potentials, there is a noticeable coloration change of the stainless steel surface of the pinhole plate in regions around the small central aperture. It is assumed that this coloration is a result of charged particle collisions after being reflected by the lens focusing electrode. A step towards the verification of this assumption was made after characterizing the plate surface composition with help of an *scanning electron microscope* (Busek, Co). Several spectra from various regions on the plate were obtained. Two of such measurements are shown in Figure 5.5.14, where the various labeled peaks represent traces of various elements.

The pinhole plate material is 304 stainless steel, which has the following composition [74]:

- 0.08% Carbon (C)
- 2% Manganese (Mn)
- 0.045% Phosphorus (P)
- 0.03% Sulfur (S)
- 1% Silicon (Si)
- 18%-20% Chromium (Cr)
- 8%-12% Nickel (Ni)
- 65%-71% Iron (Fe)

It can be observed in Figure 5.5.14(a) that, except for S, Mn and P, the rest of these elements appear on a scan performed on a region far away from the pinhole aperture, where practically no deposition can occur given the geometry of the extractor aperture. Therefore, this spectrum serves as the reference against which other measurements can be compared. The second spectrum, shown in Figure 5.5.14(b), was obtained from a region that presented considerable visual coloration, thus suggesting maximum material deposition. The background composition of the SS 304 seems to be repeated in this spectrum, as expected, but there are several differences. The most relevant are the appearance of resonances indicating the presence of Sodium (Na), Carbon (C) and Oxygen (O).

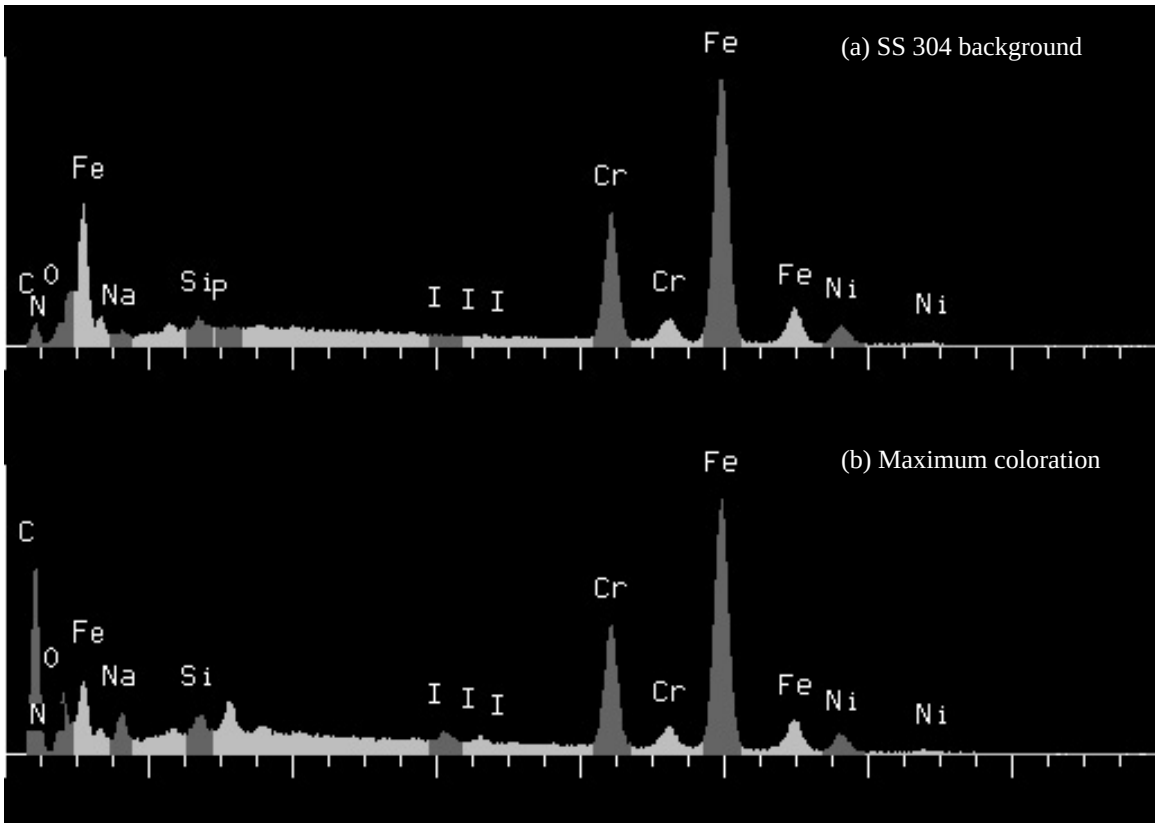

Figure 5.5.14. Electron microscope composition spectra for the pinhole plate: (a) from a region far from the central apperture where no deposition is observable, and (b) from the spot with greatest visual coloration

The solution used in these experiments is formamide (CH_3NO) heavily doped with NaI. It is interesting to note that the ratio of the peak magnitudes of C to Na is about 5:1. If we assume that Na^+ ions solvated with formamide molecules are being deposited in the plate, and that the C and Na *stick* to the SS surface without being degenerated, then the degree of solvation (number of formamide molecules for each Na^+) should be $n_s \approx 5$, which is consistent with ion identification experiments to be presented in Section 5.7.

5.6. Extraction Voltage and Beam Composition

The experiments presented in previous sections were performed under certain values of the extraction voltage, $\phi_{ex} = \phi_a - \phi_x$ selected to obtain a stable current in the electrometer's DC mode and from visual inspection of a stable cone structure. As mentioned in Section 3.1, F. de la Mora [11] performed an extensive investigation into the relationship between emitted current and liquid properties, including flow rate, for droplet beams. This investigation eventually led to Equation (3.1.21), a universal law for electrosprays in the cone-jet regime. As for the extraction voltage dependence, it could vary in a relatively narrow range without changing the amount of current emitted. Below this range, the extraction potential is not enough to sustain the conical structure and emission stops. Above this range, the cone angle increases gradually, while it is not uncommon to observe the jet moving towards the rim of the tip. Further increase of the voltage produces a very interesting phenomenon; at some critical voltage, the depressed cone breaks suddenly into two cones, each emitting a liquid jet. If the voltage continues to increase, more cones are formed, up to the point where no conical structures can be observed. These cone formations happen very rapidly, each time producing a sudden increase in measured current.

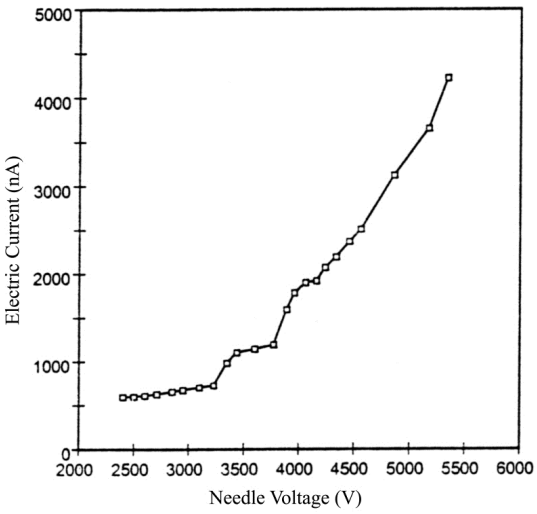

Figure 5.6.1. Current vs. voltage, from [75]

Figure 5.6.1 shows measurements by Gamero [75] in which this behavior is depicted for glycerol. In this case, the current remains fairly constant up to 3250 V. Above this value, a second cone appears and the current roughly doubles. Additional current steps occur at about 4000 and 4250 V. Beyond these values, the current continues to increase with voltage. This high-voltage range is usually referred to as the *highly stressed regime*.

Since the main interest of this research is on colloid beams in the mixed ion-droplet regime, it would be important to separately explore the effect that the extraction voltage has on the ion and droplet components. For this purpose, a set of measurements was performed while varying $\phi_{ex} = \phi_a - \phi_x$. To keep the TOF constant, the applied voltage was not changed; only the extractor voltage ϕ_x was modified.

Figure 5.6.2 shows the beam composition for increasing extraction voltages at a given focusing potential for the formamide + NaI solution. The first plot in the sequence shows a "nominal" composition of ions and droplets, similar to that encountered in previous TOF experiments. This composition remains relatively fixed up to about $\phi_{ex} = 1300$ V. Beyond 1350 V the droplet component suddenly changes to lower magnitudes and higher specific charges, suggesting the appearance of a secondary cone, characteristic of the highly stressed regime. Further increases in ϕ_{ex} cause the droplet current to decrease considerably, while the ion current dominates. It is interesting to note that this effect is produced as long as the flow rate is small enough initially to be in the ion-droplet regime. It needs to be remembered that the einzel lens filters out some particles and therefore the plots, as shown, cannot be used directly to compute the ion fraction in the beam. This calculation will be done in Section 5.8 for suitable experimental conditions.

In any case, what is observed is the possibility of controlling the ion/droplet ratio of a colloid beam. This could have important engineering implications, since it allows additional flexibility in the design, as pointed out in Chapter 2.

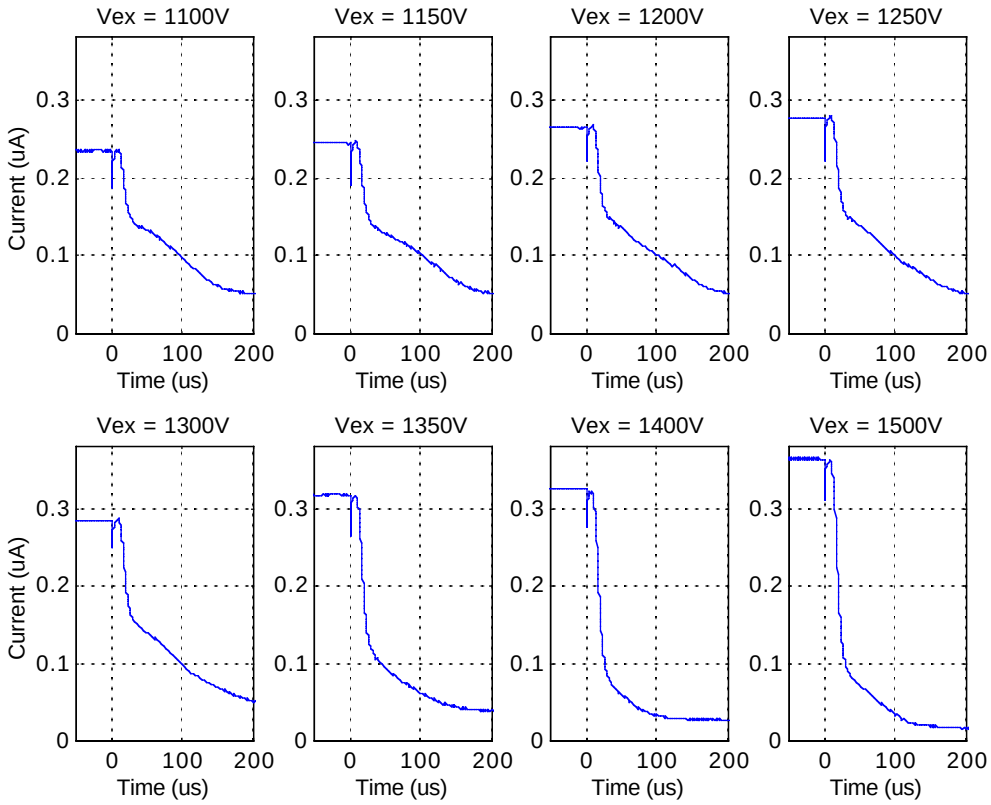

Figure 5.6.2. Time-of-flight waves for various extraction voltages for formamide + NaI with Q = 0.1 nl/s, and ϕ_a = 1100 V, for a 5 µm ID emitter and L_0 = 30 cm

The observed increase in ion current and decrease in droplet contribution is reproducible under a number of conditions. Another phenomenon is also observed when working in the ion-droplet regime. Figure 5.6.3 shows a second set of TOF curves with different experimental conditions. This time the sequence starts with an extraction voltage value close to the lower limit of cone stability.

The applied voltage in this example was fixed at $\phi_a = 725$ V, while the negative extractor voltage ϕ_x was increased from –550 to –1300 V. Normally, with this configuration, an extractor voltage of about –650 V would have been used, for a total extraction voltage of $\phi_{ex} \approx 1375$ V (10 µm ID needle emitter). However, it is observed that for smaller values of the extraction voltage, in particular for –550 V, there is an apparent suppression of droplet current with a corresponding increase in ion current. This behavior only exists in a very narrow range of extraction voltages, just slightly above that required for emission. The tools presented in the last section can be used to characterize the energy of these ions with respect to the droplets.

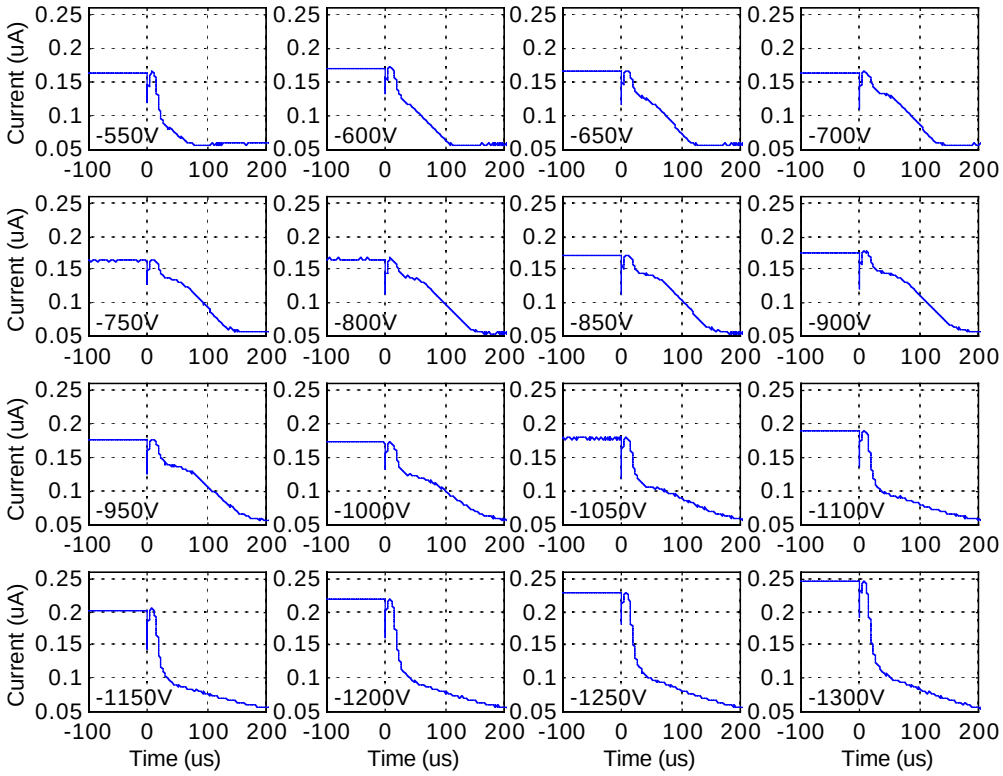

Figure 5.6.3. Time-of-flight waves for various extractor voltages for formamide + NaI with Q = 0.1 nl/s, and ϕ_a = 725 V, for a 10 µm ID emitter and L_0 = 30 cm

Figure 5.6.4 shows the results of using the einzel lens as an energy filter for a colloid beam working under the same conditions as above with $\phi_x = -550$ V (the curve obtained with $\phi_f = 1000$ V is similar to what is observed in the first plot of the sequence shown in Figure 5.6.3). As mentioned in Section 5.5, a weaker focusing potential would bring less energetic particles into focus. It is observed that at $\phi_f = 850$ V, the composition radically changes to an ion-rich mixture. On the other hand stronger focusing potentials scatter out the low energy particles, while bringing the most energetic ones into focus. This is evident when applying $\phi_f = 1106$ V to the lens. The ion contribution practically vanishes, while the droplet flux increases considerably. This suggests that, under low extraction voltage conditions, practically all ions have less energy than the droplets.

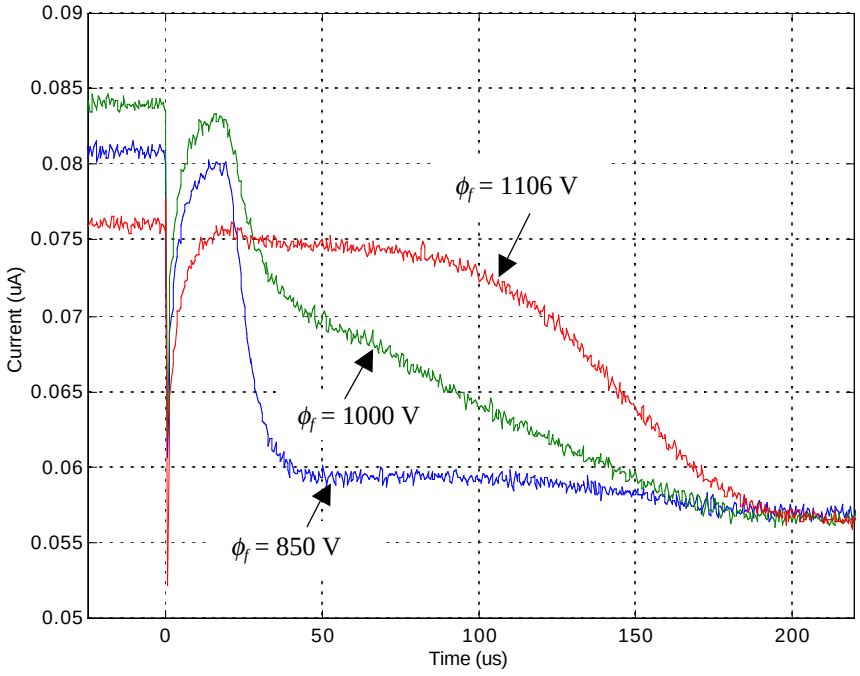

Figure 5.6.4. Variation of the beam composition with focusing potential in the low extraction voltage regime for formamide + NaI with Q = 0.1 nl/s, ϕ_a = 725 V, and ϕ_x = -550 V, for a 10 µm ID emitter and L_0 = 30 cm

5.7. Ion Identification

The TOF spectra obtained with these measurements can ultimately be used to identify the ion or ions in the beam. This identification is extremely important in characterizing the performance of a colloid thruster. All the tools required for this purpose have been described in the previous sections. As mentioned in Chapter 4, the specific charge of the analyzed particles can be calculated with Equation (4.1.2) if the flight time and the beam energy are known.

Two of the liquids described in Table 4.5.1 have the potential for emitting ions - the formamide + NaI solution and the EMI-BF_4 ionic liquid. In this section, results for both are presented.

Formamide + NaI

As discussed previously, the lens can be used as an energy-focusing device. Since some ions have energies different than most droplets, it is possible to maximize the ion current while almost completely eliminating the droplet component, especially if working under conditions that yield high ion fractions. A spectrum with such characteristics, using the continuous TOF technique with a metallic collector plate is shown in Figure 5.7.1. The relatively sharp decrease in current suggests that the population may be composed of a single ion type with some small polydispersity. For this experiment $Q = 0.1$ nl/s, $\phi_a = 1000$ V, $\phi_x = -500$ V, $\phi_f = 855$ V, and $L_0 = 74.2$ cm with a needle emitter of 15 μm ID.

Given the small signal level reached at these distances, a gain of 100 is used with the OPA602 op-amp. As mentioned earlier, such high gains limit the bandwidth of the amplifier. This is evident from the fact that the current drop shown has a time spread of about 20 μs, while the potential spread (Figure 5.7.2) is about 400 V, centered at about 750 V. If it is assumed that this current drop represents a single type of particle then, from (4.1.4), the time spread corresponding to the potential spread is about 9.6 μs, less

than what is observed. It is possible that the amplifier does not have enough bandwidth to respond to the current change.

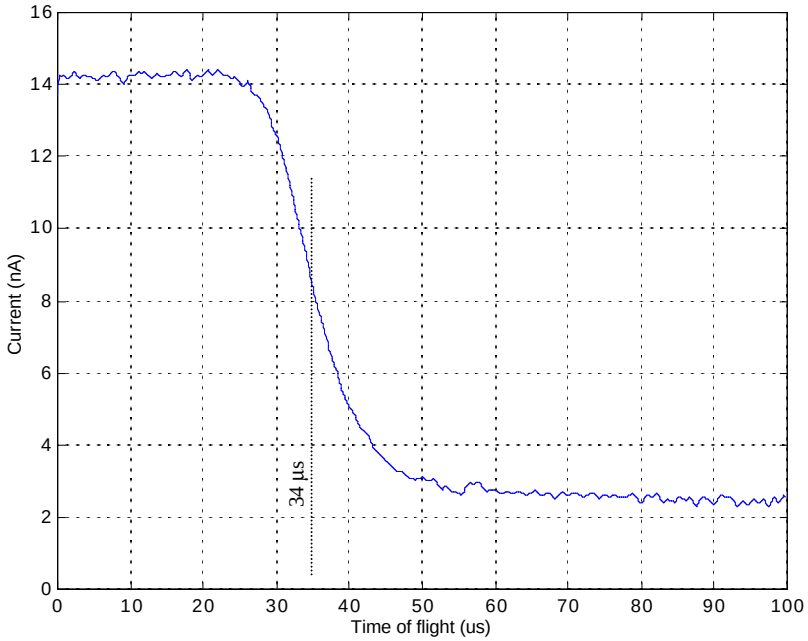

Figure 5.7.1. TOF ion spectrum for formamide + NaI with Q = 0.1 nl/s, ϕ_a = 1000 V, ϕ_{ex} = 1500 V, and ϕ_f = 855 V, for a 15 µm ID emitter and L_0 = 74.2 cm

In any case, the time distribution for the current drop is centered at about $t_f = 34\ \mu$s. Therefore the particle velocity is $v = 21.8$ km/s, which corresponds to a specific impulse of about 2200 s for the ion component. The accelerating beam potential ϕ_B is inferred from stopping potential measurements shown in Figure 5.7.2. The voltage distribution is centered at about $\phi_B = 680$ V. Here it has been taken into consideration, as discussed in Section 5.5, that there is still a droplet component, which biases the potential towards higher values. Substitution into Equation (4.1.2) results in a specific charge of $q/m = 350{,}196$ C/kg. Assuming that ions are singly charged, this translates into a mass of $m_i = 275$ amu.

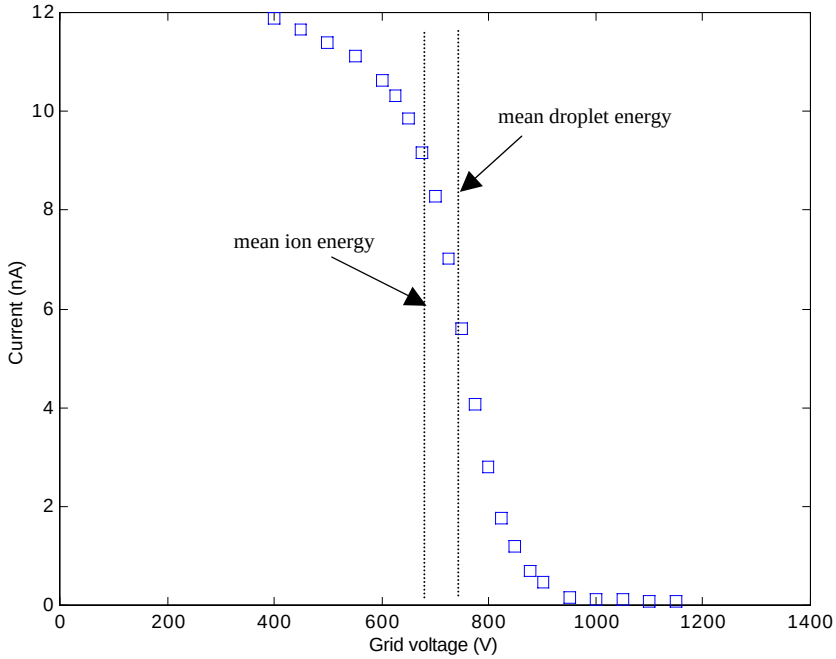

Figure 5.7.2. Stopping potential measurement for formamide + NaI with Q = 0.1 nl/s, ϕ_a = 1000 V, ϕ_{ex} = 1500 V, and ϕ_f = 855 V, for a 15 μm ID emitter and L_0 = 74.2 cm

The positive ionic species in the liquid is Na^+, which has a molecular mass of 23 amu. The ion mass measured is considerably larger, suggesting that what is extracted from the surface are solvated ions, i.e., Na^+ plus formamide (CH_3NO) molecules attached to it. The composition is then $m_i = m_{Na} + n_s m_{CH_3NO}$. Formamide molecules have a mass of 45 amu, meaning that the most probable composition is given approximately by $n_s = 5.6$. Gamero [73] has performed similar measurements and has concluded that $n_s = 4$. The degree of solvation is a function of the solution concentration [76], and therefore the use of different solutions could be reflected in these experimental results.

Given the relatively large ion fraction in these measurements, it was decided to replace the metallic plate detector by the electron multiplier (channeltron) described in Chapter 4. The advantage of using the channeltron is that it combines extremely fast response speeds with very high gains. The channeltron output signal comes in the form of a current, which needs to be conditioned as a voltage to be interfaced with the oscilloscope. Since typical gains can be as high as 10^6, there is no need to limit the bandwidth of the op-amp with the amplifier mode. Instead, the transimpedance configuration was used with a 1 MΩ resistor and a 1 pF capacitor. Since this detector occupies more space inside the chamber, the working distance was reduced to $L_0 = 63.8$ cm. The rest of the experimental parameters were $Q = 0.05$ nl/s, $\phi_a = 970$ V, $\phi_x = 0$ V, $\phi_f = 1250$ V, and a needle emitter tip ID of 5 μm. Figure 5.7.3 shows a typical TOF curve for these conditions.

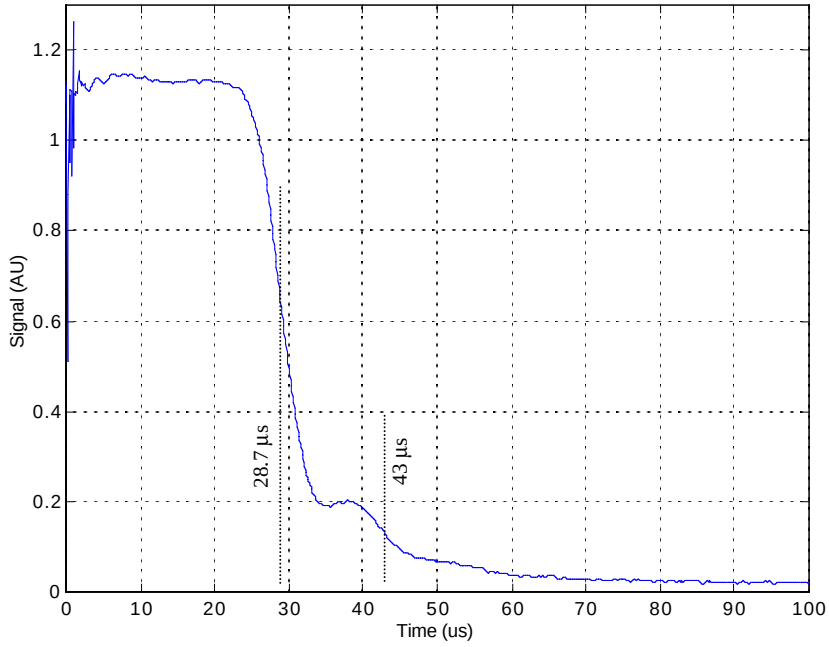

Figure 5.7.3. Channeltron TOF ion spectrum for formamide + NaI with Q = 0.05 nl/s, $\phi_a = \phi_{ex}$ = 970 V, and ϕ_f = 1250 V, for a 5 μm ID emitter and L_0 = 63.8 cm

It is known from previous experiments that even with this low flow rate there is a non-zero droplet fraction in the beam. It is observed in Figure 5.7.3 that droplets are not measured; this does not mean that they are not present, but it suggests that they do not have enough energy to produce the required electron emission. On the other hand, there is a very interesting feature not obtainable with the metallic plate detector: the ~20 μs signal drop seen in Figure 5.7.1 has been resolved into two separate steps; one centered at 28.7 μs with a maximum time spread of 6 μs and a second, smaller step (~15% of the total signal) at 43 μs with a corresponding time spread of 15 μs that extends into a relatively long tail with small amplitudes. This tail becomes negligible above 70 μs, where the background noise level of the detector is reached. It is known that this tail is not made out of droplets - if they were part of the most energetic population, their specific charge at 70 μs would be > 60 C/gr, much larger than the highest observable and theoretical values. Instead, it is possible that they represent ions with lower energies or perhaps ions with higher degrees of solvation.

The beam potential distribution is centered at $\phi_{s1} = 650$ V. From here, the mass computed for the ion in the first current drop is $m_i = 253$ amu, which corresponds to $n_s = 5.1$, slightly less than the previous result with the slow detector. Assuming that the ion represented by the second step has the same solvation composition, its potential distribution would be centered at approximately $\phi_{s2} = 300$ V. Interestingly, this value agrees with the potential measured for those ions with the smallest energies in the previous observations, shown in Figure 5.5.9. Even the current fractions are very similar: 8% in Figure 5.5.9 vs. 15% in Figure 5.7.3. These results considerably reinforce the hypothesis that only ions with very low energies are emitted from the breakup region and that there is an energy gap between such ions and the rest, which are emitted from higher potentials.

As mentioned above, the time spreads for both steps using the channeltron are also significantly shorter when compared with results from the slow op-amp amplifier. Again, assuming that each step corresponds to a single ion, the potential spreads using Equation (4.1.4) are,

$$\Delta\phi_{s1} = 2\phi_{s1}\frac{\Delta t}{t_f} = 2(650)\frac{6}{28.7} = 270 \text{ V},$$
$$\Delta\phi_{s2} = 2\phi_{s2}\frac{\Delta t}{t_f} = 2(300)\frac{15}{42.4} = 212 \text{ V}. \quad (5.7.1)$$

These spreads show very good agreement with all previous stopping potential analyses such as the focused curve shown in Figure 5.5.7 and in particular the results depicted in Figure 5.5.9, where both spreads are shown. It is concluded that these measurements are not limited by the bandwidth of the electronic components, and that the observed spread in the time of flight values is due to the intrinsic energy distribution of colloid beams and perhaps some solvation polydispersity, as suggested by *quadrupole* measurements performed by Chiu and Dressler [77] in which several degrees of solvation ($n_s = 1-6$) were observed for a formamide solution with similar characteristics.

Ionic Liquid: EMI-BF_4

The channeltron seems to be the perfect tool for analyzing colloid beams with high ion fractions. Its properties allow it to be used in practically every operation mode, in particular the single gate/pulsed TOF described in Section 4.1.

To test this operation mode, the ionic liquid EMI-BF_4, studied initially by Romero et al. [52], is used. The spectrum of this substance was already analyzed in their work, and therefore can be used in calibrating the pulsed TOF. As described in Section 4.5, ionic liquids have the unusual property of having zero vapor pressure and relatively high viscosity at moderate temperatures. It is not hard to obtain very low flow rates by using a gas feed system like the one described in Section 4.6. In the same work by Romero, it was found that under such low flow conditions a pure ionic regime is reached where the droplet current is completely suppressed. Since the channeltron seems unable to measure droplet flux, this ionic regime presents an excellent opportunity to conduct more research

using it as the main tool. Three different ions were observed. Their compositions, masses and names, as given by Ref. [52], are,

- EMI^+ $m_m = 111$ amu Monomer
- $(BF_4\text{-}EMI)EMI^+$ $m_d = 309$ amu Dimer
- $(BF_4\text{-}EMI)_2EMI^+$ $m_t = 506$ amu Trimer

The magnitude of the relative TOF signal for these ions (extracted from Ref. [52]), normalized by the monomer current level are $\hat{I}_m = 1$, $\hat{I}_d = 2$ and $\hat{I}_t = 0.58$.

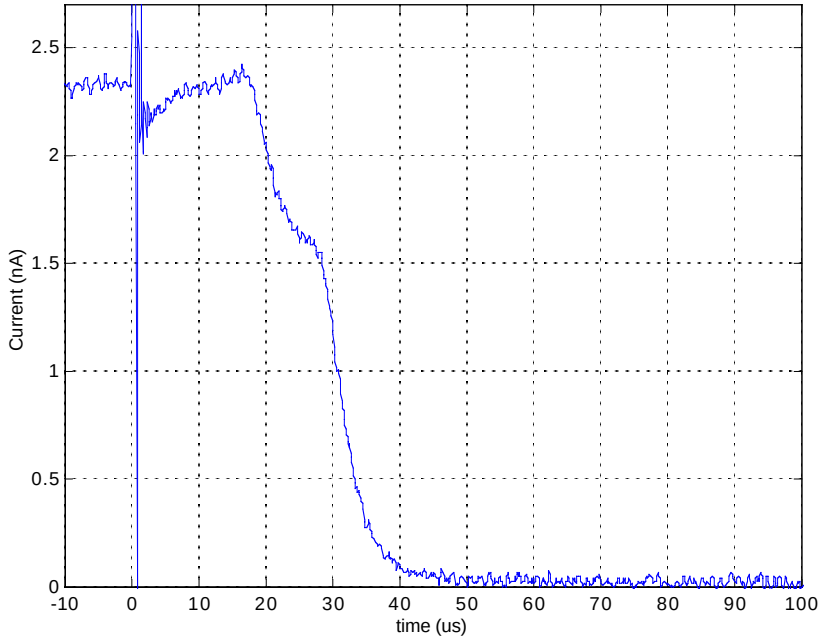

Figure 5.7.4. TOF spectrum for EMI-BF_4 using a small collector plate; ϕ_a = 970 V, ϕ_{ex} = 1180 V, and ϕ_f = 1080 V, for a 10 μm ID emitter and L_0 = 63.8 cm

In this thesis, measurements with EMI-BF_4 were carried out using a 10 μm distal coated needle emitter, $L_0 = 63.8$ cm, and power supplies set to $\phi_a = 970$ V, $\phi_x = -210$ V, and

$\phi_f = 1080$ V. Figure 5.7.4 shows measurements with the continuous TOF using first a metallic plate as current collector (the channeltron deflector) so that droplets should be detected. The electronics for these measurements have been cleaned up considerably. This is evident from the small signal level shown in this plot, which is due to the aperture located in front of the channeltron deflector, as seen in Figures 4.2.3 and 4.2.4.

Figure 5.7.4 is similar to what was observed in Ref. [52], the only difference being the signal magnitudes. These TOF measurements were performed to verify that the flow rate was low enough to reach the pure ionic regime. This is indeed the case, as no droplets can be observed after the final current drop at around 40 μs. The two steps corresponding to the monomer and dimer ions are clearly observed and their flight times are consistent with their masses. For example, the flight time of the dimer can be obtained from that of the monomer assuming that they are emitted from the same potential by,

$$t_d = t_m \sqrt{\frac{m_d}{m_m}} = 19\sqrt{\frac{309}{111}} = 31.7\ \mu\text{s}, \tag{5.7.2}$$

which is close to the observed value in Figure 5.7.4. The time spreads, however, are relatively large, corresponding to potential spreads of the order of hundreds of volts. These spreads are similar to those seen in Ref. [52]. This is in part due to the amplifier bandwidth limitation at high gains and the intrinsic beam energy spread.

Using the same argument, the trimer signal should be located at a flight time of,

$$t_t = t_m \sqrt{\frac{m_t}{m_m}} = 19\sqrt{\frac{506}{111}} = 40.56\ \mu\text{s}. \tag{5.7.3}$$

There is no evidence of any signal around this value in Figure 5.7.4.

To increase the resolution of the TOF measurements, the channeltron was used as detector. A voltage of –1.8 kV was applied to the channel body while a voltage of 200 V

was supplied to the deflector plate. The output signal was conditioned using the transimpedance configuration described in Section 4.2. The rest of the conditions were the same as in the previous example. The pulse generator/amplifier module was programmed to be normally closed and deliver 1 µs opening signals to the electrostatic gate with a repetition rate of 1 kHz. This configuration is ideal to detect the flight times of fast species with high resolution. The spectrum, recorded and displayed in the oscilloscope, is shown in Figure 5.7.5.

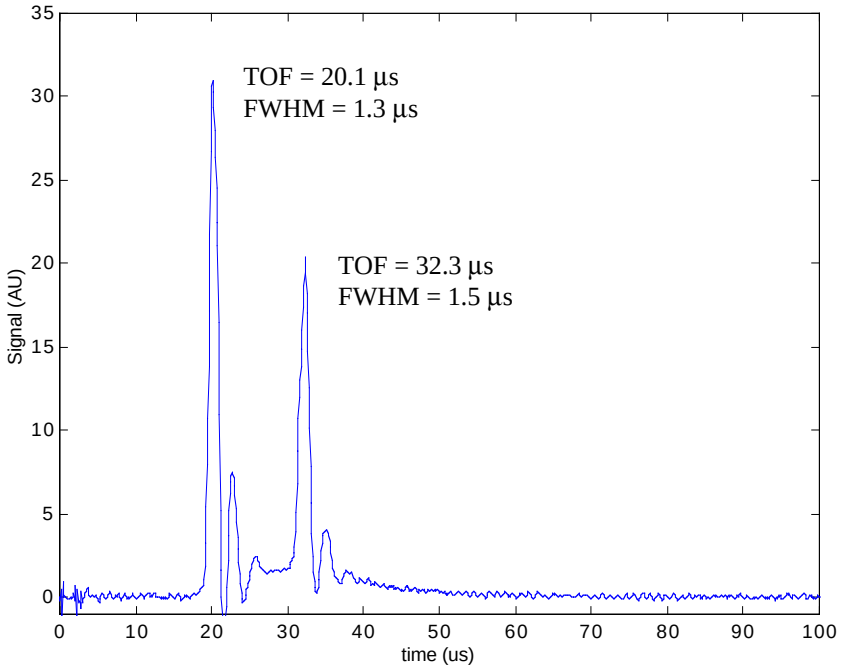

Figure 5.7.5. Pulsed Channeltron TOF spectrum for EMI-BF_4 and 1 µs pulses; ϕ_a = 970 V, ϕ_{ex} = 1180 V, and ϕ_f = 1080 V, for a 10 µm ID emitter and L_0 = 63.8 cm

The corresponding flight times are 20.1 µs for the monomer and 32.3 µs for the dimer. Each of these peaks has an associated time spread that can be characterized by its full width at half maximum (FWHM) value. For the monomer, this spread is 1.3 µs, while for the dimer is 1.5 µs.

These measurements suggest that the energy spread in the pure ionic regime is significantly smaller than any other electrospray tested, even for mixtures with very high ion fractions. As mentioned in section 4.1, if the ions have virtually no energy spread, then the time spread observed in this pulsed mode should correspond to the width of the high voltage pulse used to generate the ion packets. The observed spread in both peaks is slightly larger than the 1 μs width pulse. The reason for this can be attributed to the non-symmetrical nature of the pulse, as seen in Figure 4.2.2, or perhaps to some slight spreading induced by the electrostatic gate. Regardless, for the case in which the time in excess of the pulse width (0.3 μs for the monomer and 0.5 μs for the dimer) is due to the intrinsic energy spread,

$$\frac{\Delta\phi_m}{\phi_m} = 2\frac{\Delta t_m}{t_m} = 2\left(\frac{0.3}{20.1}\right) = 2.98\%,$$
$$\frac{\Delta\phi_d}{\phi_d} = 2\frac{\Delta t_d}{t_d} = 2\left(\frac{0.5}{32.3}\right) = 3.09\%. \tag{5.7.4}$$

Furthermore, from the TOF curves it can be seen that the emission potentials for the monomer and the dimer are slightly different,

$$\phi_m = \frac{m_m L_0^2}{2t_m^2 e} = 580 \text{ V},$$
$$\phi_d = \frac{m_d L_0^2}{2t_d^2 e} = 625 \text{ V}. \tag{5.7.5}$$

From (5.7.4-5), the energy spreads for the monomer and the dimer ions are 17 and 19 V, respectively. These values are very small compared to what is observed in other experiments, thus suggesting that in this regime, electrosprays behave in a similar way to liquid metal ion sources.

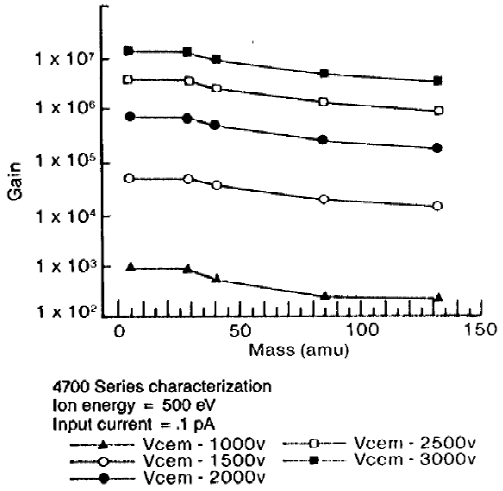

Figure 5.7.6. Channeltron electron multiplier gain variations with ion mass (from Burle handbook)

Following the tendency given by Equation (5.7.5), the trimer ion should be emitted from a potential of about 670 V, thus having a flight time of 40 μs. Nothing, but a slight wide tail can be observed at this flight time. One possible explanation for the relatively low intensity signal from this ion might be that the detection efficiency of the channeltron decreases with increasing specific ion mass. But, as seen in Figure 5.7.6, this decrease is moderate only, and this explanation may not be sufficient.

These measurements can be improved considerably by using pulses with less width. This would require decreasing the value of the resistor used to filter out the high harmonics that caused the capacitive coupling, as described in Section 4.2. The signal-to-noise ratio obtainable with electron multipliers may be high enough to eliminate some of the concerns from this type of induced noise. In addition, the buffer configuration for the op-amp amplifiers can be used without restriction, thus obtaining extremely high bandwidths compatible with the flight times of the fastest ions.

As discussed in Section 3.5, it is not clear what is the fate of the counter-ions when only one polarity is emitted. This is particularly important for ionic liquids working in the pure ionic regime. For example, for every monomer, dimer or trimer emitted, a BF_4^- counter-ion will be released. It is known that neutral BF_4 is not easily found, given its prominent aggressiveness [78]. Therefore, it must accumulate or react somehow in either the anode, the liquid or the capillary material, without being able to leave with the flow, since no droplets are emitted. It is found experimentally that the liquid container pressure needs to be increased periodically when working with small needle-emitter tip diameters in the pure ionic regime in order to maintain a certain emission level for long periods of time. This suggests that some sort of physical blockage may be occurring due to the release and accumulation of counter-ions. It is possible that, if this regime is sought for colloid thrusters, the bi-polar operation mode briefly described in Section 3.5 may become a necessity. On the other hand, larger emitters can be used since the concern from evaporation losses is eliminated in ionic liquids. Furthermore, external wetting of solid needles similar to that of FEEP's may be interesting to investigate with these non-volatile liquids.

5.8. Ion Fractions and Performance

As discussed in the first chapters, colloid thrusters are an attractive alternative for space propulsion mainly because of their extended operational flexibility in different modes, from precise control to main on-board propulsion. A good part of that flexibility comes from their ability to produce beams with different properties, in particular with different ion fractions. As was explained in Section 2.1, thrusters working in the ion-droplet mixed regime will suffer from polydispersity inefficiencies, which are not too large and can be tolerated in view of the potential gains in specific impulse and mass utilization.

The final set of experiments was designed to demonstrate this capability by operating the same electrospray source under different conditions in order to obtain ion fractions that would change the performance of the thruster. To measure the ion fraction, a way to differentiate ions from droplets is required. This is something that can be done with the TOF technique. As mentioned before, in order to have better TOF resolution, longer working distances are desirable. Focusing techniques are then applied to allow the use of relatively small detector surfaces. This technique, however, is limited by the amount of energy spread, which can be quite large as described in Section 5.5. This means that the farther away the detector, the more current will be lost by chromatic aberration. If the whole beam is to be captured, the detector should be situated relatively close to the source. It is not the intention here to identify the ions in the beam; this was done already in the last section. Therefore, there is no concern about the resolution of TOF measurements as long as the specific charge of droplets can be determined. Given this, the relative amplitudes of the different beam components will be used to compute the thruster performance, as discussed in Sections 2.1 and 4.1.

The main difficulty with short distances and large detectors is the capacitive coupling noise mentioned in Section 4.2, which increases accordingly and could obscure some of the signals, in particular that from the ions. In any case, a trade-off was made between how much noise can be accepted vs. the working distance and detector size, which can be minimized by using the einzel lens in a *semi-focusing* mode, where the mean energy is brought to focus into the detector plane, while the highest and lowest energies, which are underfocused and overfocused respectively, will cover a wider surface area that will determine the size of the metallic plate.

Figure 5.8.1 illustrates in a simulation the way in which trajectories different from the nominal energy cover a relatively large area in the detector plate, while those that have the mean energy are focused.

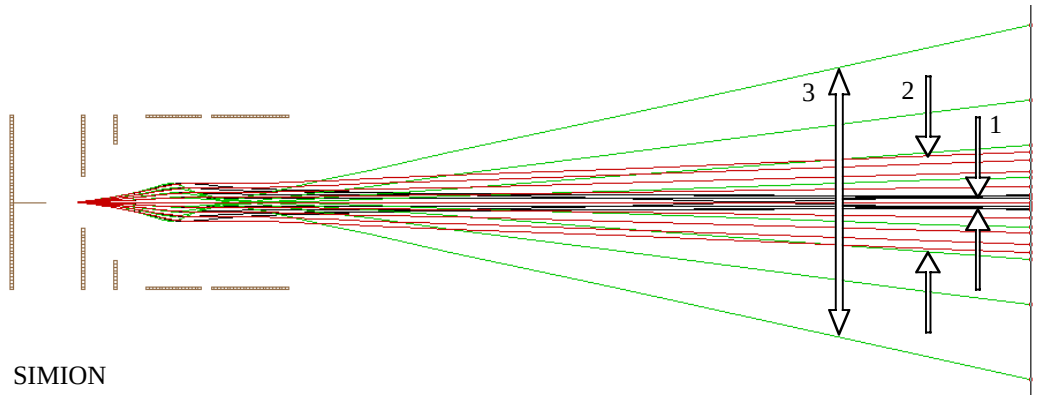

Figure 5.8.1. Simulation of trajectories with energy spread: (1) beam mean potential ϕ_B = 880 V, (2) more energetic particles ϕ_B = 945 V, and (3) less energetic particles ϕ_B = 820 V, with ϕ_f = 1350 V

Simulations such as these were used to estimate the size of the detector, the operation voltage of the lens and the working distance. To verify that the total current collected in the plate was close to the current drawn from the power supply, a 100 kΩ resistor was placed in series with the high voltage cable and the voltage across it was monitored with a voltmeter. The diameter of the plate was 12 cm, that is 3 more cm than the maximum diameter expected by the computer simulation. The working distance was 23 cm from the plate to the gate grid. As in previous experiments, this grid blocked about 15% of the current. Even though the distance is relatively long, capacitive coupling is strong. Appendix B shows how to take advantage of the noise characteristics to reduce its effects.

In all cases, the current measured from the plate varied from 75% to 85% of the total current delivered by the power supply. The loss is in part due to the grid blockage and perhaps to the einzel lens itself. In any case, these losses are small and it can be

considered that the particle fractions collected in the plate are representative of all the current that is being emitted.

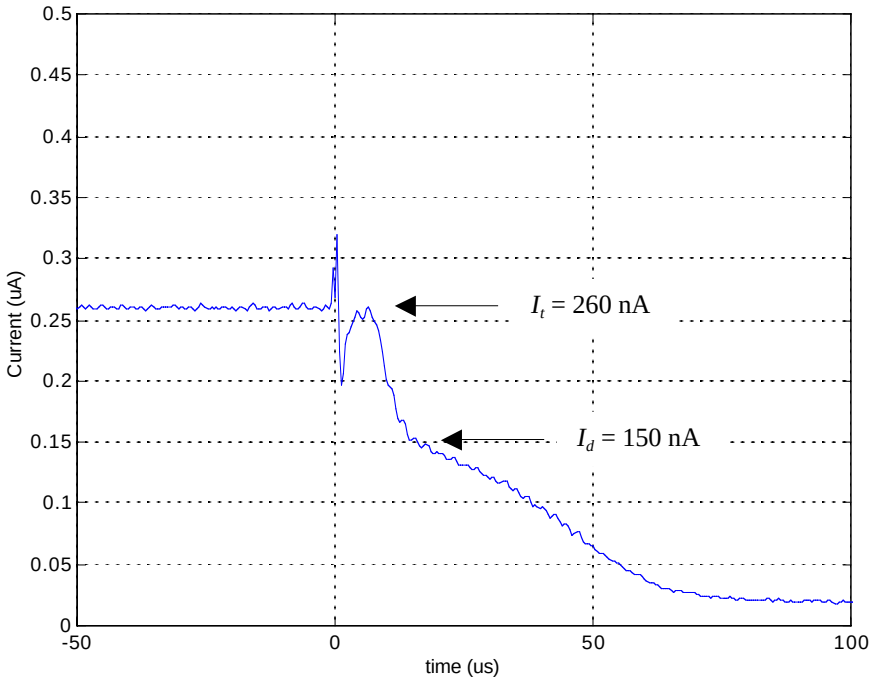

Figure 5.8.2. TOF for formamide + NaI with Q = 0.12 nl/s, $\phi_a = \phi_{ex}$ = 1020 V, and ϕ_f = 1058 V, for a 5 μm ID emitter. Detector distance = 23 cm

No comprehensive characterization of all the possible combinations of operational parameters was made with this experiment. Instead, almost everything was left constant: geometry, liquid solution, temperature, needle size, etc. Only three cases are shown with different voltages and flow rates. As will be seen, these cases demonstrate how some simple modifications can have an impact on thruster performance.

In the first case, the flow rate of formamide + NaI was chosen such that ions and droplets could be clearly observed ($Q = 0.12$ nl/s). The power supplies were set to: $\phi_a = 1020$ V,

$\phi_x = 0$ V and $\phi_f = 1058$ V. The TOF spectrum using a distal coated 5 μm ID needle emitter can be seen in Figure 5.8.2. The current is not corrected for losses in the gate grid.

In this case, the droplet to ion specific charge ratio (from previous results, assuming $n_s = 5.5$ for the solvated Na^+ ion) is $\zeta = 0.03$. Figure 5.8.3 shows the performance plots under these conditions, as described in Section 2.1. For simplicity, $\eta_p = 1$.

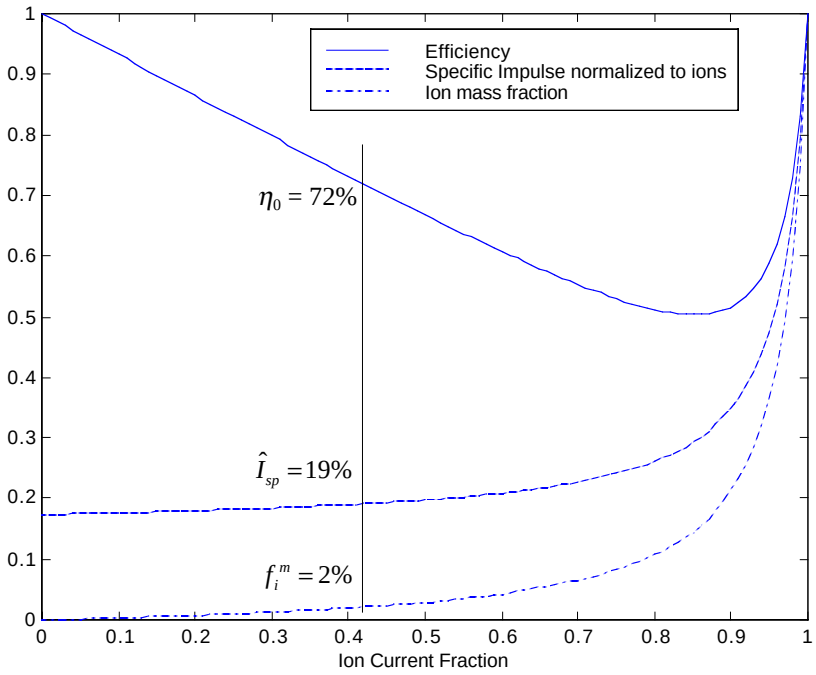

Figure 5.8.3. Efficiency, normalized specific impulse and mass ion fraction with $\zeta = 0.03$ and $\eta_p = 1$

An ion current fraction of $f_i = 0.42$ is extracted from Figure 5.8.2. It is seen that this particular mixture of droplets and ions does not improve the specific impulse in any appreciable way with respect to a pure droplet beam. This is evident from the very low ion mass fraction. Furthermore, the only parameter that changes considerably is the

efficiency, which drops to 72%. As indicated earlier in the second chapter, it appears that there is no benefit in operating colloid thrusters in the ion-droplet mixed regime for small ion fractions.

On the other hand, for large ion fractions the specific impulse and the mass ion fraction improve considerably. As discussed in Chapter 3, ion emission increases as the ratio Q/K gets smaller. In principle the same thruster could be used to achieve the performance indicated for high ion fractions by just decreasing the flow rate. Figure 5.8.4 shows the result of reducing the flow rate ($Q = 0.02$ nl/s) while maintaining all other parameters invariant.

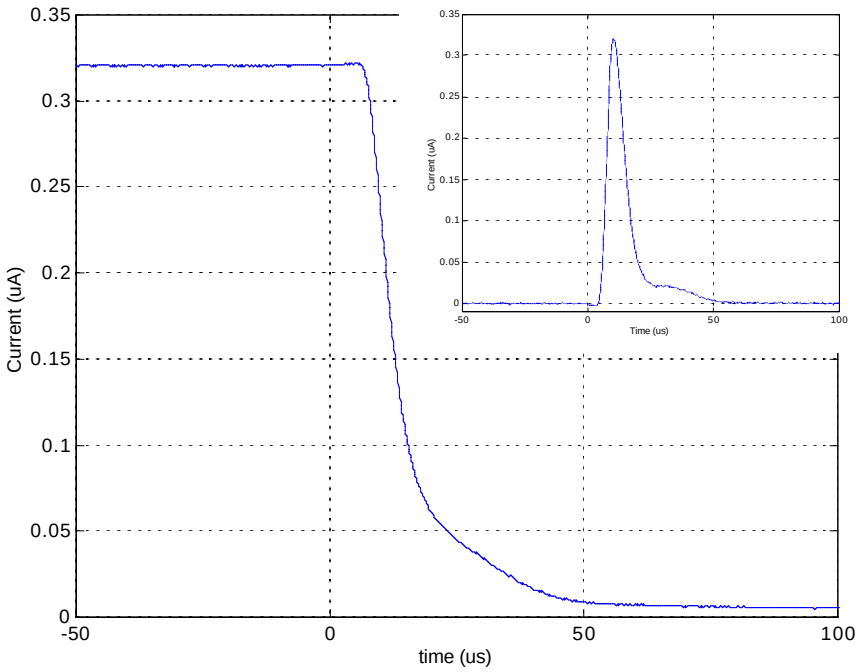

Figure 5.8.4. TOF for formamide + NaI with Q = 0.02 nl/s, $\phi_a = \phi_{ex}$ = 1020 V, and ϕ_f = 1058 V, for a 5 μm ID emitter. Detector distance = 23 cm

The inset placed in the upper right corner represents the derivative of the TOF curve, normalized to show the magnitude of the total current. This can be used to compute with more precision the ion fraction, which has increased considerably, to 93%. Not only are there many more ions in this mixture, but also the remaining droplets hold more specific charge, since their flight times became shorter. The droplet to ion specific charge ratio is close to $\zeta = 0.04$. This means that, under these conditions, the specific charge of the remaining droplets is in excess of 10 C/gr, which is the largest value achieved so far in experiments of this kind.

The performance plots in this case are shown in Figure 5.8.5.

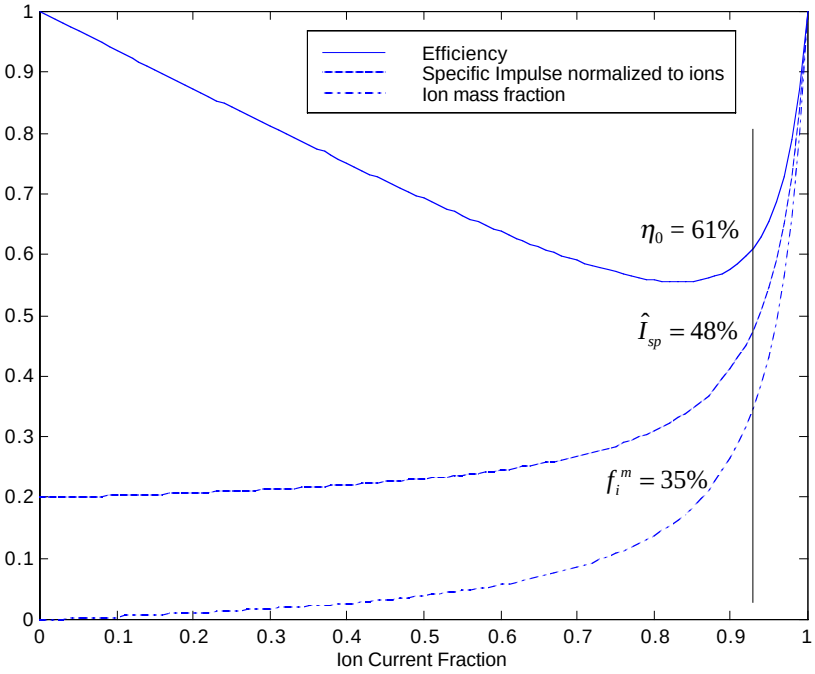

Figure 5.8.5. Efficiency, normalized specific impulse and mass ion fraction with ζ = 0.04 and η_p = 1

If a thruster efficiency of 61% can be tolerated, this operation mode has some definite advantages. For instance, the specific impulse is about half of the ion specific impulse, and 35% of the mass is taken out by the extracted ions.

These two cases demonstrate the ability of a single thruster to operate in two very different modes. In principle, the flow rate could be increased slightly more than in the first case to obtain a pure droplet beam with a specific impulse of about 200 sec. On the other hand, half of the ion specific impulse in the second case represents about 1300 sec of specific impulse. Practically every value in between could be obtained, with a respective efficiency penalty.

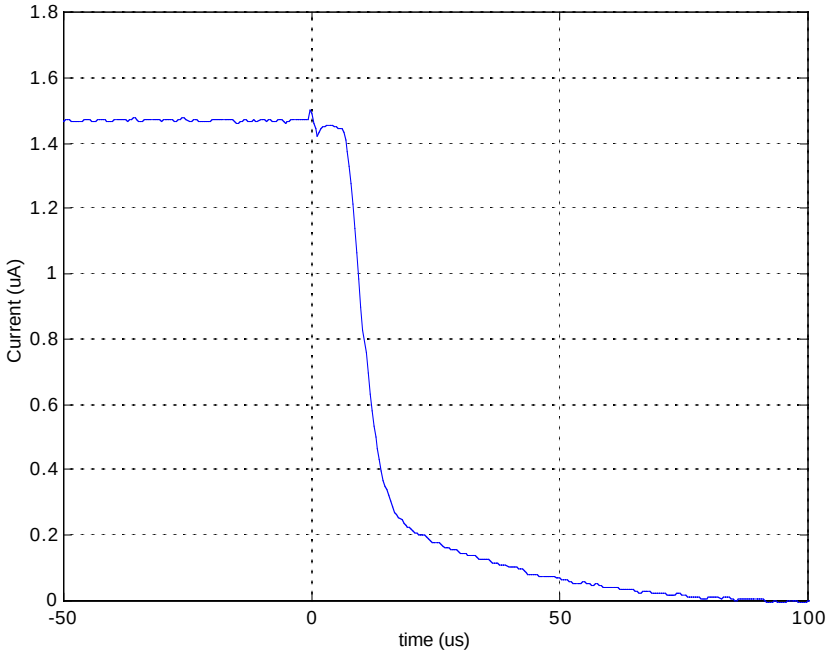

Figure 5.8.6. TOF for formamide + NaI with Q = 0.12 nl/s, ϕ_a = 1020 V, ϕ_x = -700 V, ϕ_{ex} = 1720 V, and ϕ_f = 1058 V, for a 5 µm ID emitter. Detector distance = 23 cm

Finally, a third case is analyzed, in which the flow rate was kept constant, but the extractor voltage was increased so that the highly stressed regime was achieved. As discussed in Section 5.6, high ion fractions can be obtained this way. Figure 5.8.6 shows a TOF with an extractor voltage of $\phi_x = -700$ V.

The droplet tail extends gradually into longer flight times, thus reducing the droplet to ion specific charge ratio to $\zeta = 0.025$. Once more, the ion fraction increases considerably, reaching 90%. To keep the flight times similar in the three cases, only the extractor voltage was varied. In a real thruster, the applied voltage could be increased with respect to the spacecraft potential to obtain higher specific impulses. The performance curves for this case are shown in Figure 5.8.7.

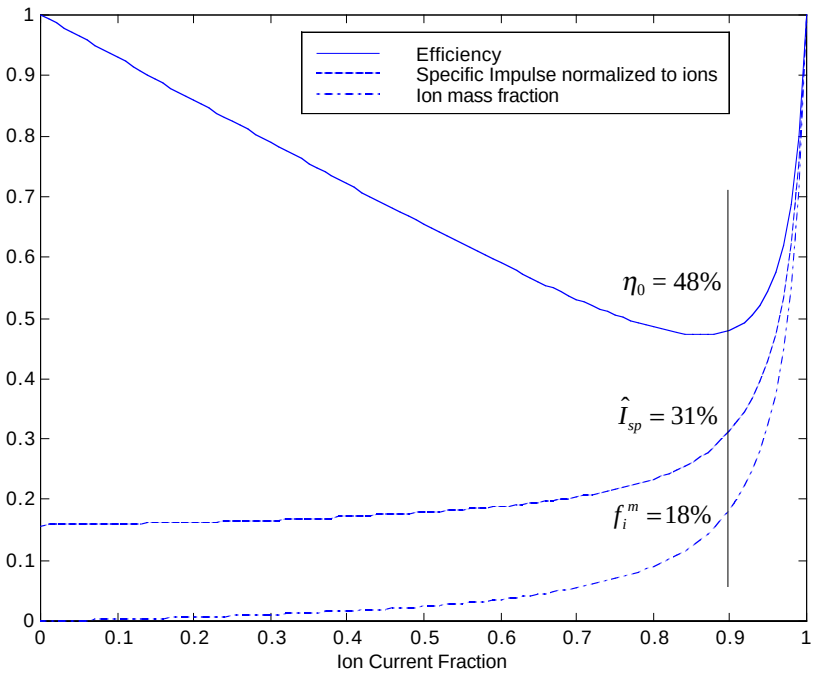

Figure 5.8.7. Efficiency, normalized specific impulse and mass ion fraction with ζ = 0.025 and η_p = 1

The efficiency penalty is more severe in this case, reaching 48%. Only 18% of the mass ejected is in the form of ions. These experiments were made under conservative voltages to keep the needle to extraction potential smaller than 2 kV. In principle, however, it should be possible to increase the potential above these values to obtain larger currents, thus moving the performance lines towards higher ion fractions and obtaining higher efficiency and specific impulse.

6. Conclusions and Recommendations

The underlying physics governing the behavior of electrospray sources is simple in nature. It is the work of scientists and engineers to transform this simplicity into a working device, in this case, for space propulsion applications. But as in many other examples in the natural world, simplicity is deceiving in the sense that it is not enough for something to work, but for it to be useful, it needs to work as expected. It needs to be predictable and controllable. This is precisely the case of colloid thrusters.

Before implementation into actual flight hardware, the thruster needs to be validated in the laboratory. Tests and evaluations are part of every new technology. Even before these steps, the basic working principles must be well understood allowing the development of models and theories useful to predict the performance and general characteristics of the new engine.

The main idea behind this research project is to increase the understanding of the fundamental operational issues of colloid thrusters, in particular their emissions. The core of the work lies in the experimental area described in chapters 4 and 5. Working with micro and nano sprays is something difficult and delicate to do. Experiments have to be performed with care and patience in order to obtain consistent, useful results. This is especially true if it is desired to obtain beams in the ion-droplet mixed regime, which is

perhaps the most interesting to work with since a good part of the flexibility promises of colloid thrusters come from this operational mode.

Many experiments performed here deal with beams in this mixed regime. It is found that the ion emission physics is quite complex and depends strongly on the laboratory conditions. In particular, the energy structure of beams in this regime has been explored. The richness of this structure has motivated the development of new hypotheses to explain its origin.

There are differences between the ion emission process in electrosprays and in liquid metal ion sources (FEEP), in particular the energy spread, which is much smaller in the case of liquid metals at low currents. It is interesting, however, to inquire about the origin of these differences. The underlying physics governing the two technologies is basically the same. The equilibrium forces that give form to the conical structure in both cases are the electric stresses and the surface tension. The fundamental difference is perhaps related to the charge transport mechanism. In the base of the cone, charge transport is mainly due to bulk conduction while, in the case of an electrospray, it gradually changes to surface convection in the transition region that forms the high velocity jet. Convection is generated by tangential electric fields that modify the potential distribution along the liquid surface, thus generating the energy spread observed in the experiments. In liquid metals there is a very small convective contribution since no continuous jet is formed. This may be one of the reasons for the small energy spreads observed in liquid metals.

If electrosprays and liquid metals share the same physical mechanics, then they should not be treated as separate technologies and, in fact, they should approach each other under certain conditions. It appears that such condition is given when reducing the ratio Q/K in electrosprays. This increases the amount of ions that are emitted from a Taylor cone, but it is not evident that this reduction alone reduces the energy spread. It would be interesting to keep on reducing the value of this ratio until pure ion emission is reached, but as discussed in Chapter 5, it is hard to increase the ion fraction in formamide solutions above ~95%, since at such flow rates the electrospray cone is marginally stable

and collapses before a pure ionic regime is reached. On the other hand, Taylor cones made out of ionic liquids have the amazing property of remaining stable at very low flow rates, even at smaller conductivities than highly doped formamide, and it is relatively easy to reach a pure ionic regime with them [52]. As pointed out in Chapter 5, in this regime, the energy spread is reduced significantly, approaching that of liquid metals. This can be the best indication that the emission mechanics in liquid metals reduces to that of electrosprays under these conditions. The physics is the same, the liquid properties, however, are so different that not every substance can be operated in the complete operational range from pure ionic to pure droplet emission.

All these findings will be of great importance when selecting a design and a propellant for space propulsion. For now, it appears that ionic liquids give the greatest flexibility. It is a matter of future work to develop the best thruster design using these liquids.

The experimental techniques developed here will be very useful in providing a full characterization of beams emitted from colloid thrusters using the selected propellant. Some of these techniques can be improved in order to increase the amount and quality of relevant data. In particular, the use of the *channeltron* seems to be an excellent alternative to study ion beams with very high resolutions. There are other electron multiplier devices, like the *micro-channel plates*, that have the potential of increasing even further the gain characteristics of the channeltron. Some of them have electro-sensitive phosphor screens that allow a direct visualization of the beam pattern.

To improve the resolution in the ion identification experiments, energy sensitive components can be added to the system, like the *electrostatic mirror* [79], which has the capability of reducing the energy spread of particle beams by compensating the difference in velocities with the difference in penetration depth into the mirror body.

Additional signal to noise ratio improvements can be achieved if *interleaved comb* electrostatic gates [63,64] are used in the purely ionic regime. As mentioned before, very fine closely spaced wires ease the voltage requirements from the pulsing module, thus

reducing capacitive coupling noise. This, along with the high gains of electron multipliers, opens the possibility of studying ion beams with the dual gate system described in Chapter 4.

There are several experimental contributions produced in this work, among them, the use of small capillary needles (5 μm) to minimize liquid evaporation in vacuum tests, allowing the extraction of highly charged nano-droplets (>10 C/gr), and the introduction and characterization of ion optics for beams in the ion-droplet mixed regime. The results concerning the energy distribution in colloid beams are important in their own right. It is found that there are at least three energy gaps, two of which overlap. In one of them (high-energy particles), droplets and ions emitted from the cone-jet transition region share similar energy characteristics. In the second, ions with smaller energies are emitted probably from this region as well, since no loss in ion potential continuity is observed, i.e., they appear to overlap with ions with higher energies. Finally, ions with significantly less energies are observed, these might come from the jet breakup region, where the normal electric field reaches a local maximum given the small radii of curvature produced during the droplet formation process.

As mentioned in the introduction, besides presenting experimental techniques and results, this research tries to justify whether colloid thrusters can be considered as a viable alternative for space propulsion. All evidence points in the direction that this is the case. Nevertheless, there are some issues that require some work before implementing colloid thrusters for in-space applications:

- **Propellant**: As widely discussed in previous chapters, the propellant needs to be compatible with space conditions, namely, it should be hard to evaporate, but if it does, it should not leave solid residues behind, or freeze [80,81], thus clogging transfer lines. It is also unclear what are the effects of long-term exposure of organic liquids to space radiation. Regardless, ionic liquids or mixtures of low vapor pressure solvents such as formamide with ionic liquids seem to be the best alternative. In any case, lifetime tests under simulated space conditions need to be

conducted to determine the chemical stability of propellants and track any changes in the performance during long operation times.

- **Fluid delivery**: Flow rate is the most important parameter in colloid thruster operations. It needs to be precisely controlled and the way to do it should be lightweight, simple, small and energy-efficient. In the end, the best solution to this problem could be to design a system to deliver exactly the demanded flow rate as given by easily measurable quantities, such as emitter size, extraction voltages and liquid properties.

- **Neutralization**: As briefly discussed in Chapter 3, electric propulsion thrusters, colloids included, require a way to neutralize the excess charge accumulated in the spacecraft due the emission of one ionic polarity. Given the low levels of current involved, the use of cold emission cathodes is an alternative to balance the charge of positive beams. It is also possible, at least in principle, to operate in bi-polar mode, where positive and negative charges are emitted either simultaneously or in closely spaced intervals. Laboratory validation of these operation modes is still required, especially in the ion-droplet mixed regime.

- **Spacecraft contamination**: Satellite manufacturers and operators are strongly concerned about the effects that thruster emissions may have on spacecraft materials and subsystems. In reality, this is usually the most relevant test for any new propulsion device. It is unclear what will be the consequences if colloid emissions collide with the vehicle's surfaces. Volatile liquids will probably evaporate, leaving salts behind, while ionic liquids working in a droplet regime, would accumulate in the surface, perhaps forming a thin layer. Analysis similar to those performed with other type of electric thrusters will be required to determine charged particle trajectories and possible backflows to the spacecraft surface.

Appendix A: Legendre Functions of Order 1/2

As mentioned in Section 3.1, the solution to Taylor's problem involves the use of Legendre functions of order 1/2. $P_{1/2}(\cos\alpha)$ is known as the Legendre Polynomial of order 1/2, while $Q_{1/2}(\cos\alpha)$ is the Legendre function of second kind of order 1/2. These are not commonly used functions, but they can be put in terms of more familiar mathematical entities, for example, in terms of complete elliptic integrals,

$$\begin{aligned} P_{1/2}(x) &= \frac{2}{\pi}\left[2E\left(\sqrt{\frac{1-x}{2}}\right) - K\left(\sqrt{\frac{1-x}{2}}\right)\right], \\ Q_{1/2}(x) &= K\left(\sqrt{\frac{1+x}{2}}\right) - 2E\left(\sqrt{\frac{1+x}{2}}\right), \end{aligned} \tag{A.1}$$

where K and E represent the complete elliptic integrals of the first and second kind, respectively defined as,

$$\begin{aligned} K(m) &= \int_0^{\pi/2}\left(1 - m\sin^2\theta\right)^{-1/2} d\theta, \\ E(m) &= \int_0^{\pi/2}\left(1 - m\sin^2\theta\right)^{1/2} d\theta. \end{aligned} \tag{A.2}$$

These Legendre functions, as given by (A.1), can be numerically evaluated and plotted as functions of α for $x = \cos\alpha$, as shown in Figure (A.1). Taylor's solution outside of the perfect conductor cone can be given either by $P_{1/2}(\cos\alpha)$ or $Q_{1/2}(\cos\alpha)$ depending on the particular selection of the origin of the angular variable in the coordinate system. In the case of Section 3.1, the $P_{1/2}(\cos\alpha)$ function was eliminated since it becomes singular outside of the cone at $\alpha = \pi$. On the other hand, if the angle α had been taken from the $-z$ direction as in Figure 3.1.2, the correct finite solution will require the elimination of the $Q_{1/2}(\cos\alpha)$ function, which is singular at $\alpha = 0$; outside of the cone in this case. This

means that both functions must be equivalent regardless of the origin selection. Since $x = \cos\alpha$, it can be easily verified using (A.1) that,

$$Q_{1/2}(\cos\alpha) = -\frac{\pi}{2} P_{1/2}[\cos(\pi - \alpha)], \tag{A.3}$$

thus proving that, up to a constant factor, both solutions are identical.

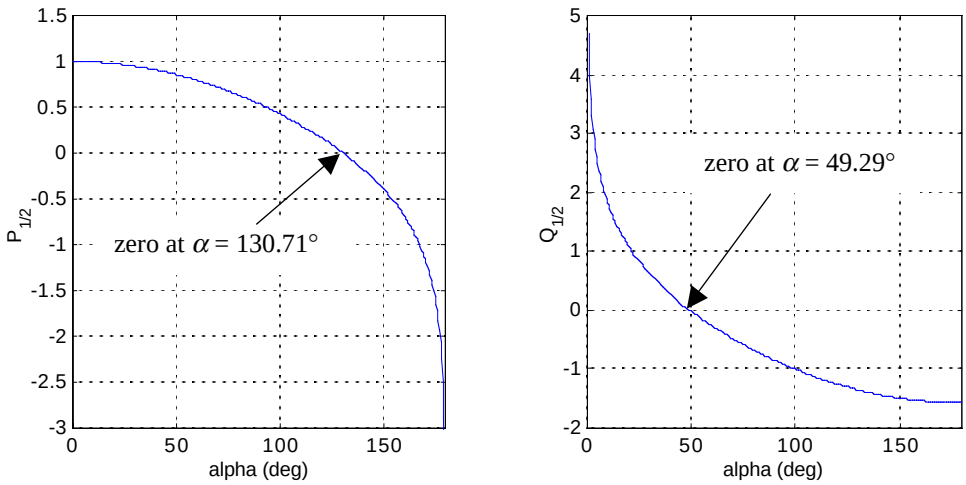

Figure A.1. Plots of Legendre polynomials of order 1/2 as functions of α

Appendix B: Capacitive Coupling

Whenever a conductive surface quickly changes its potential, there will be some radiation that can be detected by adjacent elements. In the case of TOF experiments, high-speed, high-voltage amplifiers power the electrostatic gates, while the detected signals come from metallic collectors. The high-frequency harmonic components of these pulsed signals induce some spurious voltages in the detector, which are then amplified by the electronics, contaminating the measured signals. Fortunately, this noise is not random in nature, since it depends on the geometrical arrangement of conductive elements, the physical characteristics of the transmission lines and the response of the electronic equipment. As long as the experimental characteristics remain fixed, the nature of the noise will remain, in general, unchanged. This fact can be exploited to extract useful signals from contaminated measurements.

To clean up the signal, the first step is to characterize the noise in the time domain. This is simply done by activating all the electronic components in the experimental set up without measuring the relevant signal. In the case of electrosprays, the relevant signal comes from the charged particle beam, as it drifts from the emitter towards the detector. If the liquid flow is blocked, then only the induced noise is recorded. An example of capacitive noise for a given arrangement is shown in Figure B.1.

This noise will be present in every TOF measurement performed with the same experimental characteristics. Figure B.2 shows a TOF without noise processing. As can be seen, the capacitive coupling time response is comparable to the flight time of the fastest particles in the beam. A simple way to eliminate the noise contribution from the TOF spectrum is to simply subtract its recorded signal. The result of using this procedure is shown in Figure B.3.

It must be remembered that this procedure is effective only when the experimental conditions remain fixed. If they change, then a new noise characterization is required.

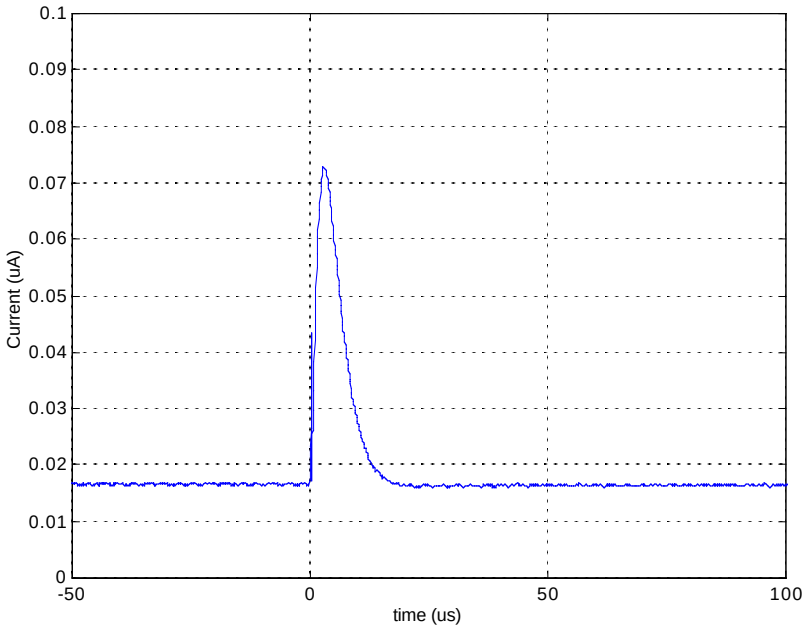

Figure B.1. Recorded capacitive noise signal

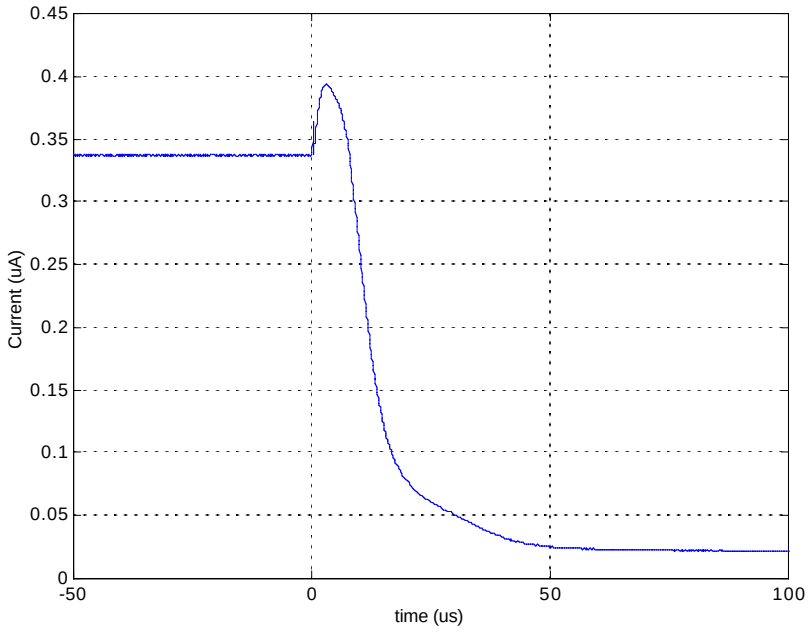

Figure B.2. TOF signal without processing

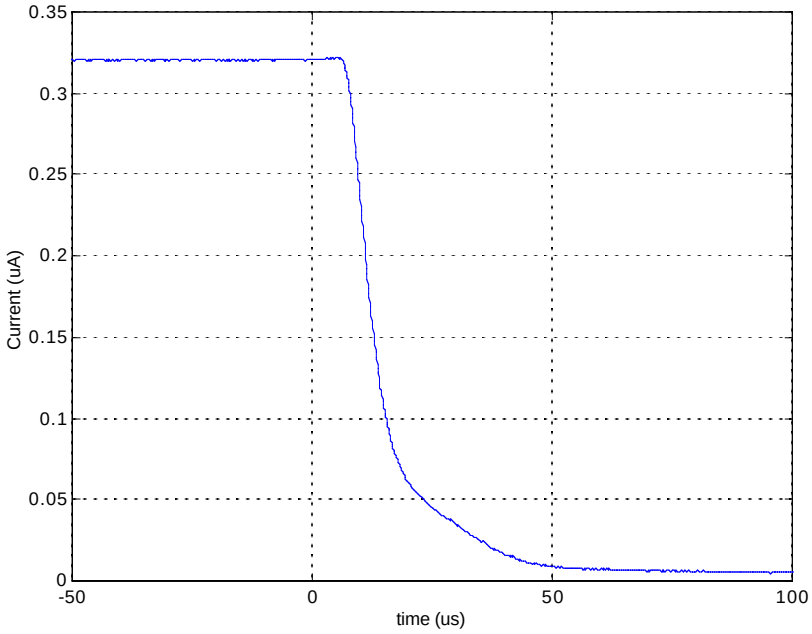

Figure B.3. TOF signal after processing

References

1. Palaszewski, B., *Atomic hydrogen propellants: historical perspectives and future possibilities*, NASA-TM-106053, N93-20614, 31st Aerospace Science Meeting, Reno, Nevada, January, 1993.

2. Krohn Jr., V.E., *Liquid metal droplets for heavy particle propulsion*, in Progr. in Astronautics and Rocketry, A.C. Press, N.Y. – London, Vol. 5 (1961).

3. Krohn Jr., V.E., *Glycerol droplets for electrostatic propulsion*, ARS Electric propulsion conference, Berkeley, CA, 1962.

4. Hendricks, C.D. and Pfeifer, R., *Parametric studies of electrohydrodynamic spraying*, 5th AIAA Electric Propulsion Conference, San Diego, California, March 1966.

5. Hunter, R.E., *Theoretical considerations on non-uniformly charged expellant beams*, ARL TN-60 136, Aug., 1960.

6. Kidd, P.W., and Shelton, H., *Life test (4350 hours) of an advanced Colloid thruster module*, 10th AIAA Electric Propulsion Conference, Lake,Tahoe, Nevada, October 1973.

7. Cohen, E., Somol, C.J. and Gordon, D.A., *A 100 kV, 10-W heavy particle thruster*, AIAA 65-377, 2nd annual meeting, S. Francisco, CA, 1965.

8. Perel, J., et al., *Research on a charge particle bipolar thruster*, AIAA 67-728, Electric propulsion and plasmadynamics conference, Colorado Springs, CO, 1967.

9. Mahoney, J.F., Daley, H.L. and Perel, J., *Performance of Colloid annular emitters*, 10th AIAA Electric Propulsion Conference, Lake Tahoe, Nevada, October 1973.

10. Daley, H.L., Mahoney, J.F., and Perel, J., *Colloid annular array thruster development*, 10th AIAA Electric Propulsion Conference, Lake Tahoe, Nevada, October 1973.

11. Fernández de la Mora, J. and Loscertales, I.G., *The current emitted by highly conducting Taylor cones*, J. Fluid Mech (1994), vol. 260, pp. 155-184.

12. Huberman, M.N. and Rosen, S.G., *Advanced high-thrust Colloid sources*, J. Spacecraft, Vol. 11, No. 7, July 1974.

13. Shtyrlin, A.F., *State of the art and future prospects of Colloidal electric thrusters*, IEPC, 1995.

14. Reichbach, J., *Micropropulsion system selection for precision formation flying satellites*, Master of Science Thesis, MIT Aero/Astro, 2001.

15. Reichbach, J.G., Sedwick, R.J. and Martínez-Sánchez, M., *Micropropulsion system selection for precision formation flying satellites*, 37th JPC, Salt Lake City, Utah, July 2001.

16. Fenn, J.B., Mann, M., Meng, C.K., Wong, S.K. and Whitehouse, C., *Electrospray ionization for mass spectrometry of large biomolecules*, Science, **246**, 64-71, 1989.

17. Krutchinsky, A.N., Chernushevich, I.V., Spicer, V.L., Ens, W. and Standing, K.G., *Collisional damping interface for an electrospray ionization time-of-flight mass spectrometer*, J. A. Soc. Mass Spectrom., 1998, 9, 596-579.

18. Rosell-Llompart, J. and Fernández de la Mora, J., *Generation of monodisperse droplets 0.3 to 4 μm in diameter from electrified cone-jets of highly conducting and viscous liquids*, J. Aerosol Sci., Vol 25, No 6, pp. 1093-119, 1994.

19. De Juan, L. and F. de la Mora, J., *Charge and size distributions of electrospray drops*, J. of Colloid and Interface Sc., Vol. 186, 280-293 (1997).

20. Fish, B.R., *Electrical generation of natural aerosols from vegetation*, Science 175:123 9-40, 1972.

21. Khayms, V., *Advanced propulsion for microsatellites*, PhD. Thesis, MIT Aero/Astro, 2000.

22. Paine, M., *Design study for a microfabricated Colloidal thruster*, Master of Science Thesis, MIT Aero/Astro, 1999.

23. Velasques, L., Akinwande, A.I. and Martínez-Sánchez, M., *A microfabricated colloidal thruster array*, AIAA-2002-3810.

24. Tang, K., Lin, Y., Matson, D. W., Kim, T. and Smith, R. *Generation of Multiple Electrosprays Using Microfabricated Emitter Arrays for Improved mass Spectrometric Sensitivity* Anal. Chem. 2001, 73, 1658-1663.

25. Taylor, G.I., *Disintegration of water drops in an electric field*, Proc. R. Soc., London A 280, 383-397.

26. Martínez-Sánchez, M., *Colloid thrusters for micro and nano-satellites*, Subcontractor Interim Report to Busek Co. Inc.

27. Rayleigh, Lord, *On the equilibrium of liquid conducting masses charged with electricity*, Philosophical magazine, XIV, pp. 184-186, 1882.

28. Fernández de la Mora, J., *On the outcome of the coulombic fission of a charged isolated drop*, J. of Colloid and Interface Sc., Vol. 178, 209-218 (1996).

29. Barrero, A., Gañán-Calvo, A.M., Davila, J., Palacio, A. and Gomez, E., *Low and high Reynolds number flows inside Taylor cones*, Phys. Rev. E, Vol 58, No 6, Dec. 1998.

30. Eggers, J., *Nonlinear dynamics and breakup of free-surface flows*, Rev. Mod. Phys., Vol. 69, No. 3, July 1997.

31. Kingham, D.R. and Swanson, L.W., *Shape of a liquid metal ion source*, Appl. Phys. A 34, 123-132 (1984).

32. Gañán-Calvo, A. M. *On the theory of electrohydrodynamically driven capillary jets*. J. Fluid Mech., vol. 335, pp. 165-188, 1997.

33. Gañán-Calvo, A. M. *Cone-Jet Analytical Extension of Taylor's Electrostatic Solution and the Asymptotic Universal Scaling Laws in Electrospraying*, Phys. Rev. Let., Vol 79, No 2, July 1997.

34. Pantano, C., Gañán-Calvo, A. M. and Barrero, A. *Zeroth-order, electrohydrostatic solution for electrospraying in cone-jet mode* J. Aerosol Sci. Vol. 25, No. 6. pp 1065-1077, 1994.

35. Carretero, J. and Martínez-Sánchez, M., *Quasi-one-dimensional Numerical Simulation of a Single-Emitter Colloidal jet*, Indianapolis, Indiana, 38 th JPC Jul 2002.

36. Higuera, F.J., *Flow rate and electric current emitted by a Taylor cone*, J. Fluid Mech., *under consideration.*

37. Glasstone, S. and Laidler, K. J. *The theory of rate processes* McGraw-Hill Book Company, Inc. New York and London, 1941.

38. Martínez-Sánchez, M., personal communication.

39. Iribarne J.V., and Thomson, B.A., *On the evaporation of small ions from charged droplets*, J. of Chem. Phys., Vol 64, No 6, March 1976.

40. Fernández de la Mora, J. and Loscertales, I.G., *Experiments on the kinetics of field evaporation of small ions from droplets*, J. Chem. Phys., (**103**), 12, Sept., 1995.

41. Gamero-Castaño, M. and Fernández de la Mora, J., *Direct measurement of ion evaporation kinetics from electrified liquid surfaces*, J. of Chem. Phys., Vol 113, No 2, July 2000.

42. Mahoney, C. and Prewett, P.D., *Field emission deposition: ion assisted deposition using liquid metal sources*, Vacuum, Vol 34, No 1-2, 301-304, 1984.

43. Prewett P.D. and Mair G.L.R., *Focused ion beams from liquid metal ion sources*, Research Studies Press, 1991.

44. Fernández de la Mora, J., *The effect of charge emission from electrified liquid cones*, J. Fluid Mech., (1992), Vol 243, pp. 561-574.

45. Amos, R. J., Evans, G. A. and Smith, R. *High Accuracy ion optics computing*. Vacuum Vol. 36 Num 11/12. pp. 945-952 1986.

46. Ward, J. W. and Seliger, R. L. *Trajectory calculations of the extraction region of a liquid-metal ion source* J. Vac. Sci. Technol., 19(4), Nov./Dec. 1981.

47. Kang, N. K., Orloff, J., Swanson, L. W. and Tuggle, D. *An improved method for numerical analysis of point electron and ion sources optics* J. Vac. Sci. Technol. 19(4), Nov./Dec. 1981 pp. 1077-108.

48. Szilágyi, Miklos, "Electron and ion optics", Plenum Press, 1988.

49. Nagy, G. A. and Szilágyi *Introduction to the theory of space-charge optics* John Wiley & Sons, New York 1974

50. Stern T.E., Gossling, B.S., Fowler, R.H., *Further studies in the emission of electrons from cold metals*, Proc. Roy. Soc., A124 (1929) 699.

51. Driesel, W., Dietzsch, Ch. and Mühle, R., *In situ observation of the tip shape of AuGe liquid alloy ion sources using a high voltage transmission electron microscope*, J. Vac. Sci. Technol. B, Vol 15, No 5, Sep/Oct 1996.

52. Romero, I., Bocanegra, R., Fernández de la Mora, J. and Gamero-Castaño, M., *A pure ionic source without drop emission from Taylor cones of ionic liquids*, Prepared for submission to J. Appl. Phys.

53. Cotter, R.J., *Time-of-flight mass spectrometry*, American Chemical Society, 1997.

54. Knorr, F.J., Ajami, M. and Chatfield, D.A., *Fourier transform time-of-flight mass spectrometry*, Anal. Chem., 1986, 58, 690-694.

55. Issendorff, B. von and Palmer, R.E., *A new high transmission infinite range mass selector for cluster and nanoparticle beams*, Rev. Sci. Instr., Vol 70, No 12, Dec. 1999.

56. Brock, A., Rodriguez, N. and Zare, R.N., *Characterization of a Hadamard transform time-of-flight mass spectrometer*, Rev. Sci. Instr., Vol 71, No 3, March 2000.

57. Guilhaus, M., *The return or time-of-flight to analytical mass spectrometry*, Adv. in mass Spectroscopy, Vol 13, 1994.

58. Gamero-Castaño, M. and Hruby, V., *Electrospray as a source of nanoparticles for efficient Colloid thrusters*, J. of Propulsion and Power, Vol 17, No 5, Sept-Oct 2001.

59. Fernández de la Mora, J., *Effect of background gas on the current emitted from Taylor cones*, J. of Colloid and Interface Sc., Vol. 171, 512-517 (1995).

60. Hruby, V., Gamero-Castaño, M., Cordero, J., Kolencik, J. and Martínez-Sánchez, M., *Colloid Thrusters for micro and nano-satellites*, Final report, Phase I SBIR NASA, July 1999.

61. Colman, R. A. and Legge, G. J. *Measurement of the optical properties of an asymmetric Einzel lens using the two-grid method* J. Appl. Phys. 74(3), 1 August 1993

62. Lozano, P. and Martínez-Sánchez, M., *The effect of using finite-width electrostatic gates in time-of-flight measurements for Colloid thrusters*, 27th IEPC, Pasadena, CA, October 2001.

63. Vlasak, P.R., Beussman, D.J., Davenport, M.R. and Enke, C.G., *An interleaved comb ion deflection gate for m/ z selection in time-of-flight mass spectrometry*, Rev. Sci. Instrum. 67 (1), January 1996.

64. Kimmel, J. R., Engelke, F. and Zare, R. N. *Novel method for the production of finely spaced Bradbury-Nielson gates* Review of Scientific Instruments Vol. 72, Num. 12 pp.4354-4357, December 2001.

65. Holbrey, J.D. and Seddon, K.R., *The phase behaviour of 1-alkyl-3-methylimidazolium tetrafluoroborates; ionic liquids and ionic liquid crystals*, J. Chem. Soc., Dalton Trans., 1999, 2133-2139.

66. Huddleston, J., Visser, A.E., Reichert, W.M., Willauer, H.D., Broker, G.A. and Rogers, R.D., *Characterization and comparison of hydrophilic and hydrophobic room temperature ionic liquids incorporating the imidazolium cation*, Green Chemistry, 2001, **3**, 156-164.

67. Welton, T., *Room temperature ionic liquids. Solvents for synthesis and catalysis*, Chem. Rev. 1999, 99, 2071-2083.

68. McEwen, A.B., Ngo, H.L., LeCompte, K. and Goldman, J.L., *Electrochemical Properties of Imidazolium Salt Electrolytes for Electrochemical Capacitor Applications*, Journal of The Electrochemical Society, 146 (5) 1687-1695 (1999).

69. Lozano, P. and Martínez-Sánchez, M., *Jets and sprays emitted from Colloid thrusters – experiments and modeling*, Proc. 3rd Int. Conf. on Spacecraft Propulsion, Cannes, 2000, ESA SP-465.

70. Lozano, P., Martínez-Sánchez, M., *Experimental Study of Colloid Plumes*, 37th JPC, Salt Lake City, Utah, AIAA 2001-3334.

71. Gamero-Castaño, M. and Hruby, V., *Electric measurements of charged sprays emitted by cone-jets*, J. Fluid Mech., (2002), Vol 459, 245-276.

72. Lozano, P. and Martínez-Sánchez, M. *Experimental Measurements of Colloid Thruster Plumes in the Ion-Droplet Mixed Regime* 38th JPC, Indianapolis, Indiana, July, 2002.

73. Gamero-Castaño, M., *Electric-Field Induced Ion Evaporation from Dielectric Liquid*, Physical Review Letters, Vol. 89, No. 14, September 2002.

74. *Handbook of Chemistry and Physics*, CRC Press, 67th Edition, 1986-1987.

75. Martínez-Sánchez, M., F. de la Mora, Hruby, V., Gamero-Castaño, M. and Khayms, V., *Research on Colloid Thrusters*, 26th IEPC, Kitakyusgu, Japan, October, 1999.

76. Matsumura, H., Mafune, F. and Kondow, T., *Formation of NaI aggregates on Ethanol solution surface*, J. Phys. Chem, B 1999, 103, 838-843.

77. Chiu, Y. and Dressler, R., *Mass Spectrometric Analysis of Nano-Electrojet Ion Emission*, Colloid Thruster/Nano Electrojet Workshop, Cambridge, MA- October 3-4, 2002.

78. F. de la Mora, J., personal communication.

79. Vialle, J. L., Baguenard, B., Bourgey, A., Cottancin, E., Lermé, J., Palpant, B., Pellarin, M., Valadier, F. and Broyer, M. *A cylindrical reflectron time-of-flight mass spectrometer* Rev. Sci. Instrum. 68 (6), June 1997.

80. Hall, C.A. and Mackie, C., *Semi-analytic solutions for freezing induced by evaporative cooling*, Int. J. of Heat and Mass Tr., Vol. 44, (2001) 1161-1170.

81. Di Marzo, M., Tartarini, P., Liao, Y., Evans, D. and Baum, H., *Evaporative cooling due to a gently deposited droplet*, Int. J. of Heat and Mass Tr., Vol. 36, No. 17 (1993) 4133-4139.